Internal Report
DESY F15-90-03
July 1990

$\pi^+\pi^-\gamma$ and K^+K^- Production in Two Photon Collisions at ARGUS

by

K. W. McLean

$\pi^+\pi^-\gamma$ and K^+K^- Production in Two Photon Collisions at ARGUS

Kenneth William McLean

June, 1990

A Thesis submitted to the Faculty of Graduate Studies and Research in partial fulfillment of the requirements for the degree of Doctor of Philosophy in Physics

Department of Physics
McGill University, Montreal

Abstract

The production of the final states K^+K^- and $\eta' \to \pi^+\pi^-\gamma$ in $\gamma\gamma$ collisions has been measured using the ARGUS detector. The product $\Gamma_{\gamma\gamma}(\eta')\mathrm{Br}(\eta' \to \rho\gamma)$ has been determined. The topological cross section for the production of charged kaon pairs in two-photon collisions has been measured and the $\gamma\gamma$-widths and interference parameters for the tensor mesons $f_2(1270)$, $a_2(1320)$ and $f_2'(1525)$ have been extracted. The helicity structure assumed for the K^+K^- continuum contribution has a significant effect on the result. Upper limits have been obtained for the $\gamma\gamma$-widths of the glueball candidate states $f_2(1720)$ and X(2230).

Sommaire

Le production des états finaux K^+K^- et $\eta' \to \pi^+\pi^-\gamma$ lors de collisions $\gamma\gamma$ a été mesurée à l'aide du détecteur ARGUS. Le produit $\Gamma_{\gamma\gamma}(\eta')\mathrm{Br}(\eta' \to \rho\gamma)$ a été déterminé. La section efficace topologique pour la production de paires de kaons chargés lors de collisions à deux photons a été mesurée et la largeur $\gamma\gamma$ ainsi que les paramètres d'interférence des mésons tensoriels $f_2(1270)$, $a_2(1320)$, et $f_2'(1525)$ en ont été déduits. Les paramètres d'hélicité présumés pour la contribution du continuum de K^+K^- ont un effet significatif sur les résultats. Des limites supérieures ont été obtenues pour les largeurs $\gamma\gamma$ des états possibles de "glueball": $f_2(1720)$ et X(2230).

Kurzfassung

Die Produktion von Endzuständen K^+K^- und $\eta' \to \pi^+\pi^-\gamma$ in $\gamma\gamma$-Kollissionen ist mit dem Detektor ARGUS gemessen worden. Das Produkt $\Gamma_{\gamma\gamma}(\eta')\mathrm{Br}(\eta' \to \rho\gamma)$ wurde dabei bestimmt. Der topologische Wirkungsquerschnitt für geladene K-Mesonen-Paarproduktion ist gemessen worden, wobei die $\gamma\gamma$-Breiten und die Interferenzparametern für die Tensormesonen $f_2(1270)$, $a_2(1320)$ und $f_2'(1525)$ bestimmt worden sind. Es wurde auch festgestellt, daß die angenommene Helizitätsstruktur des K^+K^--Kontinuumbeitrags einen signifikanten Einfluss auf das Ergebnis hat. Zum Schluss sind obere Grenzen für die $\gamma\gamma$-Breiten von den Glueballkandidaten $f_2(1720)$ und X(2230) extrahiert worden.

ACKNOWLEDGEMENTS

The ARGUS collaboration has been a very productive one – I am grateful to have had the opportunity to participate. I would like to thank the members of the collaboration for their effort and skill in maintaining the detector and the analysis software – both items are highly complex and essential for good physics. I would also like to thank my thesis adviser, Popat Patel of McGill University, for his advice and abundant patience.

Michel Feindt (DESY) lent me his η' generator which confirmed the results of my own program. R. H. P. Kleiss, and P. H. Daverveldt of the Institute Lorenz, University of Leiden, provided several advanced programs for the simulation of QED final states in two-photon collisions. Andreas Philipp, Alf Nilsson (DESY), Yorgos Tsipolitis (McGill), and H. Kolanoski (Dortmund University) deserve gratitude for many helpful discussions and for sharing their expertise in two-photon physics. Alf Nilsson and Yorgos Tsipolitis were of particular help in maintaining contact with the experiment and its software when I was not resident at DESY. H. D. Schulz, Siegfried Weseler, and Klaus Strahl were of immense help in understanding the operation of the ARGUS trigger. In particular, H. D. Schulz provided the core programs, simulating the full LTF simulation, the summation of shower counter signals over trigger elements, and the basic trigger logic, around which the rest of the trigger simulation is built. Ulf Mathiesen and Rob Kutschke helped me to survive encounters with the various computer systems. I am also grateful to Paul Mercure for his efforts in maintaining the physics department's VAX cluster. I would like to thank McGill University and the Natural Sciences and Engineering Research Council for financial support.

As a guest for several years I wish to thank DESY for the hospitality extended to me, in particular J. Zilberkweit and the rest of the staff of the DESY Gästeburo. Finally, I would like to thank my parents and friends for their encouragement – I wish to extend special thanks to the other temporarily expatriate graduate students who enlivened my stay in Hamburg: Dave Gilkinson, Doug Gingrich, Shri Kanekal, Peter Kim, Rob Kutschke, Janis McKenna, Paul Padley, Henry Seywerd, and John Swain.

Contents

List of Figures

List of Tables

PREFACE

This work describes the results of a study of the production of resonant final states in $\gamma\gamma$ collisions. These measurements were made using the ARGUS detector. The first chapter is an introduction to particle physics and a summary of current experimental and theoretical knowledge of light meson production in $\gamma\gamma$ collisions. The second chapter describes the ARGUS detector and some of the general analysis software. The calculation of the detector acceptance and trigger efficiency is described in the third chapter, along with a detailed discussion of the systematic errors involved in extracting absolute cross sections. The last two chapters describe the analysis of the exclusive channels $\gamma\gamma \to \eta' \to \pi^+\pi^-\gamma$ and $\gamma\gamma \to f_2, a_2, f_2' \to K^+K^-$, respectively.

The first appendix is a list of the ARGUS collaboration, integrated over the period of the author's membership. The second appendix lists the papers published by the collaboration during this time. The QED derivations of the $\gamma\gamma$ luminosity and kinematics are included in appendix 3. The next two appendices review the techniques of Monte Carlo simulation and maximum-likelihood parameter estimation. The remaining appendices document programs developed for the analysis described in the body of the thesis: the ARGUS trigger analysis program, and the $\gamma\gamma$ event generator.

This document is intended to fulfill the requirements for a Doctoral Thesis at McGill University. The work described here was carried out between September 1984 and February 1990.

Chapter 1

Introduction

Modern experimental physics possesses two distinct aspects: the study of complex systems in which the fundamental interactions involved are thought to be understood, and the study of simple systems at extreme scales in search of unknown interactions and structure. The physics of high energy collisions is dominated by this second aspect – current experiments probe distance scales as small as 10^{-18} m, which correspond to energies of 100 GeV in the center of mass. This inverse relation between energy and distance scale makes intuitive sense, given wave/particle duality, in that particles with a smaller wavelength (higher frequency, $E = \hbar\omega$) are sensitive to smaller structures. This can also be understood as an application of the Heisenberg uncertainty principle: $\Delta P \Delta X \geq \hbar$, which implies that the larger the momentum transfer in an experiment the smaller the scale resolvable.

In practice, nothing is simple, and high energy physics is not an exception even in the attempt to set up the "simple systems" mentioned above. Quantum field theory implies that even the vacuum has an infinite number of degrees of freedom. A spectrum of virtual particle-antiparticle pairs continuously materialize – and almost immediately annihilate to satisfy the requirement of conservation of energy, which is temporarily set aside by the uncertainty principle. If one introduces a particle into this complex vacuum any type of charge on it will interact with some of these virtual pairs. Indeed, one cannot distinguish between the particle and the virtual pairs from the vacuum surrounding it, but can only make statements about the total mass and charge within a given volume. This produces a scale dependence for both quantities.

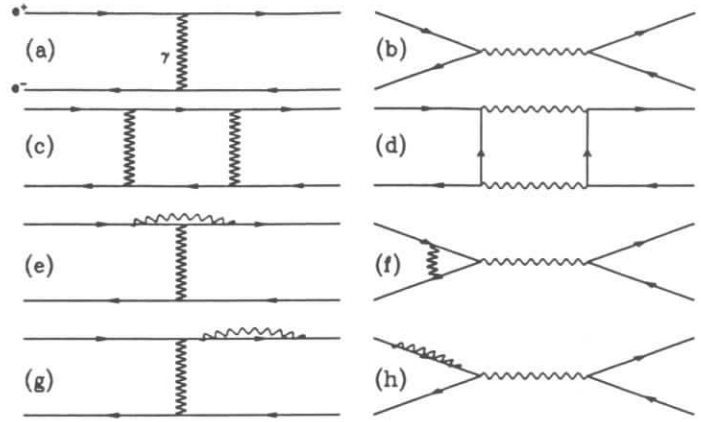

Figure 1.1: Some Feynman diagrams for $e^+e^- \rightarrow e^+e^-$. Diagrams (a) and (b) are second order in the coupling constant while the other diagrams are of fourth order. Diagrams (e) and (f) cause part of the scale dependence of the effective charge in the theory while diagrams (g) and (h) contribute to the scale dependence of the effective mass.

In the current theoretical paradigm, the duality of matter and radiation, charge and force, particle and field, has been reduced to a distinction between quantized fields with spin $\frac{2n+1}{2}\hbar$ (fermions) and spin $n\hbar$ (bosons), where n is an integer[1]. This restriction follows naturally on constructing theories invariant under Lorentz transformations. As an immediate consequence of this, bosonic wave functions must be symmetric under the exchange of two identical particles, while fermionic fields must be antisymmetric. This last requirement prevents two fermions from occupying the same state – the Pauli exclusion principle. In this framework, matter is constructed of fermionic fields and held together by forces transmitted by bosonic fields. This idea arose from successful attempts to quantize the electromagnetic field [1], which led to the theory of Quantum Electrodynamics (QED). In this picture, the interaction between two electrically charged particles is described as a combination of many processes of emission and absorption of vector bosons (figure 1.1). The probability of each process is determined by the strength of the coupling between the charge (fermion) and the field. The Feynman diagrams of

[1] Following the common usage in the subject, units are defined so that $\hbar = 1$ for the rest of this document.

Force	Carrier	Mass [GeV]	Coupling Constant	Spin	Strength	Range [m]
strong	8 gluons(g)	0	α_s	1	0.243 ± 0.020	n.a.
electromagnetic	photon(γ)	0	α	1	1/137	∞
weak	Z	91.2	G_F	1	$1.17 \cdot 10^{-5}/\mathrm{GeV}^2$	10^{-17}
	$W^{\pm}$	80.5		1		10^{-17}
gravitational	graviton	0	G_N	2	$6.7 \cdot 10^{-39}/(\mathrm{GeV/c^2})^2$	∞

Table 1.1: The forces of nature (α_s is evaluated at $Q^2 = 2.2\,\mathrm{GeV}^2/\mathrm{c}^2$, [11]).

figure 1.1 correspond to terms in a series expansion in this parameter which converges if $\alpha \ll 1$. It is only the convergence of this series that allows the effect of the field to be treated as an exchange of particles.

As far as is known, there are only four types of exchange bosons, with their corresponding forces and charges (table 1.1). Generalized versions of QED have successfully described all these interactions except gravitation, which remains a major theoretical challenge. In these theories the fermion fields are constructed with additional internal degrees of freedom and the theories are required to be invariant under rotations (gauge transformations) in these internal spaces. As the internal space at each space-time point is independent, it would be quite artificial if a theory were only invariant under identical gauge transformations at all space-time points (global gauge symmetry). Extension of the theory so that it is symmetric under local gauge transformations leads naturally to the introduction of fields coupling to the fermions. If the gauge symmetry group is noncommutative the fields will also have self-couplings – the vector bosons will carry the same charge that they couple to.

The currently known or suspected fermions are shown in table 1.2 [2,3]. These particles are arranged in three generations (e^-, ν_e, u, d), (μ^-, ν_μ, s, c), and (τ^-, ν_τ, t, b). The quarks are consistently heavier than the leptons and form a multitude of bound states known as hadrons. It was this multitude that originally inspired the quark model [4] originated by Gell-Mann [5] and Zweig [6]. In this theory quarks can only appear as bosonic $q\bar{q}$ pairs (mesons), or fermionic qqq triplets (baryons). Initially, the quark model

	Name	Symbol	Mass [GeV/c^2]	Electric Charge [e]
quarks	up	u	0.006 ± 0.001	2/3
	down	d	0.010 ± 0.001	-1/3
	charm	c	1.35 ± 0.05	2/3
	strange	s	0.199 ± 0.033	-1/3
	truth	t	> 50	2/3
	beauty	b	~ 5	-1/3
leptons	electron	e	0.000511	-1
	neutrino	ν_e	$< 4.6 \cdot 10^{-5}$	0
	muon	μ	0.106	-1
	neutrino	ν_μ	$< 2.5 \cdot 10^{-4}$	0
	tau	τ	1.784	-1
	neutrino	ν_τ	$< 3.5 \cdot 10^{-2}$	0

Table 1.2: Quarks and leptons (the quark masses are the weak current masses).

was considered only a system of organizing or labeling the hadrons, but deep-inelastic scattering of electrons on protons at the Stanford Linear Accelerator Center (SLAC) [7] demonstrated the existence of pointlike structures (partons) within the proton. This experiment was analogous to Rutherford's demonstration of the existence of the charged atomic nucleus by examining the angular distribution of α particles scattered from a beam incident on a gold foil target.

This left a slight problem: if the proton is a bound state of 3 quarks (uud) – the two identical fermions (uu) cannot be in the same state. For the proton, one can escape this problem if the uu spins are antiparallel. The problem worsened for baryons like the Ω^- (sss) a state that was predicted by the quark model. This suggested the introduction of a new type of charge: quarks could have 3 different "colours". Three differently coloured quarks could then combine to make a colourless baryon. Extension of this new quantum number to the charge of a gauge field theory produced quantum chromodynamics (QCD) [2]. This had a clearly observable consequence in the hadronic

[2]The symmetry group used, SU(3), was already familiar to physicists as the approximate symmetry induced by the near degeneracy of the u, d, and s quark masses – the "Eightfold Way" [8].

cross section in e^+e^- annihilation [2]:

$$R_\gamma = \frac{\sigma(e^+e^- \to Hadrons)}{\sigma(e^+e^- \to \mu^+\mu^-)} = N_c \sum_{quarks} e_i^2,$$

where the e_i are the quark charges and N_c the number of colours. To lowest order in α, the cross sections for these processes differ only in the electromagnetic coupling at the production vertex. The colour degree of freedom triples the number of final states available. Another confirmation of the theory was the discovery of the gluon through the observation of three-jet events in e^+e^- collisions at PETRA [9]. The process $e^+e^- \to q\bar{q}$ produces a two-jet final state when the quarks hadronize. $e^+e^- \to q\bar{q}g$ events were predicted by QCD, and the angular distributions observed confirmed the vector nature of the gluons. The strength of three-jet production has been used to determine the QCD coupling constant [2]:

$$\alpha_s(34 \text{ GeV/c}) = 0.14 \pm 0.02$$

Additional evidence for the gluon has been provided by the measurement of structure functions in deep inelastic scattering of leptons (e, μ, ν_μ) on nuclei. These describe the probability of a probe colliding with a given type of parton, as a function of the parton's momentum fraction and the probe's Q^2. It was found [10] that less than half the momentum of the proton was carried by charged partons (quarks).

At present no free quarks have been observed, due to the self-coupling of the colour field. As the presence of a colour charge in the vacuum polarizes both the virtual quarks and gluons, there is a drastic effect on the scale (Q^2) dependence of the coupling constant:

$$\alpha_s = \frac{4\pi}{\beta_0 \ln(Q^2/\Lambda^2_{\overline{\text{MS}}})}\left[1 - \frac{\beta_1 \ln(\ln(Q^2/\Lambda^2_{\overline{\text{MS}}})}{\beta_0^2 \ln(Q^2/\Lambda^2_{\overline{\text{MS}}})}\right]$$

where:

$$\beta_0 = 11 - 2N_f/3$$
$$\beta_1 = 102 - 38N_f/3.$$

N_f is the number of quark flavours ($u, d, s...$) kinematically accessible and $\Lambda_{\overline{\text{MS}}}$ is the strong interaction scale, 142 ± 31 MeV [11]. This expression becomes large when

$Q^2 < 1$ (GeV/c)^2, the typical scale of light-hadron masses. On attempting to separate the $q_1\bar{q}_2$ pair in a meson, the coupling increases. This creates a flux tube of colour field which polarizes virtual quark pairs in the vacuum. Eventually, the energy in the flux tube is sufficient to cause a virtual $\bar{q}_3q_3$ pair to materialize. The flux tube then experiences dielectric breakdown, and one is left with two mesons: $q_1\bar{q}_3$, $q_3\bar{q}_2$ – and no free quarks. The hadronization of a $q\bar{q}$ final state can be understood in a similar manner – as successive breakings in a stretching string of colour field. The range of the monopole component of the strong force has no clear definition as it is impossible to set up an experiment that would test this at distances much greater than the size of a hadron (10^{-15} m). The strong forces between colour neutral hadrons have ranges of the same order of magnitude. These forces can be understood as QCD analogs of the Van der Waal's forces of electromagnetism.

On the scale of hadronic masses, the strong coupling of QCD prevents quantitative solutions to many problems from being found. So far as the solution of a theory implies the calculation of its spectrum, QCD has not been fully successful, despite intense theoretical effort.

The weak interaction enables transitions between the different generations of quarks and leptons, and mixes the different types of quarks. This mixing follows from the difference between the weak-interaction quark eigenstates and the mass eigenstates due to the influence of the strong interaction on the latter. The two sets of eigenstates are related by a complex rotation matrix [12]. The leptons are not subject to the strong interaction, but are restricted in their decays by conservation of the number of leptons in each generation – a muon can only decay into an electron and a $\bar{\nu}_e\nu_\mu$ pair.

The theory of weak interactions is complicated by the short range of the interaction – which requires the bosons transmitting it to have very high masses. Simply introducing a mass term for the weak fields in the Lagrangian spoils gauge invariance. This problem was solved in a gauge theory based on SU(2)xU(1) developed by Glashow, Weinberg, and Salam [13]. The introduction of extra fields, known as Higgs particles, introduces extra degrees of freedom that supply the scalar helicities needed for the vector bosons

to become massive. Couplings to the Higgs also supply mass terms for the quark and lepton fields. The Z and W bosons predicted in this model were observed at the $p\bar{p}$ collider at CERN in 1982 [14]. Though every other prediction of this theory, known as the standard model, is successful, the Higgs particles have not yet been observed.

As described in table 1.2, the standard model of particle physics needs 6 fermions and leptons. One can argue the existence of the tau neutrino, ν_τ, from the principle of conservation of energy applied to τ decay; however, as opposed to the ν_e and ν_μ, there are no observations of inverse tau decay (e.g. $\nu_\tau + nucleus \rightarrow \tau + X$). This type of reaction was originally used to demonstrate that the ν_e and ν_μ were, in fact, different particles. As the masses accessible to experiment increase, the t quark has proved annoyingly elusive. This is more problematic, but one can argue that various experimental effects (e.g. $B\bar{B}$ mixing, [15]) can only be explained, within the standard model, if they are mediated by a heavy offshell t quark.

Normal matter is made up of protons (uud), neutrons (ddd) and electrons. Hence the appearance of two extra generations of quarks and leptons is somewhat curious. The existence of these three generations is actually fortuitous, in that it provides a mechanism for breaking charge parity (CP) symmetry in the standard model [12]. This, when combined with some level of proton decay as expected from grand unified theories [16], is sufficient to explain the current matter-antimatter asymmetry in the universe[17].

The standard view of physics, with four forces and twelve fermions, describes as much of reality as humanity has been able to perceive. Grand unified theories ("Theories of Everything") are theoretical attempts to unify these four forces, while providing an explanation for the diversity of the fermions and mechanisms for generating their masses (or lack thereof). Experimentally, no evidence for sub-structure of the leptons and quarks or the existence of additional vector bosons has been observed. These searches represent the forefront of particle physics.

1.1 e^+e^- Annihilation

Experiments with e^+e^- colliding beam machines have contributed a great deal to our understanding of the fundamental interactions. These studies are dominated by the analysis of hard-scattering event topologies: e^+e^- annihilation producing a highly virtual time-like photon which decays into a quark/antiquark pair (figure 1.1b with a $q\bar{q}$ pair substituted for the e^+e^- in the final state). The simplicity of the initial-state kinematics in e^+e^- collisions, the well understood QED coupling, and the elementary nature of the incident particles are a distinct improvement over fixed target or hadronic collider experiments for study of low energy standard model physics. On the other hand, typical e^+e^- annihilation cross sections are on the order of nanobarns, while pp and $p\bar{p}$ cross sections are four orders of magnitude higher at comparable energies[18] due to the strong hadronic coupling. This difference in cross sections is less of a drawback than it appears to be. The parton (quark/gluon) spectrum inside a hadron is soft. At high momentum transfer (small distances), where the application of QCD is understood best and the physics is the most interesting, the hard parton luminosities inside hadrons decrease as more of the virtual parton cloud inside the proton is resolved. Effectively, the momentum distribution of the partons, the structure function, is shifted to lower momenta. Most of the $p\bar{p}$ cross section involves low momentum-transfer reactions while only a relatively small portion contributes to high Q^2 collisions between the partons.

Due to the dominance of the virtual photon propagator ($\sim 1/4E^2$ where E is the $e^\pm$ beam energy) the e^+e^- annihilation channel cross section is:

$$\sigma(e^+e^- \rightarrow f^+f^-) = \frac{\pi\alpha^2}{12E^2}\beta(3-\beta)(3-\beta^2)Q_f^2 \simeq 21.7 \text{ nb}\frac{Q_f^2}{E^2},$$

where Q_f is the charge of the final-state particles and β is the velocity. A major limitation of experiments with colliding beams is the machine luminosity – an electron bunch is necessarily somewhat less dense than a solid target. For reference, some luminosities and energies achieved or planned at colliding beam facilities are listed in Table 1.3 [2,9,18,19].

e^+e^- Colliders				
Facility	Starting Date	Energy [GeV]	Luminosity $cm^{-2}s^{-1}$	Interaction Regions
ADONE(Frascati)	1963	2.4	$2-4\cdot10^{29}$	2
VEPP2(Novosibirsk)	1970	~ 1.4	10^{28}	2
SPEAR(SLAC)	1972	3-8	10^{31}	2
DORIS(DESY)	1974	3-10.5	$3.5\cdot10^{30}$	2
PETRA(DESY)	1978	10-45	$1.7\cdot10^{31}$	4
CESR(Cornell)	1979	8-16	10^{32}	2
PEP(SLAC)	1979	10-30	$5-8\cdot10^{31}$	1
TRISTAN(Japan)	1987	60	10^{31}	4
SLC(SLAC)	1988	100	10^{30}	1
BEPC(China)	1988	5.6	$1.7\cdot10^{31}$	2
VEPP(Novosibirsk)	1989	12	$5\cdot10^{31}$	1
LEP(CERN)	1989	80-200	$3.8\cdot10^{31}$	4
VLEPP(Serpukhov)	?	1000	10^{32}	5

Hadronic Colliders				
Facility	Starting Date	Energy [GeV]	Luminosity $cm^{-2}s^{-1}$	Interaction Regions
ISR(CERN, $pp, p\bar{p}$)	1972	6-60	$1.4\cdot10^{32}$	6
SPS(CERN, $p\bar{p}$)	1981	900	$3\cdot10^{30}$	2
TEVATRON(FNAL,$pp, p\bar{p}$)	1987	2000	10^{30}	4
HERA(DESY ep)	1991	26+820	$15\cdot10^{32}$	4
UNK(Serpukhov, pp)	?	6000	$4\cdot10^{32}$	4
LHC(CERN, pp)	?	16000	$1.46\cdot10^{33}$	7
LHC(CERN, ep)	?	50+8000	$2\cdot10^{32}$	3
SSC(USA, pp)	?	40000	10^{33}	?

Table 1.3: Particle colliders.

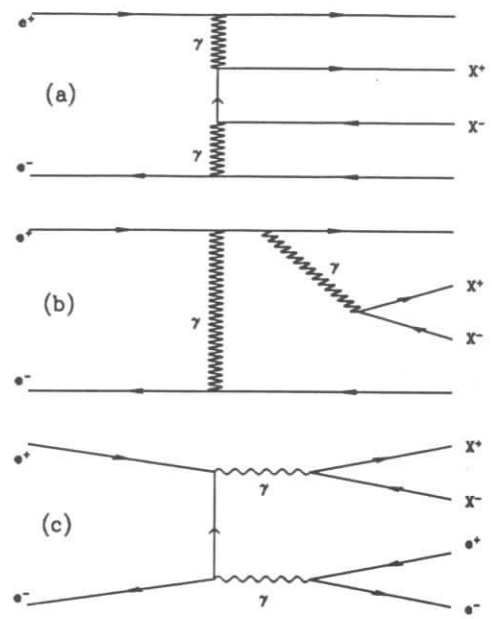

Figure 1.2: Feynman diagrams for α^4 inelastic processes. Diagram (a) is the standard two-photon or multiperipheral diagram. Diagrams (b) and (c) are suppressed by the photon propagators which must carry the full mass of the final state.

1.2 $\gamma\gamma$ Collisions

Phenomena analogous to soft hadronic reactions are also accessible in e^+e^- collisions. These reactions arise from collisions between virtual particles in the structure of the colliding leptons. To lowest order in QED perturbation theory, these can be interpreted as photon-photon collisions (figure 1.2), since the dominant part of the electron structure is the electromagnetic field. In effect, each lepton beam in an e^+e^- storage ring emits a continuous spectrum of photons, which collide to produce a concentration of energy. The investigation of the production of mesons in this type of collision is the subject of this thesis.

In classical electrodynamics, the photon and electron are structureless particles –

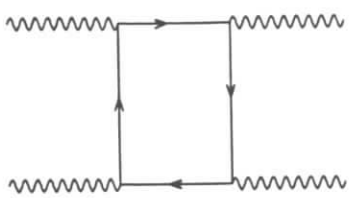

Figure 1.3: The Feynman box diagram for $\gamma\gamma \to \gamma\gamma$, this produces a small nonlinearity in Maxwell's equations.

this is implicit in the linearity of Maxwell's equations. However, QED predicts a small nonlinearity due to the presence of virtual particle/antiparticle pairs in the photon structure. The scattering of light in a background electric field was predicted in 1933 [20] and measured in 1953 [21] , while more recently a similar effect has been demonstrated for the magnetic field [22]. The cross section for elastic $\gamma\gamma$ scattering (figure 1.3) can be estimated quite simply from elementary field theory and dimensional requirements. The effective Lagrangian is $L_{eff} \sim \alpha^2 F_{\mu\nu}^4 m^{-4}$, where m is the mass of of the fermion appearing in the box diagram (figure 1.3) and $F_{\mu\nu}$ is the electromagnetic field tensor. The only other parameter in the problem is the photon energy, ω, leading to the result: $\sigma(\gamma\gamma \to \gamma\gamma) = K \cdot \alpha^4 \omega^6 m^{-8}$. This calculation was first done in full about fifty years ago [23] with the result:

$$\begin{aligned}
\sigma_{1/2} &= (973/10125\pi)\alpha^4(\hbar/mc)^2(\omega/mc^2)^6 \\
&= 129\frac{m^2}{m_e^2}(\omega/m)^6 \text{nb}, \\
\sigma_0 &= (119/10125\pi)\alpha^4(\hbar/mc)^2(\omega/mc^2)^6 \\
&= 16\frac{m^2}{m_e^2}(\omega/m)^6 \text{ nb},
\end{aligned}$$

where the subscript of σ refers to the spin of the particle in the loop of the box diagram. For visible light, this corresponds to a cross section of approximately 10^{-29} nb – an effect that would take twice the current age of the universe to measure to three standard deviations, given current laser technology [39].

The origin of modern two-photon physics is the 1960 paper by Low [24] which suggested that the lifetime of the π^0 meson be measured in e^-e^- collisions via the subprocess

$\gamma^*\gamma^* \to \pi^0 \to \gamma\gamma$. Using a double equivalent-photon approximation, an extension of the Weizsäcker-Williams method for calculating radiative processes [25], Low calculated the cross section to be:

$$\begin{aligned}
\sigma(e^+e^- \to e^+e^-R) &\simeq 15\alpha^2 log(E/m_e)^2 f(m_R/2E)\frac{(2J+1)\Gamma_{\gamma\gamma}}{m_R^3}, \qquad (1.1) \\
f(x) &= (2+x^2)^2 log(1/x) - (1-x^2)(3+x^2),
\end{aligned}$$

where E is the energy of the colliding beams, m_e the electron mass, m_R the resonance mass, and J the resonance spin. The two-photon width of the π^0 has only recently been measured in this channel [26]. The $\log(E/m_e)$ factors appear because the process can be considered as a collision of bremsstrahlung photons with spectra $1/E_\gamma$. Due to this contribution, the total $\gamma\gamma$ cross section exceeds that of e^+e^- annihilation at center of mass energies of a few GeV, even though the coupling is suppressed by an additional factor of $\alpha^2 \sim O(10^{-4})$. Bremsstrahlung also tends to be emitted at small angles with respect to the direction of the parent particle, restricting the transverse momentum of the final state in two-photon collisions to small values. Soon after Low's paper was published, Calogero and Zemach [27] discussed the production of charged pion pairs via the same mechanism. Some more approximate results, derived using the double equivalent-photon approximation (DEPA), are given below:

$$\begin{aligned}
\text{QED Fermion pairs [28]}: \quad \sigma &= \frac{224\alpha^4}{27\pi m_f^2}\ln^2(\frac{2E}{m_e})\ln(\frac{2E}{m_f}), \\
\text{QED Pion pairs [44]}: \quad \sigma &= \frac{16\alpha^4}{9\pi m_\pi^2}\ln^2(\frac{E}{m_e})\ln(\frac{E}{m_\pi}).
\end{aligned}$$

These DEPA results are usually reliable to within 20%, depending on the kinematic limitations of the final state. Modern two-photon production calculations are usually done via detailed computer calculations using exact QED matrix elements (see appendices and [29]).

The $\gamma\gamma$ production cross section can always be split up into the production of the $\gamma\gamma$ system – a pure QED process ($e^+e^- \to e^+e^-\gamma^*\gamma^*$) and the decay of the $\gamma\gamma$ system. The QED part can be subsumed into a "$\gamma\gamma$ luminosity"[3], which is actually the $e^+e^- \to$

[3]The derivation of this quantity is presented in appendix C together with a description of the notation used.

$e^+e^-\gamma\gamma \to e^+e^-X$ differential cross section for a constant $\sigma(\gamma\gamma \to X)$. The most notable aspect of the luminosity distribution is the steep decrease of luminosity as the colliding photons become more virtual and the mass of the $\gamma\gamma$ system increases. The former is a consequence of the photon propagator, which is proportional to $1/q^2$:

$$\begin{aligned} q_i^2 &= (p_i - p_i')^2 \\ &= 2m_e^2 - 2E_i \cdot E_i' + 2\vec{p}_i \cdot \vec{p}_i' \cos\theta_i \\ &= -2E_i \cdot E_i'(1-\cos\theta_i) - Q_{i,min}^2 + O(m_e^4)/E_i^2 + O(m_e^2\theta_i^2) \\ &= -E_i \cdot E_i'\theta_i^2 \quad \text{at small angles,} \end{aligned}$$

where p_i, p_i' are the four-vectors of the beam particles before and after scattering ($p_i = (E_i, \vec{p}_i)$), the θ_i are the angles of the scattered leptons, and $q_{i,min}^2 = m_e^2(E_i - E_i')^2/(E_i \cdot E_i')$. The photon propagator behaviour is also responsible for the steeply decreasing angular distribution of the scattered $e^\pm$. Scattered beam leptons from $\gamma\gamma$ reactions are rarely observed – most investigations must be done in what is known as the "no-tag mode".

The final-state mass is given by the equation:

$$W_{\gamma\gamma}^2 = S = (p_1 + p_2 - p_1' - p_2')^2.$$

On neglecting terms of order m_e^2 this becomes:

$$\begin{aligned} W_{\gamma\gamma}^2 &= 4E^2 - 4E(E_1+E_2) + 2E_1E_2(1-\cos\theta_{12}) \\ &= 4E_{\gamma_1}E_{\gamma_2} - 2E_1E_2(1+\cos\theta_{12}) \\ &\simeq 4E_{\gamma_1}E_{\gamma_2}, \end{aligned}$$

where θ_{12} is the angle between the scattered $e^\pm$. These particles are anticollinear to a good approximation. The decrease in the $\gamma\gamma$ luminosity with increasing final-state mass can be understood as the product of the two bremsstrahlung spectra, $1/E_{\gamma_i}$. When the photons are nearly real, most of the growth in the $\gamma\gamma$ total cross section is concentrated either in the prodigious production of low invariant mass final states (the mass spectrum for the channel $\gamma\gamma \to e^+e^-, \mu^+\mu^-$ peaks at $s = 8m^2$) or states with a high Lorentz boost. Experimentally, the observation of two-photon final states is restricted by the rapidity

distribution of the final state:

$$\begin{aligned} \eta &= \frac{1}{2}\log\frac{E_{\gamma\gamma} - P_{\gamma\gamma}}{E_{\gamma\gamma} + P_{\gamma\gamma}} \\ &\simeq \frac{1}{2}\log\frac{E_{\gamma_1}}{E_{\gamma_2}}, \end{aligned}$$

where:

$$P_{\gamma\gamma} = \sqrt{(E_{\gamma 1} - E_{\gamma 2})^2 + 2E_1E_2(1+\cos\theta_{12})}.$$

The rapidity distribution is flat to a first approximation, but the limits of the distribution increase logarithmically with energy. For two particle production the rapidity acceptance of the detector is limited to $|\eta| < \frac{1}{2}\log[(1-\cos\theta)/(1+\cos\theta)]$, where θ is the minimum polar angle observable.

One expects the cross section for the process $\gamma\gamma \to X$ to have $3^4 = 81$ independent components (this is related to the imaginary part of the elastic scattering amplitude $\gamma\gamma \to \gamma\gamma$ via the optical theorem, each virtual photon having three independent helicity states), but this number is reduced to 8 by considerations of symmetry under time-reversal, parity, and rotation. The cross section for any process $e^+e^- \to e^+e^-X$ can be expressed as:

$$\begin{aligned} d\sigma &= \frac{\alpha^2}{16\pi^4 q_1^2 q_2^2}\sqrt{\frac{(q_1\cdot q_2)^2 - q_1^2q_2^2}{(p_1\cdot p_2)^2 - m_e^4}}[4\rho_1^{++}\rho_2^{++}\sigma_{TT} + \\ &\quad 2|\rho_1^{+-}\rho_2^{+-}|\tau_{TT}\cos 2\phi + 2\rho_1^{++}\rho_2^{00}\sigma_{TS} + 2\rho_1^{00}\rho_2^{++}\sigma_{ST} + 2\rho_1^{00}\rho_2^{00}\sigma_{SS} \\ &\quad -8|\rho_1^{+0}\rho_2^{+0}|\tau_{TS}\cos\phi]\frac{d^3p_1'd^3p_2'}{E_1'E_2'}, \end{aligned}$$

where:

$$\begin{aligned} X &= (q_1q_2)^2 - q_1^2q_2^2 \simeq W_{\gamma\gamma}^2/4, \\ 2\rho_1^{++} &= \rho_1^{\mu\nu}R^{\mu\nu} = X^{-1}(4E\omega_2 - q_2^2 - q_1q_2)^2 + 1 + 4m_e^2/q_1^2, \\ \rho_1^{00} &= \rho_1^{\mu\nu}Q_1^\mu Q_1^\nu = X^{-1}(4E\omega_2 - q_2^2 - q_1q_2)^2 - 1, \\ |\rho_1^{+0}| &= \sqrt{(\rho_1^{00}+1)|\rho_1^{+-}|}, \\ |\rho_1^{+-}| &= \rho_1^{++} - 1. \end{aligned}$$

The ρ's can be treated as photon intensities. Two of the eight amplitudes mentioned above are not shown in the equation as they only contribute to processes with polarized e^+e^- beams. The τ amplitudes can only be measured if both the scattered beam

particles are measured or tagged – otherwise the angle between the scattering planes must be integrated over. The amplitudes involving collisions of scalar photons are also suppressed by factors proportional to the photon mass (e.g. $\sigma_{SS} \sim q_1^2 q_2^2$), as they must vanish for real photons. This leaves only one amplitude, σ_{TT}, measurable in the accessible no-tag mode where neither scattered beam particle is detected (q^2 for both photons are limited to be less than a maximum determined by the minimum scattering angle measurable by the detector). In addition to the two-photon or multiperipheral Feynman diagram (figure 1.2a), which produces final states with positive charge parity, there are small contributions from several other α^4 processes. These correspond to the lowest order Bhabha scattering graphs (figure 1.2b,c) with additional offshell photons radiating from the $e^{\pm}$ lines. These decay to final states with negative charge parity. Though these processes are of the same order in the QED coupling, α, they are suppressed by the value of the photon propagator for final-state masses comparable to those studied in $\gamma\gamma$ collisions.

The study of two-photon collisions has yielded results on many aspects of particle physics, particularly QCD. Measurements of the photon structure function were inspired by the expectation that it would be completely calculable in QCD. Measurements of α_s have been made in $\gamma\gamma$ multi-jet production. Hadron production at sufficiently high $P_\perp$ is calculable in QCD. As there are many excellent experimental and theoretical reviews of these subjects ([30]-[61]) they will not be discussed further here.

1.3 Production of Resonances in $\gamma\gamma$ Collisions

The production of resonances in $\gamma\gamma$ collisions is one of the simplest processes involving the strong interaction. Unlike the production of resonances in e^+e^- annihilation, which must have $J^{PC} = 1^{--}$, any state with positive charge parity is accessible in $\gamma\gamma$ collisions. According to Yang's law [62], $J = 1$ resonance production in collisions of real photons is impossible. However, for sufficiently high photon q^2, obtained experimentally by tagging one of the scattered beam particles so that longitudinal photon degrees of freedom are significant, the production of vector resonances has been observed [63]-[68]. The q^2 evolution of resonance production in $\gamma\gamma$ collisions immediately identified the X(1420) as a vector state after years of inconclusive partial wave analyses of its production in hadronic collisions [49]. $\gamma\gamma$ collisions have all the advantages of e^+e^- annihilation with the single drawback of low final-state energy. It is particularly interesting to study $\gamma\gamma$ resonance production as it is an exclusive process. There is less combinatoric background to confuse the analysis. Otherwise, most states with even charge parity can only be studied as inclusive phenomena, which makes detailed analyses exceedingly difficult, especially for complex final states.

As the photon can only couple directly to electric charge, the $\gamma\gamma$ coupling of mesons probes the quark content of their wave functions:

$$|M\rangle = \sum_q c_q |q\bar{q}\rangle$$

The coupling of two photons to a meson is then [47]:

$$\begin{aligned} \Gamma_{\gamma\gamma} &= \frac{1}{16\pi(2J+1)M_R} \sum_{a,b} |M_{ab}|^2 \\ &\propto m^3 \langle M|\gamma\gamma\rangle^2 \\ &\propto m^3 \langle e_q^2\rangle^2 \end{aligned}$$

where e_q is the charge of each quark contributing, M_R the meson mass, and M_{ab} the matrix element for collisions of photons with helicities a and b. The $\gamma\gamma$ width of the π^0 can be calculated theoretically to high accuracy [69]:

$$\Gamma_{\gamma\gamma} = \frac{m_\pi^3}{64\pi^3} \frac{2\alpha^2}{f_\pi^2} N_c^2 \langle e_q^2\rangle_\pi^2 = 7.63 \text{ eV}$$

This calculation is in good agreement with the world average, shown in table 1.4, and is one of the three direct measurements of the number of colours in QCD (the others are the total e^+e^- cross-section measurement and the width of the Z^0 meson).

SU(3) flavour symmetry [4,8] is useful in describing the properties of the standard mesons. Radical departures from SU(3) expectations may be indications of exotic (non $q\bar{q}$, $q = u, d, s$) contributions to a meson's structure. The SU(3) quark wave functions for the pseudoscalars are:

$$\begin{aligned} \pi^0 &= (d\bar{d} - u\bar{u})/\sqrt{2}, \\ \eta^8 &= (d\bar{d} + u\bar{u} - 2s\bar{s})/\sqrt{6}, \\ \eta^1 &= (d\bar{d} + u\bar{u} + s\bar{s})/3\sqrt{3}. \end{aligned}$$

The physical meson wavefunctions are actually mixtures of these:

$$\begin{aligned} \eta &= \cos\theta_P\eta_8 - \sin\theta_P\eta_1, \\ \eta' &= \sin\theta_P\eta_8 + \cos\theta_P\eta_1. \end{aligned}$$

The two-photon widths of the pseudoscalar nonet can then be described as:

$$\begin{aligned} \Gamma^{\eta}_{\gamma\gamma}/\Gamma^{\pi^0}_{\gamma\gamma} &= \frac{1}{3}(\cos\theta_P - r\ 2\ \sqrt{2}\sin\theta_P)^2(\frac{m_\eta}{m_{\pi^0}})^N, \\ \Gamma^{\eta'}_{\gamma\gamma}/\Gamma^{\pi^0}_{\gamma\gamma} &= \frac{1}{3}(\sin\theta_P + r\ 2\ \sqrt{2}\cos\theta_P)^2(\frac{m_{\eta'}}{m_{\pi^0}})^N, \end{aligned}$$

where, for the pseudoscalar nonet, $N = 3$. The parameter r describes the difference between the SU(3) octet and singlet wavefunctions. This formalism can be applied to the tensor meson nonet with the substitution $\pi, \eta, \eta' \rightarrow a_2, f_2', f_2$, although the value for N is less certain in this case [47].

The existing measurements of the $\gamma\gamma$ couplings of the pseudoscalar and tensor mesons are listed in tables 1.4-1.8. The most recent measurements of each collaboration have been used in the averages. The experimental production of resonances in $\gamma\gamma$ collisions is reviewed in reference [42], while possible exotic contributions are discussed in [49]. Reference [47] is an excellent theoretical review.

$\pi^0(135) \rightarrow \gamma\gamma$		
$\Gamma_{\gamma\gamma}$ [keV]	Date	Experiment
$7.25 \pm 0.18 \pm 0.14$	1985	lifetime [70]
7.74 ± 0.61	< 1988	old average [2]
$7.7 \pm 0.5 \pm 0.5$	1988	Crystal Ball/DORIS [26]
7.72 ± 0.46	average	
$\eta(549) \rightarrow \gamma\gamma$		
$\Gamma_{\gamma\gamma}$ [keV]	Date	Experiment
1.00 ± 0.22^a	1967	DESY Primakoff [71]
0.324 ± 0.046^a	1974	Cornell Primakoff [72]
$0.56 \pm 0.12 \pm 0.10$	1983	Crystal Ball/SPEAR [73]
$0.53 \pm 0.04 \pm 0.04$	1985	JADE [74]
$0.64 \pm 0.14 \pm 0.13$	1986	TPC/$\gamma\gamma$ [75]
$0.514 \pm 0.017 \pm 0.035$	1988	Crystal Ball/DORIS [26]
$0.490 \pm 0.010 \pm 0.048$	1990	ASP [76]
$\eta(549) \rightarrow \pi^+\pi^-\pi^0$		
$0.54 \pm 0.05 \pm 0.10$	1988	Crystal Ball/DORIS [77]
0.516 ± 0.026	average	

Table 1.4: Measurements of the $\gamma\gamma$ widths of π^0 and η mesons from experiments at $e^\pm$ storage rings. [a] Not included in the average following common usage [2].

$\eta'(958)$			
$\Gamma_{\gamma\gamma}$ [keV]	Decay Channel	Date	Experiment
$5.9 \pm 1.6 \pm 1.2^{c}$	$\rho\gamma$	1979	Mark II/SPEAR [78]
$5.0 \pm 0.5 \pm 0.9^{a}$	$\rho\gamma$	1982	JADE [79]
$5.8 \pm 1.1 \pm 1.2$	$\rho\gamma$	1982	Mark II/SPEAR [78]
$6.2 \pm 1.1 \pm 1.2^{b}$	$\rho\gamma$	1984	CELLO [80]
$3.80 \pm 0.26 \pm 0.43$	$\rho\gamma$	1984	PLUTO [81]
$5.1 \pm 0.4 \pm 0.7$	$\rho\gamma$	1984	TASSO [82]
3.8 ± 0.5^{c}	$\rho\gamma$	1985	Mark II/PEP [83] (prel.)
$3.76 \pm 0.13 \pm 0.47^{c}$	$\rho\gamma$	1986	ARGUS [84]
$4.5 \pm 0.3 \pm 0.7$	$\rho\gamma$	1987	TPC/$\gamma\gamma$ [85]
$4.6 \pm 1.1 \pm 0.9$	$\rho\gamma$	1987	MD1 [86] (prel.)
$4.16 \pm 0.09 \pm 0.42$	$\rho\gamma$	1990	ARGUS [this work]
4.30 ± 0.32	$\rho\gamma$	average	
3.6 ± 1.0^{c}	$\pi^+\pi^-\eta$, $\eta \to \pi^+\pi^-\pi^0$	1985	Mark II/PEP [83] (prel.)
$4.7 \pm 0.6 \pm 0.9$	$\pi^+\pi^-\eta$, $\eta \to \gamma\gamma$	1986	Mark II/PEP [87]
$4.6 \pm 0.4 \pm 0.6$	$\pi^0\pi^0\eta$, $\eta \to \gamma\gamma$	1987	Crystal Ball/DORIS [88]
$3.80 \pm 0.13 \pm 0.50$	$\pi^+\pi^-\eta$, $\eta \to \gamma\gamma$	1988	JADE [89] (prel.)
$3.8 \pm 0.7 \pm 0.6$	$\pi^+\pi^-\eta$, $\eta \to \gamma\gamma$	1988	TPC/$\gamma\gamma$ [90]
$4.7 \pm 0.2 \pm 1.0$	$\pi^+\pi^-\eta$, $\eta \to \gamma\gamma$	1988	CELLO [65] (prel.)
4.16 ± 0.36	$\pi\pi\eta$	average	
$3.4 \pm 0.8 \pm ?^{c}$	$\gamma\gamma$	1985	JADE [91]
$4.0 \pm 0.4 \pm 0.4$	$\gamma\gamma$	1988	Crystal Ball/DORIS [26]
$4.80 \pm 0.22 \pm 0.70$	$\gamma\gamma$	1988	ASP [76]
4.29 ± 0.51	$\gamma\gamma$	average	
4.25 ± 0.22	all	average	

Table 1.5: Measurements of the $\gamma\gamma$ width of the η' meson from experiments at $e^{\pm}$ storage rings. [a] When the acceptance calculation was made without taking into account the dipole character of the $\eta' \to \rho\gamma$ decay, the systematic error was 0.8 keV. To account for the dipole decay this has been extended to the value shown. [b] Calculated without a dipole matrix element, not used in the average. [c] Not used in the average because of newer results available from the same experiment (also included in the table) or the preliminary nature of the analysis. So far as possible the values shown have been corrected for the most recent values of the relevant branching ratios, $B(\rho\gamma) = 0.301 \pm 0.014$, $B(\gamma\gamma) = 0.0223 \pm 0.0018$, $B(\eta\pi\pi) = 0.649 \pm 0.020$ (assuming $B(\eta\pi^+\pi^-) = 2B(\eta\pi^0\pi^0)$).

$f_2(1270) \to \pi^+\pi^-$				
$\Gamma_{\gamma\gamma}$	Assumptions		Date	Experiment
[keV]	Helicity	Continuum		
$2.3 \pm 0.5 \pm 0.35^{a}$	2	incoherent	1980	PLUTO [92]
$3.6 \pm 0.3 \pm 0.5$	2	Born term	1981	Mark II/SPEAR [93]
$3.2 \pm 0.2 \pm 0.6^{a}$	2	incoherent	1981	TASSO [94]
$2.3 \pm 0.2 \pm 0.5^{a}$	2	incoherent	1983	JADE [95] (prel.)
$2.52 \pm 0.13 \pm 0.38$	2	Born term	1984	Mark II/PEP [96]
$2.7 \pm 0.05 \pm 0.20^{a}$	2	Born term	1984	DELCO [97]
$3.25 \pm 0.25 \pm 0.50^{a}$	2	Born term	1984	PLUTO [98]
$2.85 \pm 0.25 \pm 0.50$	2	Menessier	1984	PLUTO [98]
$2.5 \pm 0.1 \pm 0.5$	2	Menessier	1984	CELLO [99]
$3.2 \pm 0.1 \pm 0.4$	2	Born term	1986	TPC/$\gamma\gamma$ [100]
2.93 ± 0.30	2	Menessier	1986	DELCO [101]
3.34 ± 0.35^{a}	2	Lyth	1986	DELCO [101]
3.42 ± 0.37^{a}	free	Lyth	1986	DELCO [101]
3.0 ± 0.1^{a}			1988	CELLO [65] (prel.)
$3.21 \pm 0.09 \pm 0.40$	free	Born term	1988	Mark II/PEP [102] (prel.)
$2.27 \pm 0.47 \pm 0.11$	2	Born term	1989	TOPAZ/KEK [103]
$f_2(1270) \to \pi^0\pi^0$				
$\Gamma_{\gamma\gamma}$	Assumptions		Date	Experiment
[keV]	Helicity	Continuum		
$2.9^{+0.6}_{-0.4} \pm 0.6$	free	incoherent	1982	Crystal Ball/SPEAR [104]
$2.7 \pm 0.2 \pm 0.6^{a}$	2	incoherent	1982	Crystal Ball/SPEAR [104]
$3.26 \pm 0.16 \pm 0.28$	free	incoherent	1986	Crystal Ball/DORIS [105]
$3.09 \pm 0.1 \pm 0.38$	2	incoherent	1988	JADE [89] (prel.)
$f_2(1270) \to K^+K^-$				
$\Gamma_{\gamma\gamma}$	Assumptions		Date	Experiment
[keV]	Helicity	Continuum		
$2.5 \pm 0.2 \pm 1.7$	2	coherent	1989	ARGUS [this work],[106]
2.97 ± 0.14	2	average		

Table 1.6: Measurements of the $\gamma\gamma$ width of the $f_2(1270)$ meson from experiments at $e^{\pm}$ storage rings. For the average only values from the neutral pion channel and Born term or Menessier model fits [107] to the charged pion channel are used. [a] Not used in the average because of newer results available from the same experiment (also included in the table) or the preliminary nature of the analysis.

$a_2(1320)$				
$\Gamma_{\gamma\gamma}$ [keV]	Decay Channel	Helicity Assumption	Date	Experiment
$0.77 \pm 0.18 \pm 0.27$	$\pi^0\eta$	2	1982	Crystal Ball/SPEAR [104]
$1.14 \pm 0.20 \pm 0.26$	$\pi^0\eta$	2	1986	Crystal Ball/DORIS [105]
$1.09 \pm 0.14 \pm 0.25$	$\pi^0\eta$	2	1988	JADE [89] (prel.)
1.01 ± 0.19	$\pi^0\eta$	average		
$0.81 \pm 0.19^{+0.42}_{-0.11}$	$\rho^\pm\pi^\mp$	2	1983	CELLO [80]
$0.84 \pm 0.07 \pm 0.15^a$	$\rho^\pm\pi^\mp$	2	1983	JADE [95] (prel.)
$1.06 \pm 0.18 \pm 0.19$	$\rho^\pm\pi^\mp$	free	1984	PLUTO [108]
$0.90 \pm 0.27 \pm 0.16$	$\rho^\pm\pi^\mp$	2	1986	TASSO [109]
$0.90 \pm 0.09 \pm 0.22$	$\rho^\pm\pi^\mp$	free	1987	TPC/$\gamma\gamma$ [110] (prel.)
$0.97 \pm 0.10 \pm 0.22^a$	$\rho^\pm\pi^\mp$	2	1987	TPC/$\gamma\gamma$ [110] (prel.)
$1.05 \pm 0.24 \pm 0.23$	$\rho^\pm\pi^\mp$	2	1987	MD1 [86] (prel.)
$1.00 \pm 0.07 \pm 0.15$	$\rho^\pm\pi^\mp$	2	1989	CELLO [111]
0.97 ± 0.11	$\rho^\pm\pi^\mp$	average		
$1.7 \pm 0.1 \pm 0.6$	K^+K^-	2	1989	ARGUS [this work],[106]
1.00 ± 0.09	all	average		

Table 1.7: Measurements of the $\gamma\gamma$ width of the $a_2(1320)$ meson from experiments at $e^\pm$ storage rings. [a] Not used in the average because of newer results available from the same experiment (also included in the table) or the preliminary nature of the analysis.

$f_2'(1525)$					
$\Gamma_{\gamma\gamma}$ [keV]	Decay Channel	Assumptions Helicity	Assumptions Continuum	Date	Experiment
$0.11 \pm 0.02 \pm 0.04$	K^+K^-	2	incoherent	1983	TASSO [112]
$0.12 \pm 0.07 \pm 0.04$	K^+K^-	2	incoherent	1986	TPC/$\gamma\gamma$ [113]
$0.07 \pm 0.015 \pm 0.035$	K^+K^-	2	incoherent	1986	DELCO [101]
$0.031 \pm 0.005 \pm 0.008$	K^+K^-	2	coherent	1989	ARGUS [106]
$0.067 \pm 0.008 \pm 0.015$	K^+K^-	2	incoherent	1989	ARGUS [106]
0.10 ± 0.04	$K^0_SK^0_S$	2	incoherent	1986	Mark II/PEP [114]
$0.10^{+0.04+0.03}_{-0.03-0.02}$	$K^0_SK^0_S$	free	incoherent	1988	PLUTO [115]
$0.11^{+0.03}_{-0.02} \pm .02$	$K^0_SK^0_S$	2	incoherent	1989	CELLO [116]
0.083 ± 0.012	all	average of incoherent continuum measurements			

Table 1.8: Measurements of the $\gamma\gamma$ width of the $f_2'(1525)$ meson from experiments at $e^\pm$ storage rings.

1.4 Two-Photon Experiments

The critical properties of $\gamma\gamma$ collisions, from the point of view of an experimenter, are their relatively low energy and high Lorentz boost. These properties combine to make triggering and event reconstruction difficult, especially for low-mass states. As a consequence, the final state is focussed on the worst areas for detector acceptance – the endcaps and beampipe. The standard response to this problem is to install specialized forward spectrometers a short distance from the central detector down the beamline. A major compromise often has to be made between the solid angle coverage of these detectors and the positioning of the focussing quadrupoles that are essential for useful machine luminosities. For the study of exclusive final states in the resonance region (< 4 GeV) triggers sensitive to small transverse momenta and total energies much less than the beam energy are essential.

Triggering is made much easier if measurements are done in the "tagging" mode, where one or both of the scattered beam particles are detected, yielding information on the Q^2 of the colliding photons. In the "double-tag" mode one can reconstruct the mass of the $\gamma\gamma$ final state by the missing-mass technique. Unfortunately, unless 0° tagging is possible, event rates are reduced by an order of magnitude or more for each required tag, depending on the acceptance of the forward spectrometer (tagger). A proposal [117] for 0° tagging submitted by ARGUS suggested the utilization of the vertical bending magnets of the DORIS-II storage ring to separate the final-state e^+e^- in $\gamma\gamma$ collisions from the beams. Unfortunately, this was never implemented because of difficulties with background rates and operation of detectors close to the beamline [118]. MD-1 at Novosibirsk has been more successful. This experiment uses a dipole field instead of a solenoidal field for the detector [86,119] – it functions as one of the bending magnets of the storage ring! 0° tagging was also possible with the DM1 detector which used the bending magnets of the double storage ring DCI to separate electrons with an energy loss between 20% and 50% of the 1 GeV beam energy.

In general, machine effects limit tagging in $\gamma\gamma$ collisions to angles greater than 20 mrad. This kinematic range is interesting as the effects of QCD on structure func-

tions and meson form factors are more easily interpreted at high Q^2. A good example of a standard tagging system is that of the TASSO detector that operated at PETRA. This tagger consisted of lead glass blocks covering angles from 24 to 60 mrad. The PLUTO and TPC detectors both installed rather more elaborate tagging systems. PLUTO's forward spectrometers consisted of septum magnets (with a dipole field parallel to the beam) that allowed measurement of charged particle momenta at small angles in combination with drift chambers: a large angle tagger (LAT, 70-260 mrad), constructed of lead and proportional tubes, and a small angle tagger (SAT, 23-70 mrad) of lead glass, iron muon filters, and muon detectors. The TPC/$\gamma\gamma$ detector had a similar arrangement but used NaI for the SAT and lead-scintillator counters for the LAT.

Though almost every experiment at e^+e^- storage rings has published results on two-photon physics, very few were actually designed for the purpose. ARGUS is not one of the exceptions to this rule, but has still managed to make a major contribution to the field (appendix B). The beam energies of Υ experiments are insufficient to study processes like high $P_\perp$ hadron or jet production, and the study of high Q^2 processes or structure functions is prevented by both the low beam energy and the absence of taggers. However, ARGUS is exemplary in its ability to study exclusive final-state production in $\gamma\gamma$ collisions. In addition to the results presented in this thesis, the collaboration has made first observations of the final states $\omega\rho$, $K^{*0}\bar{K}^{*0}$, $\omega\omega$, and $K^{*+}K^{*-}$, the final states $\rho^0\rho^0$, $\rho^+\rho^-$ have been analyzed in detail, baryon pair production has been observed, and upper limits for $\omega\phi$ and $\phi\phi$ production have been measured. The two-photon data sample at ARGUS has by no means been exhausted.

The CLEO detector shares many of the physics goals of the ARGUS collaboration but has only managed to produce $\gamma\gamma$ results recently [120]. The practical reason for this is that the ToF and shower system of the original CLEO detector were installed outside the magnet solenoid, resulting in higher trigger thresholds and reduced efficiency for low energy photons. The design of the CLEO-II detector solves these problems and will have the additional advantage of a significant increase in machine luminosity. Colliders like LEP and the SLC will be able to study the photon structure functions at higher Q^2, but the $\gamma\gamma$ luminosity will still be restricted to low masses. It is not expected that

the η_b region ($\sim$ 10 GeV) will be accessible, though charmonium production should be observable. In the near future, the most interesting prospect for the study of exclusive processes in two-photon collisions are the B factory proposals [121]. The event rate at these facilities is expected to be three orders of magnitude higher than that currently available. As the rate of data taking (approximately 100 Hz of e^+e^- annihilation events from a raw 100 kHz rate) at these experiments is a critical limitation, it is realistic to expect that the triggers for two-photon collisions might have to be scaled by an order of magnitude – this would still represent a large increase in the available luminosity. In the long term one can imagine dedicated colliding photon facilities becoming available. In Compton back scattering one bounces low energy laser photons off a high energy $e^\pm$ beam, resulting in a beam of high energy photons. Calculations [122,123] suggest that this would result in a hundred-fold increase in $\gamma\gamma$ luminosities at invariant masses close to that of the colliding e^+e^-. The principle limitation on this sort of collider would be the available laser power.

Chapter 2

The ARGUS Experiment

The first section of this chapter discusses the physics motivation behind the design of the ARGUS detector. The second section describes the DESY accelerator system, which is an essential part of the experiment. The rest of the chapter describes, necessarily in rather coarse detail, the individual components of the ARGUS detector, the data acquisition, the offline data processing, and the initial event selection.

2.1 The ARGUS Detector

ARGUS [1] was designed as an advanced second generation detector to replace the Double Arm Spectrometer (DASP), the original proposal was submitted in October 1978 [124]. The detector was assembled in the south interaction region of the DORIS-II (Doppel Ring Speicher) storage ring at DESY. The other collision region was occupied until 1987 by a non-magnetic detector, the Crystal Ball. The new detector was dedicated to the study of the physics of e^+e^- collisions in the energy region around 10 GeV, principally because of the discovery of the Υ states in 1977 [125].

The first indication of the existence of the Υ resonances was seen [125] in fixed target experiments (protons on copper or platinum) as an enhancement, with a mass of 9.450 GeV, in the production of muon pairs. Fixed target experiments have the advantage of a high event rate (a 0.7 mm thick copper sheet making an easier target than a bunch of 10^{12} electrons). However, this advantage carries with it a high background rate; only

[1] The acronym originally stood for "A Russian German United States Swedish Collaboration" – subsequently groups from Canada (1982) and Yugoslavia (1984) joined the collaboration suggesting a change in definition to "A Rather Good Upsilon Spectrometer".

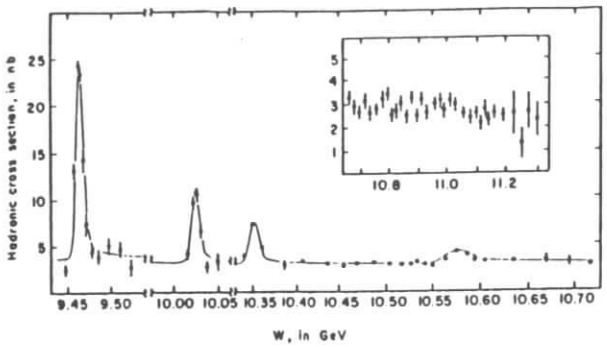

Figure 2.1: The hadronic cross section in the mass region of the Υ resonances [2,126].

a tiny fraction of collisions produced Υ resonances, and in these events the Υ was only part of a complex final state. This complication was overcome by searching for decays to muon pairs. Muons are highly penetrating particles, and can easily be separated from other particles by absorbers. More detailed studies of the Υ resonances awaited their production in e^+e^- collisions, nearly the inverse of the process through which they were discovered.

The Υ resonances are flavourless bound states of bottom (beauty) quarks and their antiparticles. The spectrum of these states is analogous to that of positronium and the bound states are labelled accordingly: $n^{2S+1}L_J$, with n being the radial quantum number, S the total spin of the two quarks, $L = S, P, D, F...$ the orbital angular momentum state, and J the total angular momentum. There is one significant difference - the binding force of the Υ resonances is provided by the strong interaction. At present, the first six n^3S_1 resonances have been observed [2,126] as peaks in the total cross section for $e^+e^- \rightarrow hadrons$ (see figure 2.1). As the other possible resonances do not have the quantum numbers of the photon, $J^{PC} = 1^{--}$ (where $P = -(-1)^L$, and $C = (-1)^{S+L}$), they cannot be produced directly in e^+e^- collisions. At present, only the six 1^3P_J and 2^3P_J states have been seen [127], having been produced in radiative decays of the S-channel resonances.

The first three n^3S_1 resonances are quite narrow, ranging in width from 52 ± 3 keV for the $\Upsilon(1S)$, to 26 ± 6 keV for the $\Upsilon(3S)$. Hadronic decays of $J^{PC} = 1^{--}$ states can proceed only through the production of three gluons; a single gluon (which has the correct J^{PC}, the same as the photon) is not allowed as the final state must be colour neutral. The $\Upsilon(4S)$ (10.580 ± 0.0035 GeV/c^2) resonance is much wider, 14 ± 5 MeV, indicating the presence of additional decay channels - final states composed of $B\bar{B}$ meson pairs (bound states of $b\bar{u}$ or $b\bar{d}$ quarks). These new mesons provide a complex set of decay channels to study.

Investigations of Υ spectroscopy and B meson decays are significant for much of particle physics. They provide information on heavy quark potentials, corrections to weak decays from Quantum Chromodynamics (QCD), weak interaction universality for the third quark/lepton generation, and the Kobayashi-Maskawa parametrization [12] of the weak interactions of quarks. The dedication of the detector to b-quark physics has proved profitable with the observation of mixing between B and $\bar{B}$ mesons, transitions between b and u quarks, and studies of many exclusive decays (the ARGUS publications list is included as Appendix B). The study of charmed mesons and tau lepton production in the continuum was also considered in the design of the detector. These studies have also proved fruitful, and many results on the production and decay of charmed mesons have been published. These include lifetime measurements and first observations of several new excited charm states. Lower limits on the mass of the ν_τ have also been published.

This type of physics requires a detector able to resolve high multiplicity events while maintaining sensitivity to secondary particles with low energies (in order to reconstruct the complex decay chains provided by the the cascade of quark flavours: $b \rightarrow c \rightarrow s$). As a consequence of the high multiplicities (on the average eight charged particles per event [128]), good charged particle identification at low momenta is essential to control combinatoric backgrounds. To reconstruct neutral particles with similar efficiency it is necessary to have a highly segmented detector with good energy resolution. In brief, the detector was designed to have high segmentation, maximal angular coverage, high resolution, low kinematic thresholds, and good particle identification for momenta below

1 GeV.

These properties also allow the study of two-photon interactions at ARGUS, although the detector was not explicitly designed for this type of physics (unfortunately, a common feature of most detectors used for two-photon analyses). Most experiments studying two-photon collisions were designed for the higher center of mass energies available at the PETRA and PEP storage rings. Though experiments at these high energy rings have the advantage of increased two-photon luminosity, this is offset by decreased acceptance and limited detector performance at the low final-state energies associated with two-photon resonance production.

ARGUS started running in October 1982 and the first useful data were collected in February 1983. Between February 1983 and November 1989 ARGUS collected a total of 445.2 pb^{-1} of luminosity, divided between the Υ resonances and nearby continuum (Table 2.1). The ARGUS luminosity and energy histories are shown in Figures 2.2 and 2.3 respectively. The analyses presented in this thesis use data collected before February 2^{nd} 1989, though the experiment continues to operate. For this period only data with optimal trigger logic settings and hardware conditions were used. Short descriptions of the storage ring and detector subsystems follow (a more detailed description of the detector can be found in reference [129]). A schematic view of the detector is shown in figure 2.5.

Run Type	Energy	Luminosity [pb^{-1}]
$\Upsilon(1S)$	9.460	47.0
$\Upsilon(2S)$	10.023	38.3
$\Upsilon(4S)$	10.560	220.4
$\Upsilon(1S)$ Scan	n.a.	11.9
$\Upsilon(2S)$ Scan	n.a.	2.3
$\Upsilon(4S)$ Scan	n.a.	31.7
Continuum	9.36-9.39	9.0
Continuum	9.98-10.00	3.0
Continuum	10.43	8.5
Continuum	10.46	58.3
Continuum	10.49-10.54	14.9

Table 2.1: Luminosity distribution of ARGUS data collection.

Experiment	Date	Luminosity [pb^{-1}]	
		Total	Selected
2	1983-1984	65.7	46.0
3	1984	22.5	0
4	1985	73.1	66.1
5	1986	104.5	98.5
6	1988	77.4	70.9
7	1989	59.0	0
8	1989	43.1	0

Table 2.2: Luminosity distribution for different running periods.

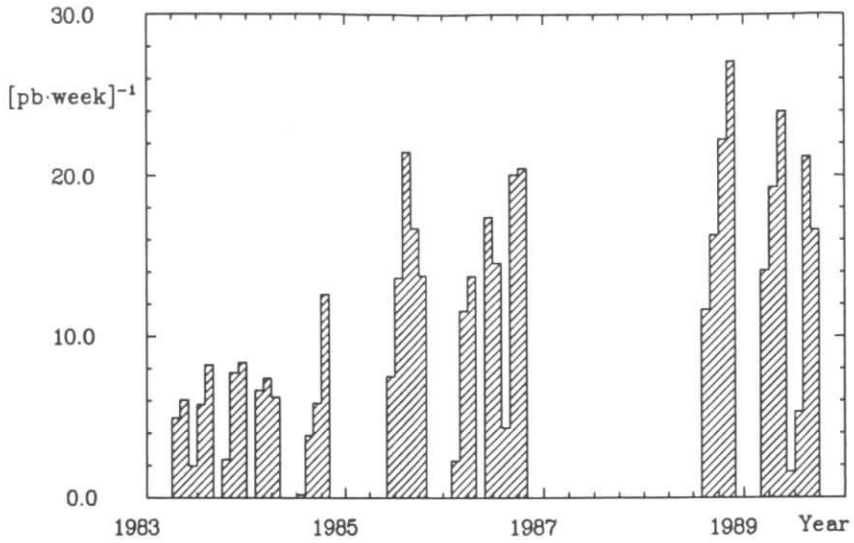

Figure 2.2: Luminosity history of the ARGUS experiment.

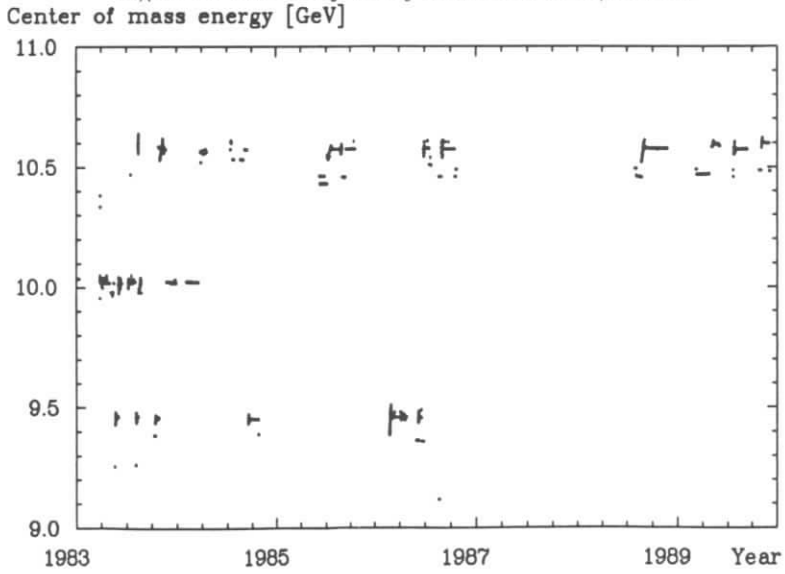

Figure 2.3: Energy history of the ARGUS experiment (each point represents an experimental run).

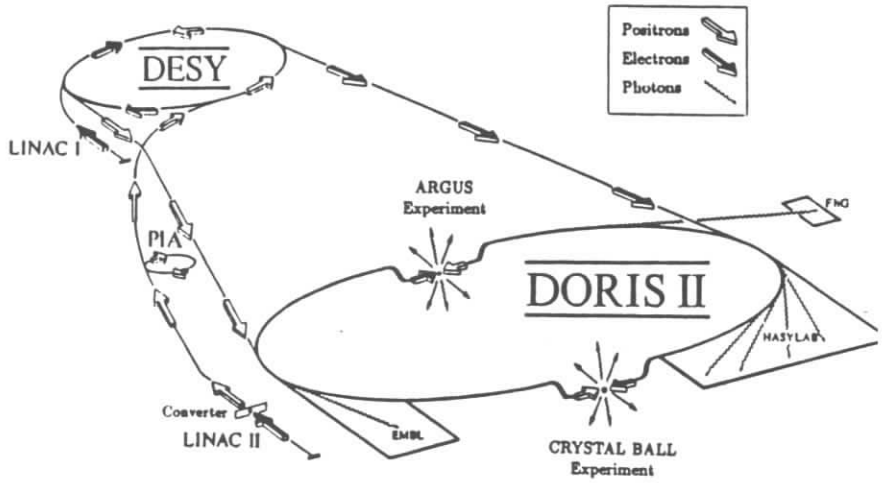

Figure 2.4: Part of the Deutsches Elektronen-Synchrotron accelerator network.

2.2 DESY and DORIS

The DORIS storage ring (Table 2.2) is part of a larger accelerator facility known as DESY (Deutsches Elektronen-Synchrotron) which is funded jointly by the City of Hamburg and the Federal Republic of Germany. The central components of the accelerator complex are the two synchrotrons which accelerate electrons, positrons, and protons for the other machines. Those parts of the accelerator network relevant to ARGUS are shown in Figure 2.4.

The first step in the acceleration chain is the creation of e^+e^- pairs by the bombardment of a tungsten foil target with an electron beam from LINAC-II. The positrons are magnetically separated and then stored by the Positron Intermediate Accumulator (PIA) until sufficient current has been accumulated to make acceleration in the central synchrotron (DESY) worthwhile. Electrons from a separate source are accelerated to 0.050 GeV by LINAC-I and then transferred to DESY, which accelerates them to the

Circumference	288 m
Radius of curvature	27.5 m
Length of straight sections	58 m
Number of bunches/beam	1
Bunch length (σ_Z)	25 mm
Bunch cross section (σ_X)	480 μm
Bunch cross section (σ_Y)	85 μm
Maximum center of mass energy	11.2 GeV
Average luminosity	$10^{31}\text{cm}^{-2}\text{s}^{-1}$
Maximum daily luminosity	1.5 pb^{-1}
Vacuum pressure	$4 - 8 \cdot 10^{-12}$ bar
Typical current	20-50 mA
Time to fill	2-10′
Time between fills	30-120′
Radio frequency	500 MHz

Table 2.3: DORIS II machine parameters.

storage ring's energy and injects. DORIS-II is capable of storing 30–50 mA in colliding beam operation with lifetimes of two to three hours at the lower current and 30 minutes at the maximum current. The beam current is limited by the aperture of the vacuum chambers, the beam-beam interaction, and the available radio-frequency power.

The DORIS-I ring was operational in 1973 but was extensively altered between 1979 and 1982 [130]. The original DORIS design was optimized for beam energies of 3.5 GeV and employed separate e^+ and e^- beam lines to minimize beam-beam space charge effects which limit luminosities in multi-bunch operation. In order to have a smaller magnet pole separation and a higher magnetic field, the new DORIS has only one vacuum pipe and the e^- and e^+ bunches follow the same orbit. These modifications were designed to improve machine operation at the energies required for Υ meson physics and to reduce power consumption. As an artifact of its original double ring design the storage ring is not planar – the collision point is 20 cm lower than the arcs. Synchrotron light from the vertical bending magnets (14 m from the interaction point) can cause

some problems for detector elements placed close to the beam.

At present DORIS-II can be operated at beam energies up to 5.6 GeV, limited by iron saturation in the dipole magnets and the amount of radio-frequency power available (1.1 MW) to replace the synchrotron radiation loss [131]:

$$\begin{aligned} \Delta E &= \frac{4\pi}{3} e^2 \beta^3 \frac{\gamma^4}{\rho} \\ &= 8.85 \cdot 10^{-5} \left(\frac{\text{m}}{\text{GeV}^3}\right) \frac{E_0^4}{\rho}, \\ P &= 8.85 \cdot 10^4 \left(\frac{\text{J} \cdot \text{m}}{\text{GeV}^4}\right) \frac{E_0^4}{\rho} (I_+ + I_-), \end{aligned}$$

where ΔE is the energy loss per turn per $e^{\pm}$, E_0 is the beam energy (both in GeV), ρ the radius of curvature of the storage ring (in meters), and P is the total radiated power (Watts). Radio-frequency cavities and klystrons can be located at three positions around the ring. DORIS-II operates in single bunch mode with an interval of 1 μs between collisions. The storage ring's luminosity is given by the expression:

$$L = \frac{I^+ I^-}{4\pi e^2 f \sigma_x \sigma_y},$$

where I^+, I^- are the positron and electron beam currents in amperes, e is the electron charge in coulombs, f the collision frequency, and the σ's are the bunch sizes. At one standard deviation, these sizes are 85 μm in the vertical direction (Y), 480 μm in the radial direction (X), and 2.5 cm in the direction[2] tangent to the beam path (Z) [132]. The large horizontal beam size is the result of synchrotron radiation, while the bunch length is limited by the properties of the synchrotron and the frequency of the power source. The beams have an energy dispersion of approximately 8 MeV.

2.3 The ARGUS Magnet System

Three elements of the storage ring's magnetic lattice intrude into the detector itself. The most important of these are two strong focusing ("mini-β") quadrupoles of 1 m focal length set at distances of 1.23 m from the interaction point (c.f. figure 2.5). These

[2]The positrons traverse the ring in a clockwise sense as viewed from above, defining the $+Z$ direction at the interaction point. The spherical coordinates: $R = \sqrt{X^2 + Y^2}$, $\phi = \tan^{-1} Y/X$ and $\cot\theta = Z/R$, are often used.

focus the beams on the collision point and allow DORIS-II to reach luminosities as high as $2 \cdot 10^{31}$ cm^{-2}s^{-1}. The focusing effect of the quadrupoles introduces beam divergences of approximately 0.9 mrad and 0.4 mrad in the X and Y directions respectively [118].

In addition to the mini-β quadrupoles there are two sets of compensation coils. One of these shields the quadrupoles from the detector's 0.755 T solenoidal field, while a second set, located in front of the quadrupoles, ensures that the DORIS beam trajectory has zero field integral through the detector, as is necessary for a symmetry of forces on the e^+ and e^- beams.

The main ARGUS magnet is composed of 13 solenoidal copper coils, 3 m in diameter, that surround the central detector. The gaps between the coils allow the passage of light guides that enable the time-of-flight and shower counters to be placed inside the coil, while their photomultipliers operate outside in a region of low magnetic field. The coils can carry a maximum current of 4500 A, which produces a field of 0.8 T. In normal running conditions a field of 0.755 T is used. The magnetic field was measured before the central components of the detector were installed [133] and parametrized to an accuracy of 0.2% for use in the reconstruction software. The coil is enclosed by an iron flux return yoke (325 metric tons) that also serves as a muon filter.

During experiment 3 (1984) the ARGUS Vertex Detection Chamber was installed. To free sufficient volume in the interaction region necessitated the truncation of the inner compensation coils. Unfortunately, moisture contamination introduced during the machining produced electrical shorts in some of the coils which forced the reduction of the central detector field to 0.48-0.54 T for the duration of that experiment. These data are not normally used for analysis.

2.4 The Beam Pipe

The aluminum beam pipe is 4 cm in radius, 1 mm thick, and is lined with lead paint in order to reduce synchrotron radiation: this corresponds to 1.13% of a radiation length. To enhance the conversion of photons to e^+e^- pairs, copper converters can be pulled into the interaction region with thicknesses of 100, 500, or 600 μm.

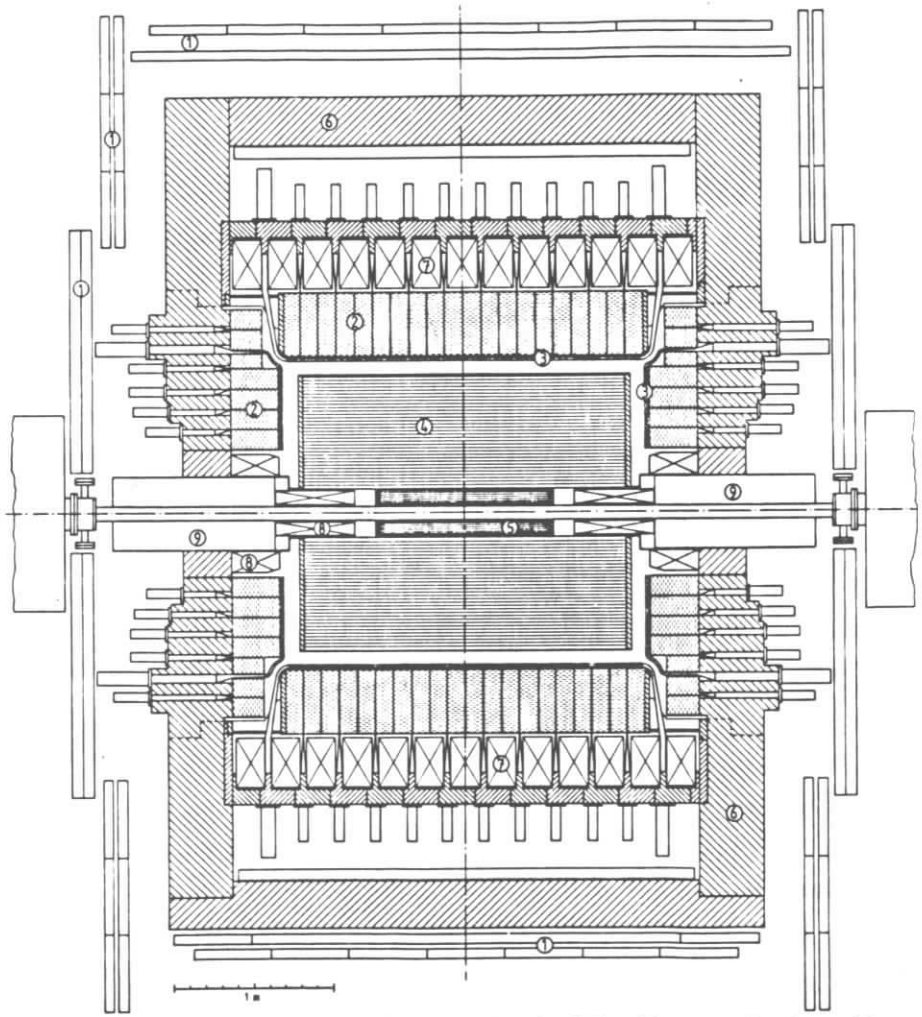

Figure 2.5: The ARGUS detector (cutaway view in YZ): (1) muon chambers, (2) shower counters, (3) time of flight counters, (4) drift chamber, (5) vertex chamber, (6) iron yoke, (7) solenoid coils, (8) compensation coils, (9) mini-β quadrupoles.

2.5 The Main Drift Chamber

The central component of the ARGUS detector is a cylindrically symmetric drift chamber [134]. The purpose of the chamber is to detect ionization trails left by the passage of charged particles through the gas. This information can be used to measure the geometry of the track and thereby determine the particle's momentum, or to determine the specific ionization (energy loss per unit length) which yields information on the particle's mass. The active components of the drift chamber consist of 5,940 sense wires (30μm gold-plated tungsten) and 24,588 field wires (76μm copper-beryllium) arranged in 36 layers.

The electrons from the ionization trails left by charged particles are swept to the sense wires by a strong electric field - the potential wires are grounded and surround the sense wires which are held at (2930.0 ± 0.5) V. The timing of this signal is used to determine a surface of constant drift time (isochrone) for each wire hit. The trajectory of the particle is tangent to these isochrones. The shape of the drift cells is almost rectangular, 18x18.8 mm^2, so as to make the isochrones nearly circular.

The ability to reconstruct tracks in three-dimensions is provided by twisting every second sense wire layer by a small angle, $\pm\alpha$, so that these α-layers form hyperboloids. The angle α varies as $\sqrt{R}$, ranging from 40 mrad for the innermost α-layer to 80 mrad at the outside of the chamber. A low-momentum charged track in the chamber will leave a noticeably curved set of hits in the layers parallel to the $Z-$axis:

$$\rho = \frac{P_\perp}{B \cdot 2.9979 \frac{GeV/c}{cm \cdot T}}$$

where ρ is the radius of curvature in centimeters, $P_\perp$ the transverse momentum in MeV/c, and B the magnetic field in Tesla. If the track makes a 90° angle with the Z-axis the α-layer hits (as viewed from the endcaps of the chamber) will appear as two similar curves rotated in ϕ by the angle $\pm\alpha(R)$. As the polar angle of the track decreases, the outer ends of the α-layer and Z-layer tracks will approach each other – and eventually coincide, if the track reaches the endcap.

The drift chamber information is reconstructed by a complex system of pattern

recognition and track fitting programs based on those of the MARK II detector [135]. The pattern recognition is initially done in two dimensions, r and ϕ, by matching circular trajectories to the drift chamber hits. This is possible because of the homogeneity of the magnetic field and the low density of the chamber gas. As the minimal requirement for the definition of a circle is the measurement of three points, all combinations of triplets of drift chamber hits are tried initially and their curvature determined. Attempts are made to extend each of these triplets through the introduction of additional hits that, on forming triplets with two of the initial hits, do not change the curvature significantly. The process is then iterated and various refinements are introduced. As the drift time information is used from the beginning of the analysis, a minimum of four hits is required for a track in order to resolve the left/right ambiguity inherent in drawing a circle tangent to a triplet of isochrones. In the three dimensional pattern recognition the α layer hits are extrapolated to each cylinder defined by an $r\phi$ track. The α layer hits form lines in the sZ plane (s = path length of the track in the $r\phi$ plane). The parameters estimated from these procedures are then refined by a least-squares fit.

The minimal track fit requires 4 hits in the axial layers and 3 hits in the α layers, resulting in an angular acceptance of $|\cos\theta| < 0.96$. The track reconstruction is efficient [136] within the kinematic limits $P_\perp > 50$ MeV/c, $|\cos\theta| < 0.92$. On requiring the track to traverse all layers of the drift chamber, the polar angle is further restricted to $|\cos\theta| < 0.76$. A rather atypical multi-hadron event [15], which nevertheless is typical of the drift chamber's performance, is shown in figure 2.6.

Physically, the drift chamber is a hollow gas-filled cylinder, 2 m long with inner and outer radii of 15 cm and 86 cm, respectively. The outer wall, which supports the wire tension (1.1 N for the field wires, and 0.7 N for the sense wires), is composed of 6 mm of aluminum, while the endcaps are 30 mm thick. To minimize multiple scattering in low momentum tracks the inner wall of the chamber is a carbon-fiber epoxy composite 3.3 mm thick (1.24% of a radiation length) coated with silver paint.

The choice of chamber gas is constrained by the required accuracy of the drift time and specific ionization measurements. If the electric field accelerates the elec-

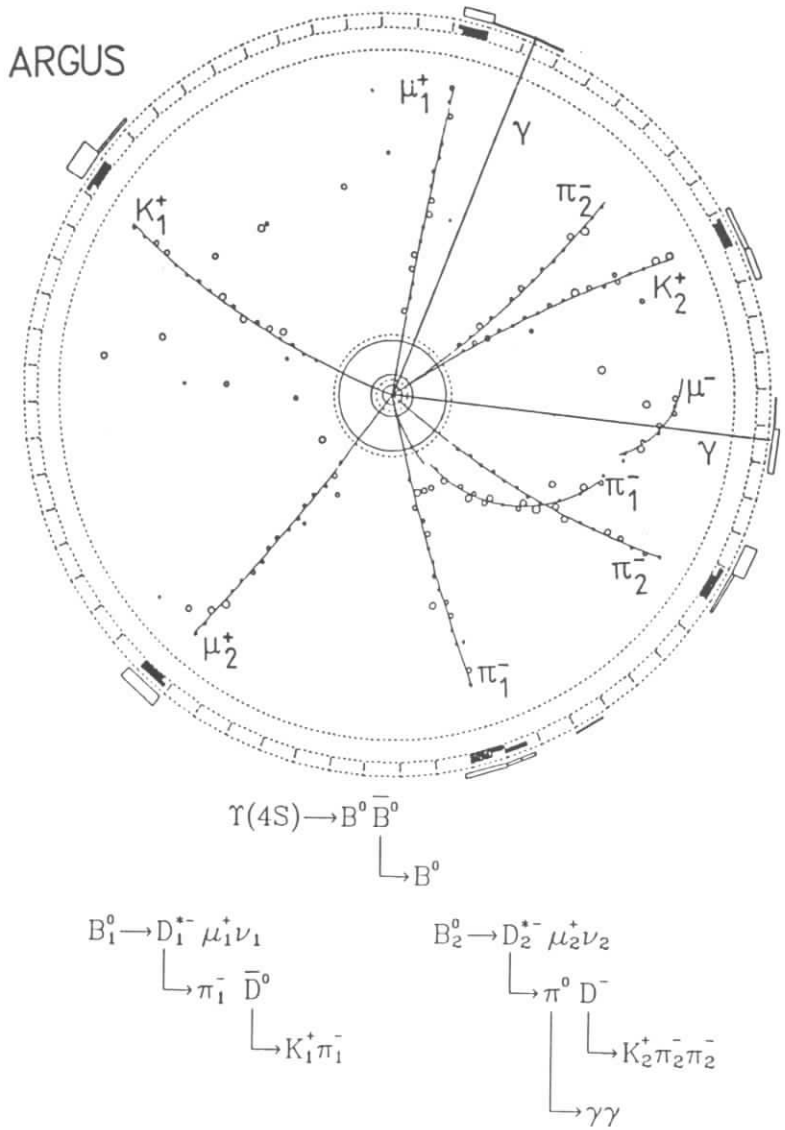

Figure 2.6: A reconstructed $B\bar{B}$ mixing event. The area of the rectangles with solid outlines is proportional to energy deposited in the calorimeter, while the shaded rectangles with dotted outlines represent ToF counters set by the event. The radii of the circles in the drift chamber are the drift distances from the wires hit in the event.

trons enough between collisions with gas molecules to cause secondary ionizations, an avalanche develops, amplifying the original signal. The choice of gas is critical as gases (or impurities) with a high electron-capture cross section may attach electrons. The ARGUS chamber ran initially with a mixture of 97% propane (C_3H_8)and 3% methylal ($CH_2(OCH_3)_2$) at a slight positive pressure (1035 mbar). Propane has the required advantages of a small diffusion coefficient, and a large radiation length (the active material in the chamber represents only 0.55% of a radiation length). When the polyatomic radicals produced in the gas ionization process neutralize they either dissociate or polymerize [137]. The polymers will condense on the cathode wires causing chamber aging. The presence of methylal, which does not polymerize and has a lower ionization potential than propane, suppresses polymerization by neutralizing the propane ions through charge transfer. The chamber gas is changed every 22 minutes at a flow rate of 12 m^3/hour to maintain homogeneity. However, most (99.8%) of this is gas that has been recycled and filtered. The gas quality is tested when gas enters and leaves the chamber by measuring the ionization from four ^{55}Fe sources.

After approximately 20 months of data-taking a small amount, 0.2%, of water vapour had to be added to cure damage resulting from contamination in the chamber. This contamination caused the current drawn by one quadrant of the chamber to increase approximately 1000 times beyond the normal value of 1 nA. This phenomenon was eventually attributed to the Malter effect [138]. Non-conductive deposits on field wires accumulate positive charge until the deposit short circuits. The electrons then released from the field wire produce more positive ions establishing a feedback loop, causing the deposit to grow, and creating a permanent discharge. The addition of water to the chamber gas coats the insulating deposits with a conducting layer, solving the discharge problem. The amount of water in the chamber must be carefully controlled – at concentrations of a few percent, electron capture by water molecules can significantly alter the wire efficiency [139].

The sense wire signals are processed by pre-amplifiers mounted on the chamber endplates. The integrated charges are then digitized by an ADC (analog-digital converter), while a discriminator starts a TDC (time-digital converter) operating in common stop

mode. The stop signal is defined by the time-delayed bunch-crossing signal gated with the first level trigger signal. The TDC discriminators also set hit registers used for fast drift chamber pattern recognition in the second level trigger processor. The timing information from the TDC is converted into a drift distance using a drift time space relation (TSR) determined from samples of at least 1,000 Bhabha events ($e^+e^- \rightarrow e^+e^-$). An approximate TSR is used to fit each calibration sample and is then iterated until the mean residual ($\langle d_{measured} - d_{TSR} \rangle$) ceases to change significantly. The standard deviation of the residuals approaches a limiting value of 190 μm for Bhabha events and 220 μm for multi-hadron events, resulting in a momentum resolution of:

$$\frac{\sigma(\mathrm{p}_\perp)}{\mathrm{p}_\perp} = \sqrt{0.0001 + (0.009 \cdot \mathrm{p}_\perp[\mathrm{GeV/c}])^2},$$

where $p_\perp$ is the transverse momentum of the particle. The constant term represents the contribution of multiple scattering which dominates the resolution below 0.8 GeV/c. The angular resolutions are $\sigma(\cot\theta) = 0.004$ and $\sigma(\phi) = 0.001$. The overall momentum scale has been refined through the analysis of decays of K^0_s and Λ with separated vertices. This results in a systematic error of less than 0.1% for the mass scale [140], limited by the statistics of the secondary vertex analysis and the accuracy with which inhomogeneities in the magnetic field have been measured.

The drift cell size was chosen to optimize the sampling of the ionization energy loss (dE/dX). As the average value of the dE/dX is determined by the physical properties of the gas as a function of particle mass and momentum, this is a useful quantity for particle identification. The relation is given to a good approximation by [2]:

$$\langle \frac{dE}{dX} \rangle = D\frac{Z\rho}{A}(\frac{Q}{\beta})^2[\ln(\frac{2m_e\gamma^2\beta^2c^2}{I}) - \beta^2]$$

where D=0.3071 MeV cm^2 g^{-1}; ρ, A, and Z, are the density of the chamber gas, the average mass number, and the nuclear charge; Q is the charge of the ionizing particle, $\gamma = E/m$, and $\beta = P/E$. One reason for using propane as a chamber gas is that it has a narrower Landau distribution (which describes the sampling variance of the dE/dX [141]) than standard chamber gases like argon, improving the separation of different particle types at low momenta.

The energy loss in each drift cell is determined from the integrated charge measured by the ADC's, which are calibrated with daily pulser runs. The raw pulse height is scaled by calibration constants determined from Bhabha events, and is corrected for space charge saturation effects (significant only for polar angles approaching 90°), and a small effect due to finite ADC integration times which produce charge loss at long drift distances. After these corrections, the dE/dX resolution varies between 4.4% and 5.5% during different run periods [142].

The distribution of dE/dX samples has a long high energy tail due to the contribution of infrequent collisions with large energy transfers. Because of this, a truncated average of the dE/dX for each track is used to estimate the most likely energy loss (30% of the samples with the largest dE/dX and 10% of those with the lowest are discarded), resulting in an approximately Gaussian distribution. This allows the definition of a χ^2 for any mass hypothesis:

$$\chi^2 = \frac{(\Delta \mathrm{E_T(m,p)} - \Delta \mathrm{E})^2}{(\sigma(\mathrm{p}) \cdot \frac{\partial \Delta \mathrm{E_T(m,p)}}{\partial \mathrm{p}})^2 + (\sigma_{<\mathrm{dE/dX}>} \cdot \Delta \mathrm{X})^2}$$

where ΔE is the average experimental energy loss per drift cell, $\Delta \mathrm{E_T(m,p)}$ the theoretical median energy loss for a given mass hypothesis and experimental momentum, ΔX is the average track length per cell, and $\sigma_{<\mathrm{dE/dX}>}$ is the dE/dX resolution. In ARGUS this measurement can be used to separate pions from kaons up to momenta of 0.7 GeV/c, and kaons from protons up to 1.2 GeV/c. Figure 2.7 shows the dE/dX distribution from a large sample of multi-hadron events, with the various particle types clearly separated in some momentum ranges.

Finally, the presence of approximately 10 kilolitres of propane in a thin pressure vessel necessitates certain safety measures. To this end, the entire inner detector is maintained in a nitrogen atmosphere.

2.6 The Vertex Detection Chamber

The Vertex Detection Chamber [143], installed in 1984, is the newest component of the detector. Structurally, the chamber is a hollow double cylinder 1 m long with an inner

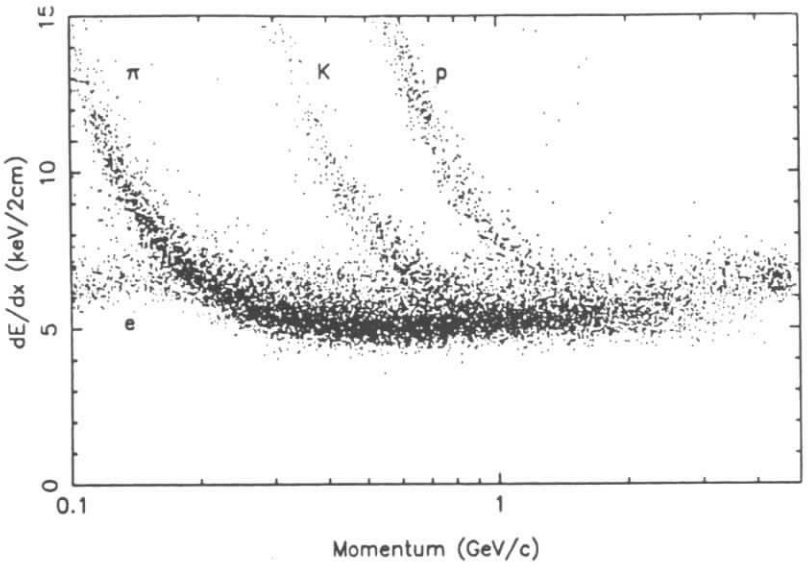

Figure 2.7: Distribution of drift chamber specific energy loss as a function of momentum for a typical multi-hadron event sample.

radius of 5 cm and an outer radius of 14 cm. The two cylinders are constructed of a carbon fibre/epoxy composite material, 0.9 mm and 1.5 mm thick, respectively. The endcaps of the chamber are constructed of 2 cm thick fibreglass. The active components of the chamber consist of 594 signal wires (20 μm diameter gold-plated tungsten-rhenium), surrounded by 1412 potential wires (127 μm diameter copper beryllium alloy), arranged in a close-packed hexagonal geometry. This is an unusual geometry for a drift chamber but has the advantages of maximizing the number of drift cells/track (8) while minimizing the ratio of field to sense wires. The inner radius of a cell is 4.5 mm and the potential wires are maintained at -3500 V. This avoids the necessity of coupling the readout electronics to the sense wires via large capacitors (the case in the main drift chamber). All sense wires run parallel to the Z axis. The gas used is CO_2 at a pressure of 1.5 bar. Following the experience with the large drift chamber, 0.3% water vapor was added to the VDC gas. The chamber electronics are read out by TDC's and calibrated by daily pulser runs.

The chamber timing information is used in a manner similar to that of the main chamber but only after the main drift chamber pattern recognition and track fit is complete. The pattern recognition is derived from main chamber tracks traced back into the VDC. The track parameter fit uses the results of the main chamber fit as constraints, allowing for multiple scattering effects which are estimated using the most likely mass hypothesis from combined dE/dX and time-of-flight particle identification. There is no attempt to increase the reconstruction efficiency for very low momentum tracks by a pattern recognition analysis employing the information from both chambers. The introduction of the VDC in the track fit improves the resolution $(\sigma(P_\perp)/P_\perp)$ for 5 GeV/c muons from $0.9\% \cdot P_\perp$ to $0.6\% \cdot P_\perp$.

The average value of the drift time space relation residuals over most of the drift cell is 50μm. A better measure of the resolution [132] is the separation of Bhabha tracks at the origin, 135 μm, corresponding to 100 μm vertex resolution in the XY plane. In more complex events the combined effects of multiple scattering and improperly assigned hits leads to a 40% increase in vertex resolution. The introduction of the VDC resulted in a 50% increase in the number of K^0_s reconstructed from secondary vertices.

2.7 The Time-of-Flight Counters

The time-of-flight or ToF system [144] of the ARGUS detector serves three purposes:

- it is one of the main sources of particle mass information,
- the barrel counters are used in both the first and second level triggers,
- the endcap counters are used in the online luminosity monitor.

The system is situated directly outside the drift chamber and is divided into three sections: the barrel and two endcaps. The barrel section covers 75% of 4π and consists of 64 rectangular scintillation counters arranged axially on a cylinder 95.1 cm in radius. Each barrel counter is a block of 2 cm thick scintillator material 1.8 m long, and is viewed by two phototubes. The two endcap sections contain 96 wedge-shaped counters which are viewed by single phototubes. The endcap counters are 2 cm thick and 48 cm

long, ranging from 5.1 cm to 11.4 cm in width. The endcaps cover 17% of 4π ($0.78 < |\cos\theta| < 0.95$). The ToF counters are connected to the phototubes by light guides which pass through slots in the ARGUS magnet coil. The phototubes are located outside the magnet so they can operate in regions relatively free from magnetic fields. They are shielded from any remaining field by soft iron and μ metal cylinders.

The ToF counter TDCs are started in common by the bunch-crossing signal, and stopped individually by discriminator signals with a cable delay of 200 ns. Each discriminator uses 80% of the appropriate phototube signal as input and also sends signals to the fast trigger logic and "Little Track Finder" (the second level trigger processor). The remaining 20% of the phototube signal is digitized and used to correct for timing jitter caused by the amplitude dependence of the discriminator threshold crossing.

The ToF counters were all pre-calibrated in an electron beam from DESY. Time variations of the calibration parameters are determined from Bhabha events ($e^+e^- \rightarrow e^+e^-$) by a simultaneous fit with the time of flight constrained to that calculated from drift chamber information (using the $e^\pm$ mass). The TDC slope parameter (nanoseconds/count) is determined daily by a laser system using a calibrated delay line as reference [145]. The limiting resolution of the ToF counters was determined by Monte-Carlo analysis [144] to be 170 ps, due principally to sampling statistics. The practical resolution is somewhat larger, 210 ps for Bhabha events, and 230 ps in multi-hadron events. This is due to the combined effects of drift in phototube amplification, uncertainty in the bunch-crossing signal (50 ps), inaccuracies in the parametrization of the pulse height correction, and multiple hits in hadronic events. Surprisingly, the resolution of the endcap counters is not much worse (approximately 260 ps), even though the light from the barrel counters is sampled twice. This is due to the wedge shape of the endcap counters which produces a "negative" attenuation length; more light from the narrow (distant) end of the wedge is focused on the guide.

In multi-hadron events, approximately 80% of tracks with $p_\perp > 0.120$ GeV/c have a clear time-of-flight measurement. Tracks with smaller transverse momentum tend to spiral in the drift chamber and may not be properly traced to the counters, even if they

eventually reach an endcap. Additional confusion is produced by events with multiple hits in a counter. However, for the two charge particle topologies relevant to this thesis at least two ToF hits are required to set the trigger – so there is little incremental efficiency loss on requiring ToF information for particle identification.

To extract mass information, the measurements of path length and momentum from the drift chamber analysis are combined with the time-of-flight measurement. The particle identification ability is limited by the Lorentz boost and mass differences of the particles in question (figure 2.8). The different particle species are separated to three standard deviations over the following momentum ranges:

- e/π separation for $p < 180$ MeV/c,
- π/K separation for $p < 750$ MeV/c,
- K/p separation for $p < 1150$ MeV/c,

providing the particle has a transverse momentum of at least 110 MeV/c so that it reaches the barrel. The masses of muons and pions are too close for separation with ToF measurements. Since the time resolution is of the same order of magnitude as the differences in flight time expected for normal particles, the ToF information is best expressed statistically. One defines a χ^2 to measure the likelihood of a particular mass hypothesis:

$$\chi^2 = \frac{\left[\frac{1}{\beta_{ToF}} - \frac{1}{\beta_{hyp}}\right]^2}{\left[\sigma^2_{ToF} + \sigma^2_{hyp}\right]},$$

where $\beta_{hyp} = p/\sqrt{p^2 + m^2_{hyp}}$ is the velocity calculated for the mass hypothesis, given the drift chamber momentum measurement, and $\beta_{ToF} = X/c\tau_{ToF}$ where X is the path length determined from the drift chamber fit, and τ_{ToF} the measured time of flight. The σ_{ToF} and σ_{hyp} are the corresponding error estimates. The χ^2 is simply the difference between measurement and theory expressed in units of the experimental error.

2.8 The ARGUS Electromagnetic Calorimeter

The ARGUS shower counter system [146] has several functions:

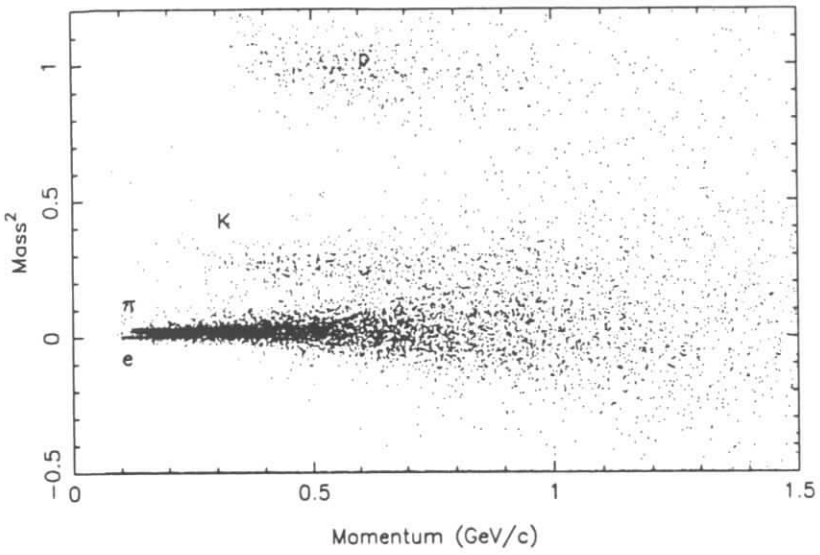

Figure 2.8: Distribution of particle masses determined from the time-of-flight analysis for a typical multi-hadron event sample.

- the first level trigger uses energy sums from various regions of the calorimeter,
- the online luminosity monitor requires angular correlations in calorimeter energy,
- photons and other neutral particles can only be detected as energy deposits in the calorimeter,
- photon showers in the calorimeter can be used to reconstruct π^0s,
- shower energy and shape can be used to separate electrons, muons, and hadrons.

The calorimeter is composed of 1760 individual shower counters covering 96% of 4π. The barrel counters are arranged in 20 rings of 64, while each endcap is composed of 240 counters arranged in 5 rings with $32 + I * 8$ ($0 \leq I \leq 4$) counters in each. The barrel counters alternate (in ϕ) between wedge shaped modules and rectangular modules. Each counter is composed of alternating layers of lead (64 1.0 mm layers in the barrel, 45 1.5 mm layers in the endcap) and scintillator (5.0 mm). Both barrel and

endcap counters represent 12.5 radiation lengths of material. The segmentation of the calorimeter corresponds approximately to one Moliere radius [147], the average lateral size of an electromagnetic shower.

The light from each shower counter's scintillator (wrapped in aluminized mylar) is reflected internally until it reaches a 3 mm thick bar of wavelength shifter running the length of the counter. The wavelength shifter absorbs the scintillation light and emits light at lower wavelengths, effectively turning some of the light through a right angle. Two nylon threads separate the wavelength shifter from the counter to ensure internal reflection. The light from the wavelength shifter is then transported to a photomultiplier by a light guide. The shower counters are mounted inside the magnet coil to allow detection of low energy photons. There are only 0.16 (0.52) radiation lengths in front of the barrel (endcap) modules. This allows detection of 30 MeV photons with an efficiency of approximately 85%. In the standard analysis a threshold of 50 MeV is used, resulting in a detection efficiency of $\geq$ 98% for photons.

The principal application of the calorimeter in analysis is the detection of energy deposited by neutral particles, principally photons, which leave no signal in the other detector components. As most photons in hadronic events come from π^0 decays, good energy resolution is required to suppress combinatoric background. With as many as ten photons in each hadronic event there are often ninety possible combinations for a π^0! The energy resolution obtained in the barrel part of the calorimeter is:

$$\frac{\sigma(E)}{E} = \sqrt{0.072^2 + \frac{0.065^2\ \text{GeV}}{E}} \qquad \text{(barrel)},$$

where the energy, E, is in units of GeV. The individual contributions to each term are given in table 2.3 [148]. In the endcap calorimeter the resolution is given by:

$$\frac{\sigma(E)}{E} = \sqrt{0.0752^2 + \frac{0.076^2\ \text{GeV}}{E}} \qquad \text{(endcap)}.$$

The resolution at high energies is determined from barrel Bhabhas and $e^+e^- \rightarrow \gamma\gamma$ events. The resolution for low energy photons is determined from the study of π^0 decays where one photon converts to an e^+e^- pair in the material of the detector [149]. This allows a high precision measurement of the converted photon's energy in the drift

Contribution	Endcap	Barrel
photon statistics	0.058 $GeV^{1/2}$	0.051 $GeV^{1/2}$
shower leakage	0.049 $GeV^{1/2}$	0.041 $GeV^{1/2}$
shower leakage	0.021	
optics (light guides)	0.020	
calibration and pedestal subtraction	0.010	
support structure	0.059	

Table 2.4: Contributions to shower counter energy resolution.

chamber; the width of the reconstructed π^0 mass distribution is then a measurement of the resolution for the unconverted photon. At low energies there is a bias in the energy scale due to the threshold for individual counters, 6 MeV, which suppresses the contribution from the edge of a shower (up to 20% of the shower energy is lost). This correction is also determined from π^0 decays with one converted photon. Photon energies are shifted by the average change in the unconverted photon energy required to make the experimental π^0 mass match the world average value [2].

In order to separate photons from high momentum π^0s, whose photon showers merge together, high spatial resolution is also needed. At high energies the angular resolution is approximately 13 mrad (10 mrad) for barrel (endcap) counters. This is derived by reconstructing the center of energy of the shower:

$$\vec{r} = \sum_i^n \vec{r}_i E_i$$

for a shower spread over n counters, with centers r_i, and energies E_i. At low energies the angular resolution decreases until it is limited by counter size (98 mrad).

The energy scale of each shower counter is determined from samples of approximately 10^5 Bhabha events (approximately 7 pb^{-1}). A laser system [145] provides daily calibration runs that are used to compensate for short-term variations in the response of the photomultipliers and electronics. The counters were originally calibrated in a test beam in order to determine the effects of shower leakage and light collection efficiency.

A Monte Carlo simulation using the EGS code [150] determined the factors for conversion of energy in scintillator to deposited energy, and the correction for absorption in the support structure. The effects of these corrections during normal detector operation were verified using Bhabha events.

The calorimeter can also be used for particle identification. At high momenta, electrons interact with the calorimeter material through radiation and to a smaller extent through ionization. The bremsstrahlung photons then produce e^+e^- pairs on scattering off the heavy lead nuclei. These secondary leptons then produce secondary photons, resulting in a cascade. The bremsstrahlung component of the shower of a relatively heavy particle like a muon is suppressed by a factor $(m_e/m_h)^2$. For these *minimum ionizing* particles only the ionization component of the interaction contributes significantly to the energy loss. These particles can be separated from electrons by their small, momentum independent, shower energies. When the heavier particle is a hadron it may also interact strongly with the nuclei in the shower counters, causing fission, pion production, or spallation reactions. This effect leads to a hadronic interaction cascade, which normally has a much wider lateral spread than an electromagnetic shower. On the basis of this difference in shape one can obtain some separation between hadronic and electromagnetic showers. One defines a parameter describing the width of a shower with N counters ($N > 3$) as:

$$f_{lateral} = \frac{E_{lateral}}{E_{lateral} + E_1 + E_2},$$
$$E_{lateral} = \sum_{i=3}^{N} \frac{(\vec{r}_i - \vec{r})^2 E_i}{< r >^2},$$

where $< r >$ is the average distance between counters and the counters are numbered in order of decreasing energy deposition. Few electromagnetic showers have an $f_{lateral} > 0.6$ while approximately half of hadronic showers do.

2.9 The Muon Chambers

There are three layers of muon chambers in ARGUS with a total of 1744 proportional counters. The inner layer, inside the iron yoke, relies on the coil as a muon filter. With the shower counters this amounts to about 3.3 absorption lengths of material, resulting

in a momentum threshold of 700 MeV/c. The yoke represents 1.8 absorption lengths producing a momentum threshold of 1100 MeV/c for the outer layers. The inner layer covers 43% of 4π, while each of the outer layers covers 87%.

Each proportional counter consists of a square cross-section aluminum tube 6 cm wide with 2 mm thick walls. A 50 μm gold plated tungsten wire, at a potential of 2350V, runs the length of each counter. The signals from the chambers are amplified and fed to a discriminator. Only the addresses of muon chambers that register a hit are read out by the data acquisition system. The efficiency of the chambers was determined to be 0.978 ± 0.001 through the analysis of cosmic-ray events [151]. An event: $e^+e^- \rightarrow \mu^+\mu^-\gamma$ is shown in figure 2.9.

The muon information can be used to calculate χ^2s for particle identification [152]. This is rather more difficult than the ToF and drift chamber analyses as the drift chamber tracks must be extrapolated through the shower counters, coil, and yoke and an estimate of the error of the extrapolation made. Provision is made for the magnetic field, energy loss, and Coulomb scattering.

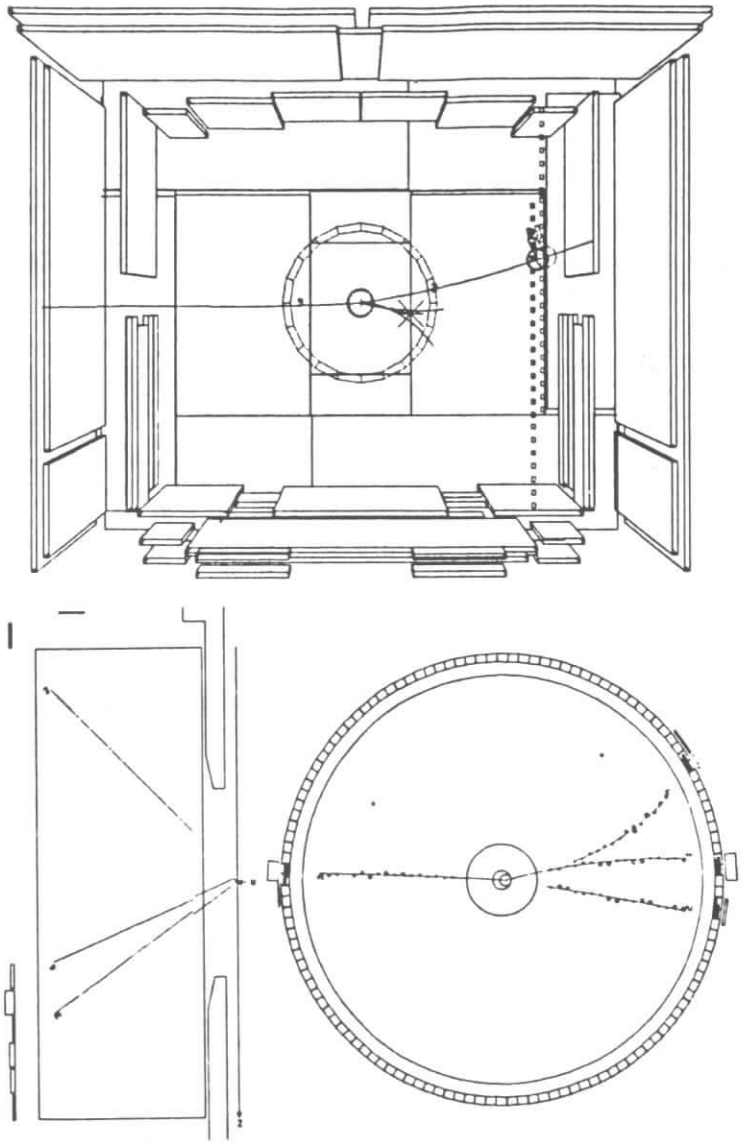

Figure 2.9: The upper part of the figure shows the muon chamber display for an event $e^+e^- \rightarrow \mu^+\mu^-\gamma$ where the photon converts to an e^+e^- pair in the inner wall of the drift chamber. The inner detector display is shown in the lower part of the figure in $r\phi$ and rZ projection.

2.10 The ARGUS Trigger

The collision rate at DORIS allows only 1 μs between bunch crossings for the decision to read out an event. This restricts the information available for a first level trigger to that from the time-of-flight and shower counters. This is available within 200 ns of the bunch crossing. A successful first level trigger [153,154] initiates the digitization of the detector signals and suppresses further triggers until this condition is cleared by either the second level trigger veto or the completion of data transfer to the online computer system. The second level trigger [155] combines drift chamber and time-of-flight information in a fast two-dimensional track search requiring approximately 20 μs. This processor reduces the event rate from 100-400 Hz to 5-20 Hz. A flow-chart of the data acquisition system is shown in figure 2.10 [153].

The shower counter information used in the first level trigger is formed from the raw analog pulse heights. These are combined by SDS (Split/Delay/Sum) units into groups consisting of 22 counters (2 counters wide in ϕ, and 11 rings long) which are then combined into larger analog sums and sent to discriminators. The SDS units in the barrel region are limited to one hemisphere in Z and include counters from the outer ring of the endcap, which has the same segmentation in ϕ as the barrel part of the calorimeter. The remaining 176 counters in an endcap are divided into 8 SDS units, each occupying a range in ϕ of approximately 45°.

The total energy trigger (ETOT) is the only trigger to use shower counter information from both the barrel and endcap. The shower counter energy from an entire $\pm Z$ hemisphere is summed and sent to a discriminator. To set an ETOT trigger both hemispheres must have a total energy above threshold. At this level the signal presented to the discriminator is proportional to the visible energy so it is impossible to define an exact threshold in terms of total deposited energy, since the fraction of energy visible in the scintillator is different in the barrel (37%) and endcap (27%). When all the energy is deposited in the barrel of the detector, the ETOT threshold ranges between 630 MeV per hemisphere and 907 MeV per hemisphere for different trigger periods, with an average value of 740 MeV.

The high energy shower trigger (HESH) is sensitive to local concentrations of energy. The shower energy from five barrel SDS units (110 counters) is summed and sent to a discriminator. The average threshold setting is approximately 1350 MeV. For different trigger periods this setting varies between 950 MeV and 2070 MeV. Each HESH element overlaps the neighboring element by one SDS unit and is confined to one Z hemisphere. There are a total of 16 "OR"ed elements, 8 in each hemisphere, corresponding to a segmentation of 56.25° in ϕ (including the 11.25° overlap between elements).

The last two data triggers use both time-of-flight and shower counter information. Only barrel ToF counters are used in these triggers and a coincidence is required between the two photomultiplier signals from each time-of-flight counter. The signals from groups of 4 ToF counters (22.5° wide in ϕ) are "OR"ed into a charged particle pre-trigger (CPPT) ToF element. For a CPPT pre-trigger element to be set, the CPPT ToF element must be in coincidence with one of the two corresponding CPPT shower counter elements ($\pm Z$). These are composed of 3 SDS units in one hemisphere of the detector. Each CPPT shower element has an SDS unit in common with the element adjacent in ϕ. The discriminators on the CPPT shower elements are set at approximately 75 MeV in order to ensure a high efficiency for minimum ionizing particles, which deposit 160-200 MeV in the barrel shower counters. This setting has varied over the history of the detector between 62 MeV and 105 MeV. In order to reach a CPPT element a charged track must have a transverse momentum of at least 110 MeV/c.

The charged particle pre-trigger requires one CPPT element set in each Z hemisphere with no ϕ restriction. The CPPT elements are also used in the coincidence matrix trigger (CMATRIX). This trigger replaces the CPPT trigger's approximate requirement of longitudinal momentum balance by approximate transverse momentum balance. This is accomplished by requiring that at least two CPPT elements be set, irrespective of hemisphere, but separated by at least 90° in ϕ. This geometric requirement raises the effective transverse momentum threshold for individual tracks in charge balanced two-prong events to 250 MeV/c, as two oppositely signed tracks with 110 MeV/c $P_\perp$ will hit the same CPPT element (forming two halves of the same circle). This trigger is of crucial importance in detecting events produced by two-photon collisions which rarely

leave large energy deposits in the calorimeter and are often Lorentz boosted along the detector axis.

In addition to the triggers discussed above, which are designed to accept most of the interesting physics events, there are two triggers used to monitor detector performance. The cosmic trigger is used to collect cosmic ray data when the storage ring is inoperative and requires a coincidence between two CPPT-ToF elements opposite in ϕ. There is also a random trigger running at a rate of 0.1 Hz that is used to determine the extent of calorimeter and drift chamber background noise.

The pre-trigger rate varies between 100-400 Hz; as it takes over a millisecond to read out an event, this rate is unacceptable. To suppress this rate a second level trigger is installed. This is derived from drift chamber and time-of-flight information. The second level trigger is based on a microprocessor and is known as the "Little Track Finder" or LTF [155,156]. The LTF provides a fast two-dimensional drift chamber pattern recognition.

The LTF processor recognizes a track if a sufficient number of drift chamber and ToF hits coincide with a predefined geometric mask. In the standard configuration, each cell in the second innermost axial layer of the drift chamber (layer 17) is matched to an arc of 21 barrel ToF counters, centered on the ϕ angle of the layer 17 drift cell. One layer 17 cell/ToF counter combination defines an LTF mask. There are a total of 1512 LTF masks. Each LTF mask corresponds to a particular ϕ and $P_\perp$ range in the drift chamber. The 21 masks corresponding to one layer 17 cell define an LTF "mushroom". The DC information is provided by the TDC hit registers. The remaining axial wires inside each mask are "OR"ed in triplets of layers to minimize sensitivity to chamber efficiency. An LTF track is defined by the coincidence of

- each of the superlayers (layer triplets),
- the "OR" of the two α layer drift chamber cells closest to the layer 17 cell,
- the signal from the layer 17 cell,
- and the coincidence of the two photomultiplier signals from the ToF counter.

The information from the α layers restricts the vertex to be within 30 cm of the origin in the Z direction. The dominant contribution to the LTF pattern recognition efficiency (85-97%) is the requirement of a hit in layer 17. This limits the LTF efficiency to the drift chamber single-hit efficiency. The ToF coincidence efficiency is better than 0.998 [157].

The LTF was extended into the VDC in 1986 through the definition of VDC extensions of the LTF mushrooms in the online VAX filter (discussed below). As it was decided that this information unduly restricted the event vertex, event rejection on this basis was never enabled.

In standard running conditions at least two LTF masks are required for the CPPT and CMATRIX triggers, one mask is required for the HESH, and none are required for the ETOT trigger. These requirements result in a second level trigger rate of 10-20 Hz. In early ARGUS running high background conditions led to an increase of the LTF threshold to as many as four masks for the triggers based on the CPPT. It was also common to require a coincidence between the CPPT and CMATRIX triggers. The average time required by the LTF to process an event is 20 μs, resulting in a contribution of 0.2% to the dead time for a first level trigger rate of 100 Hz.

2.11 Data Acquisition

The transformation of the raw detector pulse heights to a form suitable for offline analysis is accomplished by a chain of computer systems. The various analog signals are digitized by modules that are part of a CAMAC system. The digital information is then read out by a CAB (CAMAC booster [156]) microprocessor which formats the event and initiates data transfer to a DEC PDP 11/45. This, in turn, transfers the data to a DEC VAX 11/780 online computer. The average amount of digitized information per event is approximately 2 Kbytes. Originally, the CAMAC system was read out directly by the PDP, requiring about 40 ms. The introduction of the CAB reduced this to 3 ms. The delay is dominated by the data transfer rate of the online computers and related protocols. The CAB allowed ARGUS to maintain stable trigger conditions with a threshold of only two LTF masks for the CPPT based triggers. Previously, an event rate higher than 10 Hz would result in a dead time of more than 40%. With the current configuration the dead time is less than 5%.

The PDP computer is able to store events on its own disk, transfer data directly to the DESY IBM, or, in normal operation, transfer data to the VAX. The PDP/VAX link can sustain an event rate of 300 Hz, well above that of normal data taking. The PDP also controls the data taking, experiment parameters, calibration procedures, and trigger logic tester. The LTF masks are also loaded into the microprocessor from the PDP.

The VAX system runs several different tasks. The first transfers data from the PDP into a global section (essentially a Fortran COMMON accessible from several processes) formatted as a ring buffer. This first buffer is able to accumulate data for several hours before filling. A second process transfers data from this buffer to a second; in the process a software event filter (described below) rejects approximately 20% of the events. The data from the second buffer are transferred to the DESY IBM by a third process. As the IBM operates in a time sharing mode, simultaneously accepting data from several other experiments and providing computing services to over a hundred users, the buffering system on the VAX is essential for continuous data taking. The

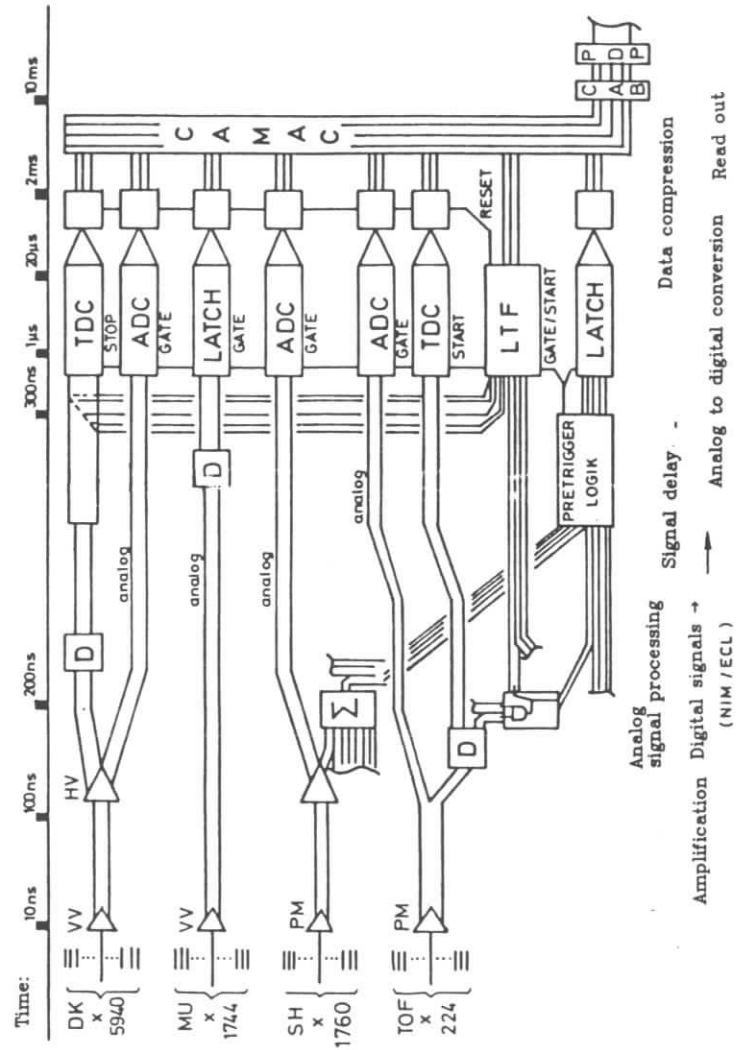

Figure 2.10: Data acquisition flow-chart.

VAX also runs an online monitoring task that uses any spare cycles left by the data transfer routines to accumulate statistics on as large a fraction of the data as possible. This program keeps statistics on hit frequency for all detector and trigger components enabling the experiment's operators to detect most system failures. ADC pulse heights are also monitored for the shower counters, drift chamber, and VDC. The monitoring task also maintains a run history display and a status display, showing the status of the data transfer tasks, and the total trigger and ETOT rates for the last day of running. An online event display is also available.

On the IBM, data from the VAX are stored on disk by a resident online process which initiates batch jobs to copy data to tapes as necessary. These jobs in turn initiate lower priority jobs to concatenate these data sets to tapes which are saved permanently (EXDATA).

2.12 Online Filter

The online event filter was introduced in 1985 in order to reduce the number of EXDATA tapes. Essentially, the filter requires that the LTF masks match CPPT elements and that events with two LTF masks have zero total charge. The following event classes are passed by the filter with no further requirements:

1. ETOT triggers,
2. HESH triggers,
3. COSMIC triggers,
4. RANDOM triggers,
5. CPPT or CMATRIX triggers with more than three LTF tracks,
6. CPPT or CMATRIX triggers with a single ETOT hemisphere above threshold,
7. any events with ambiguous or corrupted trigger or LTF information.

For the remaining event classes the following requirements apply:

1. There must be at least two LTF tracks matched to CPPT elements (i.e. the ToF counter defining the LTF mask must also belong to that of a set CPPT element).
2. A minimum of two CPPT-matched LTF tracks must be separated by at least 95° in ϕ.
3. Events with two CPPT-matched LTF masks are required to have approximate charge balance. This is determined from the range of track curvatures allowed in the LTF masks set in the event.

To verify the effect of the filter algorithm, 10% of the events that would otherwise be rejected by the filter are accepted and flagged.

2.13 Reconstruction Software and Preliminary Data Selection

The ARGUS reconstruction program is the first level of offline analysis. The program is divided into several sections which run in the following sequence.

IO: Event input/output, verification of bank structure, extraction of appropriate calibration constants from auxiliary data sets.

FA: Fast recognition of $e^+e^- \to e^+e^-$ and $e^+e^- \to \gamma\gamma$ events. Implementation of the VAX event filter offline. This step is frequently used to extract events from EXDATA tapes to determine approximate calibration constants before reconstruction is done on the entire data sample.

DT: Two dimensional drift chamber pattern recognition. For each track first approximations for $\kappa = 1/P_\perp$, d_0 ($r\phi$ component of the closest approach of track to the origin), and ϕ are determined.

D3: Three dimensional drift chamber pattern recognition. For each track initial values for the parameters $\cot\theta$ and Z_0 (Z-component of the distance of closest approach) are determined.

DF: Track fit. Refinement of track parameters and calculation of error matrix. As energy loss is no longer ignored, this step must run in parallel with the DA step.

DA: dE/dX Analysis.

VD: Vertex chamber reconstruction.

VX: Vertex-finding algorithm. A mutual point of closest approach is determined for all drift chamber tracks. Tracks with poor fits to this point are discarded and the process iterated to determine a main event vertex. The discarded tracks are searched for secondary vertices ($K^0_S \to \pi^+\pi^-$, $\Lambda \to p\pi^-$, or $\gamma \to e^+e^-$ (conversion)) A last attempt is made to form vertices by combining tracks not assigned to primary or secondary vertices with primary vertex tracks.

TF: Time-of-flight reconstruction.

SH: Shower counter reconstruction.

MU: Muon chamber reconstruction.

When the above sequence is complete a call is made to a standard routine (PHMAIN) to allow physics analysis of the event. The reconstruction of charged tracks takes most (90%) of the computer time required for event reconstruction. The program segments after the vertex algorithm can be repeated independently as calibration constants are fine tuned. Initially, events from the EXDATA tapes are used as input and all events with at least two tracks reconstructed with $d_0 < 1.5$ cm (closest approach to the origin in the XY plane) and $Z_0 < 6.0$ cm (closest approach to the origin in Z) are written to an EXPDST output tape, the first level of reconstructed data.

The events on the EXPDST tapes are dominated by Bhabha events ($e^+e^- \to e^+e^-$) which are essential for calibration. For physics analysis, two types of data sets with these events excluded are available: multi-hadron tapes (EXMUHA), and two-prong tapes (EXTWOP). The EXMUHA events are selected as follows:

1. Any events with more than 2 tracks from a reconstructed vertex with $r_{vertex} < 1.5$ cm and $|Z_{vertex}| < 6.0$ cm are accepted.

2. Any events with no fitted vertex, at least 1.7 GeV in the shower counters, and with more than 2 tracks that intersect a cylinder about the origin defined by $|d_0| < 1.0$ cm and $|Z_0| < 5.0$ cm are accepted.

The criteria for the EXTWOP tapes were developed by H. D. Schultz and are somewhat more complicated. The following event classes are accepted:

1. Muon pairs. Exactly two oppositely charged tracks with either a fitted vertex with $r_{vertex} < 1.5$ cm and $|Z_{vertex}| < 6.0$ cm, or $|d_0| < 1.0$ cm and $|Z_0| < 5.0$ cm. Each track must have a hit in at least one muon chamber layer, shower energy less than 0.6 GeV/c, $|\cot\theta| < 1.127$, and a momentum between 2 and 7 GeV/c. The two tracks must also be collinear to within 11.5°.

2. $\gamma\gamma$ events and τ pairs. Exactly two oppositely charged tracks with the same vertex requirement as in the previous class. The total shower energy must be less than 2.5 GeV.

3. All events without a fitted vertex but with at least three tracks with $|d_0| < 2.0$ cm and $|Z_0| < 6.0$ cm, excluding those in EXMUHA category 2.

4. Events with two opposite sign tracks fitted to a vertex within $r_{vertex} < 1.5$ cm and $|Z_{vertex}| < 6.0$ cm, except those excluded by anti-Bhabha cuts or accepted in EXTWOP category 1 or 2. Any number of tracks not fitted to the main vertex are allowed.

5. Events without a fitted vertex but with exactly two tracks with $|d_0| < 2.0$ cm and $|Z_0| < 6.0$ cm, except those excluded by anti-Bhabha cuts or accepted in EXTWOP category 1 or 2.

It should be noted that, although there is no overlap between the EXMUHA and EXTWOP data sets, the latter also contain some classes of multi-hadron events (selection categories 3 and 4). This complicates the analysis of low multiplicity processes; in particular, events from the process $\gamma\gamma \to K^0_s K^0_s$ are divided between both types of tapes. In order not to be rejected as Bhabha candidates, events from EXTWOP

categories 4 and 5 must have $|\cos\theta| < 0.866$ for at least one of the tracks. In addition, the tracks assigned to the vertex region must satisfy at least one of the following requirements:

1. At least one track has a shower counter energy less than 1.5 GeV.
2. At least one track has a momentum less than 3 GeV/c and a shower energy less than 4 GeV.
3. The acollinearity of the two tracks is greater than 15°.
4. At least one track has a specific energy loss outside the range 2.0 → 4.4 keV/cm.

To facilitate physics analysis the EXTWOP and EXMUHA tapes are converted into a compressed format (minidst) that excludes most of the raw detector information. This format was developed for use with the ARGUS Kinematical Analysis Program (KAL) [158]. Physics analysis can be done either via FORTRAN66 subroutines in the ARGUS reconstruction program or by using the KAL language. KAL simplifies a great deal of the software work involved in analysis.

2.14 Selection of $\gamma\gamma$ Events

The general properties of the $\gamma\gamma$ events found at ARGUS have been discussed in reference [118]. In the analyses presented in this thesis only "no-tag" events are studied. In these events both of the beam particles miss the detector, which therefore reconstructs only the outcome of the $\gamma\gamma$ collision itself. As discussed in the introduction, the $\gamma\gamma$ luminosity is a steeply falling function of $S = W^2_{\gamma\gamma}$. These properties result in the main restriction for $\gamma\gamma$ event selection:

$$\sum_{\substack{\text{charged}\\ \text{tracks}}} |\vec{p}| + \sum_{\substack{\text{neutral}\\ \text{clusters}}} E < 4 \text{ GeV}$$

The charged tracks and shower counter signals used are selected conservatively: energy in isolated (single) shower counters is ignored in the sum, and only charged tracks from a reconstructed vertex or with $|d_0| < 1.5$ cm, and $|Z| < 6.0$ cm and hits in the inner drift chamber layers are used.

At this point, possible candidates for beam-gas collisions and cosmic ray events are identified. To separate beam-gas events, all events with proton candidates, as determined from dE/dX, are flagged. Proton candidates must have at least 5 dE/dX samples with a mean of at least 4.3 keV/cm in addition to satisfying at least one of the following requirements: $\chi^2_{proton} < 3$, $|\vec{p}| > 0.8$ GeV/c, or the minimum χ^2 must be that of the proton hypothesis. As it takes approximately 6 ns for a $\beta = 1$ transit of the drift chamber, any charge balanced two-prong events with a difference between the two time-of-flight measurements of more than 5 ns are flagged as cosmic event candidates, providing the tracks are collinear to within 26° ($\cos\theta_{X^+X^-} < -0.9$.).

2.15 Luminosity

The experimental luminosity (L) is defined as:

$$N_{e^+e^-\to X} = L\sigma^*_{e^+e^-\to X}$$

where $N_{e^+e^-\to X}$ and $\sigma^*_{e^+e^-\to X}$ are the number of events and visible cross section for the process $e^+e^- \to X$. An accurate determination of the luminosity is essential, as this determines the scale for the measurement of all absolute rates. In e^+e^- collisions the luminosity is usually determined from Bhabha scattering, as the cross section for this process is determined to high accuracy by QED alone.

In the ARGUS online system, luminosity is determined from endcap CPPT elements (11 shower counters in coincidence with the "OR" of 3 ToF counters in a ϕ range of 22.5°). At least two of these, opposite in ϕ and Z, must have at least 1 GeV energy deposited. In the offline analysis [159] strict Bhabha selection requirements can be made to minimize systematic error. On limiting the solid angle to the barrel of the detector, the Bhabha cross section is:

$$\sigma_{Bhabha} = 11.38\ nb\frac{100GeV^2}{4E^2_{Beam}}.$$

The systematic error using this Bhabha selection is less than 2%. The analyses presented in this thesis use older luminosity determination algorithms with systematic errors of 3-5% [160].

2.16 Particle Identification

As described above, there are several sources of information on particle identity: dE/dX, ToF, muon chambers, and shower counters. The muon chamber and shower counter information is useful in specialized analyses, but the ToF and dE/dX information has a wider range of application. The standard ARGUS particle identification uses dE/dX and ToF information translated into χ^2 values. From this a likelihood ratio for a mass hypothesis for a particular track is defined as:

$$\mathrm{P(X)} = \frac{\mathrm{f_X}\exp(-\chi^2_{\mathrm{X}}/2)}{\sum_{\mathrm{i}}\mathrm{f_i}\exp(-\chi^2_{\mathrm{i}}/2)} \qquad (\mathrm{i,X} \subset \mathrm{e},\mu,\mathrm{K},\mathrm{P},\pi),$$

where the f_i are the relative abundances of the different particle types and $\chi^2 = \chi^2_{dE/dX} + \chi^2_{ToF}$. Normally, the abundances used are only estimates. In the most common type of analysis one wishes only to eliminate background from misidentification so as to improve the signal to noise ratio. A track is associated with a particular mass hypothesis if it has a likelihood of more than 5%. The ability to separate different types of particles is only weakly dependent on the abundances. The acceptance of this technique is well reproduced by Monte Carlo, so long as the resolution used in the data χ^2 calculation is correct. Contamination from misidentification does not usually present a problem. It either produces a smooth background under a signal which can be fitted or, as is often the case in charm physics, reflections of different signals (e.g. $D^+ \to K^+\pi^+\pi^-$ being identified as $D_s^+ \to K^+K^-\pi^+$). The latter complicate the analysis but can still be understood. In inclusive production [128] one can determine the relative abundances of different particle types by maximizing the likelihood as a function of these parameters. It is important to include the exact resolution, which often is only approximately Gaussian.

Chapter 3

Acceptance Calculation

This chapter discusses investigations common to the analyses presented in the rest of the thesis. As two-photon collisions produce final states with low energies and multiplicities they are particularly sensitive to details of detector performance. In order to calculate the reconstruction efficiency, the behaviour of the detector is simulated by a program called SIMARG, which is described in the first section. One of the most critical contributions to the acceptance is the trigger efficiency. This has been investigated in detail, and the results presented in the second section have been used to calculate trigger efficiencies for several ARGUS analyses. The next two sections discuss improvements made in the shower counter simulation. For the trigger simulation the original Monte Carlo shower simulation has been replaced by a parametrization derived from experimental data. Finally, in the last section a check of the acceptance calculation technology developed in the body of the chapter is made using the production of QED final states.

3.1 Computer Simulation Of The Detector

Most of the ARGUS acceptance calculations are made using the SIMARG Monte Carlo simulation [161]. This program has as its goal the simulation of all interactions between the material of the detector and the particles produced in an e^+e^- collision. As input data the program is given a list of these particles produced by a Monte Carlo generator, along with their momenta, masses, and interaction vertex. SIMARG then traces each of these tracks through the detector material in short steps with provision made for

decay, absorption, energy loss, scattering, and the production of secondary particles (e.g. δ-electrons, photon conversion, shower counter albedo). For muons and hadrons the interactions with the detector materials are simulated according to the GHEISHA Monte Carlo code [162], while for electrons and photons the EGS Monte Carlo program is used [150].

During particle tracing the energy deposited in each shower and ToF counter is recorded. When the tracing is complete the tracks are checked for intersections with the other detector components (drift, vertex, and muon chambers) using the GEANT [163] software package. At this point a drift time-space relation determined from experimental data is used to calculate drift times for each hit in the drift chamber and VDC. The energy loss for each drift cell is also generated independently after tracking (the energy loss from the tracking algorithm is not used as the steps are not clearly associated with individual drift cells). The energy loss is derived from measurements made with a prototype drift chamber in a test beam. The results are then digitized and arranged in a bank format similar to that of experimental data. These banks also include information on the generated Monte Carlo tracks and secondaries. Finally, the output event is processed by the ARGUS reconstruction program which also adjusts the SIMARG data for experimental effects like ToF resolution and wire efficiency. At this point, the SIMARG output can be passed through the same analysis cuts as experimental data in order to calculate the effects of geometric acceptance and resolution.

3.2 Trigger Simulation

It is obvious that for certain event topologies, particularly those with low charged multiplicity, low total energy, or a non-spherical shape (e.g. τ pair production or two-photon collisions), the true acceptance for the ARGUS detector is not determined completely by the geometry, tracking, and reconstruction efficiencies that the SIMARG program was designed to reproduce. In brief, one has to worry about trigger efficiency when calculating the acceptance. The simplest way to accomplish this is to make severe cuts on the kinematics of each event to ensure that all relevant thresholds have been exceeded and accept the lower efficiency of such an analysis. In some situations one can cancel trigger

acceptances between different channels and measure a ratio of cross sections instead of an absolute value. Infrequently, one can determine the acceptance for a particular final state if it is also found as a subset of an event type with high trigger efficiency. One can then determine the trigger efficiency by examining that subset of the high trigger efficiency events where the interesting part of the event is not essential for the trigger. This technique was applied in the ARGUS analysis of $\Upsilon(1S) \rightarrow$ *nothing visible* [1]. Such approaches can be very useful as they cancel systematic uncertainties. However, in order to measure absolute cross sections one must, in general, have some way of determining the trigger probability of a SIMARG event in order to convolute the trigger efficiency with the geometric acceptance. A program (TRIGGR) to simulate the trigger has been developed and is described in appendix F. The extraction of the trigger efficiencies used therein is described in the next two sections.

3.2.1 Determination of First Level Trigger Efficiencies

As discussed in the previous chapter, the first level trigger is derived from information from the shower and time of flight counter systems. Providing a track actually intersects a counter, the ToF system responds with an efficiency better than 99.8%. The trigger electronics efficiency also exceeds this value [157]. The principal restrictions on the first level trigger efficiency are the discriminator thresholds required for the calorimeter pulse heights. In order to reproduce this efficiency in Monte Carlo these thresholds have been derived in terms of the energy deposited in the calorimeter. This procedure is described in the following paragraphs and the results are used to determine the efficiency for minimum ionizing particles and related systematic errors.

In the calorimeter component of the trigger, pulses from various groups of counters are analog summed and sent to a discriminator which is set once the total pulse exceeds a fixed amplitude. The information available to reconstruct the trigger thresholds after the fact consists solely of time-integrated ADC pulse heights, so the relation between the signal originally sent to the discriminator and the energy deposited is complicated by

[1] This analysis searches for $\Upsilon' \rightarrow \pi^+\pi^-\Upsilon$ events where the Υ decays to undetectable particles ($\nu\bar{\nu}$ or exotics). These processes would be observable in exclusive $\pi^+\pi^-$ events as enhancements in the recoil mass spectrum [164].

fluctuations in shower development and the type of shower (electromagnetic, hadronic, or minimum ionizing). These effects determine the time evolution of the shower and the shape of the pulse seen by the discriminator. This will smear the threshold shape when expressed as a function of the raw ADC pulse height. On neglecting these effects one would expect the trigger threshold to be a step function in terms of raw ADC pulse height:

$$PH_{raw} = \sum_{\substack{trigger \\ element}} ADC_i$$

No information on the time development of the showers is available in Monte Carlo so the integrated pulse heights must also be used there. These correspond to the calibrated pulse height in data:

$$PH_{cal} = \sum_{\substack{trigger \\ elements}} C_i \cdot ADC_i$$

So the threshold relevant to Monte Carlo events, expressed in terms of visible energy (energy in scintillator), will never be a simple step function.

To determine the first level trigger efficiency, one examines the probability for each type of trigger element to be set as a function of visible energy deposited. This can be convoluted with the appropriate Monte Carlo pulse height distribution to obtain the efficiency. These threshold shapes are derived from events where the trigger element in question is not essential for the event trigger. For this purpose the entire multi-hadron (EXMUHA) data sample is used in a highly compressed format which includes information on each event's trigger logic, the calibrated ADC pulse height in each element, and information on whether electromagnetic or minimum ionizing particles are tracked to each trigger element. Representative threshold shapes are shown in figures 3.1 through 3.3.

The trigger efficiency distributions have been determined for the entire history of the ARGUS detector through November 1988. This history has been divided into 38 trigger periods which are distinguished by changes in trigger logic, calorimeter or drift chamber threshold settings, or cumulative detector aging effects (principally loss of phototube gain). These periods can be distinguished by studying the visible cross sections (figures 3.4-3.8) for the trigger sensitive processes $e^+e^- \rightarrow \mu^+\mu^-$ and $e^+e^- \rightarrow e^+e^-X^+X^-$, where

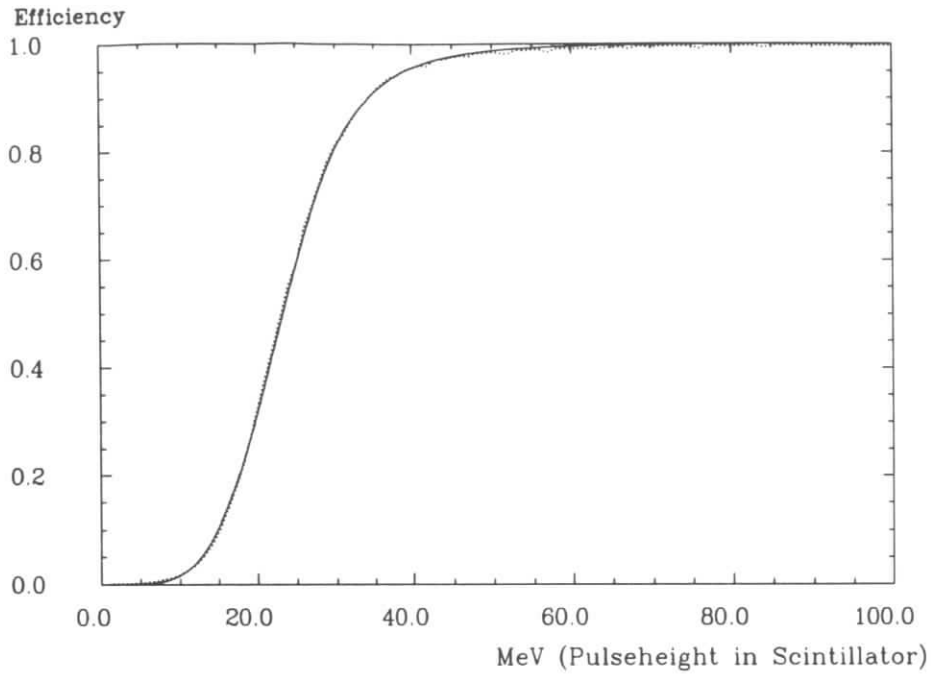

Figure 3.1: CPPT threshold shape, the solid line is the fit used in simulation, while the dotted line is the experimental distribution.

$X = e, \mu, \pi, K, p$ and the e^+e^- in the final state are not observed. For each of these trigger periods the threshold shapes of the shower counter trigger elements have been parametrized. These results are used to calculate trigger efficiencies for Monte Carlo events using the simulation program described in appendix F.

The systematics of this procedure can be studied through the use of minimum ionizing signals from muon pair events: $e^+e^- \rightarrow \mu^+\mu^-$. Dividing the muon CPPT element line shape (figure 3.9) from these events by the CPPT threshold curve should give the untriggered muon line shape. The ratio of areas yields the minimum ionizing efficiency. One can reverse this process by using a CPPT line shape for muon pair events generated by the SIMARG program. Multiplication by the threshold function should then yield the experimental line shape. This has been done for ARGUS experiments 2 through

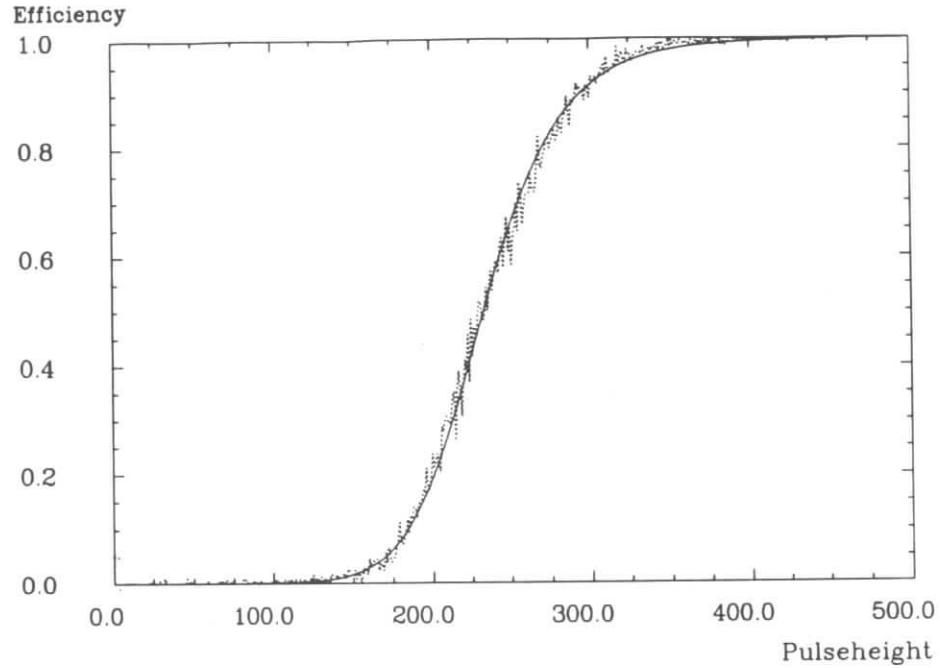

Figure 3.2: ETOT threshold shape, the solid line is the fit used in simulation, while the dotted line is the experimental distribution.

6 and the results are shown in table 3.1. In determining the CPPT efficiency from experimental data, the extrapolation of the line shape to low pulse heights results in a larger error and systematically lower efficiency. At low pulse heights calorimeter noise contributes false signals, and the trigger threshold behaviour is distorted by the ADC thresholds. The two methods of determining the efficiency for minimum ionizing particles are consistent, and the difference, 0.7% (excluding experiment 3), is a conservative estimate of the systematic error involved in using the threshold functions extracted from the data. It also includes systematic effects from the simulation of muon showers in SIMARG, which are actually expected to dominate, given the difference in data and SIMARG minimum ionizing line shapes evident in figure 3.9.

A number of other systematic effects contribute. The threshold smearing, as dis-

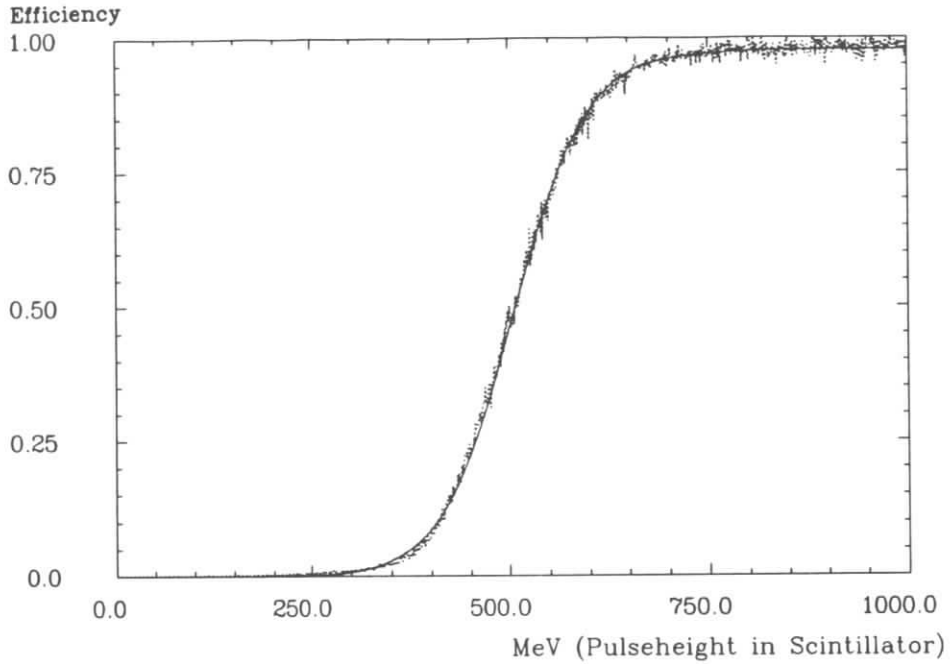

Figure 3.3: HESH threshold shape, the solid line is the fit used in simulation, while the dotted line is the experimental distribution.

cussed above, arises from using calibrated integral pulse heights. This smearing is essential, as the Monte Carlo efficiency must be calculated from visible energy. Most of the processes that smear the visible energy are reproduced in Monte Carlo; sampling of shower fluctuations in scintillators, photon counting statistics, etc. There are, however, some additional contributions to the experimental resolution that only distort the experimental visible energy. These arise from calibration error, pedestal subtraction and light guide optics. As the raw (untriggered) pulse height spectrum is steeply decreasing ($\sim 1/PH$) this contribution, approximately 2%, can cause a systematic shift of visible energies to higher values. This effect shifts the thresholds by 2%, leading to a decrease in the minimum ionizing efficiency of 0.6%. Using threshold shapes determined from trigger elements hit by only electromagnetic or minimum ionizing particles gives some indication of the importance of shower development on the threshold shape. These

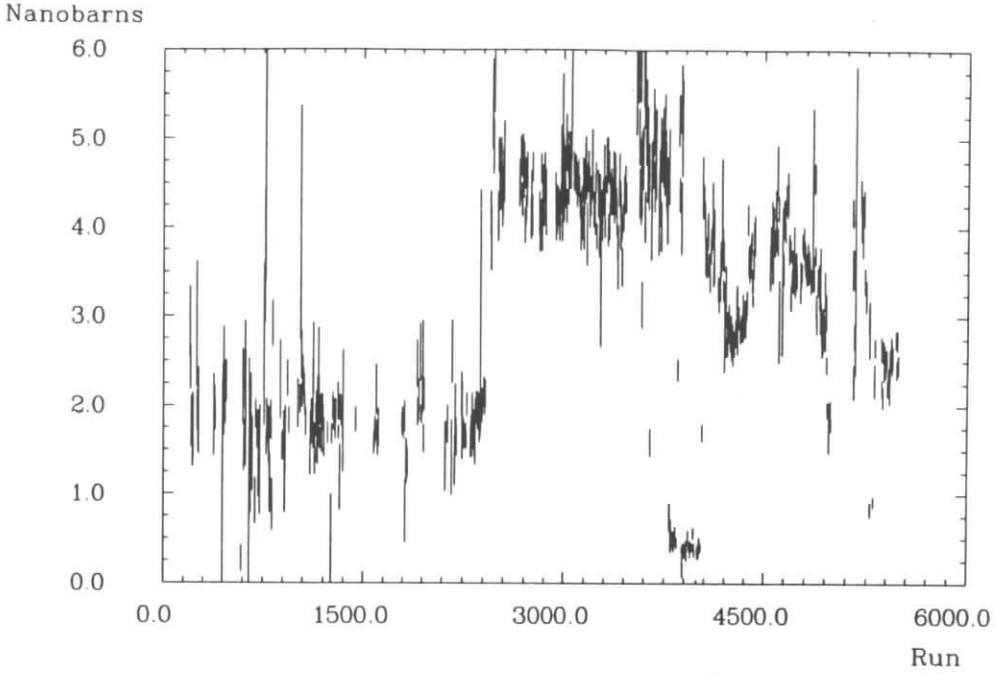

Figure 3.4: Visible cross section for $\gamma\gamma \to X^+X^-$ events, Experiment 2.

thresholds change the minimum ionizing particle efficiency by approximately 0.5%. The measured threshold shapes are distorted at extreme values[157] by the ADC thresholds, electronics noise, and shower development. It is estimated that these hardware effects produce an additional 1% uncertainty.

This analysis suggests a total systematic error of 1.6% for the Monte Carlo calculation of the CPPT efficiency for minimum ionizing particles (table 3.2). As this type of particle is the most sensitive to trigger inefficiency this value is taken as a conservative estimate of the systematic error involved in calculating the trigger efficiency for particles inducing electromagnetic or hadronic showers.

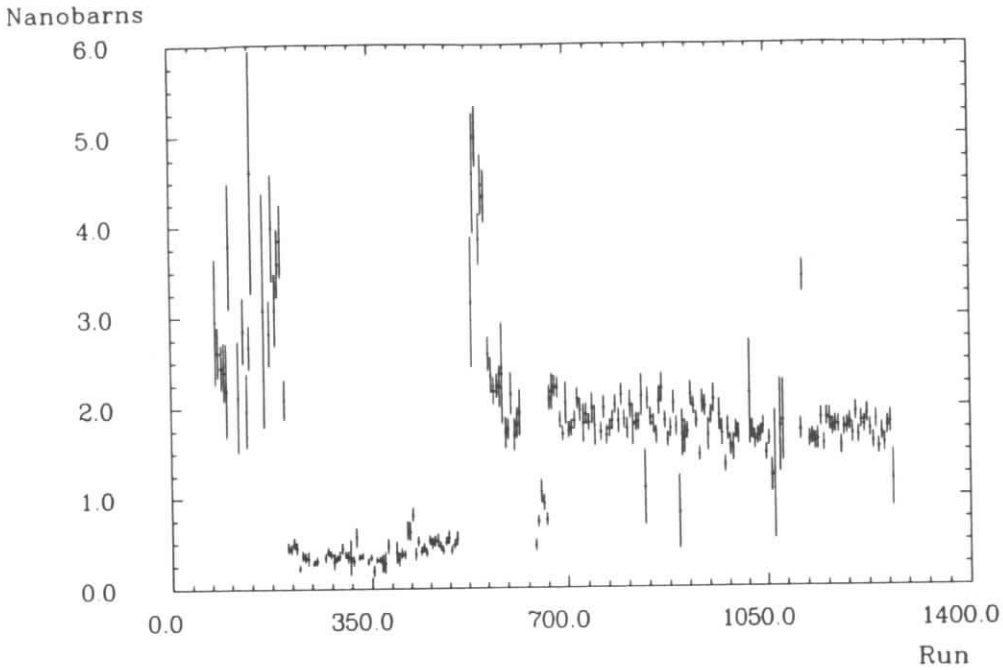

Figure 3.5: Visible cross section for $\gamma\gamma \to X^+X^-$ events, Experiment 3.

3.2.2 Determination of Second Level Trigger Efficiencies

The second level trigger is provided by the Little Track Finder (LTF) described in the previous chapter. This processor uses information from both drift chamber and ToF TDC's. As discussed above the ToF are highly efficient so the LTF inefficiency is dominated by the drift chamber contribution (figure 3.10).

To measure this efficiency and study its variations over the ARGUS history Bhabha scattering events ($e^+e^- \to e^+e^-$) have been used. These trigger independently via the total energy trigger (ETOT) which requires no LTF tracks. The Bhabha events are selected from the lowest level of reconstructed data (EXPDST) by the following requirements:

- each event must have exactly two tracks with opposite charges;

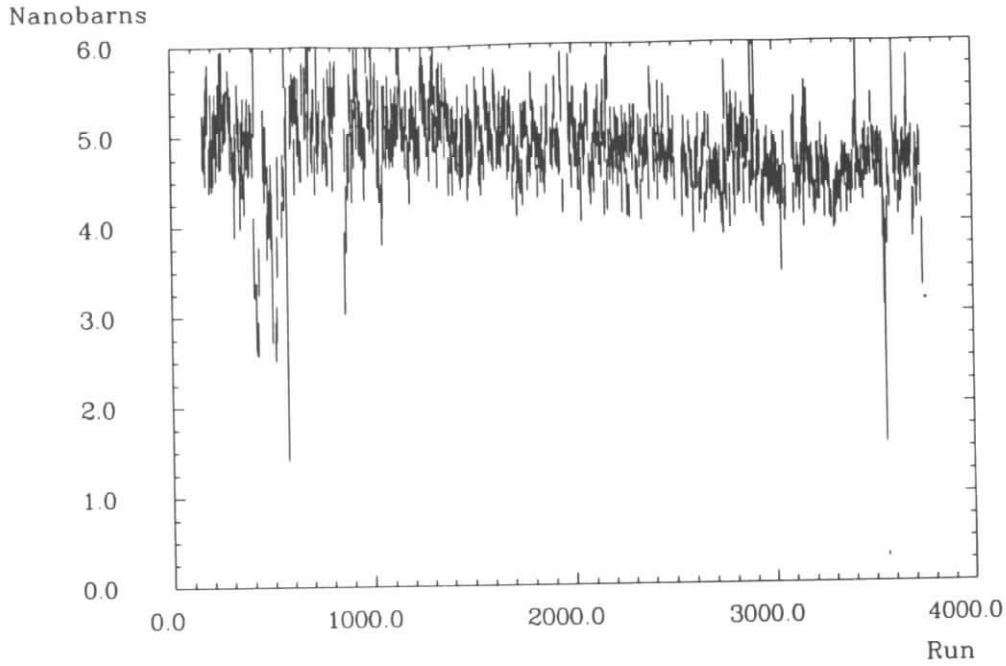

Figure 3.6: Visible cross section for $\gamma\gamma \to X^+X^-$ events, Experiment 4.

- the HESH pre-trigger must be set in addition to the ETOT to ensure that the LTF bank is read out by the data acquisition;
- both tracks must have at least 3 GeV in the shower counters;
- $\cos\theta_{e^+e^-} < -0.97$ (collinearity);
- $P_\perp > 0.125$ GeV/c and $|\cot\theta| < 1.125$ (detector barrel).

For the events selected the information from the LTF trigger bank, ToF bank, and drift chamber layer 17 are written to compressed data sets for further analysis. This has been done for the entire multi-hadron data sample to study systematic effects. An LTF track is matched to a drift chamber track if:

- there is at most one intervening ToF counter between the LTF mask's and the ToF counter assigned to the drift chamber track by the track fit and ToF reconstruction

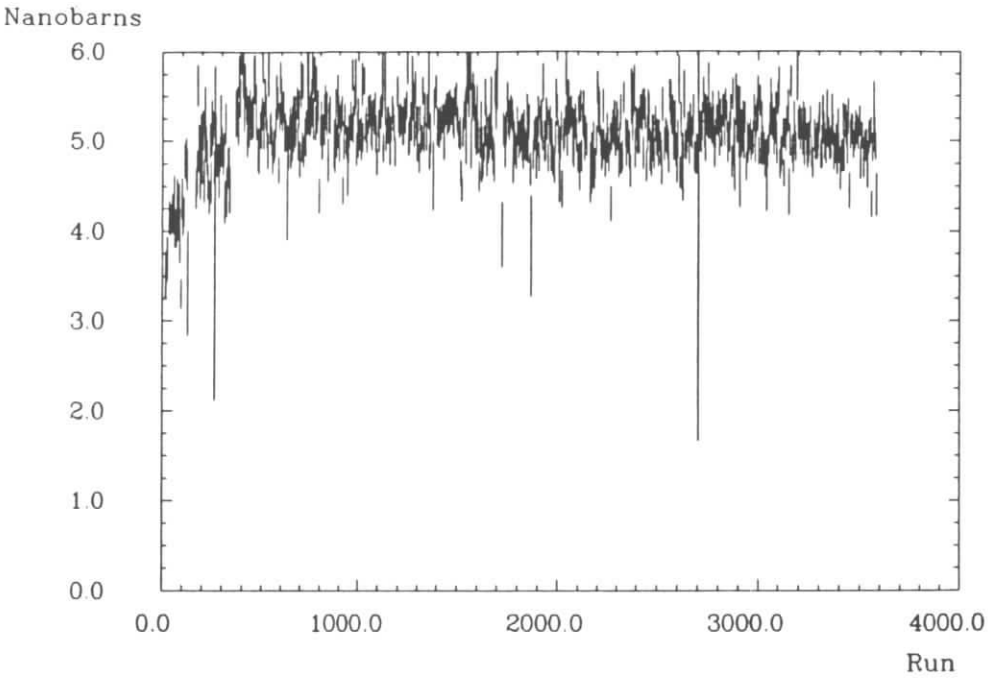

Figure 3.7: Visible cross section for $\gamma\gamma \to X^+X^-$ events, Experiment 5.

(14.1° in ϕ);

- there is at most a 12.5° difference (2.5 layer 17 cells) between the wire assigned to the LTF mask and the ϕ of the reconstructed track at layer 17 of the drift chamber.

These requirements are sufficiently loose to ensure that any LTF track in an event is matched to the appropriate drift chamber track (this has been studied via Monte Carlo analysis). The efficiency is defined as the probability for having at least one LTF track matched to a reconstructed track in the drift chamber. The variations of this quantity over the ARGUS history are shown in figures 3.11-3.15.

The LTF inefficiency is used in the trigger simulation program to discard the same fraction of Monte Carlo LTF tracks (these are originally generated with 100% drift chamber efficiency). Initially, the Bhabha efficiency was used directly. For each trigger

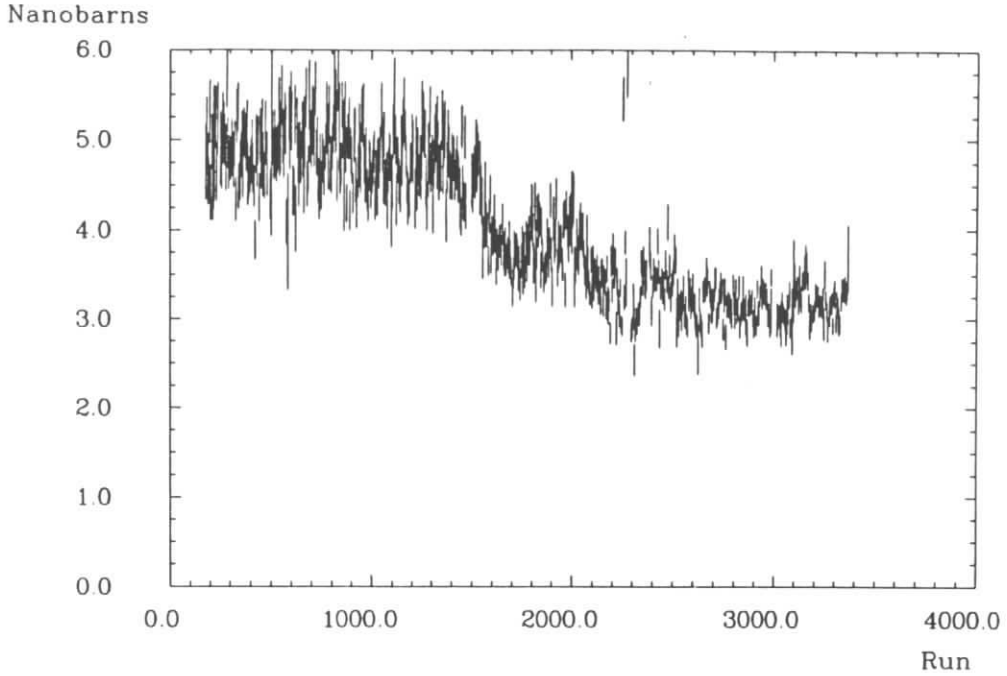

Figure 3.8: Visible cross section for $\gamma\gamma \to X^+X^-$ events, Experiment 6.

period a distribution of efficiencies was accumulated, parametrized, and used to generate LTF efficiencies for the simulation. The error on the Bhabha LTF efficiency was estimated to be 1%, due principally to the requirement of a reconstructed drift chamber track and the statistical error on the efficiency determination.

This method ignored the effect on the LTF efficiency of energy loss and path length variations in the drift chamber, in other words, the effect of the TDC start discriminator threshold. From figure 3.16, which shows the Bhabha LTF efficiency for various trigger periods as a function of $\cot\theta$, it is clear that there is a change in LTF efficiency over the detector barrel. For the early ARGUS experiments this 40% variation in the path length resulted in a change in LTF efficiency of less than 4%. The corresponding change in the ionization per drift cell is the same order as that expected from the specific ionization (dE/dX) for different particle types in the transverse momentum range accessible to the

Experiment Number	Efficiency		
	Monte Carlo	Data	Average
2	94.0 ± 0.6	$92.7 \pm 0.6 \pm 0.7$	93.3 ± 0.7
3	92.5 ± 0.6	$90.5 \pm 0.9 \pm 0.7$	91.5 ± 1.0
4	96.3 ± 0.7	$95.8 \pm 0.5 \pm 0.7$	96.1 ± 0.4
5	97.5 ± 0.7	$97.5 \pm 0.4 \pm 0.7$	97.5 ± 0.2
6	96.7 ± 0.7	$96.0 \pm 0.5 \pm 0.7$	96.4 ± 0.4

Table 3.1: CPPT efficiencies for 5 GeV muons.

Minimum Ionizing Studies	Comparison with data	0.7%
	Calibration threshold shift	0.6%
Threshold Determination	Particle type effects	0.5%
	Shower fluctuations, electronics noise	1.0%
	Statistical error	0.6%
	Parametrization of thresholds	0.3%
	Smoothing of distributions	0.1%
Total		1.6%

Table 3.2: Systematic uncertainties in determining CPPT efficiency.

LTF ($P_\perp > 0.111$ GeV/c). A systematic error of 2% was attributed to the neglect of both these effects.

In experiment 6 a period of low drift chamber efficiency increased the change in Bhabha LTF efficiency over the barrel of the detector to 12%. At this point it was decided to use a fixed Bhabha LTF efficiency for each trigger period, a simplification that had negligible effect on the calculated trigger efficiency. More importantly, the variation of the LTF efficiency with dE/dX and path length was included in the simulation. This was extrapolated from the angular variation of the Bhabha LTF efficiency:

$$\begin{aligned} \eta_{LTF} &= \eta_{ToF} \cdot \alpha(1 - e^{-\beta X^2}) \\ X &= \frac{\Delta E(m,p,\theta)}{\Delta E(m_e, 5\mathrm{GeV/c}, 0^\circ)}, \end{aligned}$$

where $\Delta E(m,p,\theta)$ is the energy loss per drift cell as a function of mass, momentum, and polar angle. At this point a ToF inefficiency, η_{ToF}, was introduced due to photomultiplier

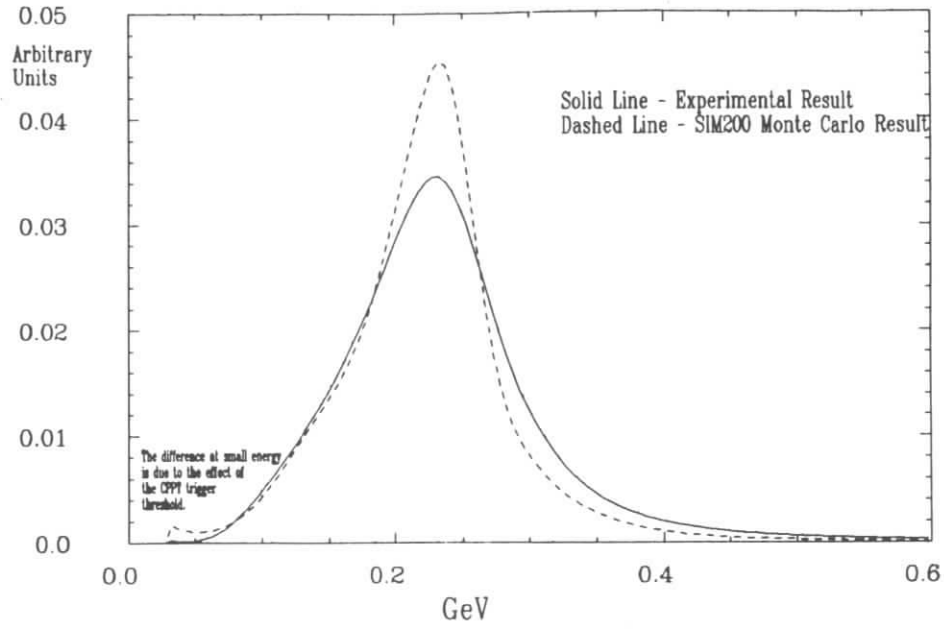

Figure 3.9: CPPT muon line shapes from $e^+e^- \to \mu^+\mu^-$ events. The dashed curve is the result of SIMARG simulation, without trigger efficiency, while the solid curve is experimental data. Both curves are normalized to unit area.

malfunctions during the experiment. The systematic error in the improved description was again estimated to be 2%.

The systematics of this LTF simulation were verified through the analysis of multi-hadron data taken with the ETOT trigger. To limit ambiguous LTF mask assignments, only tracks that were isolated in the drift chamber were used in the multi-hadron LTF efficiency calculation. The data were also divided into low and high multiplicity samples to check possible contamination from ambiguous assignments. The geometric acceptance of the LTF was found to be well described by the simulation program as a function of transverse momentum and polar angle. Within this acceptance ($\cot\theta < 1.15$, $P_\perp > 0.111$ GeV/c) the efficiency distribution was also found to be satisfactory. The

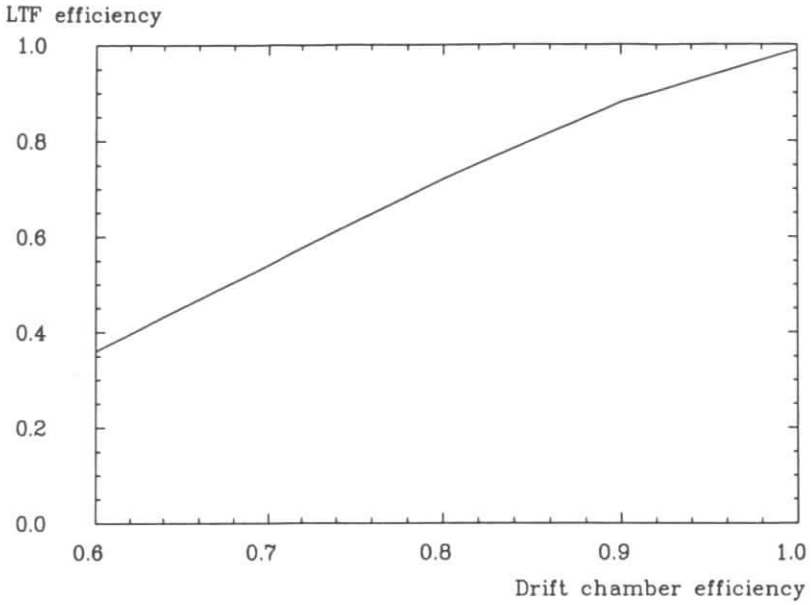

Figure 3.10: The probability of at least one LTF track being found per drift chamber track as a function of the drift chamber wire efficiency.

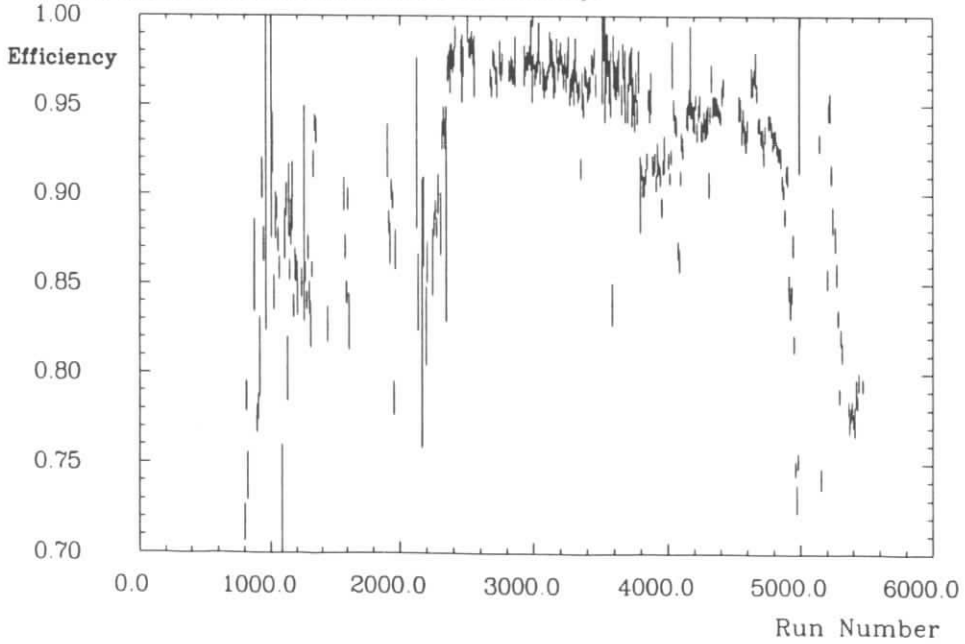

Figure 3.11: LTF efficiency for 5 GeV/c $e^{\pm}$ for experiment 2.

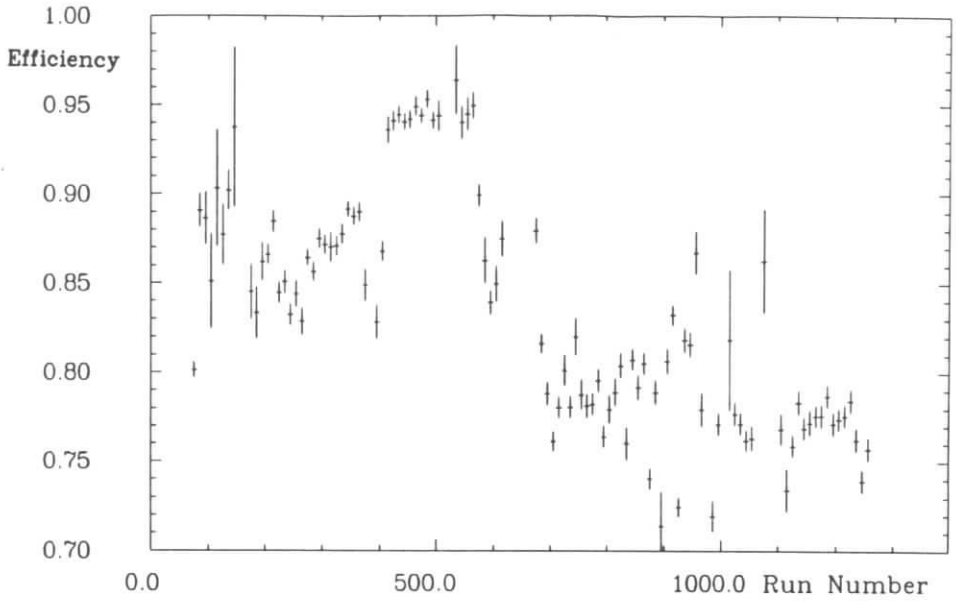

Figure 3.12: LTF efficiency for 5 GeV/c $e^{\pm}$ for experiment 3.

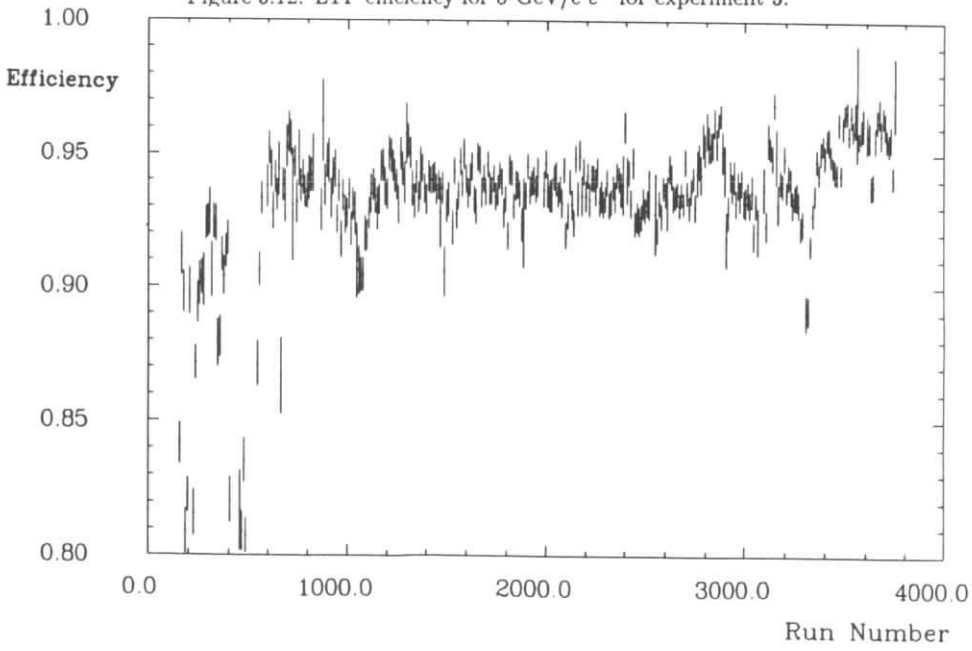

Figure 3.13: LTF efficiency for 5 GeV/c $e^{\pm}$ for experiment 4.

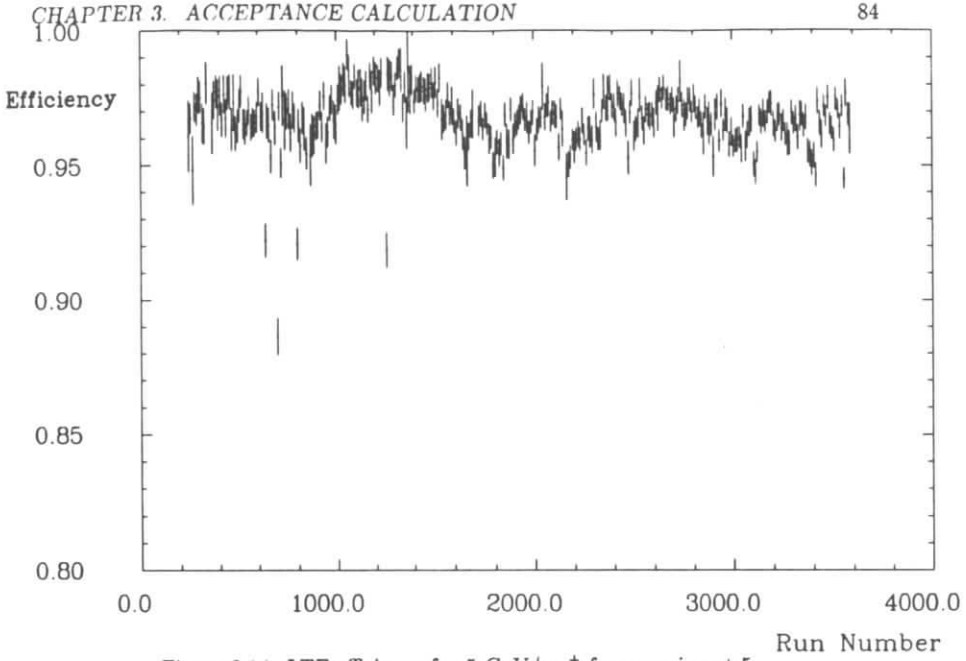

Figure 3.14: LTF efficiency for 5 GeV/c $e^{\pm}$ for experiment 5.

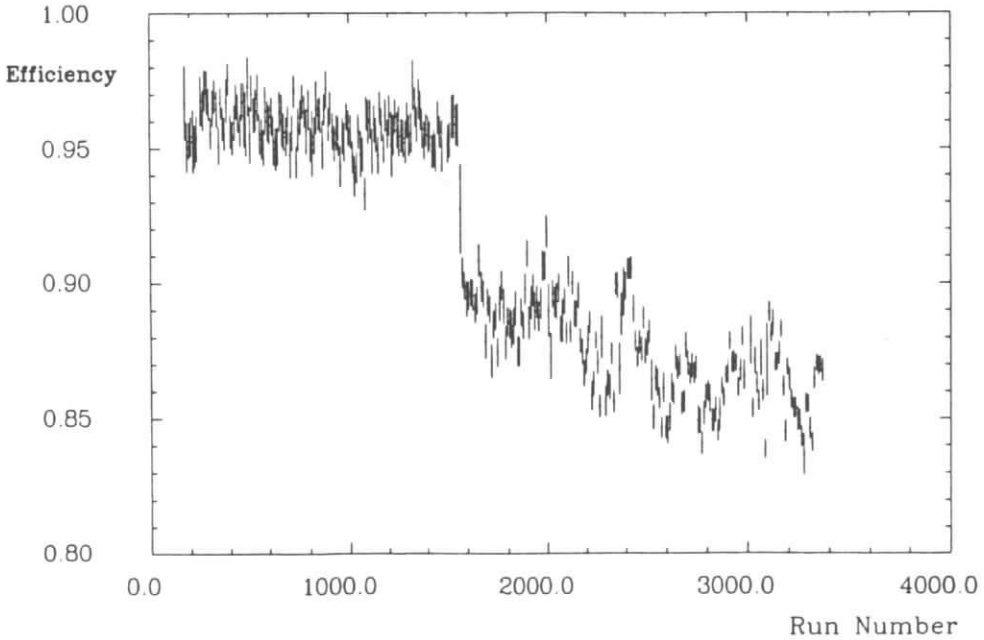

Figure 3.15: LTF efficiency for 5 GeV/c $e^{\pm}$ for experiment 6.

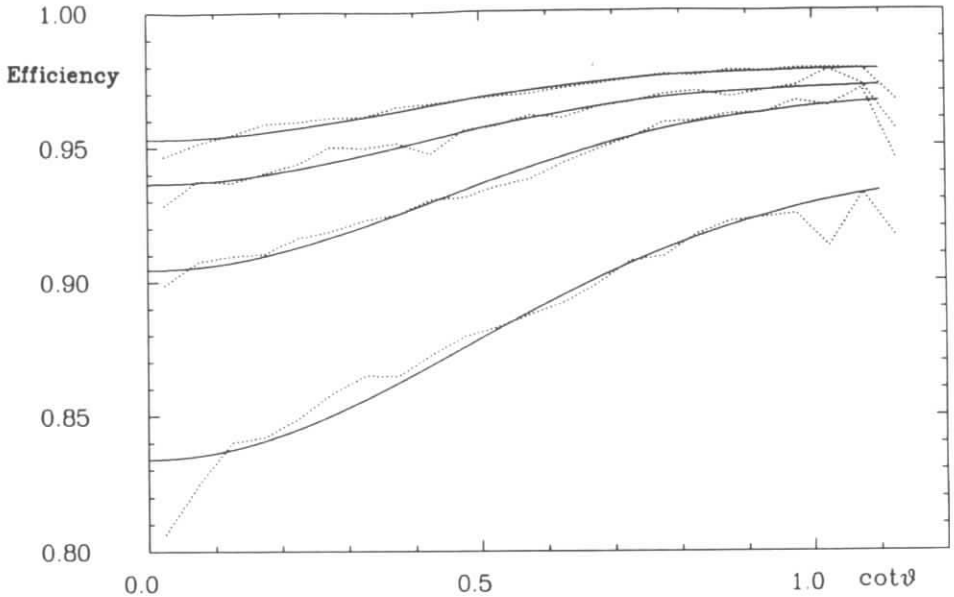

Figure 3.16: $\cot\theta$ variation ot the LTF efficiency for 5 GeV $e^{\pm}$ (dotted lines) from different experimental runs. The solid lines are the fits to the distributions used in the trigger simulation.

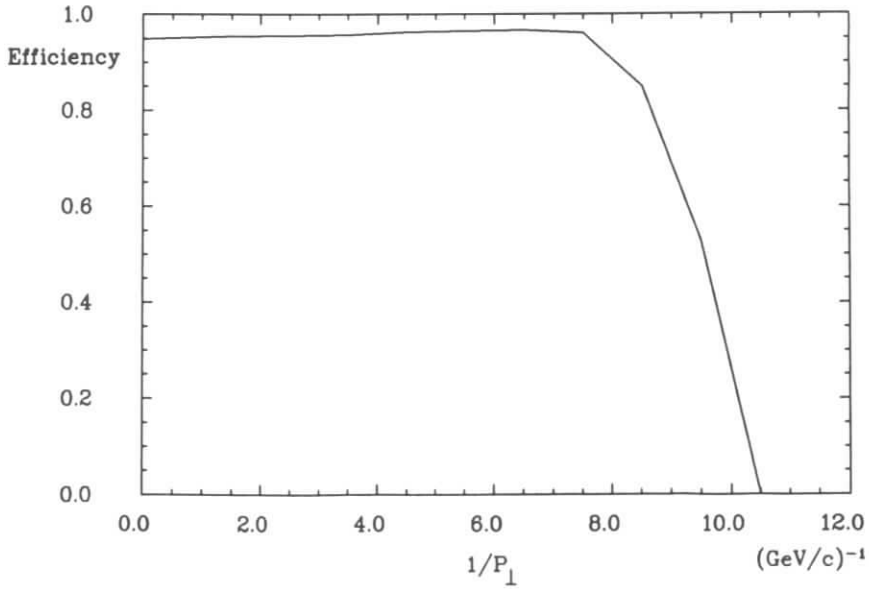

Figure 3.17: LTF efficiency from multi-hadron events.

efficiency increased by 1.6-2.0% as the transverse momentum decreased to 0.125 GeV/c (figure 3.17). This effect can be attributed to the rise in drift chamber dE/dX at low momenta.

As discussed in the last section of this chapter, there are some problems in simulating low momentum track efficiency. One of these problems was the creation of too many drift chamber hits in the SIMARG simulation. This caused multiple LTF tracks to be assigned to single charged tracks, effectively cancelling the contribution of the LTF inefficiency. This is particularly difficult to simulate as the efficiency for a track to leave two hits when it passes through two drift cells in a layer is not simply the square of the single hit efficiency. To estimate the sensitivity to this effect, a second LTF simulation was developed. This uses only the drift chamber track fit, drift chamber layer 2 TDC information, and ToF TDC hit information to calculate the most likely LTF mask for each Monte Carlo track. As only one LTF mask is assigned to each drift chamber track this simulation is an underestimate of the efficiency. In a standard analysis the average of the two calculations is used with the difference quoted as the systematic error from LTF simulation (this varies from 20% near threshold to 1% at high momentum).

Process	Signal Widths		Fraction in	Number of
	σ_A [MeV]	σ_B [MeV]	Gaussian A [%]	Events
$K^0_s \to \pi^+\pi^-$	5.0 ± 0.8	11.2 ± 0.3	56 ± 2	273065 ± 1147
$\Lambda \to \pi^- p$, $\bar{\Lambda} \to \pi^+ \bar{p}$	1.75 ± 0.06	4.2 ± 0.2	69 ± 7	18221 ± 246
$\phi \to K^+K^-$	4.1 ± 0.2	11 ± 2	67 ± 6	14769 ± 193

Table 3.3: Information from the fits shown in figure 3.18.

3.3 Simulation of Shower Energy Deposition

The interaction of charged particles with matter proceeds through several processes: ionization, bremsstrahlung, pair production, and hadronic interactions. The simulation of these processes for an acceptance calculation is quite difficult, especially in material as dense as the ARGUS shower counters, and great effort has been spent writing elaborate software for this purpose [150,162]. The simulation of a hadronic cascade is especially difficult, given the limitations of current knowledge of nuclear interaction cross sections for exclusive final states. As any such attempt must be an approximation, it is clear that it is best to base the simulation of these processes directly on experimental data.

To simulate the calorimeter contribution to the trigger efficiency, kaons and pions produced in the decays of Λ, K^0_s, and ϕ particles are used[2]. These events are taken from multi-hadron data sets to minimize trigger bias. The signals for the three decay channels are shown in figure 3.18. The fits shown are described in table 3.3. Only signals from the barrel calorimeter are used, so each decay must have at least one particle within $|\cos\theta| < 0.7$. The standard ARGUS particle identification based on dE/dX and ToF (described in the previous chapter) is used with a likelihood cut of 5%.

To fully describe the showers of pions and kaons, one needs to know the distributions of shower energies, cluster sizes, and energy distribution within each cluster as functions of momentum and angle. Optimally, one should also separate the showers of positive and negative tracks. Given the size of the data sample available, this is far too much to ask. In the trigger simulation only the distribution of shower energies as a function

[2]This analysis was done in collaboration with Alf Nilsson (DESY).

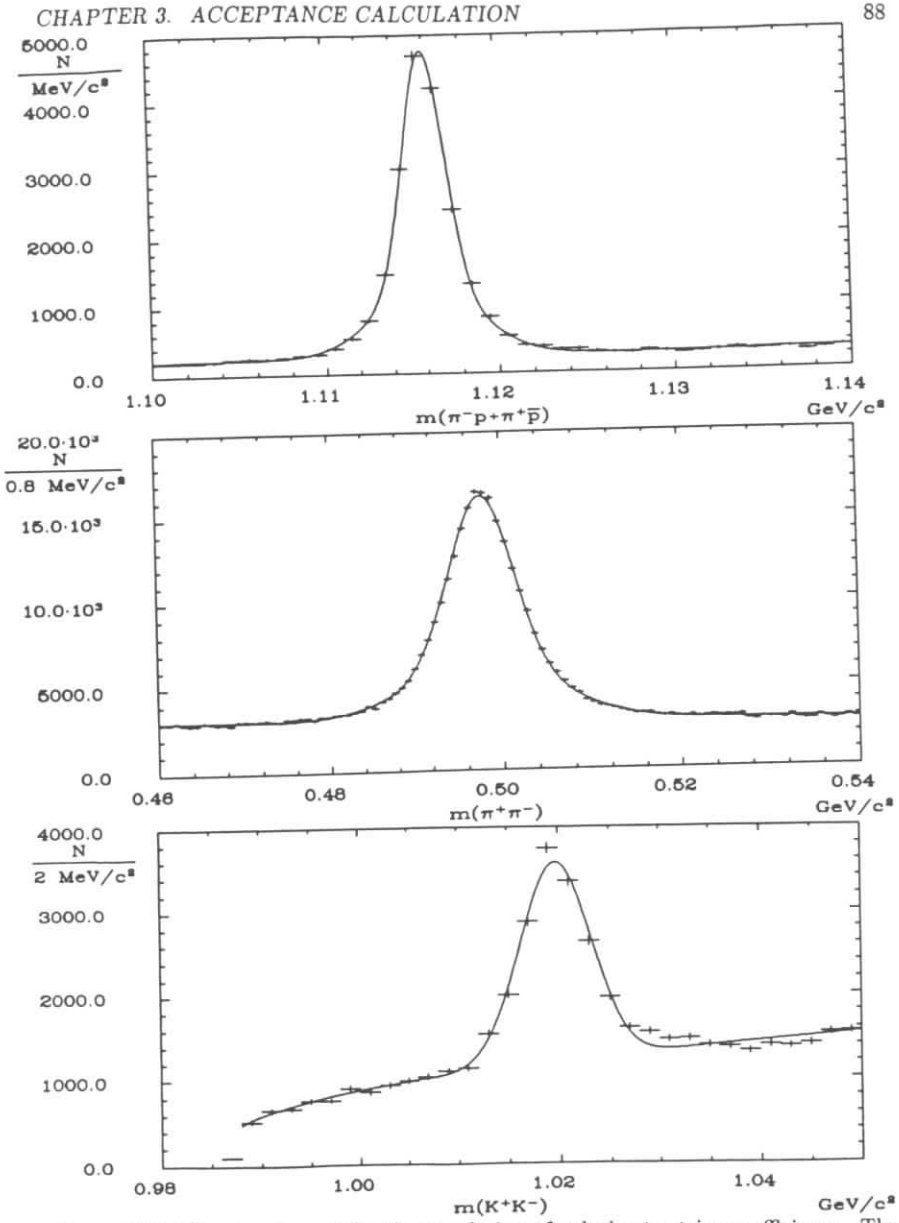

Figure 3.18: The signals used for the simulation of calorimeter trigger efficiency. The line shapes in the fits shown are parametrized by double Gaussians. The backgrounds are parametrized by polynomials with appropriate threshold factors.

of momentum is used. For each track traced to a shower counter, an energy is picked randomly from this distribution and assigned to the counter corresponding to the shower maximum of the original SIMARG shower – no attempt is made to include cluster size or shower shape effects. As the calorimeter trigger elements have a very large granularity (the energy is summed over groups of a minimum of 66 shower counters) these approximations have a a very small effect on the trigger efficiency for an event (0.3-0.8%).

It was originally intended that the background contributions apparent in figure 3.18 be eliminated by subtracting appropriately normalized distributions taken from the side bands of the signals (table 3.4). However, these distributions were indistinguishable from those taken from the signal regions. The difference between the two distributions corresponds to a $\chi^2/n_{d.f.}$ ($d.f.$ =degrees of freedom) of 1.3 for the pion samples and 1.5 for the kaon sample. The trigger efficiencies calculated using distributions taken from the different regions differed by 0.2%. This is easily understood: the low momenta most critical for the trigger are also those cleanly separated by ToF and dE/dX particle identification. The side bands are themselves clean samples of pions and kaons.

The average shower energies generated from the distributions used in the trigger simulation agree well with those extracted from the channels studied in the following chapters (figures 3.19, 3.20). SIMARG reproduced these distributions well for pions but for kaons the discrepancy between the SIMARG result and that observed in the data was sufficient to motivate this analysis. For the kaon sample the shower distributions for positive and negative tracks are combined as there is no significant difference between them ($\chi^2/n_{df} = 1$). As this produced a change in the calculated trigger efficiency for K^+K^- pairs of less than 0.1%, it seems that the smaller size of the $\phi \rightarrow K^+K^-$ data sample is not a problem. As can be seen from figure 3.19, the π^+ and π^- distributions are different at low momenta, so the trigger simulation uses the separated distributions. For final states composed of pions, the introduction of these shower distributions in the simulation produced a change in acceptance of less than 1%, as expected. The situation for kaons was rather worse, with the acceptance for K^+K^- pairs increasing by

Particle	Signal Region [GeV]	Sideband [GeV]
K^0_s	0.475-0.525	0.45-0.47,0.53-0.55
Λ	1.113-1.119	1.141-1.166
ϕ	1.00-1.04	1.04-1.118

Table 3.4: Mass cuts (GeV/c^2).

approximately 10%.

3.4 Calorimeter Backgrounds and Topology Depletion

As described in the previous chapter, the ARGUS shower counters can detect photon energies as low as 30 MeV. Since backgrounds in the shower counters increase significantly at low energies, a threshold of 50 MeV is used in the analyses discussed in this thesis. Despite this restriction, background noise in the calorimeter must still be treated with some care in the analysis of exclusive topologies.

The largest source of calorimeter noise arises from physical malfunctions in a shower counter's readout electronics, resulting in intermittent false signals. In the standard calorimeter reconstruction software, most counters that show an excessively high hit rate in a group of runs are flagged as bad and ignored (approximately 0.05%). This has been done in a conservative manner in order to maintain a maximal coverage of solid angle – in the reconstruction of complex events this is more critical than a small increase in the large combinatoric background. However, from the point of view of extracting well-defined topologies, any background that changes the topology must be well understood and, if possible, suppressed.

To this end all remaining shower counters with anomalous hit rates are eliminated in this analysis. Any shower counters with occupation rates more than five standard deviations from the average of the ten neighboring counters (neglecting any dead counters, and ignoring those with the two highest rates) are excluded from the analysis. On the average (2.1 ± 0.1)% of single-counter photon candidates and (0.6 ± 0.1)% of cluster

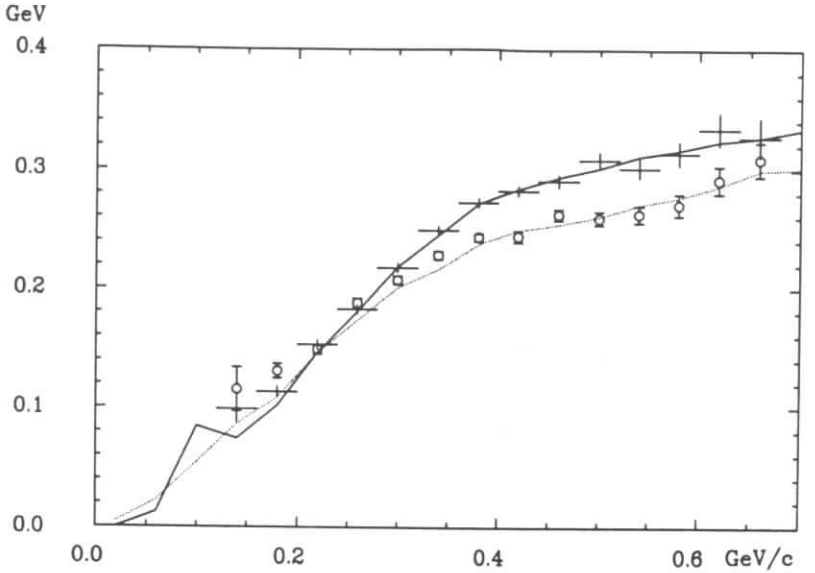

Figure 3.19: Average energy deposited in shower counters by π^+ (crosses and solid line) and π^- (circles and dotted line) from exclusive $\eta' \to \pi^+\pi^-\gamma$ events (points with error bars) and pions from K^0_s and Λ decays (lines).

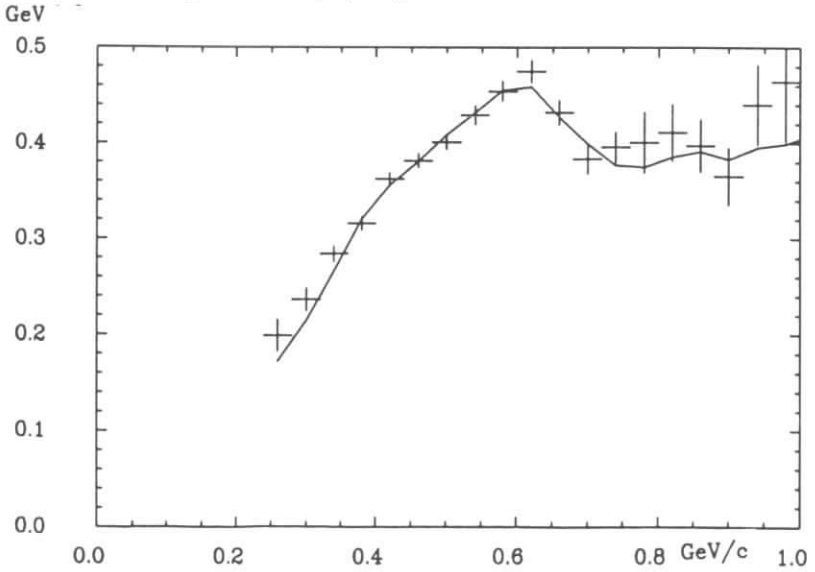

Figure 3.20: Average energy deposited in shower counters by K^+ and K^- from exclusive K^+K^- events (points with error bars), and kaons from ϕ decays (line).

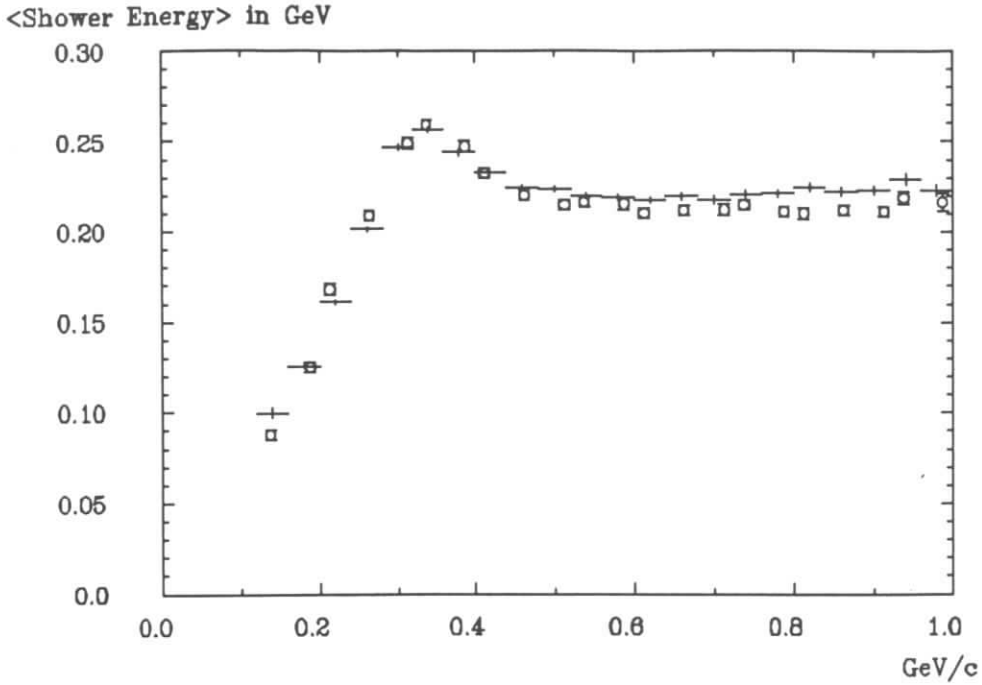

Figure 3.21: Average energy deposited in shower counters by $\mu^{\pm}$ from cosmic events (crosses) compared to that generated by the SIMARG Monte Carlo (circles).

photon candidates are rejected by this restriction.

A second source of fake photons is shower splitting. This effect is caused by a combination of natural fluctuations in shower development and small inefficiencies in the cluster finding algorithm – deposited energy that should be assigned to an existing cluster is assigned to a new one. For charged particle showers this background is easily reduced by ignoring any calorimeter signals that have small opening angles with charged tracks in an event – a cut of $\cos\theta_{X^{\pm}\gamma} < 0.9$ is sufficient. Unfortunately, this restriction suppresses sensitivity to events with photons, as it eliminates 21% of the available solid angle in an event with two charged particles. Shower splitting produces a small loss of signal events to topologies with too many reconstructed photons. Application of the opening-angle restriction would eliminate the contamination from topologies with fewer

photons, but would allow topologies with more photons to migrate into the data sample, a situation difficult to model reliably.

All relevant contamination rates can be extracted from the data in a straightforward manner. Cosmic muons will trigger the detector if they pass through the beam pipe in coincidence with the bunch-crossing signal. These can be clearly separated from normal muon pair events, τ pair production, and $\gamma\gamma$ collisions, as the two tracks in a cosmic event are highly collinear and the time of flight measurements are at least six nanoseconds apart (the minimum time required to traverse the central detector). From this analysis it was determined that the photon rejection algorithm reduces the contamination rate from $(21.6 \pm 0.2)\%$ to $(4.5 \pm 0.1)\%$ for single counters, and from $(4.5 \pm 0.1)\%$ to $(3.5 \pm 0.2)\%$ for clusters of counters. To determine the amount of shower splitting one simply plots the photon frequency after the restriction $\cos\theta_{X^{\pm}\gamma} < C$, versus the parameter C – the events with shower splitting show up as an excess as $C \to 1$. For cosmic muons these rates were determined to be $2.9 \pm 0.1\%$ for single counters and $2.7 \pm 0.1\%$ for clusters. For kaons the rates were determined from exclusive $K^+K^- + n\gamma$ final states. These were found to be $10.7 \pm 1.1\%$ and $5.7 \pm 2.3\%$ for the splitting away of single counters and clusters respectively. One can suppress both noise sources to some extent by considering only clusters of shower counters as photon candidates.

3.5 Some Acceptance Tests

The PLUTO collaboration [165] has determined the total rate of hadron pair production for $W_{\gamma\gamma}$ above 2 GeV/c^2 to be:

$$\frac{\sigma(\gamma\gamma \to h\bar{h})}{\sigma(\gamma\gamma \to \mu^+\mu^-)} = 0.042 \pm 0.013 \pm 0.008$$

The main difficulty in this type of analysis is the elimination of background from the two dominant QED processes: $\gamma\gamma \to e^+e^-$, $\mu^+\mu^-$. For high masses (> 1.6 GeV/c^2) this can be achieved through the use of muon chamber and calorimeter information. At low masses the situation is much more difficult, particularly in the case of μ/π separation. The PLUTO group has also managed to measure the $\pi^+\pi^-$ cross section to final-state masses as low as 0.5 GeV/c^2 [98]. This was accomplished by studying two-

prong production at extreme rapidities, and was possible only because of the specially designed forward spectrometers which allowed positive identification of electrons and muons to angles as small as 70 mrad. In the intermediate mass region the cross section is dominated by the production of the $f_2(1270)$ meson in the reaction $\gamma\gamma \to f_2 \to \pi^+\pi^-$. The analysis of this channel is complicated by the calculation of the QED contribution and interference with the $\pi^+\pi^-$ continuum [99,107].

To verify the mechanics of the acceptance calculation described in the first part of this chapter, the production of exclusive two-prong final states in $\gamma\gamma$ collisions has been investigated. Events with two oppositely charged particles were selected from the $\gamma\gamma$ data sets described in the previous chapter. To reject $\tau^+\tau^-$ events and incompletely reconstructed final states with higher multiplicities, the total transverse momentum of the events is required to be less than 0.1 GeV/c. Events with additional neutral particles are rejected by requiring that there be no isolated clusters in the calorimeter with an energy of more than 0.05 GeV. Both charged tracks must be within the fiducial region of the CPPT trigger elements, so the transverse momentum of each track is required to be greater than 0.11 GeV/c, and a polar angle requirement of $|\cos\theta| < 0.75$ is made. After assigning each track a pion mass (no attempt at particle identification is made) the spectrum shown in figure 3.22 is observed. The curve shown is a Monte Carlo simulation using event generators developed by P. H. Daverveldt [29] for the production of e^+e^- and $\mu^+\mu^-$ pairs, and the SIMARG/TRIGGR acceptance calculation. At masses below 1.5 GeV/c^2 there is a clear signal for production of the $f_2(1270)$ resonance as expected. For masses above 2.0 GeV/c^2 the ratio of the observed spectrum to that for QED pair production is:

$$\frac{N(\gamma\gamma \to X^+X^-)}{N(\gamma\gamma \to e^+e^-) + N(\gamma\gamma \to \mu^+\mu^-)} = 1.048 \pm 0.027 \pm 0.051 \quad \text{(ARGUS)}$$
$$= 1.021 \pm 0.007 \pm 0.004 \quad \text{(PLUTO)},$$

where the statistical uncertainty is dominated by the relatively small number (1725) of Monte Carlo events generated in this mass range, compared to the 9440 events observed experimentally. The systematic uncertainty can be broken down as follows: pre-trigger simulation, 1.6% per track; LTF efficiency determination, 2.4% per track; LTF simulation, 1.1%; luminosity, 3%; and photon noise correction, 1.1%. The value attributed

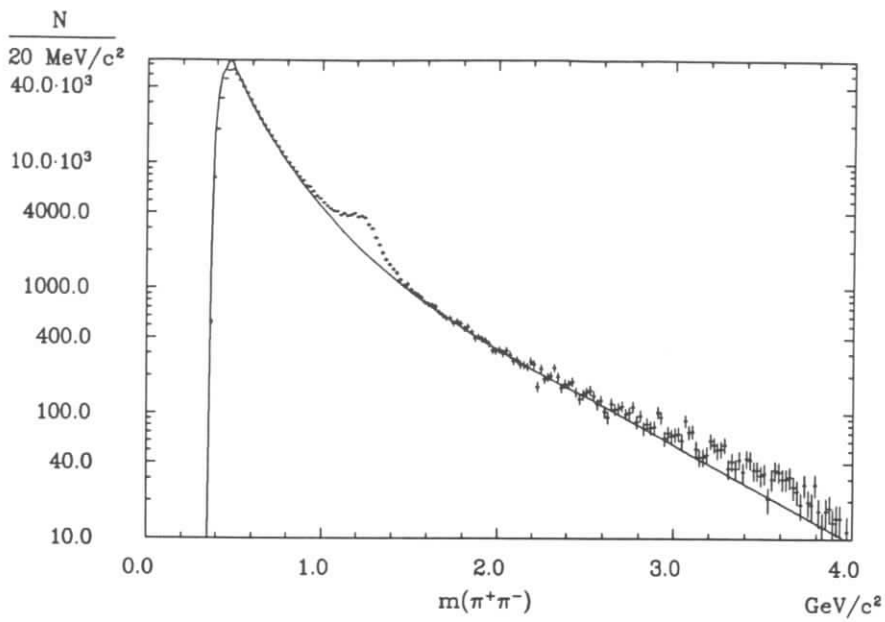

Figure 3.22: The $m_{\pi\pi}$ spectrum for final states $\gamma\gamma \to X^+X^-$ (points with error bars). The curve shown is a fit to the Monte Carlo simulation. The statistical uncertainty is 4 times that of the data for $M_{X^+X^-} > 1$ GeV and 10 times that of the data at lower masses).

to PLUTO has been calculated using the result [165] discussed above, after noting that the visible cross section for $\gamma\gamma$ QED production of e^+e^- and $\mu^+\mu^-$ pairs is almost equal ($N_{e^+e^-} = 0.96 \cdot N_{\mu^+\mu^-}$) in this mass region. The two measurements are in good agreement.

At low masses the situation is not as good. The Monte Carlo QED spectrum exceeds that of the data below invariant masses ($m_{X^+X^-}$) of 0.6 GeV/c^2 by $(20 \pm 3 \pm 9)$%, which includes a large (8%) contribution to the systematic error from the LTF simulation. In this mass range $\pi^+\pi^-$ events are also expected to contribute an additional 5-10% [98] of the experimental cross section. As mentioned previously, the LTF simulation has been studied in this region and seems to be reproduced well. The same applies to

the simulation of the calorimeter efficiency – the Monte Carlo reproduces the observed calorimeter energy for $e^{\pm}$, $\mu^{\pm}$, $K^{\pm}$, and $\pi^{\pm}$ (figures 3.19-3.21). The observed excess of events in the Monte Carlo simulation at low masses seems to be due to e^+e^- final states which contribute 50% more than $\mu^+\mu^-$ pairs. This suggests a possible culprit in that the Monte Carlo event generator simulates only the multiperipheral ($\gamma\gamma$ collision) diagrams for $e^+e^- \rightarrow e^+e^-X^+X^-$. The contribution of Bhabha scattering with an off-shell radiated photon decaying to a lepton pair is not included in the simulation. For large final-state masses this contribution is propagator suppressed, but the low mass region in question corresponds to Q^2 around 0.17 $(\mathrm{GeV/c^2})^2$. In addition, the identical particles in the $e^+e^-e^+e^-$ final state are not properly symmetrized, as the photon propagator suppresses this contribution in most kinematic regions. There are event generators that include these effects [29], but the computer time required to repeat the simulation with these models is prohibitive. In practice, analyses are checked for sensitivity to the threshold region by varying the minimum transverse momentum required for the charged tracks setting the trigger.

One can limit the observed spectrum to the process $\gamma\gamma \rightarrow \mu^+\mu^-$ using information from the ARGUS muon chambers. If one makes the additional restriction that there must be at least one hit in any layer of the muon chambers in each event, the spectrum in figure 3.23 is observed. For masses above 1.6 $\mathrm{GeV/c^2}$ the ratio of the observed rate of muon production to that predicted by the combination of the Daverveldt event generator and the SIMARG/TRIGGR acceptance calculation is:

$$\frac{N_{experimental}(\gamma\gamma \rightarrow \mu^+\mu^-)}{N_{theory}(\gamma\gamma \rightarrow \mu^+\mu^-)} = 1.032 \pm 0.029 \pm 0.053,$$

where the systematic errors are the same as in the analysis of the X^+X^- topology, except for a small additional uncertainty from the muon chamber acceptance. The somewhat antiquated muon chamber simulation [3] used does not reproduce the threshold efficiency particularly well. The systematic uncertainty from this source is estimated to be approximately 1.6%, even after eliminating the threshold region, $m_{\mu^+\mu^-} < 1.6$ $\mathrm{GeV/c^2}$, from the analysis.

[3] Although an improved version of this program exists, a repetition of the simulation would require too much computer time to be worthwhile.

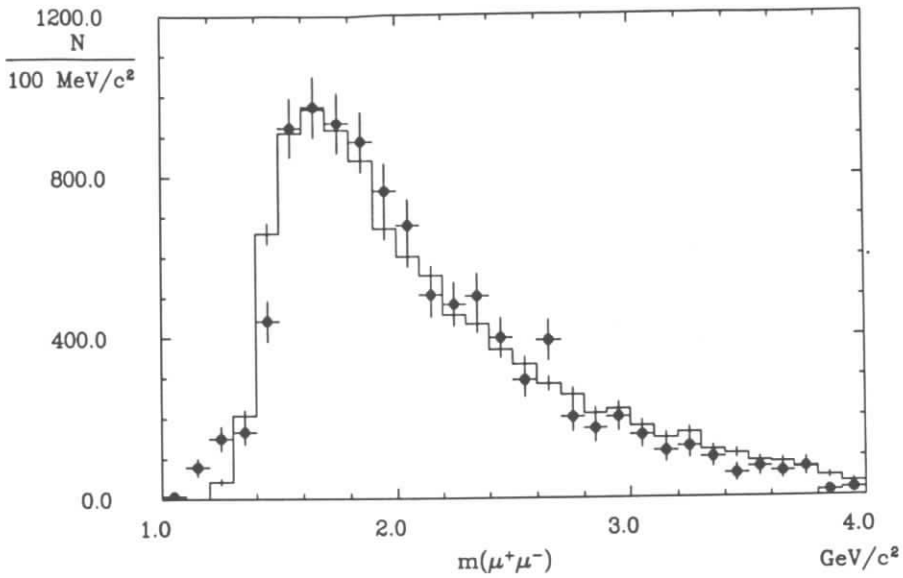

Figure 3.23: The mass spectrum for the process $\gamma\gamma \rightarrow \mu^+\mu^-$.

The trigger simulation has also been used [4] in the analysis of $\Upsilon(1S) \rightarrow$ *nothing visible* [164]. The acceptance for $\Upsilon(2S) \rightarrow \pi^+\pi^-\Upsilon(1S) \rightarrow \pi^+\pi^-$ + *nothing visible* was determined from the process $\Upsilon(2S) \rightarrow \pi^+\pi^-\Upsilon(1S) \rightarrow \pi^+\pi^-e^+e^-$, where the e^+e^- pair hit the endcaps of the detector, but still deposited sufficient energy in each hemisphere (9.46/2 GeV) to guarantee a total energy trigger. The trigger efficiency for the $\pi^+\pi^-$ pair could then be measured directly from the data. The results of a Monte Carlo calculation using the trigger simulation were in good agreement. In conclusion, the detector acceptance for the topologies relevant to this thesis is well understood.

[4] This trigger analysis was done in collaboration with Alf Nilsson (DESY).

Chapter 4

Analysis of $\gamma\gamma \to \eta' \to \pi^+\pi^-\gamma$

This chapter describes, in considerably greater detail, the analysis of η' production in $\gamma\gamma$ collisions originally published in reference [84]. Since that time the luminosity available at ARGUS has increased by 250%. This extended data sample is the largest in existence and has been used, in conjunction with new versions of the luminosity and trigger acceptance calculations, to improve upon the original results. The first section reviews the history and properties of the η' meson. The second section of the chapter discusses the theoretical matrix element and describes some details of the acceptance calculation. The extraction and fitting of the signal for $\gamma\gamma \to \eta' \to \pi^+\pi^-\gamma$ is described in the third and fourth sections, respectively. In the final section the value of $\Gamma_{\gamma\gamma}(\eta') \cdot Br(\eta' \to \pi^+\pi^-\gamma)$ is calculated, and several systematic checks are presented.

The data sample used for this analysis represents an integrated luminosity of (112.1 ± 3.4) pb^{-1} for the published data sample (experiments 2 and 4) and (281.5 ± 8.4) pb^{-1} for the extended data sample (experiments 2, 4, 5, and 6). The data were collected at center of mass energies between 9.4 GeV and 10.6 GeV, including data taken on the $\Upsilon(1S)$, $\Upsilon(2S)$, and $\Upsilon(4S)$ resonances, in the nearby continuum, and during resonance scans. Only data taken with the main drift chamber, time of flight counters, calorimeter, and magnet system in good operating condition have been used.

4.1 The $\eta'(958)$

The $\eta'(958)$ ($I^G(J^P)C = 0^+(0^-)+$) was the first resonance [78] to be observed in $\gamma\gamma$ collisions. This measurement was made by the Mark II collaboration at SPEAR using the decay mode $\eta' \to \rho^0\gamma \to \pi^+\pi^-\gamma$ which has a branching ratio [2,166] of $(30.1 \pm 1.4)\%$. This channel is also used in the ARGUS analysis. The only other decay chain with a comparable branching ratio, $(17.2 \pm 0.6)\%$, that is accessible to a solenoidal detector is $\eta' \to \eta\pi^+\pi^- \to \gamma\gamma\pi^+\pi^-$. In this channel the photons are marginally more energetic, but the pions have significantly smaller momenta – near the trigger thresholds for most experiments. At ARGUS these thresholds correspond to $m(\eta\pi^+\pi^-) = 0.9$ GeV/c^2 for events taken with the CPPT trigger and 1.1 GeV/c^2 for CMATRIX triggers. Though the $\eta' \to \eta\pi^+\pi^-$ final state has been observed by ARGUS in both the $\eta \to \gamma\gamma$ and $\eta \to \pi^+\pi^-\pi^0$[167] decay modes, an analysis of these channels would have much larger statistical and systematic errors than one using the $\pi^+\pi^-\gamma$ final state.

4.2 Matrix Element and Acceptance Calculation

To extract a value for the radiative width from the η' signal, one must calculate the acceptance for the process and the integral of the product of the $\gamma\gamma$ luminosity and cross section. This integral cannot be solved analytically, unless a series of approximations is used. To calculate the integral a Monte Carlo program has been developed (appendix G), which employs expressions for the $\gamma\gamma$ luminosity derived by Budnev et al.[45]. This technique has the advantage that it also generates the kinematical distributions for the final state which are used to calculate the acceptance. The acceptance calculation is actually a convolution of detector resolutions with an integration of the $\gamma\gamma$ luminosity and cross section over a complicated region defined by the hardware. In addition to the general purpose $\gamma\gamma$ Monte Carlo event generator written by the author, an independent program using a rather different algorithm [1], developed specifically for η' production in $\gamma\gamma$ collisions, has been used to verify the simulation. The two programs agree well in all aspects. The expression for the $\gamma\gamma$ cross section used in the ARGUS simulation [168]

[1]This simulation was provided by Michael Feindt of the PLUTO collaboration and is used in that group's analysis[81].

is:

$$\sigma_{\gamma\gamma}(s, q_1^2, q_2^2) = \frac{1}{4\sqrt{X}}(\nu^2 - m^2\tilde{Q}^2)F^2(q_1^2, q_2^2)\frac{\sqrt{s}\Gamma}{(s-m^2)^2 + \Gamma^2 m^2},$$

where $X = (q_1 \cdot q_2)^2 - q_1^2 q_2^2$, $\tilde{Q} = (q_1 - q_2)/2$, $P = q_1 + q_2$, $\nu = P \cdot \tilde{Q}$, m and Γ are the central mass and width of the η', and $\sqrt{s}$ is the mass of the final state. The photon form factor has the normalization, $F^2(0,0) = 64\pi\Gamma_{\gamma\gamma}/m^3$, and the photon q^2 dependence has been parametrized according to the GVDM model (p.110 in [39]). In the limit $q_i^2 \simeq 0$, the expression for the cross section reduces to:

$$\sigma_{\gamma\gamma}(s, 0, 0) = 8\pi\frac{\sqrt{s}}{m}\frac{\Gamma \cdot \Gamma_{\gamma\gamma}}{(s-m^2)^2 + \Gamma^2 m^2}.$$

In the narrow resonance limit this equation in turn reduces to:

$$\sigma_{\gamma\gamma}(s, 0, 0) = 8\pi^2\frac{\Gamma_{\gamma\gamma}}{m}\delta(s - m^2).$$

As the η' is a narrow resonance (approximately 200 keV), the analysis is insensitive to the details of the expression used for the cross section.

After 153,760 Monte Carlo events were generated, the strength of η' production, before introducing acceptance, was calculated to be:

$$\begin{aligned}\frac{\sigma(e^+e^- \to e^+e^-\eta')}{\Gamma_{\gamma\gamma}(\eta')} &= \int \frac{\sigma_{\gamma\gamma\to\eta'}(W_{\gamma\gamma}, Q_1^2, Q_2^2)}{\Gamma_{\gamma\gamma}(\eta')} L_{\gamma\gamma}(E_i, \phi_i, \theta_i) dW dLIPS_3 \\ &= 0.1823 \pm 0.0006 \text{ nb/keV}. \end{aligned} \quad (4.1)$$

The error is a combination of the statistical error in the MC calculation (0.0002), the difference between the PLUTO and ARGUS generators (0.0001), the precision of the ARGUS $\gamma\gamma$ luminosity algorithm (< 0.0002) and sensitivity to the $\gamma\gamma$ cross-section expression (0.0005). This value can be compared with that calculated using Low's formula [24] which yields 0.2072 nb/keV. The result has an additional uncertainty of approximately 2% due to radiative corrections [85].

The acceptance is dependent on the dynamics of the η' decay. The final state is initially generated according to three-particle ($\pi^+\pi^-\gamma$) phase space in the $\gamma\gamma$ center of mass system. These events are converted into $\rho\gamma$ final states by importance sampling (c.f. appendix D) using the matrix element described below. The final state is then

Lorentz boosted to the laboratory frame using the $\gamma\gamma$ center of mass kinematics generated by the luminosity calculation. Finally, the $e^+e^-\pi^+\pi^-\gamma$ four-vectors are passed to the SIMARG and TRIGGR programs for the detector simulation and trigger efficiency calculation.

The matrix element, which includes the effects of the magnetic dipole transition and ρ propagator, is given by:

$$|\mathrm{M}(m_{\pi^+\pi^-}, \mathrm{E}_\gamma, \theta)|^2 \propto \frac{\mathrm{P}_\pi^2 \mathrm{E}_\gamma^2 \sin^2(\theta) m^2_{\pi^+\pi^-}}{(m_\rho^2 - m^2_{\pi^+\pi^-})^2 + m_\rho^2 \Gamma^2(m_{\pi^+\pi^-})}. \tag{4.2}$$

This expression is similar to that used in the TASSO [82] and TPC/$\gamma\gamma$ analyses [85]. E_γ and P_π are, respectively, the energy of the photon and pion in the ρ rest frame while θ is the π/γ angle. The $\pi^+\pi^-$ system is polarized, since the absence of a photon mass limits the helicity of the system recoiling against it to be ± 1, given that the helicity of the η' must be zero. The ρ width is parametrized, following Jackson [169,170], as $\Gamma(m) = \Gamma_0 \cdot 2P^3/(\mathrm{P}_0 \cdot (\mathrm{P}_0^2 + \mathrm{P}^2))$, where P is the π momentum in the $\pi^+\pi^-$ rest frame, P_0 is the π momentum for $m_{\pi^+\pi^-} = m_\rho$, m_ρ is the mass of the ρ pole, and $m_{\pi^+\pi^-}$ is the mass of the two pion system. The standard particle data book values [2] for m_ρ and Γ_0 have been used in the simulation. The rate for production of the final state as a function of $m_{\pi^+\pi^-}$ is then:

$$\frac{d^2\Gamma}{dm_{\pi^+\pi^-} d\cos\theta} \propto |M|^2 E_\gamma P_\pi m_{\pi^+\pi^-},$$

where the simple relation:

$$\begin{aligned} E_{\gamma:\pi^+\pi^-} &= \gamma(1+\beta) E_{\gamma:\eta'} \\ &= (E_{\pi^+\pi^-:\eta'} + |P_{\pi^+\pi^-:\eta'}|) E_{\gamma:\eta'}/m_{\pi^+\pi^-} \\ &= \frac{m_{\eta'}}{m_{\pi^+\pi^-}} E_{\gamma:\eta'} \end{aligned}$$

has been used ($E_{a:x}$ is the energy of a in the rest frame of x). The generator used in the PLUTO analysis is slightly different. If one translates their cascaded two-body decay algorithm [81] into a three-body phase space formalism, the matrix element has an additional factor of $(m_{\pi\pi}/m_\rho)(2P_0^2/(P_0^2 + P^2))$.

The E_γ^2 dependence is due to the magnetic dipole nature of the η' decay which was originally observed by Rittenberg [171]. This type of coupling can also be derived from

basic symmetry principles [168]. There exist only two dynamical four-vectors that can be used in the matrix element:

$$\begin{aligned} P_\delta &= (E_\rho, -E_\gamma, 0, 0) \quad (\rho), \\ Q_\sigma &= (E_\gamma, E_\gamma, 0, 0) \quad (\text{photon}). \end{aligned}$$

The Lorentz invariant matrix element is then:

$$\begin{aligned} T^{\mu\nu} &\propto \epsilon^{\mu\nu\delta\sigma} P_\delta Q_\sigma, \\ T^{ab} &= \lambda^a_\mu(\rho) \lambda^b_\nu(\gamma) T^{\mu\nu}, \\ T^{++} &= -T^{--} \propto i m_{\eta'} E_\gamma, \end{aligned}$$

where the following polarization vectors have been used:

$$\begin{aligned} \lambda^0(\rho) &= (E_\gamma, -E_\rho, 0, 0)/m_\rho, \\ \lambda^\pm(\rho) &= (0, 0, \pm 1, -i)/\sqrt{2}, \\ \lambda^\pm(\gamma) &= (0, 0, \mp 1, -i)/\sqrt{2}. \end{aligned}$$

The T^{+-} matrix element is identically zero. In the quark model view of the decay, the η' is initially composed of two quarks with spins antiparallel, one of which emits a photon. The resultant spin flip allows the formation of a ρ meson in which the quarks have parallel spins.

To maximize computer efficiency, only 39,166 of the generated η' events (25%) are passed to the SIMARG program for processing. These events have $P_\perp(\pi^\pm) > 0.1$ and $|\cot\theta(\pi^\pm)| < 1.33$, which ensures that there is a reasonable chance of setting the trigger. On requiring that a trigger be set, the acceptance is found to be 11.0%[2]. The trigger calculation produces a probability for each Monte Carlo event which is used in subsequent calculations; only those events with zero trigger probability ($\sim 10,000$) are actually discarded. As the events were generated with a 5 GeV beam energy, a correction ($\pm 5\%$) is made to the $\gamma\gamma$ luminosity to account for the distribution of beam energies in the data. The expression of Low [24] is used for this purpose (equation 1.1). The average increase in $\gamma\gamma$ luminosity is $(1.83 \pm 0.05)\%$). The error is due to the double equivalent-photon approximation used to derive Low's formula.

[2]This number, and subsequent efficiencies, refer to the 1989 calculations for the extended data sample.

4.3 Separation of the Signal

From a data sample of about $3 \cdot 10^7$ reconstructed events on the EXPDST tapes, approximately $1.5 \cdot 10^6$ are selected as candidates for charge balanced X^+X^- events from $\gamma\gamma$ collisions. Approximately $1.3 \cdot 10^6$ events remain after removing cosmic rays and events from beam-gas collisions. A pion mass is assigned to both charged tracks in each event. No particle identification is used, as a clean separation of the η' signal can be achieved with kinematic cuts alone. Studies of the vertex distributions indicate that the contribution from beam-gas or beam-wall events is consistent with zero.

The charge balanced two-prong topologies with additional photons are divided into three classes:

A_1 : events containing a single shower counter with no other energy in the calorimeter (except that assigned to charged particle interactions);

A_C : events containing a neutral cluster with no unassigned energy in the calorimeter;

B : events with one independent shower counter cluster with additional single counter hits. The single counter hits in this data sample are treated as noise and ignored in the analysis.

Only calorimeter signals with a deposited energy of 50 MeV or more are considered. The ratio of populations in samples A and B (table 4.1) is consistent with that expected from the calorimeter noise remaining after the hot-counter rejection described in the previous chapter. This division is motivated by an attempt to minimize signal loss due to calorimeter noise – the only events lost are those with (a) a noise cluster in the calorimeter or (b) events where the photon deposits energy in a single shower counter in coincidence with shower counter noise.

The major background for η' production comes from $\gamma\gamma \to l^+l^-\gamma$ ($l = e, \mu$) events. These are $\gamma\gamma$ QED processes with final-state bremsstrahlung or incompletely reconstructed calorimeter interactions. Bremsstrahlung from the incident $e^\pm$ beams is more abundant due to the Lorentz boost, but this contribution is focussed along the beam pipe. Figure 4.1 shows the cosine of the minimum opening angle between the photon

Data sample	n_A	n_B	$n_B/(n_{A_C}+n_B)$	noise
Experiments 2,4 1986[a]	64586	9616	0.168	0.12 ± 0.04
Experiments 2,4 1989	61103	9295	0.171	0.083 ± 0.006
Experiments 2,4,5,6 1989	174759	25613	0.166	0.090 ± 0.006

Table 4.1: Initial event samples. $n_A = n_{A_1} + n_{A_C}$. The noise level is the sum of that determined from cosmic events and the expected rate for charged particle shower splitting. The ratio, $n_B/(n_{A_c}+n_B)$, is consistently larger than this, as there are valid $X^+X^- + n\gamma$ events with $n > 1$ included in data sample B. [a] These numbers differ slightly from those published [84]; events failing the data quality cuts have been removed. Previously, this was only done after all other cuts had been made.

and the charged tracks in the event. The character of the distribution changes drastically around $cos(\theta_{X\pm\gamma}) \sim 0.9$. If one requires $cos(\theta_{X\pm\gamma})$ to be less than 0.8 most of these QED events are removed and an η' signal is clearly visible (figure 4.2).

To ensure that the events arise from completely reconstructed $\gamma\gamma$ collisions, a cut on the coplanarity of the events is made, $\cos(\phi_{X^+X^-} - \phi_\gamma) < -0.8$. This is a geometric expression of transverse momentum balance (figure 4.3). To reinforce this, the components of the final-state transverse momentum normal and parallel to the plane containing the beam axis and photon momentum (figure 4.4) are required to be less than 0.05 GeV/c and 0.1 GeV/c, respectively. These requirements also limit the photon Q^2 contributing to the collisions to values on the order of $P_\perp^2(1 - \frac{m(\eta')}{2E})$.

As the final-state mass resolution is dominated by the photon energy resolution, one can, following earlier work [78,81,85], compensate for this by scaling the photon energy so that its transverse momentum and that of the X^+X^- system are equal in magnitude:

$$\vec{P}_\gamma^{\,*} = \vec{P}_\gamma \cdot \left[\frac{P_\perp(X^+X^-)}{P_\perp(\gamma)}\right],$$

$$\chi^2_{tuning} = \frac{(E_\gamma - E_\gamma^*)^2}{\sigma^2(E_\gamma)}.$$

The rationale behind this energy tuning is that the final-state transverse momentum is expected to be very small, since the events are collisions of virtual bremsstrahlung from the incident e^+e^-. This can be seen (figure 4.4) in the comparison of the components of final-state transverse momentum with respect to the plane containing the photon and

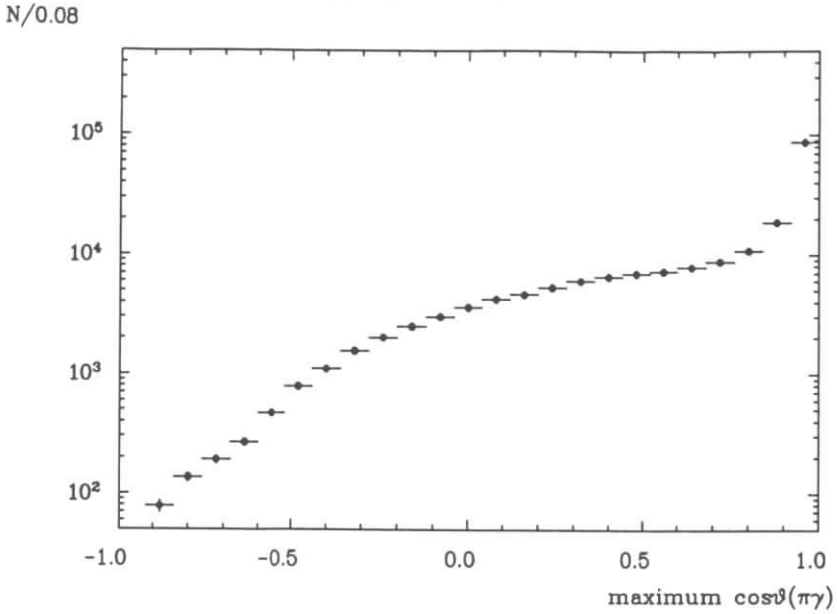

Figure 4.1: The maximum value of $\cos\theta_{X^\pm\gamma}$ in each event; this is required to be less than 0.8 in the analysis.

$e^\pm$ vectors. These two distributions would be identical if the photon energy resolution were negligible. The η' line shape deviates slightly from a Gaussian due to the energy dependent detector resolution (figure 4.5). The energy tuning further distorts the line shape, as the transverse momenta of the events are not identically zero. In an alternative energy tuning, one scales the photon energy so that the final-state transverse momentum component parallel to the X^+X^- transverse momentum is zero:

$$\vec{P}^*_\gamma = \vec{P}_\gamma\left[\frac{(\vec{P}_{X^+X^-} \wedge \hat{Z}) \cdot (\vec{P}_\gamma \wedge \hat{Z})}{P^2_\perp(\gamma)}\right].$$

This weaker requirement does not appreciably change the shape of the distribution. With the standard energy tuning, an η' signal is visible with only the topology requirements (figure 4.6). The χ^2_{tuning} distribution (figure 4.7) from the scaling of the photon energies is concentrated at values near zero as expected. The photon energy distributions before and after tuning are shown in figure 4.8. One should note that, although this technique is not essential to the analysis, it is useful for studying systematic effects arising from background underneath the η' signal (section 4.4).

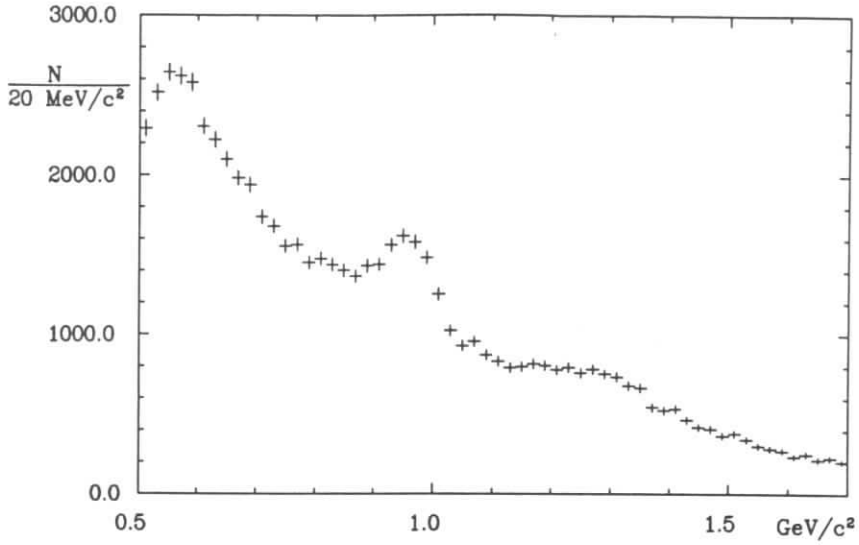

Figure 4.2: $m(X^+X^-\gamma)$ mass spectrum (without energy tuning) requiring only that $\cos\theta_{\pi^\pm\gamma} < 0.8$.

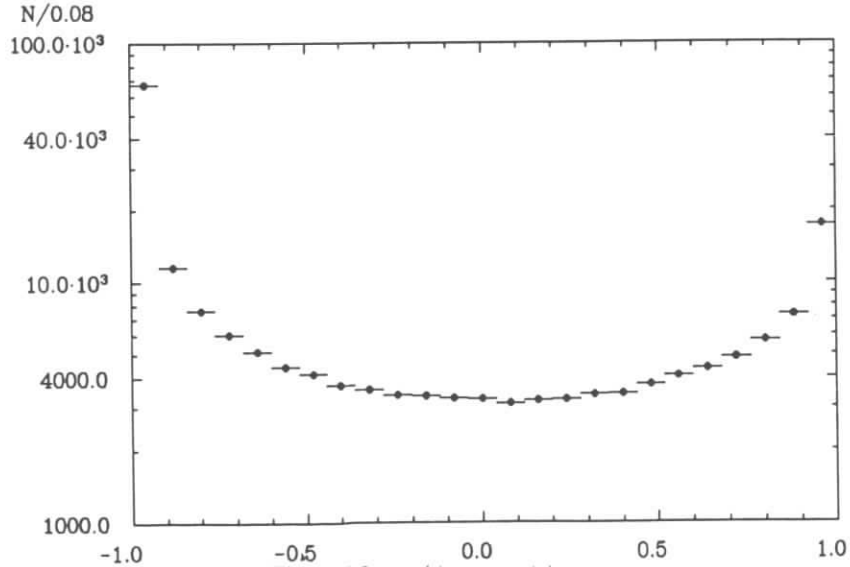

Figure 4.3: $\cos(\phi_{X^+X^-} - \phi_\gamma)$.

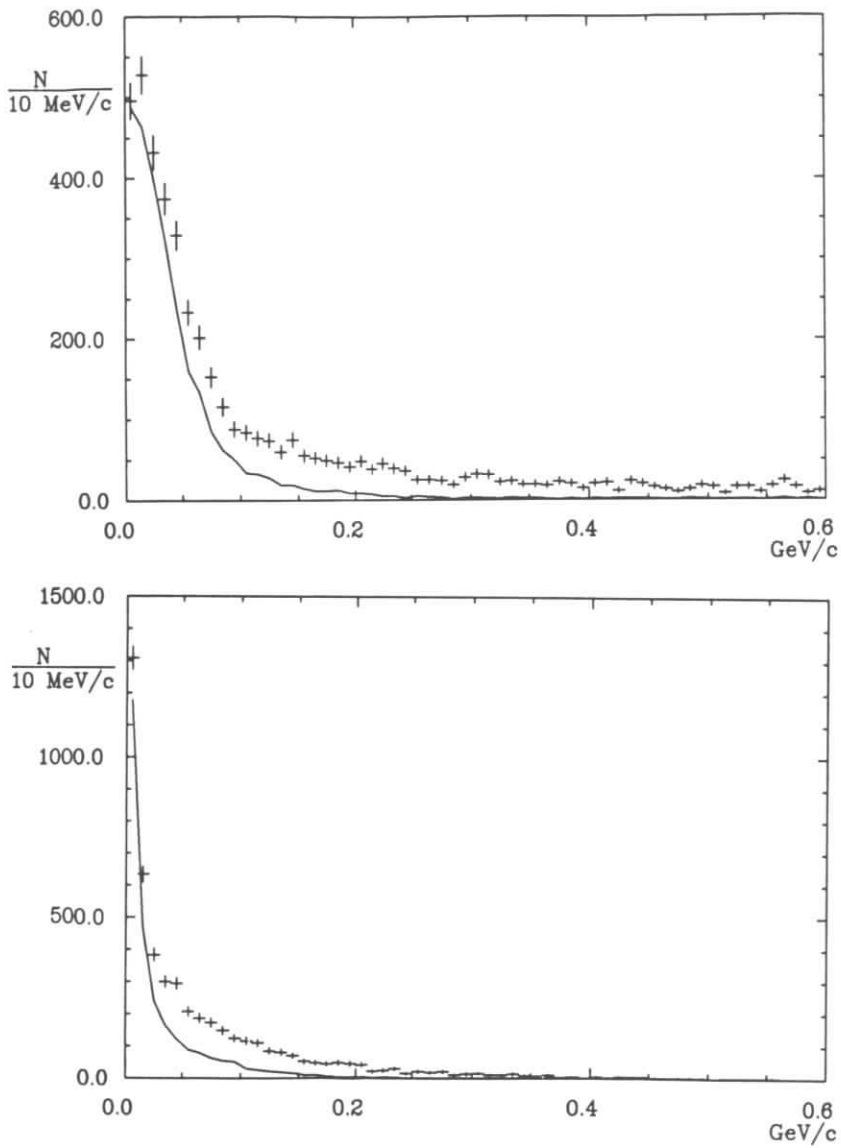

Figure 4.4: Components of $\vec{P}_\perp(\pi^+\pi^-\gamma)$, parallel (upper plot) and transverse (lower plot) to $\vec{P}_\perp(\gamma)$. The points with error bars are from data while the lines are from the simulation. Only events surviving all other cuts, with 0.87 GeV $< m(\pi^+\pi^-\gamma) <$ 1.03 GeV, have been used. The excess of events at high $\vec{P}_\perp$ is background.

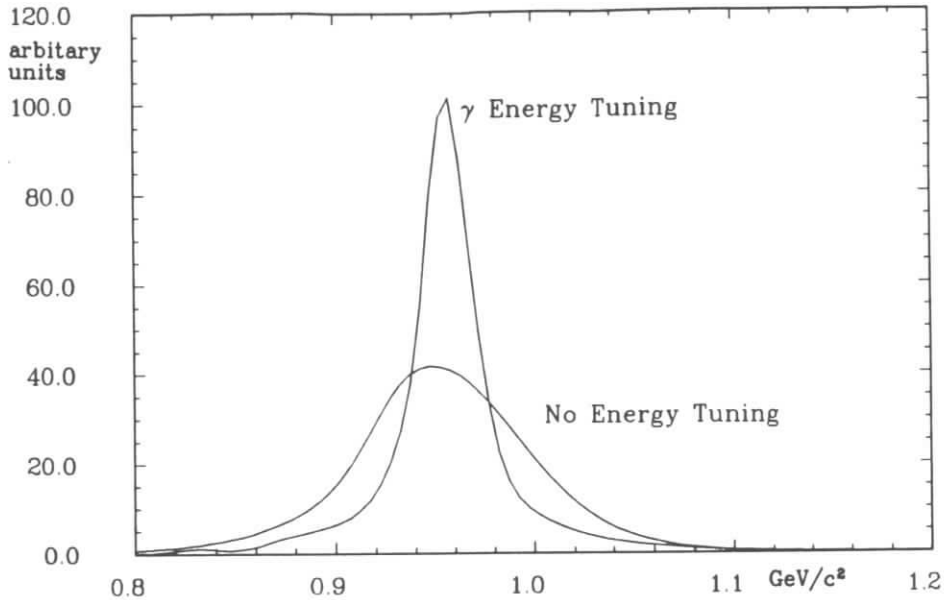

Figure 4.5: η' line shapes from Monte Carlo events, before and after the γ energy tuning.

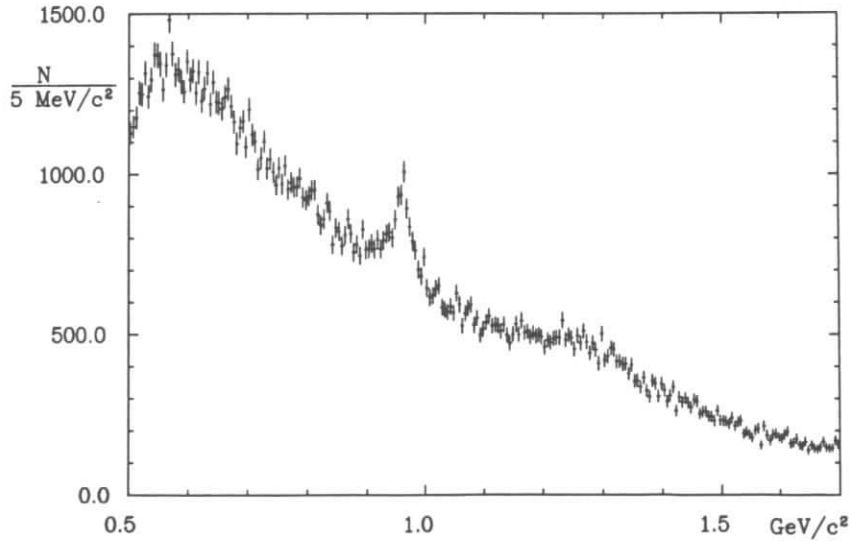

Figure 4.6: $X^+X^-\gamma$ mass spectrum after the γ energy tuning; no kinematic cuts have been made.

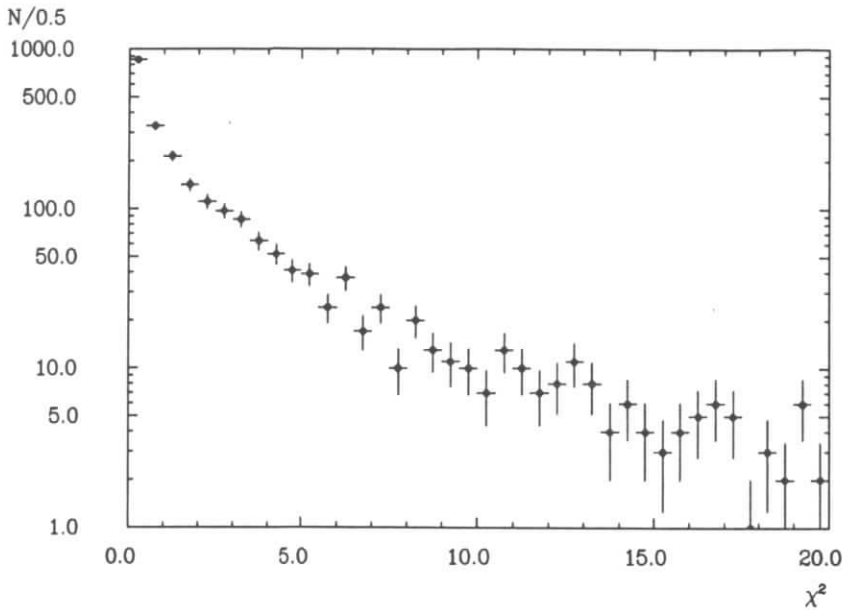

Figure 4.7: χ^2 distribution for γ energy tuning. Only events surviving all analysis cuts, with 0.87 GeV $< m(\pi^+\pi^-\gamma) <$ 1.03 GeV, have been used.

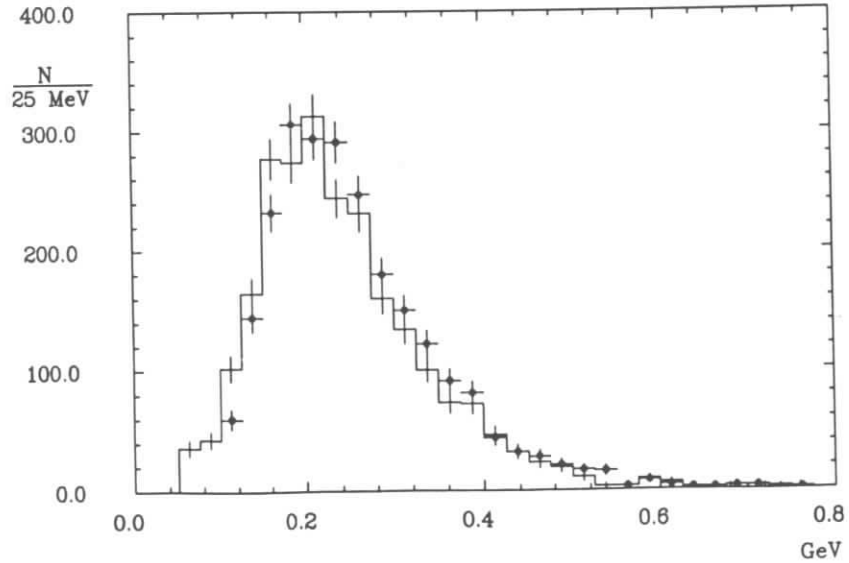

Figure 4.8: γ energy spectrum with (circles) and without (histogram) the energy tuning. Events surviving all cuts, with 0.87 GeV $< m(\pi^+\pi^-\gamma) <$ 1.03 GeV, have been used.

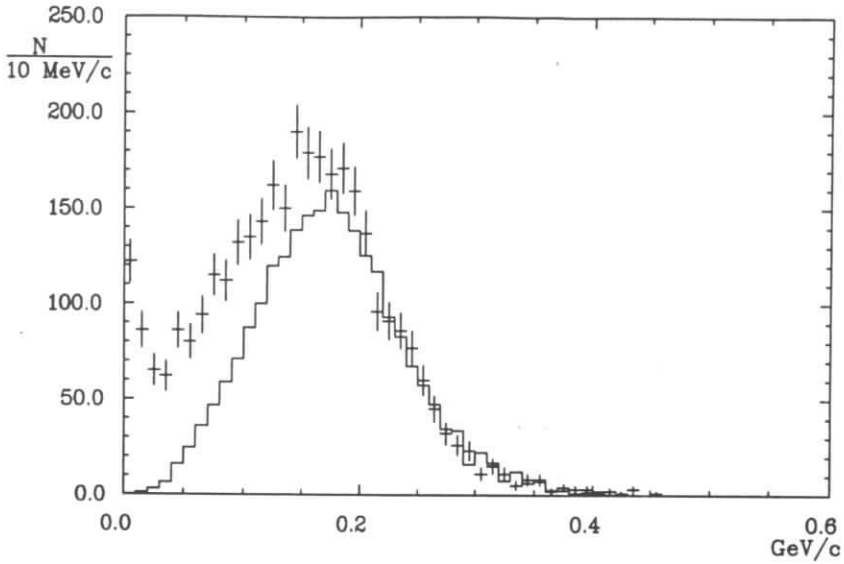

Figure 4.9: $P_\perp(X^+X^-)$ distribution from data (points with error bars) and Monte Carlo (histogram). Only events surviving all other cuts, with 0.87 GeV $< m(\pi^+\pi^-\gamma) <$ 1.03 GeV, have been used. The excess of events at low values of $P_\perp(X^+X^-)$ is background.

In exclusive two charged particle topologies from $\gamma\gamma$ processes, the transverse momentum will also balance. To reject any of these events appearing in the $X^+X^-\gamma$ data sample because of calorimeter noise, the X^+X^- system was required to have a transverse momentum of at least 0.1 GeV/c (figure 4.9). This also restricted the energy tuning so that no photon energies were scaled into regions where there is poor efficiency or resolution. Finally, the charged tracks were required to have $|P_\perp| > 0.1$ GeV/c and $|\cot\theta| < 1.33$, as the Monte Carlo events used to calculate the acceptance were generated with these cuts. 5,969 events survive. The combined mass spectra from all data are shown in figures 4.10-4.11. This signal is exceptionally clean, especially after a cut has been made on the $\pi^+\pi^-$ mass.

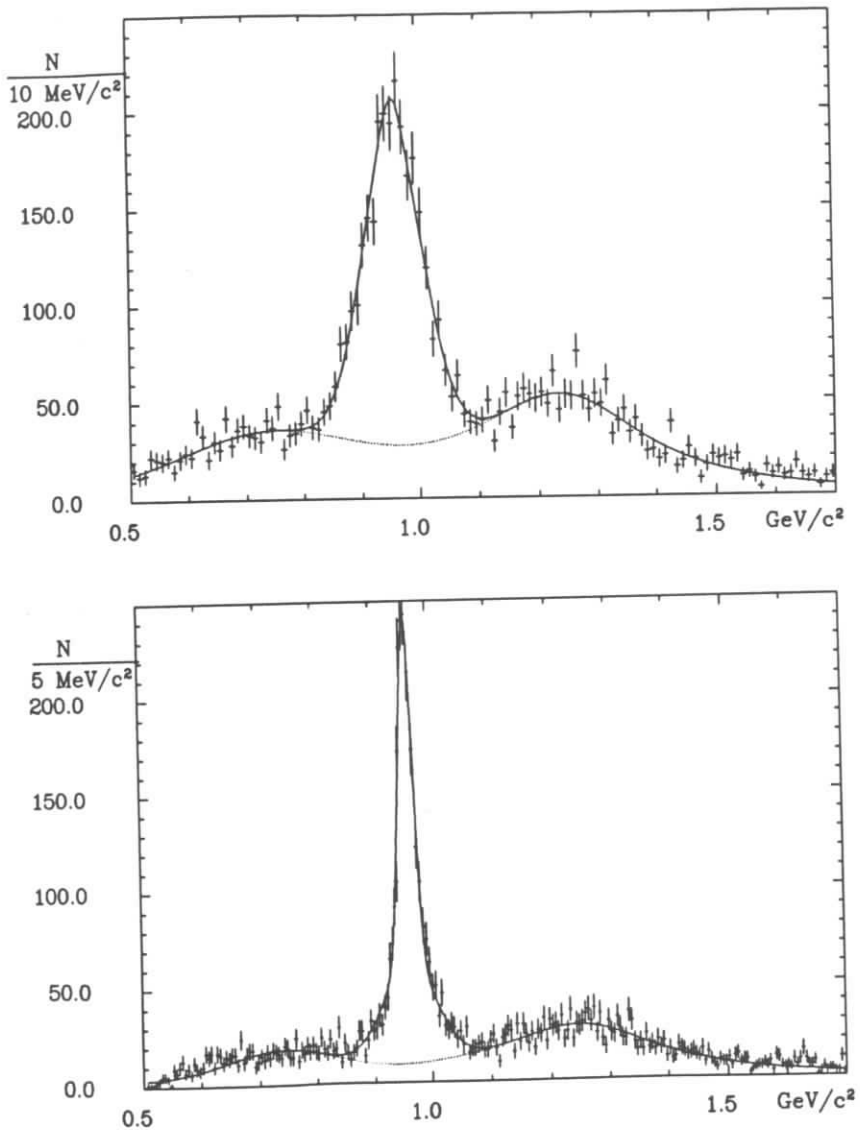

Figure 4.10: $X^+X^-\gamma$ mass spectra after all kinematic cuts. The lower plot is the spectrum after γ energy tuning.

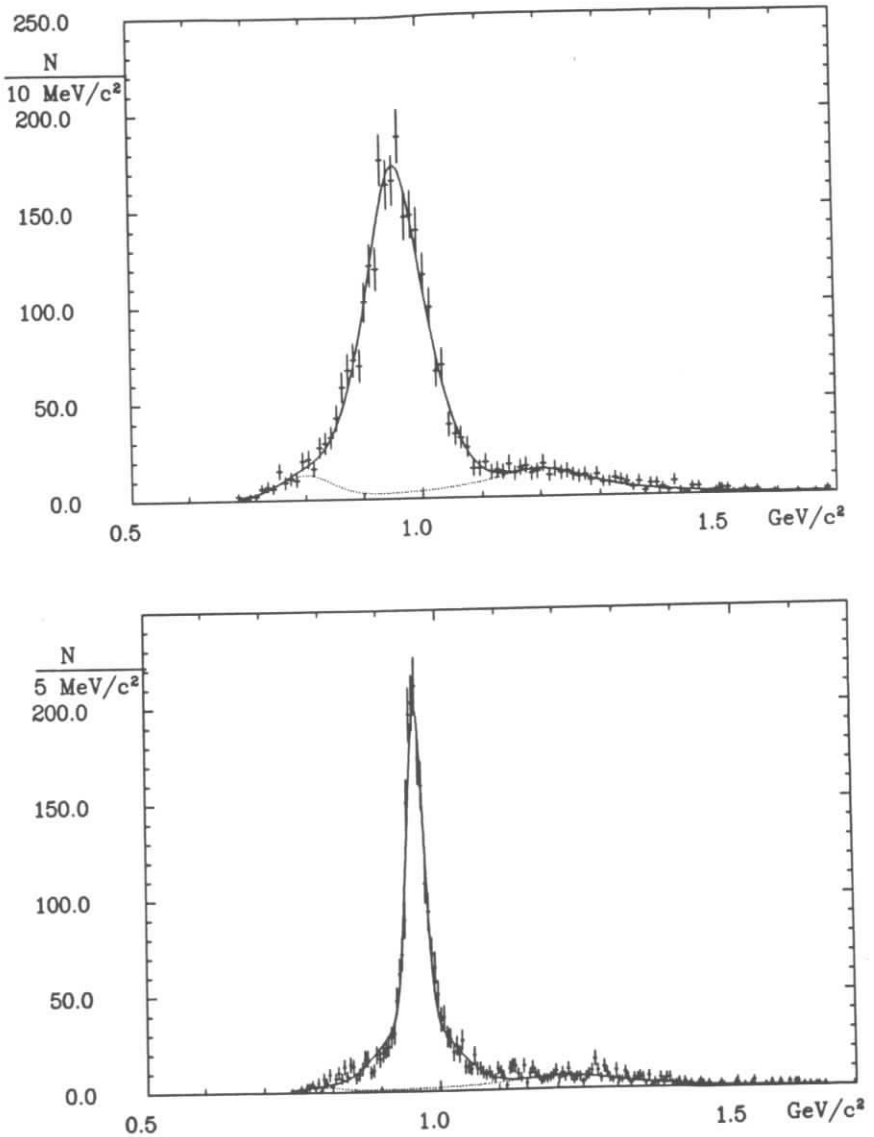

Figure 4.11: $X^+X^-\gamma$ mass spectra after all kinematic cuts and requiring 0.63 GeV $< m(X^+X^-) <$ 0.83 GeV. The lower plot is the spectrum after γ energy tuning.

4.4 Fitting the Signal

As discussed above, the main background for the $\pi^+\pi^-\gamma$ final state comes from QED events. This contribution is almost eliminated by the kinematic cuts described, and the remainder is confined to masses below that of the η'. At higher masses events from $\gamma\gamma \to a_2(1320) \to \rho^{\mp}\pi^{\pm} \to \pi^+\pi^-\pi^0$ with one photon lost (sample A) or ignored (sample B) are clearly seen in figures 4.10-4.11. The first observation of the a_2 resonance in $\gamma\gamma$ collisions [80] was actually made in this incompletely reconstructed channel. This resonance has also been observed, with a much stronger signal, in the fully reconstructed mode at ARGUS, but has not yet been quantitatively analyzed. These two contributions suggest a physically motivated background parametrization of the form:

$$f(W) = \frac{\alpha}{1+\beta(W^2-\gamma^2)^2} + \zeta\frac{(\log W/\omega)^{2\epsilon}}{W^{\delta}}$$

where $W = m(X^+X^-\gamma)$. The logarithmic term is inspired by the functional form of the QED cross sections in the DEPA approximation and fits the raw $\gamma\gamma \to X^+X^-$ distribution reasonably well. The first term, a relativistic Breit-Wigner form, describes the a_2 production. In practice, the remnant of the QED contribution is better described by a Gaussian. The η' line shape is adequately described by a sum of two Gaussians [3]:

$$\frac{dN}{dW} = \frac{N\cos^2\chi}{\sqrt{2\pi}\sigma_1}e^{-(W-m(\eta'))^2/2\sigma_1^2} + \frac{N\sin^2\chi}{\sqrt{2\pi}\sigma_2}e^{-(W-m(\eta'))^2/2\sigma_2^2}$$

To extract the number of η' mesons produced, the mass spectrum is fitted using a least squares method (appendix E). The results of these fits are shown in figures 4.10-4.11 and have a χ^2 per degree of freedom close to unity.

The largest contribution to the systematic error on the number of η' mesons is taken as the standard deviation of the results from fits to four different spectra: with and without the energy tuning, with two binnings in each case. As the signal-to-noise ratio increases as the line shape narrows, the comparison of the tuned and untuned spectra is a useful estimate of the sensitivity of the signal to the background parametrization. This contribution is typically on the order of $4-6\%$.

[3] The η' mass resolution is actually a convolution of an energy dependent resolution function and the photon energy spectrum - a rather complicated mathematical expression.

One can test the quality of the background parametrization by studying spectra produced by mixing Monte Carlo η' events with background from the data. This background $\pi^+\pi^-\gamma$ mass spectrum is selected by ***excluding*** all events with a $\pi^+\pi^-$ mass between 0.63 and 0.83 GeV/c^2 – the region corresponding to ρ meson production. The remaining η' contribution ($\sim 17\%$) is removed by subtracting, after appropriate normalization, the $\pi^+\pi^-\gamma$ mass spectrum selected by ***requiring*** 0.63 GeV $< m(\pi^+\pi^-) <$ 0.83 GeV. After this subtraction, the remaining η' contribution is consistent with zero. The η' line shape generated in Monte Carlo is then added to the background distribution to produce a synthetic spectrum. Fits to these synthetic distributions using the Breit-Wigner plus Gaussian background parametrization (figures 4.12-4.13) measure the Monte Carlo η' contribution to within 1%. When fitting with the background spectrum of equation 4.4, the number of Monte Carlo η' mesons is underestimated by about 15%. This parametrization does not reproduce the curvature of the background underneath the η' peak. On raising the $P_\perp$ threshold for the pions this underestimate decreases, as the background is reduced. The same quantitative behaviour is seen on repeating these studies with the experimental $\pi^+\pi^-\gamma$ spectrum. This agreement suggests that the synthetic spectrum method is a good test of the background parametrization – parametrizations which underestimate the number of Monte Carlo events produce the same underestimate when used in fitting the experimental spectrum. If the background shape used in the synthetic spectrum was incorrect one would not expect this behaviour.

The total systematic error in determining the number of η's is taken as the sum, in quadrature, of:

1. the standard deviation of the fits with different energy tunings and binnings (σ(fits));
2. the averaged MINUIT error (appendix E), in excess of that expected from the statistics of the η' signal (Δ(MINUIT));
3. the error estimated by mixing Monte Carlo events with backgrounds taken from experimental data (1%).

This is a conservative estimate.

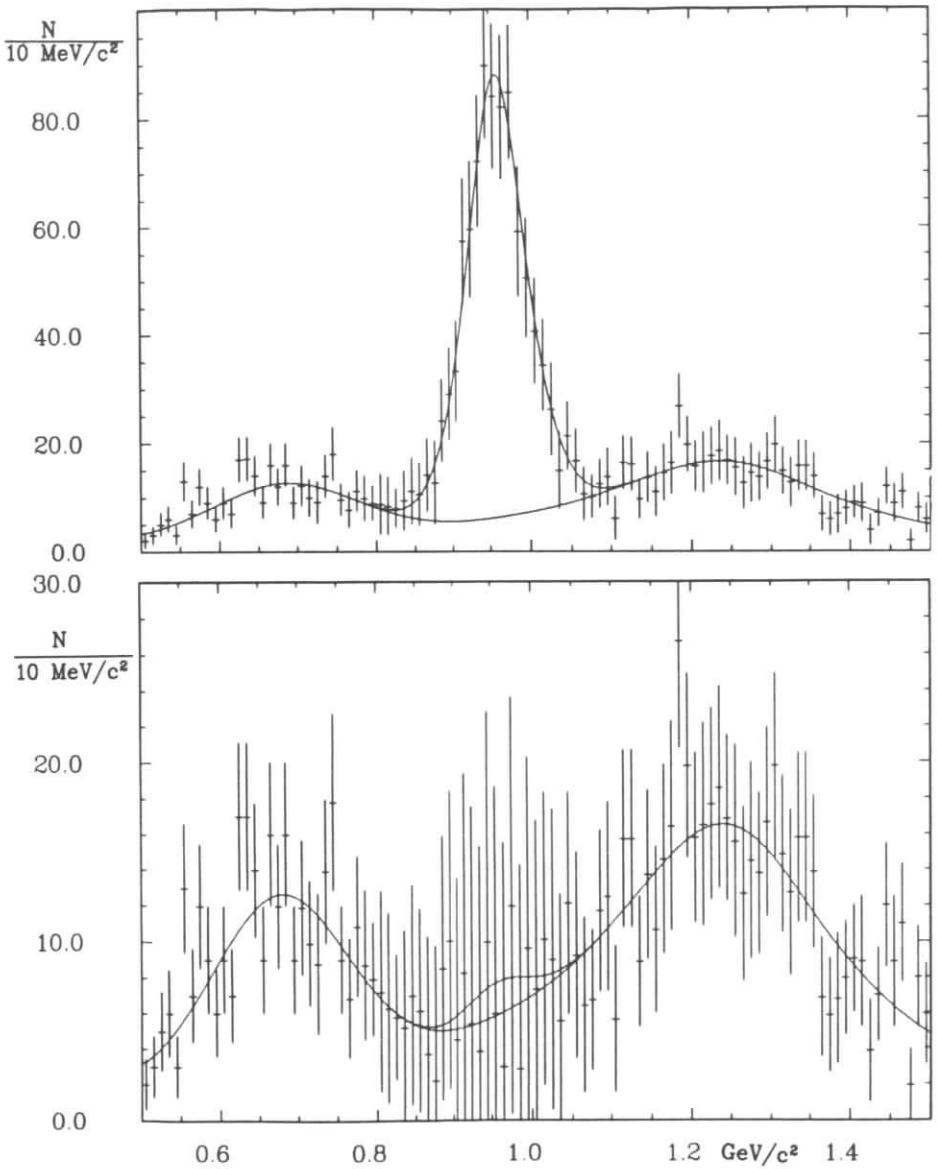

Figure 4.12: The Monte Carlo line shape without γ energy tuning combined with background extracted from the data by excluding events with 0.63 GeV $< m(\pi^+\pi^-) <$ 0.83 GeV. The lower curve shows the background distribution without the Monte Carlo.

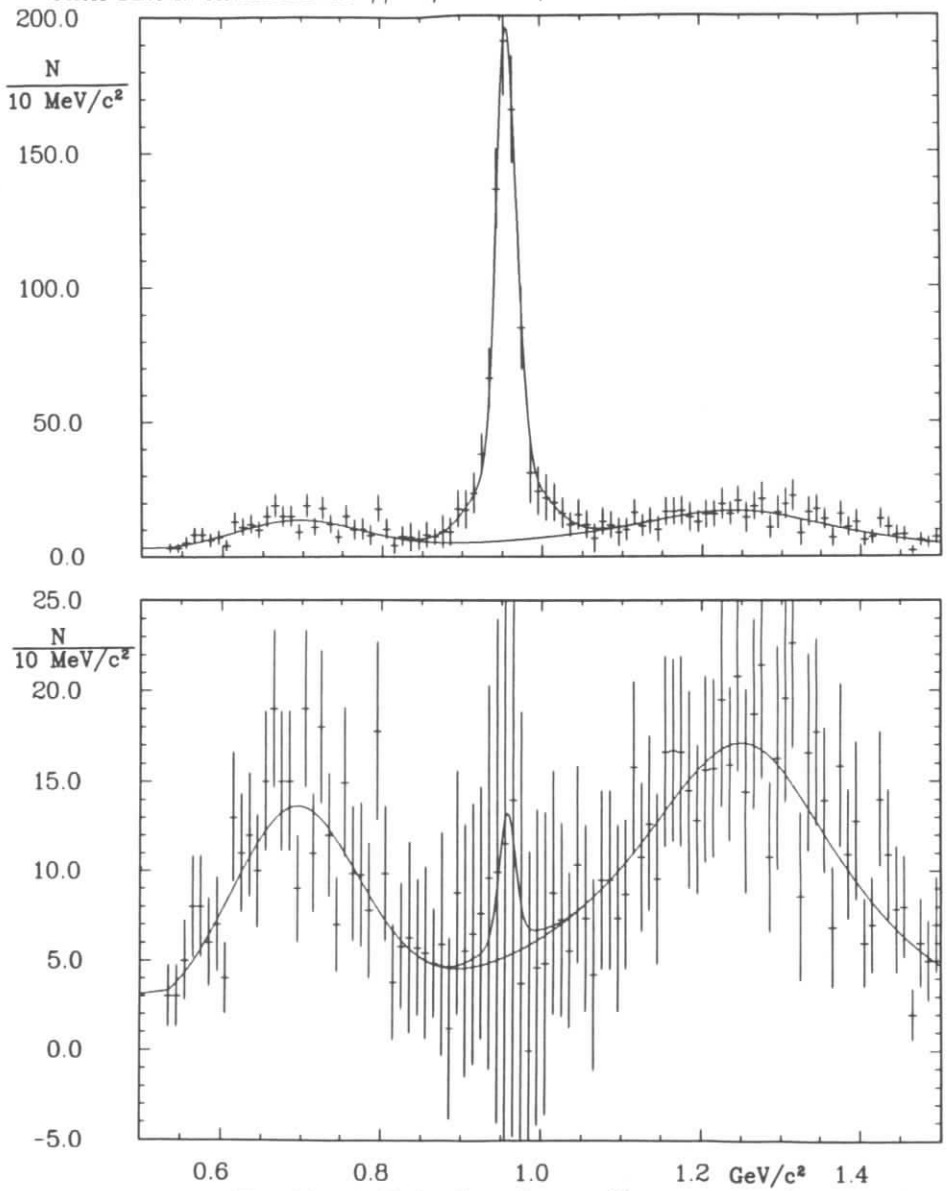

Figure 4.13: The Monte Carlo line shape with γ energy tuning combined with background extracted from the data by excluding events with 0.63 GeV $< m(\pi^+\pi^-) <$ 0.83 GeV. The lower curve shows the background distribution without the Monte Carlo.

The averaged results of the fits are shown in table 4.2. The number of events gained by including experiments 5 and 6 is more than one would expect from the extra luminosity. The trigger conditions during the later experiments were optimal, while in experiment 2, 22% of the luminosity used was taken with a coincidence required between the CPPT and CMATRIX triggers. The difference between the 1986 analysis of experiments 2 and 4 and the re-analysis in 1989 is due to several factors. The low level (EXPDST) data sample used in the 1986 analysis was originally reconstructed with the software version and calibration constants current when the data were being taken. Newer reconstruction versions were used to reprocess data selected as $\gamma\gamma$ event candidates (chapter 2). In 1987 the reconstruction and selection of the entire low level data sample was repeated from raw data tapes. In addition to this, run quality requirements were reassessed; in particular, runs with visible multi-hadron cross sections inconsistent with that expected from data taken concurrently were excluded.

The only difficulty with the fits described in table 1.3 is the high value for the tuned η' mass. This has no significant effect on the analysis. ARGUS has done well, as other experiments have missed by up to 30 MeV! A similar mass shift is seen in Monte Carlo (the fits described are to the pure line shape – not the background/MC mixture) but is only 30% as strong. Kinematically, this is related to the cut on the transverse momentum of the $\pi^+\pi^-$, which allows photons with energies less than 100 MeV to be scaled to higher energies but prevents scaling in the opposite direction. As the photon spectrum and energy resolution are not symmetric about 100 MeV, the cut results in a mass shift. The difference between the shift in Monte Carlo and data could arise from a 1.1% uncertainty in the calorimeter energy scale, which is not unreasonable.

To determine the true number of η' mesons one must correct for topology loss due to noise photons. This was determined directly from the η' data and found to be consistent with the calorimeter noise determined from cosmic ray events. Using the same fitting method as described above, the η' populations of the three subsets of the data (1986 analysis) were found to be:

$$N(A_1) = 201.9 \pm 14.2 \pm 39.5 \quad \text{(sample } A_1\text{)}$$

Data sample/analysis date	$n(\eta')$	σ(fits)	Δ(MINUIT)
Experiments 2,4 1986	$830 \pm 29 \pm 37$	14	33
Experiments 2,4 1989	$804 \pm 28 \pm 48$	20	43
Experiments 2,4,5,6 1989	$2291 \pm 48 \pm 108$	75	74

Table 4.2: Fitted number of η' mesons (the errors are explained on page 115).

Spectrum Type	$m(\eta')$ [MeV]	σ_1 [MeV]	σ_2 [MeV]	$\cos^2\chi$ [%]	$<\sigma>$ [MeV]
untuned/data	955.3 ± 1.6	51.9 ± 1.8	12.5 ± 0.8	97.7 ± 2.6	51.0 ± 1.8
tuned/data	961.0 ± 0.5	44.7 ± 3.9	12.7 ± 0.9	51.4 ± 4.0	29.1 ± 2.1
untuned/MC	955.0 ± 1.8	58.1 ± 0.7	32.2 ± 0.5	51.6 ± 22.7	45.6 ± 6.9
tuned/MC	957.0 ± 0.8	56.4 ± 2.9	13.5 ± 0.8	33.8 ± 3.7	28.0 ± 1.1

Table 4.3: η' fit parameters (for functional form see page 114).

$$N(A_C) = 560.4 \pm 23.7 \pm 38.8 \quad \text{(sample } A_C\text{)}$$
$$N(B_C) = 86.0 \pm 9.3 \pm 8.7 \quad \text{(sample } B\text{)}$$

where $N(A_C)$ and $N(B_C)$ are determined from a fit to both spectra, using the same line shape parameters (χ, σ_1, σ_2). The parameters required to correct for topology loss are then:

$$P_{1C} = \frac{N(A_1)}{N(A_1)+N(B)} = 0.265 \pm 0.052$$
$$P_{1C\ noise} = \frac{N(B)}{N(B)+N(A_C)} = 0.133 \pm 0.023$$

The probability of finding cluster noise ($P_{cluster\ noise} = 0.042 \pm 0.009$ for experiments 2 and 4, 0.035 ± 0.002 for the full data sample) in the calorimeter is determined from cosmic ray events. Finally, the correction for topology loss is found to be:

$$C = \frac{1}{1 - P_{1C} \cdot P_{1C\ noise}} \cdot \frac{1}{1 - P_{cluster\ noise}} = 1.099 \pm 0.017 \text{ (Exp. 2,4 1986)}$$

$$= 1.073 \pm 0.007 \text{ (Exp. 2,4 1989)}$$
$$= 1.085 \pm 0.007 \text{ (Exp. 2,4,5,6 1989)}$$

This includes a small additional correction of 1.5-3.5% for dead counters and counters removed from the analysis by the hot-counter rejection algorithms. The newer analyses have a slightly stronger hot-counter rejection algorithm.

4.5 Calculation of $\Gamma_{\gamma\gamma}(\eta')$ and Systematic Checks

In section 4.2, the efficiency of the trigger and fiducial region cuts was found to be 11.0%. Of the Monte Carlo events which passed the trigger simulation, 26.2% are eliminated on requiring that they survive the reconstruction and data selection algorithms used to select the three preliminary data samples (A_1, A_C, and B). This loss is due to several effects:

1. loss of photons due to detector geometry ($\sim 7\%$);
2. three-prong events corresponding to $e^\pm$ tags ($\sim 7\%$, assuming GVDM);
3. additional charged tracks appearing in the event because of decays in flight, drift chamber fit over-efficiencies or albedo from the scattered $e^\pm$ interacting in the compensation coils or quadrupoles ($\sim 7\%$);
4. two-prong events corresponding to $e^\pm$ tags ($\sim 4\%$);
5. additional photons appearing in the event because of shower splitting or albedo from the scattered $e^\pm$ interacting in the compensation coils or quadrupoles ($\sim 5\%$).

The number of tags expected in the generalized vector dominance model model (GVDM) is actually an overestimate [85] but, as the final-state transverse momentum restrictions limit the Q^2's of the colliding photons to small values, the result is insensitive to the ansatz used for the form factor. Although the total sensitivity (equation 4.1) decreases by 6.6% on substituting a VDM form factor, the measured $\gamma\gamma$ width changes by only 0.44%, as the extrapolation to $Q^2 = 0$ for those events used is relatively small.

Of the Monte Carlo events selected, 47.1% survive the cuts designed to separate the signal from the backgrounds: 40% are lost from the three cuts on the transverse momentum of the final state [4], 4% from the anti-bremsstrahlung cut, and 11% from from the cut on the $\pi^+\pi^-$ transverse momentum [5]. The total efficiency for the triggering, reconstruction, and selection of η' mesons is then 3.8% in the new analysis with the extended data sample and 4.2% for the old analysis. This difference is due to the new LTF algorithm discussed in chapter 3.

Combining these results with those from the previous section yields the following values for the product of two-photon width and $\pi^+\pi^-\gamma$ branching ratio:

$$\Gamma_{\gamma\gamma}(\eta') \cdot Br(\eta' \to \pi^+\pi^-\gamma) = 1.13 \pm 0.04 \pm 0.13 \text{ keV} \quad (1986 \text{ Exp. } 2\,\&\,4)$$
$$= 1.16 \pm 0.04 \pm 0.10 \text{ keV} \quad (1989 \text{ Exp. } 2\,\&\,4)$$
$$= 1.25 \pm 0.03 \pm 0.11 \text{ keV} \quad (1989 \text{ Exp. } 2,\ 4,\ 5\,\&\,6)$$

The new results also include a 1.2% correction for the shape of the decay matrix element (described below). The three values are reasonably consistent and the third entry represents the highest precision measurement available. The only measurement with comparable systematic uncertainty is that of the Crystal Ball collaboration in the elastic two-photon scattering channel [26], which is based on a much smaller data sample. Using the current [2] value of the branching ratio $Br(\eta' \to \pi^+\pi^-\gamma) = 0.301 \pm 0.014$, the two-photon width of the η' is found to be:

$$\Gamma_{\gamma\gamma}(\eta') = 4.16 \pm 0.09 \pm 0.42 \text{ keV}$$

where the error in the $\pi^+\pi^-\gamma$ branching ratio has been added in quadrature. The details of the systematic error calculation are shown in table 4.4. Note that the errors assigned to photon and charged particle reconstruction (table 4.4) are conservative estimates as they are as large as the inefficiencies.

Figures 4.14-4.15 show evidence for ρ production in the η' decay. The result of the Monte Carlo, also shown in figure 4.15, appears to underestimate the number of η's with

[4] This value is, again, dependent on the ansatz made for the photon propagator; it varies inversely with the total sensitivity.

[5] These fractions do not exactly reproduce the 47.1% cut rejection, as they are calculated individually with the other cuts in place, i.e., they are calculated in parallel rather than in series.

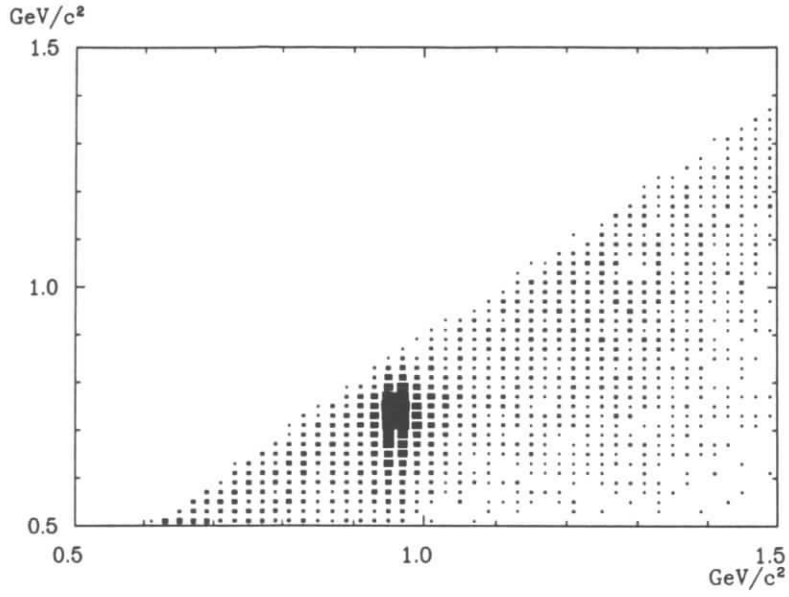

Figure 4.14: $m(X^+X^-)$ vs. $m(X^+X^-\gamma)$ with all cuts and photon energy tuning.

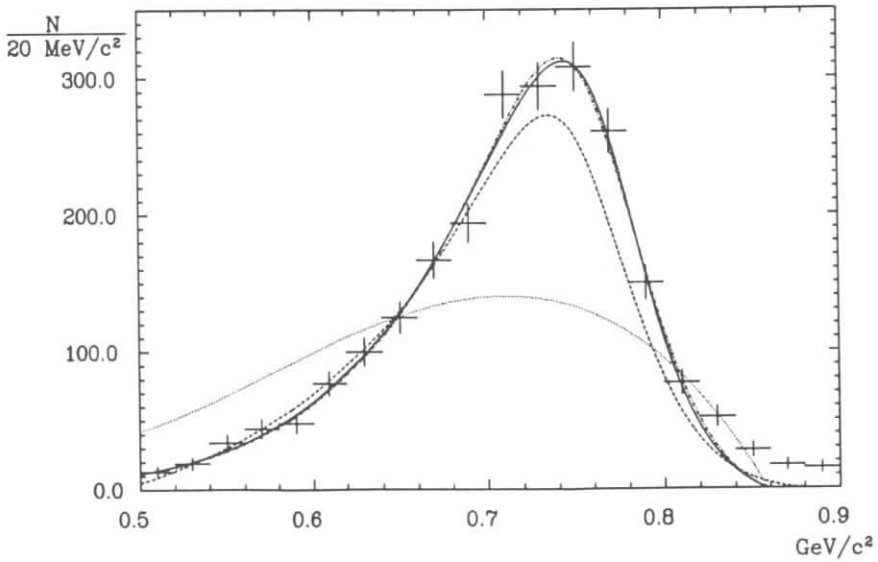

Figure 4.15: The $m(X^+X^-)$ distribution after applying all cuts and requiring 0.87 GeV $< m(\pi^+\pi^-\gamma) <$ 1.03 GeV. The dotted line shown is the distribution expected from three-particle phase space alone. The dashed line is the Monte Carlo distribution discussed in section 4.3, while the solid and dash-dotted lines are the results of the fits with ρ/ω interference and a free ρ shape, respectively.

		Systematic error [%]	
Type	Source	1986 analysis	1989 analysis
e^+e^- luminosity		5.0	3.0
$\gamma\gamma$ luminosity	integration	0.3	0.3
	radiative corrections	2.0	2.0
	energy scaling	0.1	0.1
trigger efficiency	pre-trigger	2.3	2.3
	shower simulation	1.3	1.3
	LTF efficiency	1.4	1.4
	LTF simulation	6.1	4.6
acceptance	calorimeter	2.0	2.0
	drift chamber	2.0	2.0
	MC statistics	1.0	1.0
	noise correction	1.5	0.7
fitting	standard deviation	4.0	4.3
	MC studies	1.2	1.2
	tuning/binning	1.6	1.6
ρ shape		3.3	2.1
Total		10.8	8.9

Table 4.4: Systematic error of the η' analysis.

$m(\pi^+\pi^-)$ in the region of the ω mass (0.782 GeV/c²). A goodness-of-fit test yields a χ^2 of 55.6 for 15 degrees of freedom, using the interval $0.5 < m(\pi^+\pi^-) < 0.82$ GeV/c². Contributions of higher magnetic multipoles to the matrix element would only worsen the situation. If one frees the parameters of the rho line shape, an excellent fit (with a χ^2 of 8.5/13 d.f.) is found for the values:

$$m(\rho) = (776 \pm 4)\ \text{MeV}$$
$$\Gamma(\rho) = (140 \pm 6)\ \text{MeV}$$

which should be compared to the standard values [2]:

$$m(\rho) = (770 \pm 4)\ \text{MeV}$$
$$\Gamma(\rho) = (153 \pm 2)\ \text{MeV}.$$

When the acceptance calculation is repeated using the fitted values there is a $(1.1 \pm 0.1)\%$ decrease.

It has been suggested [172] that the discrepancy in the $\pi^+\pi^-$ mass spectrum is the result of interference with the channel $\eta' \to \omega\gamma \to \pi^+\pi^-\gamma$. As this branching ratio is very small, $(0.051 \pm 0.01)\%$, the interference term ($\propto \sqrt{B_{\rho\gamma}B_{\omega\gamma}}$) dominates the effect. The effect is also enhanced by a factor of approximately $\sqrt{\Gamma_\rho/\Gamma_\omega}$, as it is concentrated in a narrow mass interval. The interference between the ρ and ω matrix elements was described by:

$$\frac{dN}{dm_{12}} \propto E^3_{\gamma;\eta'} P_{\pi^\pm;\pi^+\pi^-} |M_\rho + Ce^{i\phi} M_\omega|^2$$

where:

$$\begin{aligned} C^2 &= \frac{Br(\eta' \to \omega\gamma) \cdot Br(\omega \to \pi^+\pi^-\gamma)}{Br(\eta' \to \rho\gamma) \cdot Br(\omega \to \pi^+\pi^-\gamma)} \cdot \frac{I_\rho}{I_\omega} \\ &= 0.027 \pm 0.005 \\ I_i &= \int_{2m(\pi^\pm)}^{m(\eta')} E^3_{\gamma;\eta'} P_{\pi^\pm;\pi^+\pi^-} |M_i|^2. \end{aligned}$$

This expression fits the experimental data with a χ^2 of 7.7 for 13 degrees of freedom. The parameters from the ρ/ω interference fit are:

$$\begin{aligned} Br(\eta' \to \omega\gamma) \cdot Br(\omega \to \pi^+\pi^-\gamma) &= 0.0007 \pm 0.0005 \\ \phi &= (28 \pm 13)^\circ, \end{aligned}$$

in reasonable agreement with a measurement of $\rho\omega$ interference in $J/\psi \to \omega\eta, \rho\eta$ [173], where $\phi = (46 \pm 15)^\circ$. The strength of ω production is consistent with that expected within the large errors. The acceptance decreases by $(1.3 \pm 0.1)\%$ on repeating the calculation with this matrix element. This implies a correction to the two-photon width of $(+1.2 \pm 0.3)\%$, taking the average of the correction using a free ρ shape, and that calculated with the ρ/ω interference. An additional systematic error of 2.1% is estimated by comparing the acceptance calculated with our matrix element (equation 4.2) with that calculated using the matrix element of the PLUTO analysis [81].

To check the estimate of the systematic error presented above, the sensitivity of the result to variations of the selection cuts, trigger requirements, experimental history,

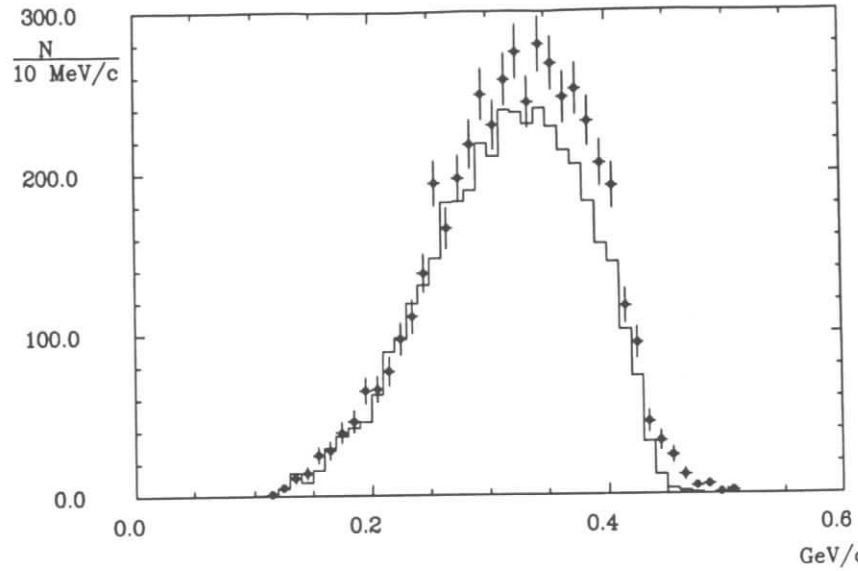

Figure 4.16: The $P_\perp(\pi^\pm)$ distribution for data (points with error bars) and Monte Carlo (histogram). Only events surviving all analysis cuts, with 0.87 GeV $< m(\pi^+\pi^-\gamma) <$ 1.03 GeV, have been used.

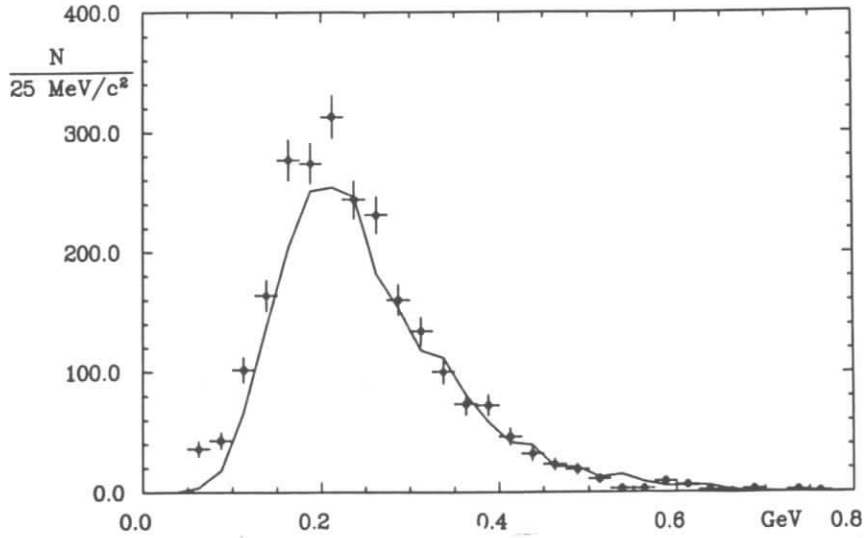

Figure 4.17: The E_γ distribution for data (points with error bars) and Monte Carlo (histogram). Only events surviving all analysis cuts, with

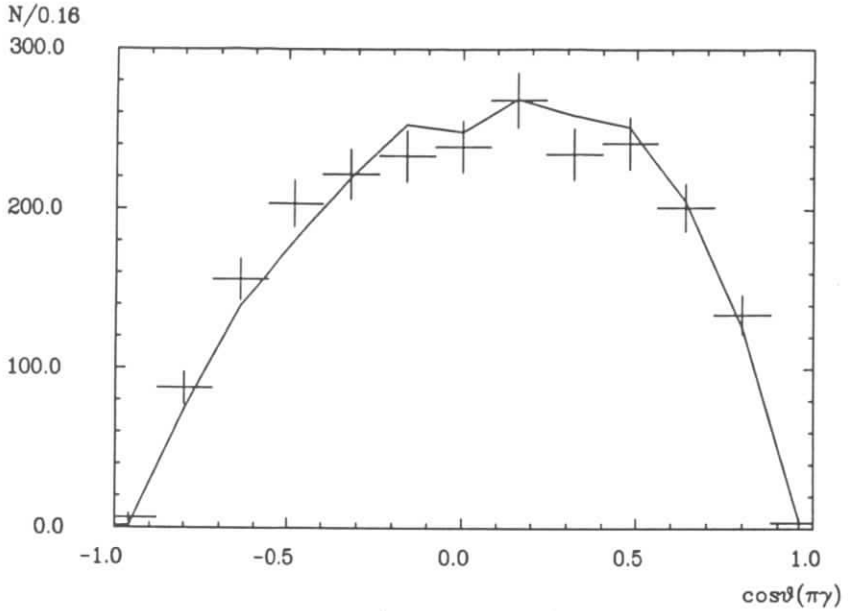

Figure 4.18: The distribution of the $\pi^{\pm}\gamma$ angle in the $\pi^+\pi^-$ center of mass system. This distribution is background subtracted (unlike 4.16-17) which is only possible because the background shape is independent of the final-state mass.

and fiducial region has been studied (tables 4.4-6). The $\Gamma_{\gamma\gamma}$ measurement is reasonably stable with respect to these variations. The most serious systematic shifts occur on strengthening the restrictions that affect the $m(\pi^+\pi^-)$ distribution, i.e., cuts on $m(\pi^+\pi^-)$, $P_\perp(\pi^\pm)$ and the exclusive CPPT trigger subset which is populated by events below the CMATRIX $P_\perp$ threshold. This effect is due to the discrepancy between the theoretical and experimental matrix elements, which also leads to disagreement in the E_γ and $P_\perp(\pi^\pm)$ distributions (figures 4.16-4.17). The theoretical matrix element overestimates the contribution of the the tails of the $\pi^+\pi^-$ mass distribution, so that the acceptance of the cut is underestimated, and the result shifted to greater values. This shift is the principal reason why no restriction has been placed on the $m(\pi^+\pi^-)$ distribution in the analysis. Finally, figure 4.18 shows the distribution of the $\pi^{\pm}\gamma$ decay angle in the $\pi^+\pi^-$ center of mass system; this is in good agreement with the $\sin^2\theta$ matrix element expected if the η' meson is a pseudoscalar.

In conclusion, the production of η' mesons in $\gamma\gamma$ collisions and the dynamics of their decay have been studied with high precision. Theoretical implications of this measurement will be discussed in chapter 6.

Subset	$n(\eta')$	$\Gamma_{\gamma\gamma} \cdot Br(\pi^+\pi^-\gamma)$ [keV]
Experiment 2	$240 \pm 15 \pm 31$	$0.99 \pm 0.06 \pm 0.16$
Experiment 4	$535 \pm 23 \pm 69$	$1.20 \pm 0.05 \pm 0.19$
Experiment 5	$975 \pm 31 \pm 80$	$1.31 \pm 0.04 \pm 0.16$
Experiment 6	$494 \pm 22 \pm 42$	$1.26 \pm 0.06 \pm 0.16$
CPPT only	$138 \pm 12 \pm 31$	$0.94 \pm 0.08 \pm 0.22$
CMATRIX only	$1113 \pm 33 \pm 61$	$1.25 \pm 0.04 \pm 0.12$
CPPT and CMATRIX	$965 \pm 31 \pm 58$	$1.24 \pm 0.04 \pm 0.12$
average $\pm$ standard deviation		1.17 ± 0.14

Table 4.5: The results of systematic studies for the η' analysis are shown. The data have been divided into subsets defined by experiment or trigger requirement.

$\lvert\cot\theta\rvert <$	$P_\perp(\pi^\pm) >$ [GeV]	$n(\eta')$	$\Gamma_{\gamma\gamma} \cdot Br(\pi^+\pi^-\gamma)$ [keV]
1.333	0.100	$2291 \pm 48 \pm 109$	$1.25 \pm 0.03 \pm 0.11$
1.125	0.100	$2218 \pm 47 \pm 129$	$1.23 \pm 0.03 \pm 0.12$
1.000	0.100	$1965 \pm 44 \pm 102$	$1.25 \pm 0.03 \pm 0.11$
0.900	0.100	$1708 \pm 41 \pm 76$	$1.27 \pm 0.03 \pm 0.11$
1.333	0.100	$2291 \pm 48 \pm 109$	$1.25 \pm 0.03 \pm 0.11$
1.333	0.150	$2377 \pm 49 \pm 86$	$1.32 \pm 0.03 \pm 0.11$
1.333	0.200	$2232 \pm 47 \pm 66$	$1.35 \pm 0.03 \pm 0.11$
1.333	0.250	$1706 \pm 41 \pm 80$	$1.40 \pm 0.03 \pm 0.12$
1.333	0.300	$724 \pm 27 \pm 53$	$1.30 \pm 0.05 \pm 0.14$
average $\pm$ standard deviation			1.30 ± 0.05

Table 4.6: The results of systematic studies for the η' analysis are shown. The fiducial region used for the analysis has been varied.

Cut type	value	$n(\eta')$	$\Gamma_{\gamma\gamma} \cdot Br(\pi^+\pi^-\gamma)$ [keV]
ρ mass range	0.00-4.00	$2291 \pm 48 \pm 109$	$1.25 \pm 0.03 \pm 0.11$
[GeV]	0.59-0.86	$2437 \pm 49 \pm 63$	$1.46 \pm 0.03 \pm 0.12$
	0.63-0.86	$2241 \pm 47 \pm 53$	$1.47 \pm 0.03 \pm 0.12$
	0.00-0.83	$2334 \pm 48 \pm 248$	$1.29 \pm 0.03 \pm 0.17$
$P_\perp(\pi^+\pi^-)$	0.025	$2762 \pm 53 \pm 200$	$1.33 \pm 0.03 \pm 0.14$
[GeV/c]	0.050	$2062 \pm 45 \pm 93$	$1.01 \pm 0.02 \pm 0.09$
	0.075	$2272 \pm 48 \pm 286$	$1.15 \pm 0.02 \pm 0.17$
	0.100	$2291 \pm 48 \pm 109$	$1.25 \pm 0.03 \pm 0.11$
	0.150	$2334 \pm 48 \pm 248$	$1.20 \pm 0.03 \pm 0.10$
$P_\perp(\|\|\gamma)$	0.050	$1639 \pm 40 \pm 47$	$1.17 \pm 0.03 \pm 0.09$
[GeV/c]	0.100	$2291 \pm 48 \pm 109$	$1.25 \pm 0.03 \pm 0.11$
	0.150	$2424 \pm 49 \pm 201$	$1.24 \pm 0.03 \pm 0.14$
	0.200	$2453 \pm 50 \pm 310$	$1.23 \pm 0.03 \pm 0.18$
$P_\perp(\perp\gamma)$	0.025	$1862 \pm 43 \pm 63$	$1.23 \pm 0.03 \pm 0.10$
[GeV/c]	0.050	$2291 \pm 48 \pm 109$	$1.25 \pm 0.03 \pm 0.11$
	0.100	$2485 \pm 50 \pm 195$	$1.20 \pm 0.02 \pm 0.13$
	0.150	$2605 \pm 51 \pm 198$	$1.22 \pm 0.02 \pm 0.13$
$\cos\theta_{X\gamma}$	0.7	$2086 \pm 46 \pm 114$	$1.20 \pm 0.03 \pm 0.11$
	0.8	$2291 \pm 48 \pm 109$	$1.25 \pm 0.03 \pm 0.11$
	0.9	$2459 \pm 50 \pm 168$	$1.30 \pm 0.03 \pm 0.13$
E_γ	0.050	$2291 \pm 48 \pm 109$	$1.25 \pm 0.03 \pm 0.11$
[GeV]	0.075	$2330 \pm 48 \pm 72$	$1.28 \pm 0.03 \pm 0.10$
	0.100	$2320 \pm 48 \pm 102$	$1.29 \pm 0.03 \pm 0.11$
	0.150	$2003 \pm 45 \pm 162$	$1.25 \pm 0.03 \pm 0.10$
average $\pm$ standard deviation			1.25 ± 0.10

Table 4.7: The results of systematic studies for the η' analysis are shown. The specified cut is varied while all other cuts are maintained at their standard values. The main cause of variation in the systematic error is the quality of the fits used; this is strongly dependent on the quantity of background introduced or rejected by changing the various cuts.

Chapter 5

Analysis of $\gamma\gamma \to K^+K^-$

This chapter describes the ARGUS analysis of the K^+K^- final state produced in two-photon collisions[1]. The first three sections of the chapter describe the separation of the signal, acceptance calculation, and systematic checks. The measurement of the topological cross section for $\gamma\gamma \to K^+K^-$ is discussed in the fourth section. This measurement makes the single assumption that the angular momentum of the intermediate state is less than three. Results obtained with the requirement of helicity two dominance of the J=2 partial wave, a more restrictive assumption, are also presented. The production of the standard tensor ($J^{PC} = 2^{++}$) mesons $f_2(1270)$, $a_2(1320)$ and $f_2'(1525)$ contributes to the final state. As each of these mesons has three two-photon widths (including the helicity one contribution which can be observed only at high values of $P_\perp(K^+K^-)$ or q^2), which can interfere with each other and the continuum contribution to each helicity wave, the analysis is quite complex. Thus simplifying assumptions must be introduced. The ARGUS data sample is the largest currently available and the resonance analysis, described in the fifth section of the chapter, is more general than its predecessors [112]-[116]. The effect of interference with the K^+K^- continuum is included for the first time, and the resonance interference parameters are also determined for the first time in the charged $K\bar{K}$ final state. The final sections of the chapter describe upper limits obtained for production of the $\theta/f_2(1720)$ and X(2230) mesons and evidence for a small helicity one contribution to the total cross section.

[1] A paper [106] describing this analysis has been accepted for publication in Zeitschrift für Physik C.

5.1 Selection of $\gamma\gamma \to K^+K^-$ Events

The data sample used for this analysis represents an integrated luminosity of (281.5 ± 8.4) pb^{-1} and is identical to the extended data sample used in the η' analysis described in the previous chapter. The preliminary selection algorithm used to separate $\gamma\gamma$ events with charged two-prong topologies, including the rejection of beam-gas and cosmic ray events, is also the same. All events containing two oppositely charged tracks within the solid angle $-1.2 < \cot\theta < 1.2$, and with $P_\perp > 0.15$ GeV/c are considered as K^+K^- candidates. These restrictions are slightly stronger than those used in the generation of the Monte Carlo events used in the acceptance calculation and correspond approximately to the fiducial region of the trigger. In this respect, the $\cot\theta$ requirement is particularly weak, so as to maximize sensitivity to the helicity structure of the final state. These events are analyzed with a kaon mass hypothesis for both tracks. No additional charged tracks in the the detector are allowed unless they are consistent with decays in flight or artifacts from imperfect drift chamber reconstruction. No photon signals arising from clusters of shower counters are allowed with energies of more than 50 MeV. Photon candidates from isolated single shower counter hits are treated as noise. Excluding these events from the analysis, after the appropriate correction for topology depletion from calorimeter noise and inefficiencies in the calorimeter reconstruction, does not change the results significantly. The combination of cluster noise in the calorimeter and cluster calorimeter signals from charged particles unmatched to their drift chamber tracks produces a topology depletion of $(9.2 \pm 2.3)\%$.

The most critical element in extracting a signal for K^+K^- production is the rejection of misidentified events from two-photon production of e^+e^-, $\mu^+\mu^-$, and $\pi^+\pi^-$ final states. The first two of these processes contribute $1.6 \cdot 10^6$ events to the two-prong data sample, while the K^+K^- channel contributes $O(10^3)$ events. Particle identification is therefore critical. The tails of the resolution functions involved must be well understood if one is to control these backgrounds. Particle identification was derived from the specific ionization measurement (dE/dx) in the drift chamber and the time of flight (ToF) determination from the scintillation counters. For each charged particle, the particle

identification information from these detector elements is used to calculate χ^2 values for several different mass hypotheses. The average of these individual χ^2 distributions, calculated for independently identified data samples (e.g. pions from cleanly separated K^0_s vertices), has been normalized to unity to compensate for imperfections in the treatment of the detector resolution in the χ^2 calculation. The dE/dx χ^2 values from both particles in an event are summed and used to calculate a likelihood ratio:

$$P_\alpha = \frac{f_\alpha \, e^{-x_\alpha^2/2}}{\sum_\beta f_\beta \, e^{-x_\beta^2/2}}, \quad (\alpha, \beta = e^+e^-, \mu^+\mu^-, \pi^+\pi^-, K^+K^-, p\bar{p}). \tag{5.1}$$

This likelihood ratio applies to the the entire event, as opposed to that used in the standard particle identification (chapter 2), where likelihood ratios are calculated for single tracks. The difference between this result and a simple product of individual track likelihood ratios rests on the assumption that no mixed-flavour final states contribute. This assumption is impossible to make in any type of inclusive analysis and is equivalent to assuming that any backgrounds from incompletely reconstructed two-photon, e^+e^- annihilation, or $e^+e^- \to \tau^+\tau^-$ events are small. The relative abundances, f_α, used in the calculation of the likelihood ratio were: $f_{e^+e^-} = 5.0$, $f_{\mu^+\mu^-} = 5.0$, $f_{\pi^+\pi^-} = 1.0$, $f_{K^+K^-} = 0.04$, $f_{p\bar{p}} = 0.01$. These were estimated from previous results in two-photon interactions. The analysis is insensitive to the exact values of these abundances.

As a preliminary step in the identification process, it was required that the K^+K^- likelihood ratio, calculated using dE/dx information only, be in excess of 0.1%. At this point the signal was still swamped by background from the two-photon QED final states e^+e^- and $\mu^+\mu^-$. As discussed in chapter 3, these processes have been simulated using the event generator of Daverveldt [29], the ARGUS detector simulation [161], and the author's trigger simulation. The QED contribution that survived the dE/dX likelihood requirement represented a rejection power of 40:1. For final-state masses above 1.7 GeV/c^2 (with both particles in each event assigned a kaon mass), where no significant contribution from misidentified $\gamma\gamma \to \pi^+\pi^-$ events is expected, the data were well described by the QED simulation alone.

The remaining QED background was rejected by making restrictions on the particle masses as derived from the ToF information. A scatter plot of the two m^2_{ToF}

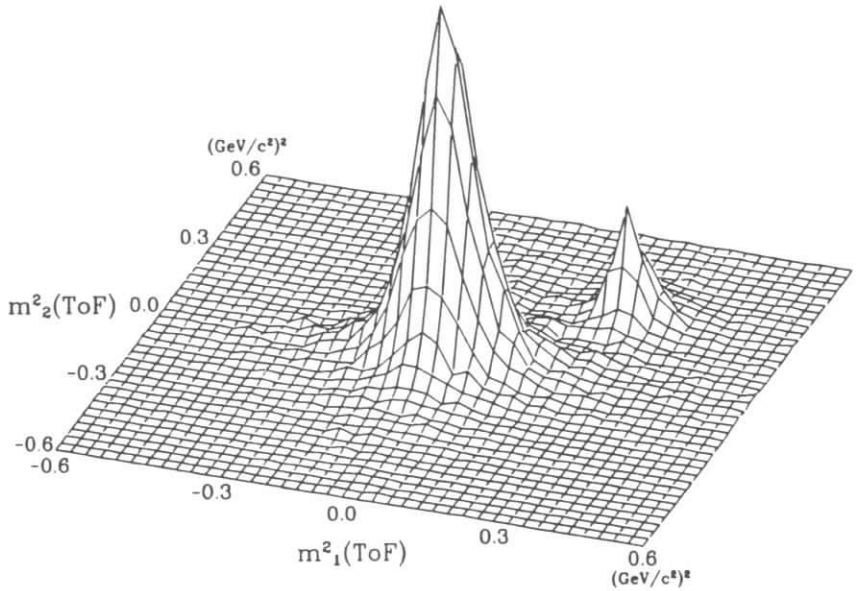

Figure 5.1: The signal in the ToF mass^2 plane after requiring a dE/dx K^+K^- likelihood ratio of at least 0.1%. The axes are the masses^2 for each of the two particles in an event as determined from momentum and ToF measurements. Enhancements are seen near the origin (two-photon production of e^+e^-, $\mu^+\mu^-$, and $\pi^+\pi^-$ pairs) and in the region expected to be populated by kaon pair production.

from each event is shown in figure 5.1. Enhancements are visible around the points $C_{++} = (m^2_{K+}, m^2_{K-})$ and (0,0) corresponding to signals for K^+K^- production and QED background, respectively. The 1,556 events within a circle of radius $r_{KK} = ((m^2_{ToF:X+} - m^2_{K+})^2 + (m^2_{ToF:X-} - m^2_{K-})^2)^{1/2} < 0.15$ (GeV/c^2)^2 about the point C_{++} were selected as K^+K^- candidates. As the ToF m^2 resolution is symmetric, the background from pairs of lighter particles can be estimated from regions of the same size around the three symmetric points: $C_{+-} = (+m^2_{K+}, -m^2_{K-})$, $C_{--} = (-m^2_{K+}, -m^2_{K-})$ and $C_{-+} = (-m^2_{K+}, +m^2_{K-})$. These regions should contain approximately equal contributions from the two-photon production of e^+e^-, $\mu^+\mu^-$ and $\pi^+\pi^-$ pairs, since the ToF m^2 resolution, 0.07 (GeV/c^2)^2 for a momentum of 0.7 GeV/c, is larger than the m^2's of the particles contributing to the background (less than 0.02 (GeV/c^2)^2). The events in these regions are a useful background sample. The average of the three populations is 12 ± 2

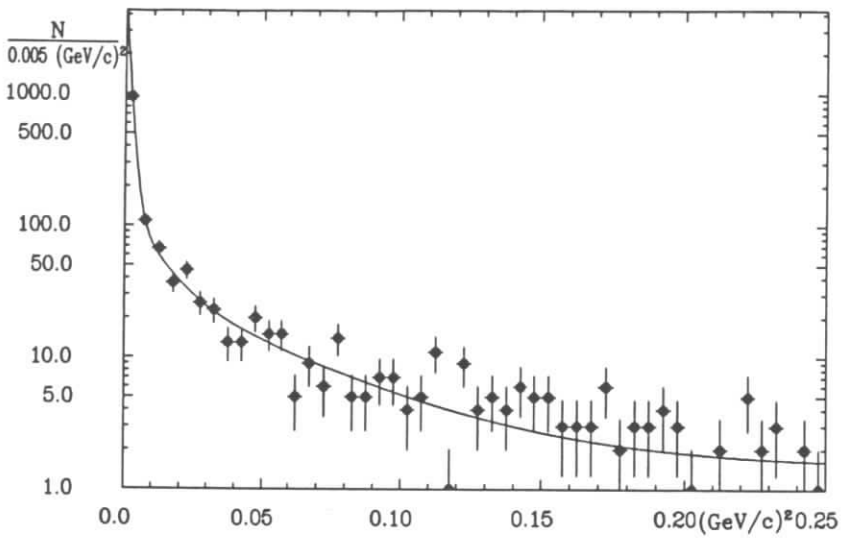

Figure 5.2: The transverse momentum distribution for K^+K^- data (points with error bars). The curve shown is the Monte Carlo distribution weighted with the cross section from resonance fit 1B.

events for final-state masses less than 1.8 GeV/c^2. The corresponding estimate from the Monte Carlo simulation is 16 ± 4, in good agreement. On rejecting any events with high transverse momentum or hits in the muon chambers, 7 ± 2 events remain in the background samples, and 13 ± 7 events survive in the QED Monte Carlo sample. As the muon chamber threshold for a misidentified muon pair corresponds to $m(K^+K^-) > 1.7$ GeV/c, muons from kaon decays in the material of the shower counters or flux return yoke do not appreciably affect the analysis. No significant contribution is expected from $\tau^+\tau^-$ production, which is suppressed by particle identification and the kinematics of the τ decay. The presence of misidentified events from $\tau^+\tau^- \to K^\mp l^\pm \nu_\tau \bar{\nu}_\tau \bar{\nu}_{l^\pm}$ where $l = e, \mu$, or $\tau^+\tau^- \to K^\mp \pi^\pm \nu_\tau \bar{\nu}_\tau$, would produce an excess of events in regions C_{-+} and C_{+-}, which has not been observed. An alternate particle identification method, requiring a likelihood ratio of at least 10%, as calculated using the sum of dE/dx and ToF χ^2 values, yields consistent results and has been used in the estimation of the systematic error.

The $e^\pm$ in the reaction $e^+e^- \to e^+e^-K^+K^-$ are scattered at very small angles. The polar angles of these leptons were restricted to be less than 20° by rejecting all events in which they were observed (anti-tagging); this is implicit in the combination of the two-prong topology and K^+K^- identification requirements. The transverse momentum of the K^+K^- pair was required to be less than 0.2 GeV/c to ensure that the photons were nearly real. The average photon q^2 with these cuts is 0.004 $(GeV/c)^2$ and is insensitive to details of the q^2 dependence of the cross section. The situation is equivalent to that described in the η' analysis, where the transverse momentum requirement suppresses any sensitivity to the q^2 evolution of the meson form factor. These requirements also ensure that only the contributions of helicities zero or two need be considered in the analysis. The helicity one contribution is suppressed by a factor $\sim q^2/m^2(K^\pm)$. Figure 5.2 shows the transverse momentum distribution of the selected events, compared to a Monte Carlo estimate using a GVDM propagator [39]; they are in excellent agreement. After the transverse momentum cut, 1,262 events remain.

The resulting K^+K^- invariant mass distribution is shown in figure 5.3. The f_2 and a_2 mesons appear as a combined peak and there is a clear signal for the f_2'. Also shown is the QED background distribution estimated from the populations of the the regions $C_{\pm-}$ and C_{-+} in the ToF plane. The QED background is significant only for K^+K^- invariant masses larger than 1.8 GeV/c^2, well above the region of interest.

5.2 Acceptance Calculation

In order to calculate the acceptance, a Monte Carlo program was used to simulate the reaction $e^+e^- \to e^+e^-K^+K^-$. The program used the exact luminosity functions for transverse photons [45], a constant differential $\gamma\gamma$ cross section, and was corrected for the beam energy distribution of the data using the formula of Low [24], as described in the previous chapter. 361,032 Monte Carlo events were generated with K^+K^- masses between 1.0 and 2.5 GeV/c^2. The convolution of the two-photon luminosity with a constant cross section of one nanobarn was calculated to be 5.960 ± 0.12 pb. A 2% estimate of the effect of radiative corrections has been included in the error in analogy to the η' calculation [85]. Of these events, 24.1% were passed to SIMARG after requiring

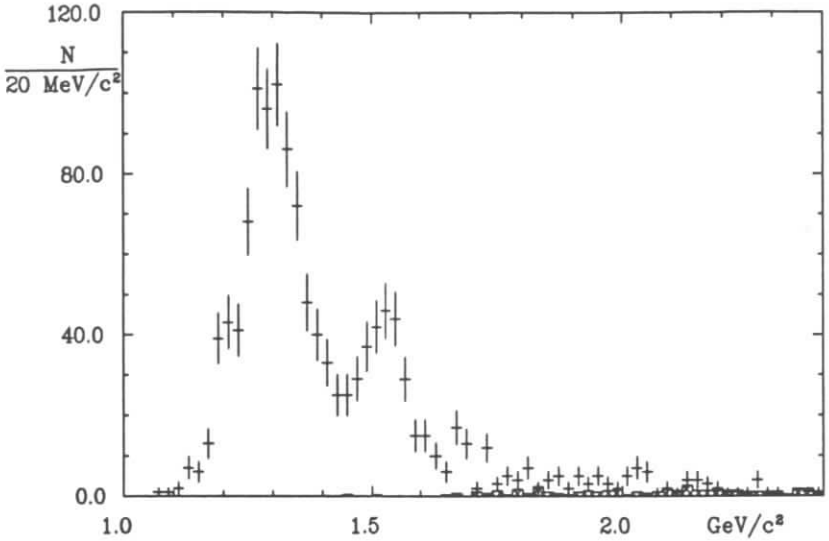

Figure 5.3: The K^+K^- spectrum after requiring a dE/dx K^+K^- likelihood ratio of at least 0.1% and a distance of less than 0.15 $(GeV/c^2)^2$ from the $(m^2_{K^+}, m^2_{K^-})$ point in the ToF plane. The shaded histogram is the background from two-photon QED channels, as estimated from similar cuts centered on the points: $(m^2_{K^+}, -m^2_{K^-})$, $(-m^2_{K^+}, m^2_{K^-})$ and $(-m^2_{K^+}, -m^2_{K^-})$.

that the K^+K^- vectors be close to the fiducial region necessary for the trigger ($P_\perp >$ 0.1 GeV/c, and $|\cot\theta| < 1.333$). In turn, 97.5% of these events were successfully reconstructed, survived the lowest level of data selection (EXPDST), and were processed by the TRIGGR simulation. The average efficiency of reconstruction, fiducial region cuts, and triggering was found to be 11.2%. The acceptance at various steps in the calculations is shown in figure 5.4.

In the analysis of two-photon collisions, knowledge of the acceptance for a final state only allows one to extract a cross section for $e^+e^- \to e^+e^-X$. A more useful quantity is the sensitivity, the convolution of the acceptance and $\gamma\gamma$ luminosity normalized so that it represents the number of events expected in a given $W_{\gamma\gamma}$ and final-state phase-space region per unit of $\gamma\gamma$ cross section. This quantity, corrected for topology depletion, is

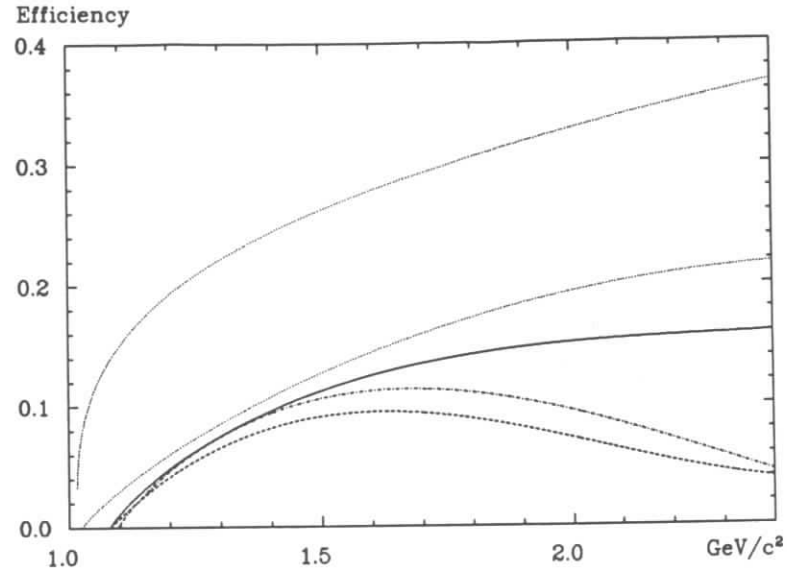

Figure 5.4: The acceptance for a K^+K^- final state with $\{JM\} = \{00\}$ is shown as a function of the invariant mass of the final state. The top three curves represent the application of the following requirements in series: preliminary fiducial region $|\cot\theta| < 1.33$, $P_\perp(K^\pm) > 0.1$ GeV/c; geometric trigger acceptance; trigger and reconstruction efficiency. The lower two curves represent the additional requirement of a dE/dX + ToF χ^2 likelihood ratio of more than 10% (dot-dashed), and a dE/dX χ^2 likelihood ratio of 0.1% in addition to a ToF r_{KK} cut of less than 0.15 $(GeV/c^2)^2$ (dashed).

plotted in figure 5.5 as a function of mass and the angle between the e^+e^- collision axis and K^+K^- decay axis in the $\gamma\gamma$ center of mass system.

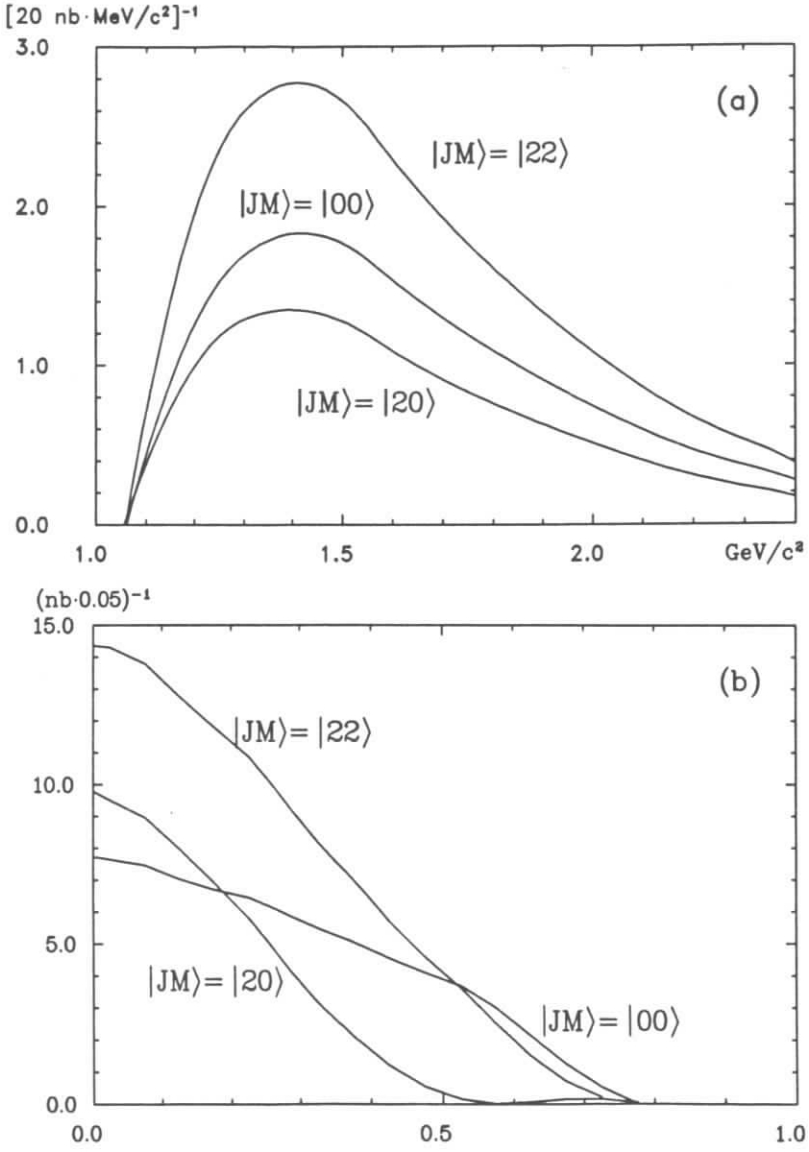

Figure 5.5: Sensitivity for the K^+K^- final state as a function of (a) $W_{\gamma\gamma}$, and (b) $\cos\theta$ for each partial wave, $\{JM\} = \{22\}$, $\{20\}$, and $\{00\}$.

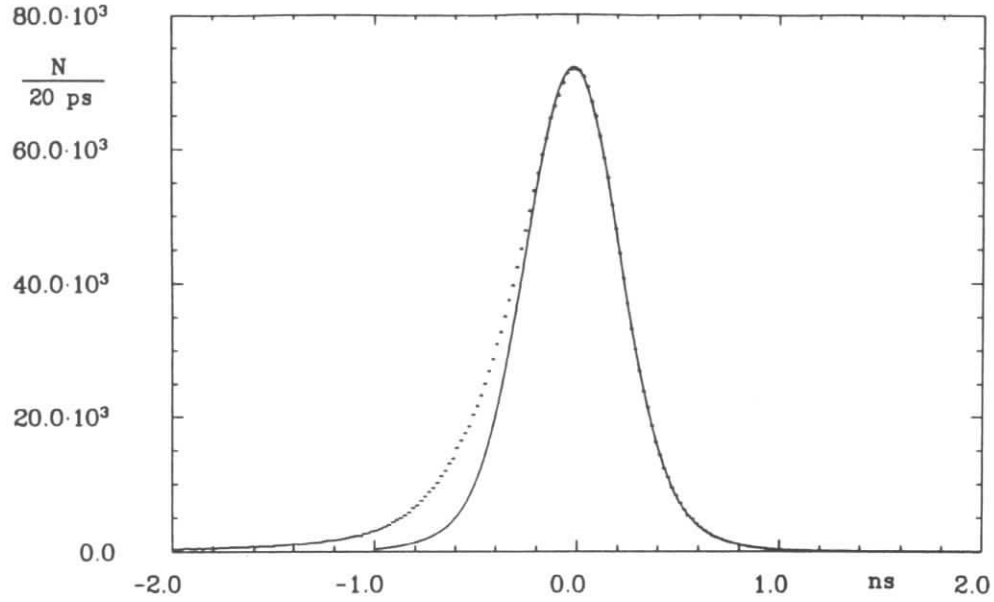

Figure 5.6: ToF distribution for all $\gamma\gamma$ two-prong events. The double Gaussian fit shown is limited to the region $\tau_{\mathrm{ToF}} > 0.2$ ns.

5.3 Systematic Error

The systematic error in the normalization of the acceptance is 8.4%. Most contributions to this uncertainty are similar to those of the η' analysis. The systematic error can be broken down into contributions due to uncertainties in the particle identification efficiency (±5.0%); trigger simulation, $\gamma\gamma$ luminosity calculation, event reconstruction and Monte Carlo simulation (±5.7%); contributions from QED events (±2.0%), and luminosity measurement (±3.0%). For K^+K^- invariant masses above 1.8 GeV/c², there is an additional uncertainty of ±10% from subtraction of the background from QED two-photon processes. The uncertainty associated with the LTF efficiency calculation (3.0%) is less than that of the η' analysis because the kaons have higher transverse momenta than the pions from the η' decay. Systematic variations of the $P_\perp$ and $\cot\theta$ restrictions produce variations within the systematic error calculated.

The systematic uncertainty associated with the particle identification is estimated

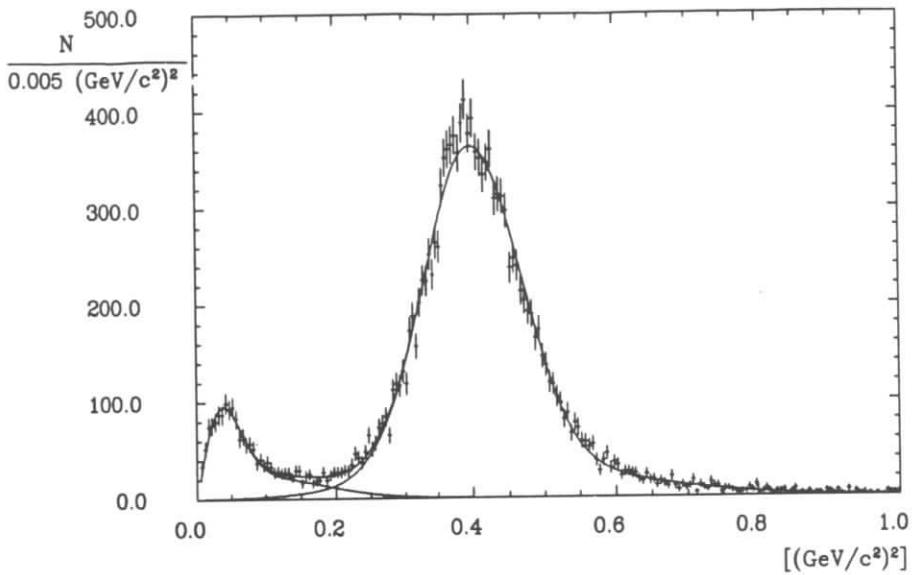

Figure 5.7: Distribution of $r_{KK} = ((m^2_{ToF;X^+} - m^2_{K^+})^2 + (m^2_{ToF;X^-} - m^2_{K^-})^2)^{1/2}$ for events with the 0.1% dE/dX likelihood cut. The curves shown are fits to the distribution using line shapes consisting of double Gaussians multiplied by r_{KK}.

from studies of the dE/dX and ToF resolutions. The inefficiency and related error from requiring the presence of particle identification information (i.e. a ToF counter hit and enough drift chamber energy loss signals to calculate a truncated mean) is small because of the trigger requirements. The efficiency of the dE/dX cut is better than 99% over most of the mass region, so this contribution to the systematic error should be less than the inefficiency. The use of χ^2 parameters in particle identification cuts has the benefit that the efficiency calculated is quite robust so long as the χ^2 values are well normalized. The disadvantage is that any contamination of the signal is difficult to estimate if the shape of the resolution distribution is not studied in detail. This is the reason the time of flight restrictions were made on the r_{KK} parameter instead of a χ^2.

The time of flight resolution used initially by the SIMARG simulation was an underestimate. To determine this ToF resolution directly from the data sample used in the analysis, the time of flight was calculated, assuming m = 0, for all $\gamma\gamma \to X^+X^-$

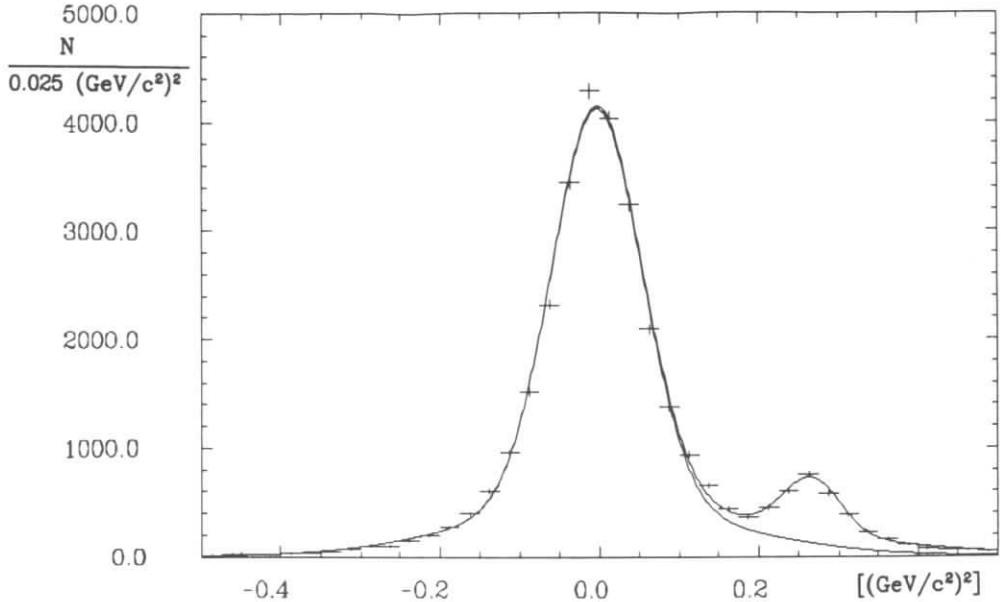

Figure 5.8: ToF m($K^\pm$) distribution for events with the 0.1% dE/dX likelihood cut. The fits shown consist of two double Gaussians.

events passing the topological restrictions required for the K^+K^- sample but with no identification requirement. The contribution of muon and pion pairs skews this distribution slightly to negative values so only the peak and positive part of the distribution ($\tau_{ToF} > -200$ ps) could be used to calculate the resolution. The reliability of this approximation was checked with the Monte Carlo $\gamma\gamma \to l^+l^-$ sample ($l = e, \mu$). The ToF distribution was fitted with a double Gaussian with resolution parameters:

$$(80 \pm 1)\% \quad (220 \pm 2) \text{ ps}$$
$$(20 \pm 1)\% \quad (388 \pm 6) \text{ ps}$$

This fit and the ToF distribution are shown in figure 5.6. When these values are corrected for the contribution of error from the drift chamber measurement and the $m^2 = 0$ approximation, the true ToF resolution is found to be:

$$(80 \pm 1)\% \quad (209 \pm 2) \text{ ps}$$
$$(20 \pm 1)\% \quad (309 \pm 6) \text{ ps}$$

The average of these two contributions is the standard 230 ps resolution quoted in the ARGUS detector paper [129]. It is the departure from a single Gaussian that is relevant to this analysis because of the cut made on the ToF mass information. When the measured resolution is used in the Monte Carlo simulations for K^+K^- and the various backgrounds, the r_{KK} distribution seen in the data is reproduced rather well. Similar studies of the dE/dX resolution for cosmic ray muons did not affect the acceptance calculated for the K^+K^- signal, but resulted in a $(40\pm10)\%$ reduction in the contribution of misidentified QED events as estimated by Monte Carlo simulation.

The distribution of r_{KK}, the distance of the measured ToF masses from the (m_{K^+}, m_{K^-}) point in the ToF plane, is shown in figure 5.7 with curves superimposed showing the fitted K^+K^- and QED contributions. These are practically indistinguishable from fits to the Monte Carlo distributions themselves. The efficiency of the r_{KK} cuts made on the fitted K^+K^- contribution (89.9%) is comparable to that calculated using Monte Carlo data ($90.7 \pm 1.4\%$) weighted with the cross section measured as described below. This agreement, and the derived cross sections, are stable for reasonable variations of the r_{KK} cut (between 0.1 and 0.2 $(GeV/c^2)^2$). The value of 0.15 $(GeV/c^2)^2$ was chosen as it is the minimum of the distribution between $r_{KK} = 0$ (where the K^+K^- contribution dominates) and 0.387 $(GeV/c^2)^2$ (where the QED contribution is concentrated). Fits have also been made to the two dimensional ($m^2_{K^+}$, $m^2_{K^-}$) distribution and its projections (figure 5.8), with similar results. The mass of the $K^\pm$ in these fits is shifted to slightly higher values (0.513-0.526 GeV/c^2); this is consistent with the accuracy of the ToF scale [157]. The r_{KK} scale used in the Monte Carlo calculation has been corrected for this effect. Translating this uncertainty in the mass scale into an 11.6% uncertainty in the scale of r_{KK} leads to an additional contribution of 3% to the systematic error. An independent estimate of the sensitivity to the particle identification algorithm can be made by comparing the calculated cross sections using the two identification methods:

1. requiring at least a 10% likelihood ratio using equation 5.1 with $\chi^2 = \chi^2_{dE/dX:K^+} + \chi^2_{dE/dX:K^-} + \chi^2_{ToF:K^+} + \chi^2_{ToF:K^-}$;
2. requiring at least a 0.1% likelihood using equation 5.1 with $\chi^2 = \chi^2_{dE/dX:K^+} + \chi^2_{dE/dX:K^-}$ with a cut on $r_{KK} < 0.15$ GeV/c^2.

The difference between these methods ranges between 3-6%. The variation is dependent on the strength of the cuts and has been traced to the change in the contribution of QED contamination in the sample identified using only χ^2 derived cuts. On combining the various effects discussed, the systematic error in the acceptance of the particle identification algorithm is estimated to be 5%.

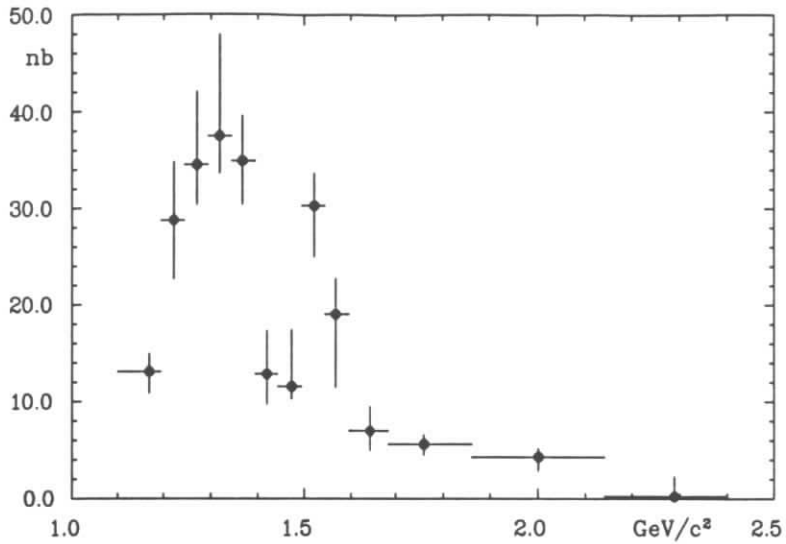

Figure 5.9: The cross section for $\gamma\gamma \to K^+K^-$, assuming only $J < 3$.

5.4 Measurement of the Topological Cross Section

Assuming that contributions from angular momenta higher than 2 are negligible, the full angular distribution can be described as:

$$\frac{d\sigma}{d\Omega} = \sigma_{2\pm2}|Y_{22}|^2 + \sigma_{20}|Y_{20}|^2 + \sigma_{00}|Y_{00}|^2 + 2\sqrt{\sigma_{20}\sigma_{00}}|Y_{00}\overline{Y_{20}}|\cos\zeta \qquad (5.2)$$

The σ_{JM} are cross sections for the partial waves involved while ζ is the relative phase of the 00 and 20 partial waves. As the distributions involved are not linearly independent ($|Y_{20}| = \sqrt{5}|Y_{00}| - \sqrt{6}|Y_{22}|$) one cannot determine all four parameters unambiguously. However, one can still extract the total cross section using a three parameter fit – fixing any one of the four parameters does not restrict the shape of the angular distribution used in the acceptance calculation.

To calculate the topological cross section, the K^+K^- spectrum of figure 5.3 is divided into bins, containing at least 50 events, with a minimum size of 50 MeV/c². As the

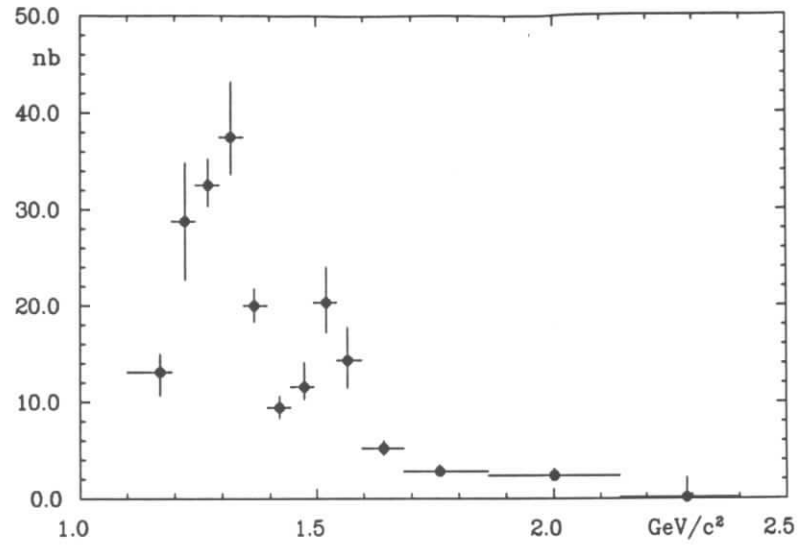

Figure 5.10: The cross section for $\gamma\gamma \to K^+K^-$, assuming only $|JM\rangle = |22\rangle$ and $|JM\rangle = |00\rangle$ contribute.

q^2 of each colliding photon is small, one can reconstruct the angle, θ, between the $\gamma\gamma$ collision axis and the K^+K^- decay axis by assuming that the photons are collinear with the colliding beams (this has a resolution of 0.007 in $\cos\theta$). The angular distribution for the events of each bin is then fitted using equation 5.2 with $\zeta = \pi/2$ and the likelihood function:

$$\log L = \sum_{\text{data}} \log \frac{d\sigma(\cos\theta_i)}{d\Omega} - \sigma_{22}W_{22} - \sigma_{20}W_{20} - \sigma_{00}W_{00}.$$

The W_{JM} are the $|Y_{JM}|^2$ moments of the Monte Carlo sensitivity distributions in each bin. The θ_i are the measured decay angles for each event in the bin. This method avoids the loss of information inherent in fitting binned distributions. The results of the fits are shown in figure 5.9. The errors shown are statistical only (these are the Δ_i' defined in appendix E). If one sets σ_{20} to zero, as expected from helicity two dominance, the cross section in figure 5.10 is obtained. This distribution has slightly smaller errors.

5.5 Extraction of Resonance Parameters

The reaction $\gamma\gamma \to K^+K^-$ is dominated by the production of the $f_2(1270)$, $a_2(1320)$ and $f_2'(1525)$ mesons. In this analysis the contribution of the helicity one $\gamma\gamma$ width is ignored, as it is suppressed by the restriction on the transverse momentum of the final state. Despite this, each of the three mesons still has an independent complex coupling to the $\gamma\gamma$ system for helicities zero and two, so there are, in principle, ten parameters (six $\gamma\gamma$ widths and four relative phases) for the resonant contributions to the final state alone. To complicate matters further, there is no guarantee that the continuum contribution is confined to the helicity zero partial wave. The resonance contribution to the helicity two partial wave may not be added to the continuum incoherently. The matrix element for each helicity contribution to the continuum should then have a free magnitude and phase as a function of the invariant mass of the final state.

The helicity structure and relative phases of the production amplitudes of the tensor mesons are not well known experimentally. However, one expects a ratio between the helicity two to helicity zero components of at least 6:1, simply by comparing the Clebsch-Gordan coefficients for $\langle JM|\lambda_1\lambda_2\rangle = \langle 22|11\rangle$ and $\langle 20|1-1\rangle$ (where the λ_i are the helicities of the colliding photons). Theoretical arguments based on a variety of models [39,47] show that this is a reliable assumption, with pure helicity two being favoured. It is natural to expect interference between the resonance amplitudes and K^+K^- continuum, as significant helicity two contributions are expected in both the Born term and QCD limits [39,174]. Interference effects have been shown to be significant in the $\pi^+\pi^-$ final state [99,107]. In charged kaon pair production, the relative phases of the three resonances are expected to be zero, while in the production of neutral kaon pairs the f_2:a_2 phase is expected to be 180°. These results require only the weak assumptions of approximate SU(3) flavour symmetry and OZI suppression [175].

Previous analyses of the K^+K^- channel [112,113] assumed an incoherent continuum, while analyses of the neutral channel assumed the absence of continuum. It has been suggested that the agreement between the results of the neutral channel analyses, free of the complications of continuum production of K^+K^- pairs, and the charged channel, confirm the incoherent continuum assumption in the latter analyses. However, at the level of statistics of the neutral channel analyses ($\sim$ 8 events in the f_2' region in [115], and 18 in [116]) a significant continuum contribution cannot be ruled out. A continuum cross section which is 10% of the resonant cross section can alter the parameters of the latter at the 30% level!

The assumption of the absence of a continuum contribution to the $\gamma\gamma$ production of neutral kaon pairs, the Born approximation, rests on the fact that there is no electric charge for the photons to couple to. However, if this reasoning were correct one would expect the Born approximation to describe quantitatively the continuum production in the charged final state. This approximation does not work well even for $\pi^+\pi^-$ production, where final-state re-scattering and other strong interaction effects are expected to be less important [39]. Indeed, the Crystal Ball [104,105] and JADE collaborations [89] have both measured significant $\pi^0\pi^0$ production.

In view of these complications, to extract the resonance parameters from the data, we parametrized the cross section as described below. The production, by two real photons, of a single tensor meson with subsequent decay to a K^+K^- pair can be written [39] as:

$$\frac{d\sigma_{\gamma\gamma\to R\to K^+K^-}(W_{\gamma\gamma},\cos\theta)}{d\Omega} = \frac{40\pi}{W_{\gamma\gamma}^2}(|A_0|^2 + |A_2|^2),$$

where $W_{\gamma\gamma}$ is the mass of the kaon pair. The helicity amplitudes are:

$$\begin{aligned} A_0 &= BW(W_{\gamma\gamma})\cdot(W_{\gamma\gamma}/m)^2\cdot(\Gamma_{\gamma\gamma}^{(0)})^{1/2}\cdot Y_{20}(\cos\theta,\phi), \\ A_2 &= BW(W_{\gamma\gamma})\cdot(\Gamma_{\gamma\gamma}^{(2)})^{1/2}\cdot Y_{22}(\cos\theta,\phi). \end{aligned}$$

The relativistic Breit-Wigner amplitude is given by:

$$BW(W_{\gamma\gamma}) = m\sqrt{\Gamma(W_{\gamma\gamma})\cdot Br(K^+K^-)}/(W_{\gamma\gamma}^2 - m^2 + im\Gamma(W_{\gamma\gamma})).$$

Here m is the mass of the tensor meson and $\Gamma(W_{\gamma\gamma})$ its mass-dependent width:

$$\Gamma(W_{\gamma\gamma}) = \Gamma(m)\cdot(k^*(W_{\gamma\gamma})/k^*(m))^5\cdot(m/W_{\gamma\gamma})\cdot(h(W_{\gamma\gamma})/h(m)),$$

where $k^*(W_{\gamma\gamma})$ is the kaon momentum in the tensor meson rest frame and $h(W_{\gamma\gamma})$ is the decay form factor [170], $h(W_{\gamma\gamma}) \propto (9 + 3(k^*r)^2 + (k^*r)^4)^{-1}$. This factor is derived by

treating the decay as non-relativistic quantum mechanical tunnelling from a square-well potential. The effective interaction radius, r, is taken as 1 fm. A 10% variation of this parameter affects the values of the two-photon widths at the 2% level. The product $\Gamma(W) \cdot Br(R \to K^+K^-)$ represents the partial width into K^+K^-, and does not have the same mass dependence as the $\Gamma(W)$ in the denominator of the Breit-Wigner, which represents the total width. Introducing the appropriate mass dependences in the total widths affects the results at the 5% level.

As the K^+K^- mass region under investigation is expected to have contributions from three tensor mesons, $f_2(1270)$, $a_2(1320)$, and $f_2'(1525)$, interference between them must be included. The continuum K^+K^- amplitudes (G_M) are also expected to interfere. This leads to a total amplitude T_M for $\gamma\gamma \to K^+K^-$ for helicity M (zero or two) of:

$$T_M = A_M(f_2) + \exp(i\phi_{f_2:a_2}) \cdot A_M(a_2) + \exp(i\phi_{f_2:f_2'}) \cdot A_M(f_2') + \exp(i\phi_M) \cdot G_M.$$

The two phases $\phi_{f_2:a_2}$ and $\phi_{f_2:f_2'}$ represent the interference between the resonances, while the ϕ_M are the overall phase differences between the resonances and continuum. As the sensitivity to the $\{JM\} = \{20\}$ partial wave is poor, no attempt has been made to measure the $M = 0$ resonance phases.

A complete partial wave analysis would involve the parametrization of both the magnitude and phase of each helicity contribution to the continuum by a series of polynomials. As the data sample is too limited for a complete analysis, certain assumptions had to be made. The most critical of these involves the continuum contribution, the functional form of which is unknown. The results presented below are averages of the results of several fits using different continuum parametrizations:

$$\begin{aligned} W_{\gamma\gamma}^2 \int |G_M|^2 d\Omega &= \alpha(m - m_t)^{2\beta}(1 + \gamma(m - m_t) + \delta(m - m_t)^2 + \epsilon(m - m_t)^3) \\ &= \alpha(\log m/m_t)^\beta (m/m_t)^{-\gamma} \\ &= \alpha(m - m_t)^{2\beta} exp(\gamma(m - m_t) + \delta(m - m_t)^2 + \epsilon(m - m_t)^3) \\ &= \alpha \int B_M(m, \cos\theta, \phi) d\Omega, \end{aligned}$$

where m_t is the production threshold and G_M represents the continuum contribution.

B_M refers to the Born term contribution for helicity M [39]. Several other parametrizations were tried in the fits, including an interpolation of Born term and QCD predictions based on that used in [93], but these consistently yielded likelihoods much worse than fits with the expressions listed above. For each calculation, only those parametrizations that yield reasonable likelihoods (within 15 units of the fit with the maximum value) are used. The systematic error for each result is the sum in quadrature of the standard deviation of the results from these "good" continuum parametrizations, the error from correlations (Δ_i^{corr}, as described in appendix E) and the systematic error from normalization. The continuum phase was assumed to be constant.

To further simplify the analysis it was assumed that the continuum is either entirely coherent ($\{JM\} = \{22\}$) or incoherent ($\{JM\} = \{00\}$) except in the case of fits using a modified Born term. In this parametrization the Born term contribution for each helicity was scaled by a complex constant. However, the magnitude of the helicity zero contribution in these fits was consistently less than 5%. One should note that this is the first analysis to be even this general. The incoherent continuum hypothesis has a smaller likelihood and was included principally to demonstrate consistency with previous analyses that made this assumption. For this reason, the helicity zero resonant contribution was also added incoherently to the continuum in the $\{JM\} = \{00\}$ fits. The masses and widths of the resonances involved were constrained to the world average values [2].

To study the eight remaining parameters describing the amplitudes T_M, the cross-section parametrization discussed above was fitted to the data set used for figure 5.3. The maximum-likelihood method described in appendix E was used. The results of the coherent fits are shown in tables 5.1 and 5.2, while the results of the incoherent fits are shown in tables 5.3 and 5.4. These tables also list the assumptions made in each fit. In fit 1A, the f_2 and a_2 contributions are free and the results are determined using a coherent continuum:

$$\begin{aligned} \Gamma_{\gamma\gamma}(f_2) \cdot Br(f_2 \to K\bar{K}) &= (0.104 \pm 0.007 \pm 0.072) \text{ keV}, \\ \Gamma_{\gamma\gamma}(a_2) \cdot Br(a_2 \to K\bar{K}) &= (0.081 \pm 0.006 \pm 0.027) \text{ keV}, \end{aligned}$$

Fit	$\Gamma_{\gamma\gamma} \cdot Br(K\bar{K})$ [eV]			
	f_2	a_2	f_2', JM = 22	f_2', JM = 20
1A	$104.0 \pm 7.0 \pm 72.0$	$81.0 \pm 6.0 \pm 27.0$	$35.7 \pm 5.5 \pm 9.6$	0
1B	$(130.0^{+34.0}_{-24.0})$	(48.0 ± 10.0)	$31.4 \pm 5.0 \pm 7.7$	0
1C	$(130.0^{+34.0}_{-24.0})$	(48.0 ± 10.0)	$32.2 \pm 4.9 \pm 8.8$	0
1D	$(130.0^{+34.0}_{-24.0})$	(48.0 ± 10.0)	$33.4 \pm 5.6 \pm 11.3$	0
1E	$(130.0^{+34.0}_{-24.0})$	(48.0 ± 10.0)	$27.7 \pm 7.6 \pm 9.3$	$45.0 \pm 6.8 \pm 43.8$
1F	$(130.0^{+34.0}_{-24.0})$	(48.0 ± 10.0)	$26.2 \pm 7.3 \pm 8.7$	$48.5 \pm 7.0 \pm 42.7$
1G	$161.7 \pm 9.1 \pm 49.9$	$81.5 \pm 6.1 \pm 31.5$	$50.5 \pm 6.9 \pm 13.8$	0.0
1H	$(130.0^{+34.0}_{-24.0})$	(48.0 ± 10.0)	$44.7 \pm 6.6 \pm 9.6$	0.0

Table 5.1: Two-photon widths from fits with a coherent continuum. Entries without errors are fixed in the corresponding fits, while values in parentheses are used as constraints. More information on the fits is given below.

Fit	Relative Phases [degrees]			Log Likelihood
	$\phi_{f_2:a_2}$	$\phi_{f_2:f_2'}$	ϕ_2	
1A	0	0	$-122 \pm 7 \pm 14$	66.9
1B	0	0	$-116 \pm 9 \pm 14$	65.8
1C	0°	$-5 \pm 5 \pm 15$	$-91 \pm 14 \pm 27$	66.1
1D	$30 \pm 12 \pm 24$	$32 \pm 13 \pm 26$	$-126 \pm 8 \pm 14$	66.3
1E	0	0	$-108 \pm 8 \pm 17$	66.0
1F	0	$-2 \pm 5 \pm 22$	$-121 \pm 14 \pm 28$	66.3
1G	0	0	0	61.0
1H	0	0	0	57.0

Table 5.2: Phases from fits with a coherent continuum. Entries without errors are fixed in the corresponding fits.

Fit	$\Gamma_{\gamma\gamma} \cdot Br(K\bar{K})$ [eV]			
	f_2	a_2	f_2', JM = 22	f_2', JM = 20
2A	$91.0 \pm 7.0 \pm 27.0$	$126.0 \pm 7.0 \pm 28.0$	$74.9 \pm 8.5 \pm 14.8$	0
2B	$(130.0^{+34.0}_{-24.0})$	(48.0 ± 10.0)	$67.3 \pm 8.1 \pm 15.1$	0
2C	$(130.0^{+34.0}_{-24.0})$	(48.0 ± 10.0)	$57.5 \pm 6.7 \pm 12.7$	0
2D	$(130.0^{+34.0}_{-24.0})$	(48.0 ± 10.0)	$57.9 \pm 7.4 \pm 12.1$	0
2E	$(130.0^{+34.0}_{-24.0})$	(48.0 ± 10.0)	$28.7 \pm 9.0 \pm 10.2$	$121.0 \pm 13.1 \pm 31.6$
2F	$(130.0^{+34.0}_{-24.0})$	(48.0 ± 10.0)	$35.7 \pm 8.7 \pm 11.7$	$80.1 \pm 9.1 \pm 38.2$

Table 5.3: Two-photon widths from fits with an incoherent continuum. Entries without errors are fixed in the corresponding fits, while values in parentheses are used as constraints. More information on the fits is given below.

Fit	Relative Phases [degrees]		Log Likelihood
	$\phi_{f_2:a_2}$	$\phi_{f_2:f_2'}$	
2A	0	0	56.6
2B	0	0	54.6
2C	0	$27 \pm 6 \pm 11$	56.4
2D	$16 \pm 10 \pm 10$	$40 \pm 10 \pm 17$	56.4
2E	0	0	57.1
2F	0	$22 \pm 10 \pm 15$	57.5

Table 5.4: Phases from fits with an incoherent continuum. Entries without errors are fixed in the corresponding fits.

where the phase differences between the resonances were fixed at zero and helicity two dominance was assumed. The result is consistent with the world average values, also derived with the assumption of helicity two dominance [2,42]:

$$\begin{aligned}\Gamma_{\gamma\gamma}(f_2)\cdot \mathrm{Br}(f_2 \to K\bar{K}) &= (0.130^{+0.034}_{-0.024})\ \mathrm{keV},\\ \Gamma_{\gamma\gamma}(a_2)\cdot \mathrm{Br}(a_2 \to K\bar{K}) &= (0.048 \pm 0.010)\ \mathrm{keV}.\end{aligned}$$

This is also demonstrated by the decrease of 1.1 in the likelihood when these world averages are introduced as constraints in fit 1B. The values for the $\gamma\gamma$ widths from reference [42] were used instead of those of [2] as they include some newer results and exclude one that has remained unpublished [95]. The unconstrained results in the incoherent case (fit 2A) are

$$\begin{aligned}\Gamma_{\gamma\gamma}(f_2)\cdot \mathrm{Br}(f_2 \to K\bar{K}) &= (0.091 \pm 0.007 \pm 0.027)\ \mathrm{keV},\\ \Gamma_{\gamma\gamma}(a_2)\cdot \mathrm{Br}(a_2 \to K\bar{K}) &= (0.126 \pm 0.007 \pm 0.028)\ \mathrm{keV}.\end{aligned}$$

There is a likelihood decrease of 2.0 on imposing the world average values as constraints (fit 2B), demonstrating that the incoherent continuum ansatz is less consistent with the known $\Gamma_{\gamma\gamma}$ values for the f_2 and a_2 than a coherent continuum. Together with a likelihood difference of more than 10 between the coherent and incoherent fits with the f_2 and a_2 widths constrained to the world average, this provides strong evidence of a coherent contribution in addition to the resonances. Unfortunately, the quality of the results for the f_2 and a_2 mesons was limited by the difficulty of separating the two merged resonances and by the uncertainty in the continuum contribution. Because of this, the contributions of these two resonances were constrained to the world averages [2,42] to study the f_2' with less uncertainty from the continuum.

The most striking effect of the coherent continuum is a suppression of the $\gamma\gamma$-width of the f_2' of approximately 50% with respect to the incoherent case. The interference term is of the form $A\cos(\phi_R - \phi_2)$ where ϕ_R varies from $-\pi$ to 0 in a counterclockwise sense on traversing the resonance. However, ϕ_2 is determined to be close to $-\pi/2$, so the integral of the interference term is positive. The main effect of the interference term is to change the resonance shape (figures 5.11 and 5.12). In fits E and F an additional

incoherent $\{JM\} = \{20\}$ term is allowed. A large change occurs because of the absence of interference and the lower sensitivity to helicity zero contributions. A similar effect is responsible for the larger fractional error in the coherent results. One should note that there is only an increase in the fit likelihood of 0.5 on freeing both the the helicity of the f_2' and the $f_2 : f_2'$ relative phase. The assumptions of helicity two dominance and zero relative phase are consistent with the data. Fits 1G and 1H, assuming a coherent continuum with $\phi_2 = 0$, are included for reference.

The preferred value for the strength of f_2' production in two-photon interactions is:

$$\Gamma_{\gamma\gamma}(f_2')\cdot \mathrm{Br}(f_2' \to K\bar{K}) = (0.0314 \pm 0.0050 \pm 0.0077)\ \mathrm{keV},$$

with the assumptions of helicity two dominance, 0° phase relative to the $f_2(1270)$, and a coherent continuum contribution (fit 1B, shown in figure 5.12). This is to be compared to the current world average value [42] of (0.09 ± 0.02) keV. All the experiments contributing to this value assumed the continuum and resonant contributions added incoherently. If this assumption was made in the ARGUS analysis the result would be

$$\Gamma_{\gamma\gamma}(f_2')\cdot \mathrm{Br}(f_2' \to K\bar{K}) = (0.0673 \pm 0.0081 \pm 0.0151)\ \mathrm{keV},$$

again with helicity two dominance and 0° resonance phase (fit 2B). This value is quite consistent (0.9σ) with the world average.

The relative phases of the resonances are consistent with zero as expected. These phases in the case of a coherent continuum (fit 1D) are:

$$\begin{aligned}\phi_{f_2:a_2} &= (30 \pm 12 \pm 26)^\circ\\ \phi_{f_2:f_2'} &= (32 \pm 13 \pm 26)^\circ\end{aligned}$$

In this fit the magnitudes of the f_2 and a_2 contributions are constrained to their world averages, and helicity two dominance is assumed. If the restriction $\phi_{f_2:a_2} = 0$ is made, $\phi_{f_2:f_2'} = (-5 \pm 5 \pm 15)^\circ$.

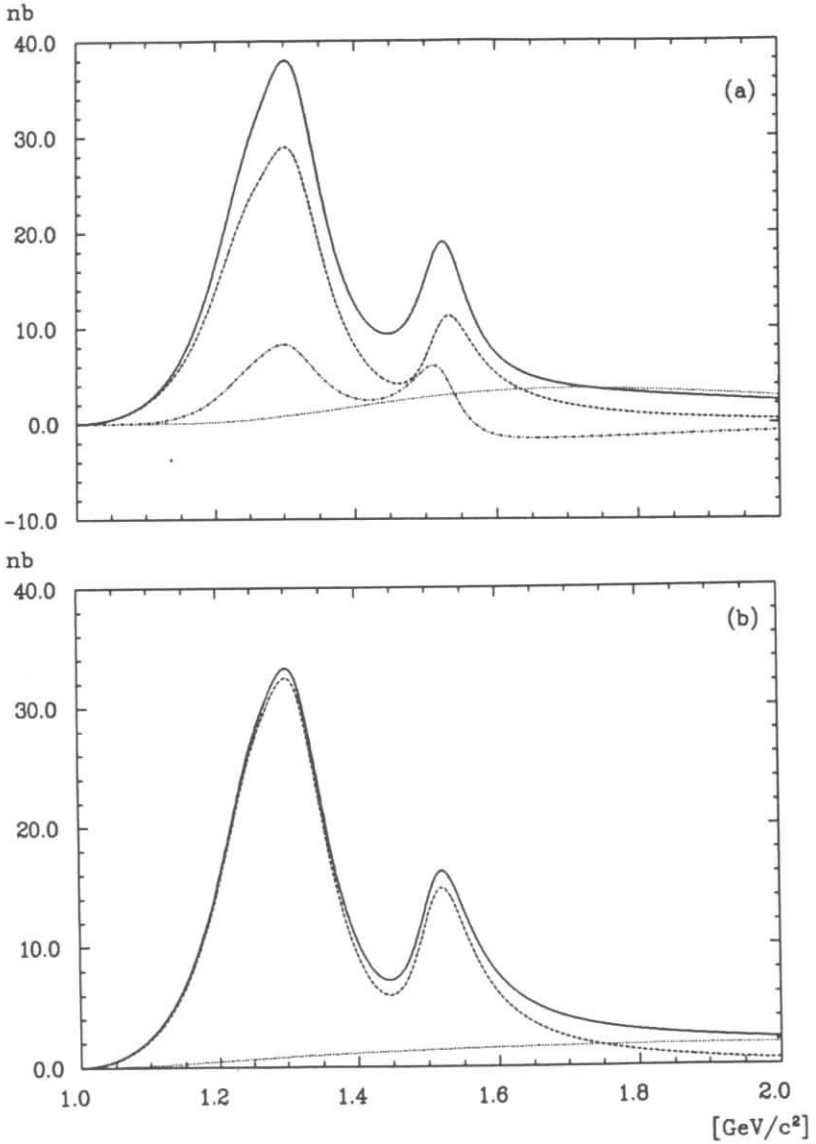

Figure 5.11: Resonance fits to the K^+K^- cross section: (a) results of fit 1B (coherent continuum); (b) results of fit 2B (incoherent continuum). The different contributions to the cross section shown are total (solid line), resonant (dashed), interference term (dot-dashed), and continuum (dotted).

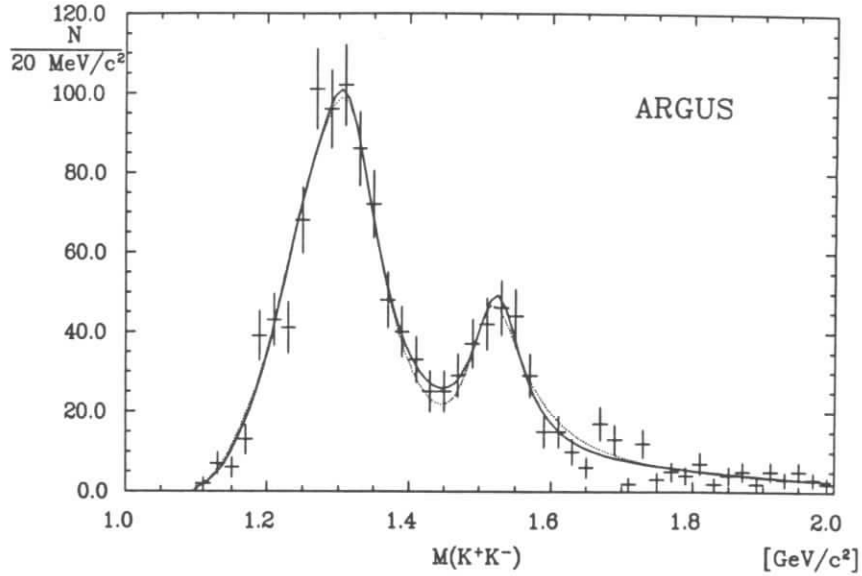

Figure 5.12: The cross sections of figure 5.11, weighted with experimental sensitivity, are shown superimposed on the $m(K^+K^-)$ distribution. The solid line is the result of fit 1B (coherent continuum) while the dotted line is the result of fit 2B (incoherent continuum).

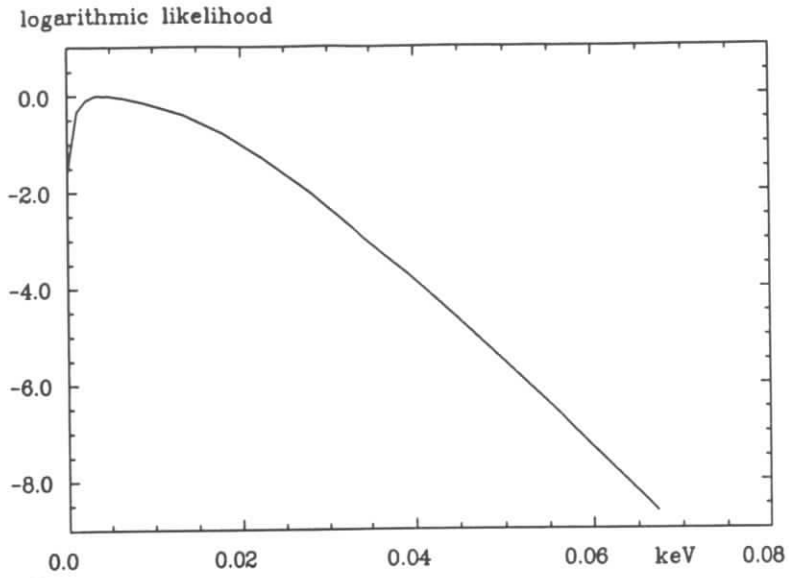

Figure 5.13: The likelihood distribution for a coherent continuum fit, as a function of the $\gamma\gamma$ width of the $\theta/f_2(1720)$, assuming helicity two.

5.6 Upper Limits for Exotic Contributions

The $f_2(1720)$ (formerly $\theta(1690)$) is now a well established resonance [2] and is considered a glueball candidate [176]. Because of this, limits on its $\gamma\gamma$-width are of interest. Current theoretical estimates [177] suggest that $\Gamma(f_2(1720) \to \gamma\gamma) \cdot \mathrm{Br}(f_2(1720) \to K\bar{K})$ should be approximately 95 eV, which is close to current experimental sensitivities. Helicity two dominance is also expected in $f_2(1720)$ production. To search for any contribution from this resonance, the matrix element for the $f_2(1720)$ was introduced into the cross section allowing interference with the other contributions. The mass and width of the $f_2(1720)$ were constrained [176] to be (1.707 ± 0.011) GeV/c^2 and (0.162 ± 0.025) GeV/c^2 respectively. In addition to the $f_2(1720)$ parameters, only the f_2' $\gamma\gamma$-width, the relative f_2':$f_2(1720)$ phase, and the continuum parameters were free in the fit All other parameters were as in fit 1B. The continuum parameterization that yielded the best likelihood for

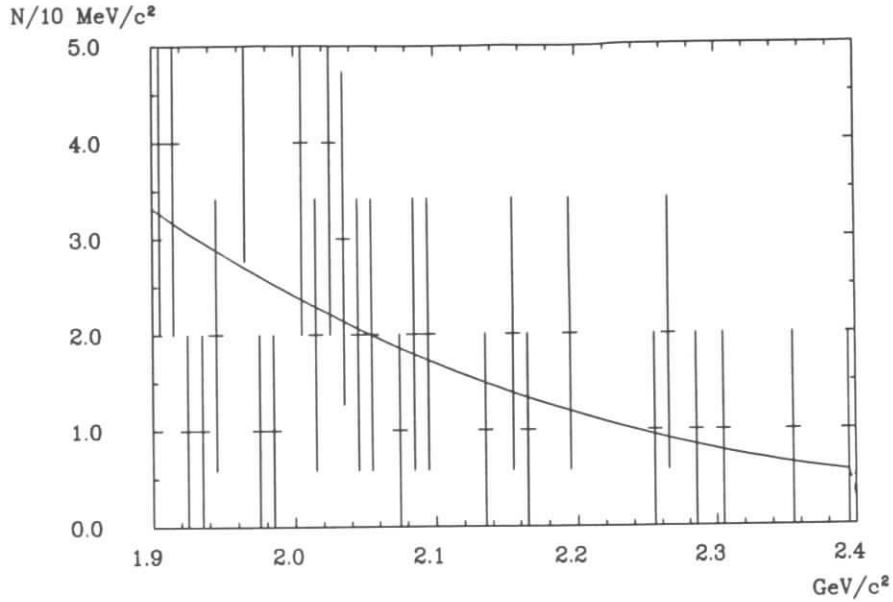

Figure 5.14: m(K^+K^-) distribution used for the X(2230) upper limit. The curve shown is the extrapolation (from 2 GeV/c^2) of resonance fit 1B.

a fit with the free $f_2(1720)$ contribution was used to analyze the overall likelihood distribution. The likelihood was then maximized for different hypothetical values of $\Gamma(f_2(1720) \to \gamma\gamma) \cdot \mathrm{Br}(f_2(1720) \to K\bar{K})$, and the resulting distribution integrated (figure 5.13). This leads to the results:

$$\frac{\Gamma_{\gamma\gamma}^{(2)}}{0.058} + \frac{\Gamma_{\gamma\gamma}^{(0)}}{0.24} < \frac{1.0 \text{ keV}}{\mathrm{Br}(f_2(1720) \to K\bar{K})} \text{ at 95\% c.l.}$$

The $f_2(1720)$ helicity zero upper limit is much weaker due to the reduced acceptance (50% of the helicity two acceptance) and the absence of any other helicity zero contributions. This analysis employed a coherent continuum contribution.

The X(2230) is less well established than the $f_2(1720)$, but is also considered a glueball candidate. No events were observed in the relevant mass region between 2.21

and 2.25 GeV/c^2, leading to the result:

$$\frac{\Gamma^{(2)}_{\gamma\gamma}}{0.019} + \frac{\Gamma^{(0)}_{\gamma\gamma}}{0.043} < \frac{1.0 \text{ keV}}{\text{Br}(X(2230) \to K\bar{K})} \text{ at 95\% c.l.}$$

assuming that $J_{PC} = 2^{++}$ for the X(2230). This is in agreement with a likelihood analysis using the mass region between 1.8 and 2.4 GeV (figure 5.14), with the mass and width of the X(2230) constrained to be 2.227 ± 0.008 GeV/c^2 and 0.021 ± 0.018 GeV/c^2, respectively. Theoretical expectations [177] are on the order of 1 eV if the X(2230) is a 2^{++} glueball state.

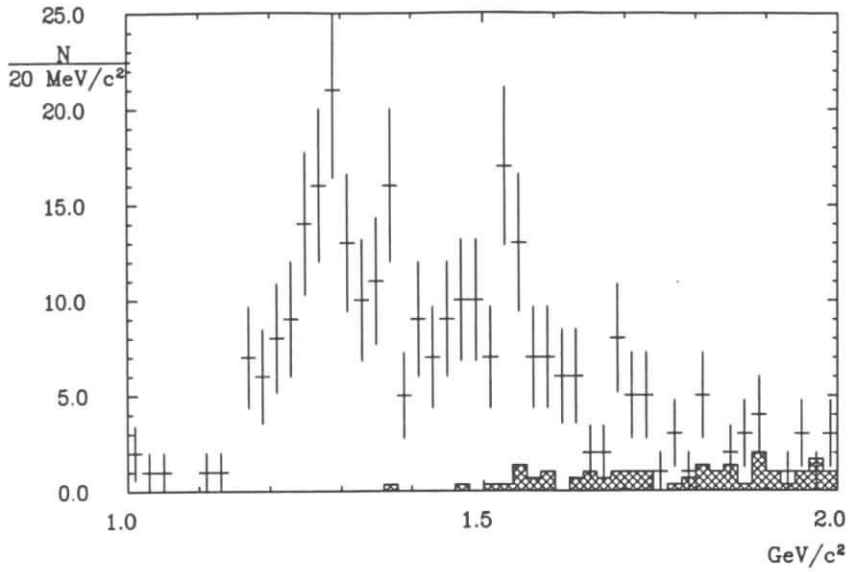

Figure 5.15: m(K^+K^-) distribution for events with $P_\perp(K^+K^-) > 0.2$ GeV/c^2. The shaded histogram is the estimate of the QED background from the symmetric regions of the ToF mass^2 plane.

5.7 $\gamma\gamma \to K^+K^-$ production at high $P_\perp(K^+K^-)$

Recently, the production of the vector particles $f_1(1285)$ and $f_1(1425)$ has been observed in tagged two-photon collisions where one photon has high q^2 [63]-[67]. ARGUS has confirmed these results qualitatively [68] by studying the production of these final states at high final-state transverse momentum. Unfortunately, the ARGUS results are difficult to express quantitatively as the photon q^2's are not measured.

Even though vector particles with even charge parity cannot decay to two pseudoscalars, it is still interesting to see whether any {JM} = {21} contribution can be extracted. On making the inverse of the standard cut, $P_\perp(K^+K^-) > 0.2$ GeV/c^2, the mass spectrum in figure 5.15 results. This analysis also has a relaxed identification requirement: $r_{KK} < 0.2$ (GeV/c^2)^2. Eighteen percent of the total K^+K^- production

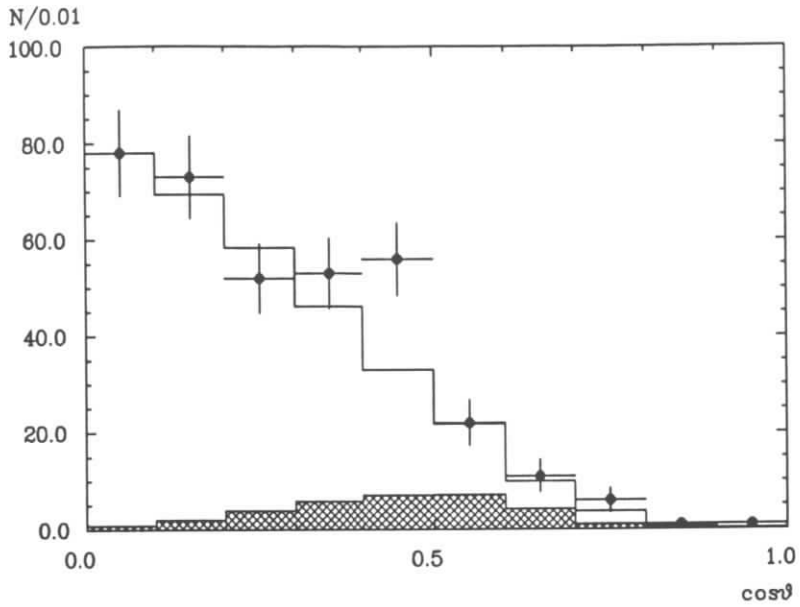

Figure 5.16: Decay angle distribution for high $P_\perp(K^+K^-)$ events. The histogram shown is the GVDM extrapolation of the fit to the data for $P_\perp(K^+K^-) < 0.2$ GeV/c., while the shaded area is the Monte Carlo prediction for $\{JM\} = \{21\}$ with a flat $\sigma_{\gamma\gamma}$.

survives. The f_2 and a_2 contributions appear to be resolved, which suggests either large helicity one couplings with a relative phase different from zero, or a nontrivial q^2 evolution of the relative phases of the helicity two contributions.

The angular distribution, integrated over the entire mass range, shows qualitative evidence for helicity one production. This is shown in figure 5.16 along with an extrapolation of the helicity two contribution using a GVDM propagator and the cross section from resonance fit 1B. This corresponds to a $\{JM\} = \{21\}$ contribution of $(1.7 \pm 0.5 \pm 0.9)\%$ of the total cross section. Unfortunately, these results cannot be expressed more quantitatively because of the low statistics, lack of q^2 information, and complexity of the process.

Chapter 6

Conclusions

The production of η' mesons in two-photon collisions has been measured in the $\pi^+\pi^-\gamma$ final state with a precision exceeding that of all existing measurements. The data sample used in the 1990 ARGUS analysis is the largest in existence (2300 η's). The strong signal, in combination with the resolution and solid angle coverage of the calorimeter, produces an excellent signal-to-background ratio. This allows the analysis to forego restrictions on the $\pi^+\pi^-$ invariant mass. Consequently, the result is less affected by details of the final-state matrix element. The matrix element itself has been measured and is consistent with the expected coherent contributions of ρ and ω production. The product of the two-photon width and $\pi^+\pi^-\gamma$ branching ratio is

$$\Gamma_{\gamma\gamma}(\eta') \cdot Br(\eta' \to \pi^+\pi^-\gamma) = 1.25 \pm 0.03 \pm 0.11 \ \text{keV}.$$

Using the current [2] value of the branching ratio $Br(\eta' \to \pi^+\pi^-\gamma) = 0.301 \pm 0.014$ the two-photon width of the η' is found to be

$$\Gamma_{\gamma\gamma}(\eta') = 4.16 \pm 0.09 \pm 0.42 \ \text{keV},$$

where the error in the $\pi^+\pi^-\gamma$ branching ratio has been added in quadrature. This result is the most accurate available (figure 6.1) and is quite consistent with the old world average of (4.27 ± 0.23) keV. Including the ARGUS result, the world average becomes (4.25 ± 0.22) keV. Using a combination of recent measurements [42] of the $\gamma\gamma$ branching ratio of the η' ($Br(\eta' \to \gamma\gamma) = 0.0223 \pm 0.0018$), the total width of the η' meson is found to be (191 ± 18) keV. This is in agreement with the direct measurement of [178] (280 ± 100) keV.

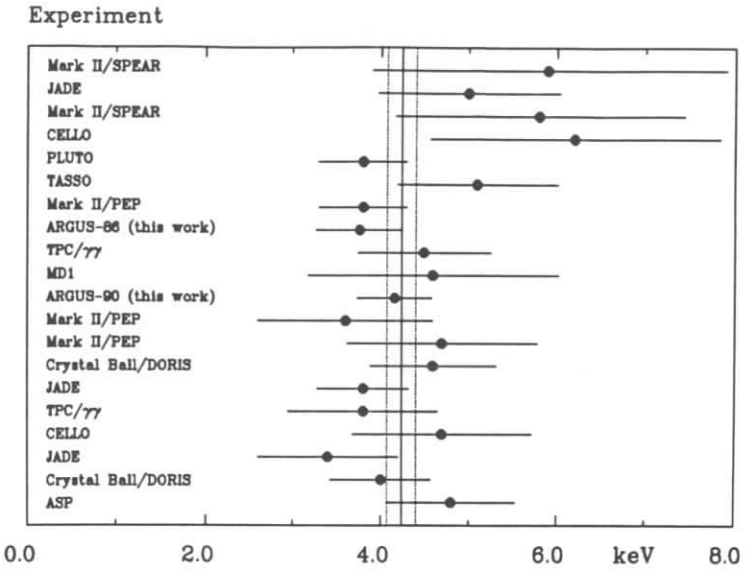

Figure 6.1: Measurements of the two-photon width of the η', the solid vertical line represents the world average while the dotted vertical lines are the 1σ contours. See table 1.5, page 20 for references and numerical values.

The new world average value of $\Gamma_{\gamma\gamma}(\eta')$ can be combined with the those of $\Gamma_{\gamma\gamma}(\pi^0) = 7.72 \pm 0.46$ eV and $\Gamma_{\gamma\gamma}(\eta) = 0.516 \pm 0.026$ keV (the latter from $\gamma\gamma$ collision experiments only [2],p.119) to obtain the pseudoscalar nonet flavour SU(3) mixing parameters as defined in reference [39]:

$$\begin{aligned} \Gamma^{\eta}_{\gamma\gamma}/\Gamma^{\pi^0}_{\gamma\gamma} &= \frac{1}{3}(\cos\theta - r\ 2\sqrt{2}\sin\theta)^2(\frac{m_\eta}{m_{\pi^0}})^N \\ \Gamma^{\eta'}_{\gamma\gamma}/\Gamma^{\pi^0}_{\gamma\gamma} &= \frac{1}{3}(\sin\theta + r\ 2\sqrt{2}\cos\theta)^2(\frac{m_{\eta'}}{m_{\pi^0}})^N \end{aligned} \qquad (6.1)$$

where, for the pseudoscalar nonet, $N = 3$. We find the singlet/octet mixing angle $\theta = -17.5° \pm 1.1°$ and the nonet symmetry breaking parameter $r = 0.91 \pm 0.03$. This is in reasonable agreement with the results of detailed analyses of vector/pseudoscalar production in J/ψ decays; $\theta = (-19.1 \pm 1.4)°$ [179], and $\theta = (-19.2 \pm 1.4)°$ [180]. This departure from the prediction of the Gell-Mann/Okubo mass formula, $-(11.2 \pm 0.2)°$ [8,47], can be explained by breaking of the SU(3) flavour symmetry or higher order effects [181]. One can also introduce a gluonium component in the η' wave function in

addition to the SU(3) $q\bar{q}$ components [182]:

$$|\eta'\rangle = X_{\eta'}|u\bar{u} + d\bar{d}\rangle + Y_{\eta'}|s\bar{s}\rangle + Z_{\eta'}|gg\rangle. \quad (6.2)$$

The first analysis of this type [183] ignored the contribution of doubly OZI suppressed (DOZI) diagrams and found that a significant glue contribution to the η' wave function was possible, but not essential. The newer analyses [179,180], which allow a DOZI contribution, find that the η' wave function is saturated by $|q\bar{q}\rangle$. The DM2 experiment estimates that $|Z_{\eta'}|^2 \simeq 1\%$. The suppression of the gluonium content of the η' is no surprise as the DOZI coupling ($\sim 10\%$) implies an effective $\langle g\eta'|gg\rangle$ transition. Though the gg are in a colour octet state, there is no clear reason to expect the singlet $\langle\eta'|gg\rangle$ coupling to be suppressed, especially given the fact that the transition $J/\Psi \rightarrow \gamma\eta'$ occurs strongly. As one cannot have a coupling to a state without introducing some degree of mixing, it seems that the theoretical frame work for these analyses may be oversimplified.

The reaction $\gamma\gamma \rightarrow K^+K^-$ has also been analyzed in detail. Topological cross sections have been determined for this process with minimal assumptions. Production of the tensor mesons f_2, a_2, and f_2' has also been observed. Assuming helicity two dominance and fixing the phases between the resonances to be zero, the strength of f_2' production was found to be $\Gamma_{\gamma\gamma}(f_2') \cdot \mathrm{Br}(f_2' \rightarrow K\bar{K}) = (0.031 \pm 0.005 \pm 0.008)$ keV, with a coherent continuum hypothesis or $(0.067 \pm 0.008 \pm 0.015)$ keV with an incoherent continuum hypothesis. The incoherent result is in good agreement with the world average of 0.09 ± 0.02 keV [42]. The measurements contributing to this average (figure 6.2) either assume an absence of continuum (in the neutral channel) or an incoherent continuum (in the charged channel). Neither of these assumptions is justified by existing measurements. In the ARGUS analysis the continuum contribution has been treated coherently with a constant phase. The fits with a coherent continuum are found to have significantly better likelihoods than the incoherent analyses. The relative phases $f_2 : a_2$ and $f_2 : f_2'$ have been determined for the first time in the charged kaon final state and are found to be $(30 \pm 12 \pm 24)°$ and $(32 \pm 13 \pm 26)°$, consistent with zero as expected from SU(3) flavour symmetry and OZI suppression of disconnected decay diagrams [175].

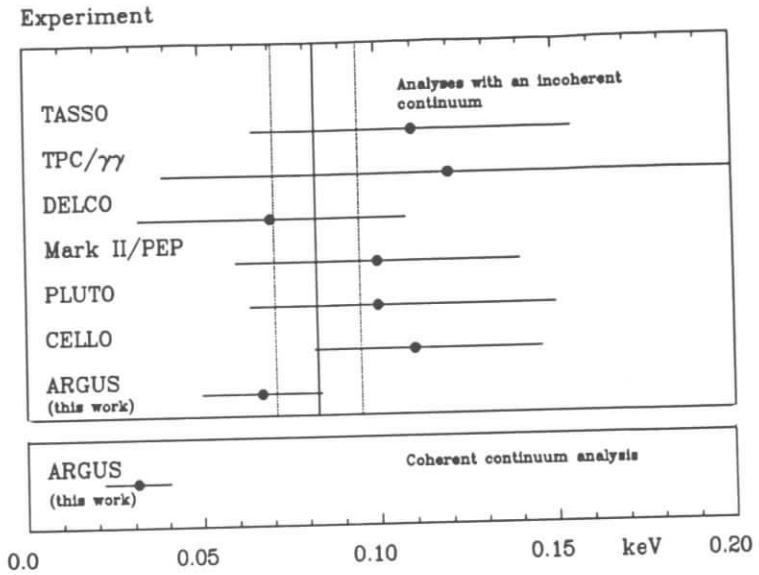

Figure 6.2: Measurements of the two-photon width of the f_2', the solid vertical line represents the world average while the dotted vertical lines are the 1σ contours. See table 1.8, page 22 for more information.

There have been many attempts ([184]-[190]) to calculate the tensor meson $\gamma\gamma$-widths. The present measurement, taken together with the world average values for the f_2 and a_2, and assuming that $50\% < \mathrm{Br}(f_2' \rightarrow K\bar{K}) < 100\%$, is consistent with only one model [188]. This agreement is improved if one takes into account recent data on f_2' decays to K^+K^-, $\pi^+\pi^-$, and $\eta\eta$ observed in J/ψ decays [191], which yield a value for the branching ratio of $\mathrm{Br}(f_2' \rightarrow K\bar{K}) = (72^{+7}_{-13})\%$, assuming that no other decay modes contribute.

The coherent continuum measurement of $\Gamma_{\gamma\gamma}(f_2')$, assuming $\mathrm{Br}(f_2' \rightarrow K\bar{K}) = 100\%$ ($\Gamma_{\gamma\gamma}(f_2') = (0.031 \pm 0.005 \pm 0.008)$ keV), can be combined with the world averages for $\Gamma_{\gamma\gamma}(a_2) = (1.00 \pm 0.09)$ keV and $\Gamma_{\gamma\gamma}(f_2) = (2.97 \pm 0.14)$ keV, to obtain the tensor nonet flavour SU(3) mixing parameters. One can use the pseudoscalar mixing formula (equation 6.1) with the substitution $\pi^0, \eta, \eta' \rightarrow a_2, f_2', f_2$. This formula, with $N = 3$, leads to values for the singlet/octet mixing angle $\theta_T = (22.9 \pm 1.1)°$ and the nonet symmetry

breaking parameter $r_T = 1.06 \pm 0.06$. With N = −4 the results are $\theta_T = (29.3 \pm 1.1)°$ and $r_T = 0.92 \pm 0.06$, which is consistent with the value of $\theta_T = 28°$ expected from the quadratic mass formula [8,2].

No evidence for production of the glueball candidate states $f_2(1720)$ and X(2230) is observed. With no assumptions on helicity content and with arbitrary phases between the states involved, the following upper limits were determined: $\Gamma_{\gamma\gamma}(f_2(1720)) \cdot Br(f_2(1720) \to K^+K^-) < 0.24$ keV and $\Gamma_{\gamma\gamma}(X(2230)) \cdot Br(X(2230) \to K^+K^-) < 0.043$ keV with 95% confidence. These values are consistent with glueball interpretations of the two resonances. The $f_2(1720)$, even if 100% glue, should be measurable in $\gamma\gamma$ collisions given data samples a few times the size of those currently available [177]. Finally, a small contribution to K^+K^- production with $\{JM\} = \{21\}$ has been observed, amounting to $(1.7 \pm 0.5 \pm 0.9)\%$ of the total K^+K^- cross section.

Appendix A

List of Collaborators

This list includes all present and former members (*) of the ARGUS collaboration. Collaborators who have changed institutes or returned to the collaboration after extended absences are listed under their new institutes (#).

H. Albrecht, A. A. Andam*, U. Binder*, P. Böckman*, G. Drews*, R. Gläser, G. Harder, H. Hasemann*, I. Lempke-Koppitz*, A. Krüger, A. Nippe, T. Oest, A. Philipp*, M. Reidenbach, M. Schäfer, W. Schmidt-Parzefall, H. Schröder, H. D. Schulz, F. Sefkow, F. Selonke*, R. Wurth, A. Yagil*
DESY, Hamburg, West Germany

R. D. Appuhn, J. P. Donker*, A. Drescher, B. Grawe*, C. Hast, G. Herrera, D. Kamp*, H. Kolanoski, A. Lange, A. Lindner, R. Mankel, A. Markees*, U. Matthiesen*, H. Müller-Lüdenscheidt*, H. Scheck, G. Schweda, B. Spaan, A. Walther, D. Wegener
Institut für Physik[1], *Universtät Dortmund, West Germany*

M. Paulini, K. Reim, U. Volland, H. Wegener
Physikalisches Institut[2], *Universität Erlangen-Nürnberg, West Germany*

R. Heller*, W. Funk, J. Stiewe, S. Werner
Institut für Hochenergiephysik[3], *Universität Heidelberg, West Germany*

S. Ball#, J. C. Gabriel#, C. Geyer, W. Hofmann#, A. Hölscher, B. Holzer, S.Khan, J. Spengler#
Max-Planck-Institut für Hochenergiephysik, Heidelberg, West Germany

N. N. Brown*[4], C. E. K. Charlesworth[5], K. W. Edwards[6], W. R. Frisken[7], Ch. Fukunaga*[5], D. J. Gilkinson*[5], D. M. Gingrich*[5], M. Goddard*[6], H. Kapitza[7],

[1]Supported by the German Bundesministerium für Forschung und Technologie under contract number 054DO51P.

[2]Supported by the German Bundesministerium für Forschung und Technologie under contract number 054ER11P(5).

[3]Supported by the German Bundesministerium für Forschung und Technologie under contract number 054HD24P.

[4]McGill University, Montreal, Quebec, Canada.

[5]University of Toronto, Toronto, Ontario , Canada.

[6]Carleton University, Ottawa, Ontario, Canada.

[7]York University, Downsview, Ontario, Canada.

P. C. H. Kim*[5], R. Kutschke[5], D. B. MacFarlane#[4], J. A. McKenna*[5], K. W. McLean[4], A. W. Nilsson[4], R. S. Orr[5], P. Padley*[7], J. A. Parsons[5], P. M. Patel[4], J. D. Prentice[5], S. C. Seidel[5], H. C. J. Seyerd*[5], B. J. Stacey*[5], J. D. Swain[5], G. Tsipolitis[4], K. Tzamariudaki, T. S. Yoon[5], J. C. Yun*[6]
Institute of Particle Physics[8], *Canada*

R. Ammar*, D. Coppage*, R. Davis, S. Kanekal*, N. Kwak*
University of Kansas[9], *Lawrence, U. S. A.*

T. Ruf, S. Schael, K. R. Schubert# , K. Strahl# , R. Waldi# , S. Weseler#
Institute für Experimentelle Kernphysik[10], *Universität Karlsruhe, West Germany*

B. Boštjančič, G. Kernel, P. Križan [11], E. Križnič, M. Pleško#
Institut J. Stefan and Oddelek za fiziko, Univerza v Ljubljani, Yugoslavia[12]

H. I. Cronström, L. Jönsson, Y. Oku*
Institute of Physics[13], *University of Lund, S-22362, Sweden*

A. Arefiev*, A. Babaev, M. Danilov, B. Fominykh, A. Golutvin, I. Gorelov, V. Lubimov, V. Matveev*, V. Nagovistin*, A. Rostovtsev, V. Ryltsov*, A. Semenov, S. Semenov, V. Shevchenko, V. Sopov*, V. Soloshenko, V. Tchistilin, I. Tichomirov, Yu. Zaitsev
Institute of Theoretical and Experimental Physics, Moscow, USSR

R. Childers, C. W. Darden, R. C. Fernholz*
University of South Carolina[14], *Columbia, USA.*

H. Gennow*
University of Stockholm, Stockholm, Sweden

[8]Supported by the Natural Sciences and Engineering Research Council, Canada.

[9]Supported by the U.S. National Science Foundation

[10]Supported by the German Bundesministerium für Forschung und Technologie under contract number 054KA17P.

[11]Supported by the Alexander v. Humboldt Stiftung, Bonn.

[12]Supported by Raziskovlna skupnost Slovenje and the Internationales Büro KfA, Jülich.

[13]Supported by the Swedish Research Council.

[14]Supported by the U.S. Department of Energy under contract DE-AS09-80ER10690.

Appendix B

A List of ARGUS Publications

Published in Refereed Journals

- H. Albrecht *et al.* (ARGUS collaboration), "Evidence for F^* meson production in e^+e^- annihilation at 10 GeV centre-of-mass energy", Phys. Lett. **146B** (1984) 111-115
- H. Albrecht *et al.* (ARGUS collaboration), "Production and decay of the charged D^* meson in e^+e^- annihilation at 10 GeV centre-of-mass energy", Phys. Lett. **150B** (1985) 235-241
- H. Albrecht *et al.* (ARGUS collaboration), "Production and decay of the F meson in e^+e^- annihilation at 10 GeV centre-of-mass energy", Phys. Lett. **153B** (1985) 343-347
- H. Albrecht *et al.* (ARGUS collaboration), "Search for narrow states coupling to τ pairs in radiative Υ decays", Phys. Lett. **154B** (1985) 452
- H. Albrecht *et al.* (ARGUS collaboration), "Search for fractionally charged particles produced in e^+e^- annihilation", Phys. Lett. **156B** (1985) 134
- H. Albrecht *et al.* (ARGUS collaboration), "A determination of the muon pair branching ratio of the Υ' meson", Z. Phys. **C28** (1985) 45-50
- H. Albrecht *et al.* (ARGUS collaboration), "Observation of antideuteron production in electron positron annihilation at 10 GeV centre-of-mass energy", Phys. Lett. **157B** (1985) 326-332
- H. Albrecht *et al.* (ARGUS collaboration), "Direct evidence for W exchange in charmed meson decay", Phys. Lett. **158B** (1985) 525
- H. Albrecht *et al.* (ARGUS collaboration), "Radiative decays of the $\Upsilon(2S)$ into the three χ_b states", Phys. Lett. **160B** (1985) 331
- H. Albrecht *et al.* (ARGUS collaboration), "Observation of B-meson decay into J/ψ", Phys. Lett. **162B** (1985) 395-399
- H. Albrecht *et al.* (ARGUS collaboration), "An upper limit on the mass of the tau neutrino", Phys. Lett. **163B** (1985) 404-407
- H. Albrecht *et al.* (ARGUS collaboration), "Upper limit for the emission of monoenergetic photons in $\Upsilon(1S)$- and $\Upsilon(2S)$-meson decays", Z. Phys. **C29** (1985) 167-173

- H. Albrecht *et al.* (ARGUS collaboration), "Observation of a new charmed meson", Phys. Rev. Lett. **56** (1986) 549-552
- H. Albrecht *et al.* (ARGUS collaboration), "Search for gluinos in decays of the $\chi_b(1\,^3P_1)$ meson", Phys. Lett. **167B** (1986) 360-364
- H. Albrecht *et al.* (ARGUS collaboration), "An upper limit for two-jet production in direct $\Upsilon(1S)$ decays", Z. Phys. **C31** (1986) 181-184
- H. Albrecht *et al.* (ARGUS collaboration), "Observation of F decays into $\overline{K}^*K$", Phys. Lett. **179B** (1986) 398-402
- H. Albrecht *et al.* (ARGUS collaboration), "Search for exotic decay modes of the $\Upsilon(1S)$", Phys. Lett. **179B** (1986) 403-408
- H. Albrecht *et al.* (ARGUS collaboration), "Measurement of tau decays into three charged pions", Z. Phys. **C33** (1986) 7-12
- H. Albrecht *et al.* (ARGUS collaboration), "Determination of the branching ratio for the decay $B^0 \to D^{*-}\pi^+$", Phys. Lett. **182B** (1986) 95-100
- H. Albrecht *et al.* (ARGUS collaboration), "The decay $D^0 \to \overline{K}^0\phi$", Z. Phys. **C33** (1987) 359-362
- H. Albrecht *et al.* (ARGUS collaboration), "Observation of octet and decuplet hyperons in e^+e^- annihilation at 10 GeV centre-of-mass energy", Phys. Lett. **183B** (1987) 419-424
- H. Albrecht *et al.* (ARGUS collaboration), "Reconstruction of B mesons", Phys. Lett. **185B** (1987) 218-222
- H. Albrecht *et al.* (ARGUS collaboration), "Evidence for the decay $\tau^- \to \nu_\tau\omega\pi^-$", Phys. Lett. **185B** (1987) 223-227
- H. Albrecht *et al.* (ARGUS collaboration), "Search for lepton number and lepton flavour violation in tau decays", Phys. Lett. **185B** (1987) 228-232
- H. Albrecht *et al.* (ARGUS collaboration), "The hadronic transitions from $\Upsilon(2S)$ to $\Upsilon(1S)$", Z. Phys. **C35** (1987) 283
- H. Albrecht *et al.* (ARGUS collaboration), "Observation of inclusive D_S production in B meson decay", Phys. Lett. **187B** (1987) 425-430
- H. Albrecht *et al.* (ARGUS collaboration), "Observation of B^0-$\overline{B}^0$ mixing", Phys. Lett. **192B** (1987) 245-252
- H. Albrecht *et al.* (ARGUS collaboration), "Search for the decay $D_S \to \rho^0\pi$ as evidence for quark annihilation", Phys. Lett. **195B** (1987) 102-106
- H. Albrecht *et al.* (ARGUS collaboration), "Search for the decay $\tau^- \to \nu_\tau\eta\pi^-$", Phys. Lett. **195B** (1987) 307-310
- H. Albrecht *et al.* (ARGUS collaboration), "First observation of $\gamma\gamma \to \omega\rho^0$", Phys. Lett. **196B** (1987) 101-106

- H. Albrecht *et al.* (ARGUS collaboration), "Measurement of the decay $B^0 \to D^{*-}\ell^+\nu$", Phys. Lett. **197B** (1987) 452-456
- H. Albrecht *et al.* (ARGUS collaboration), "First observation of $\gamma\gamma \to K^{*0}\overline{K}^{*0}$", Phys. Lett. **198B** (1987) 255-260
- H. Albrecht *et al.* (ARGUS collaboration), "First observation of $\gamma\gamma \to \omega\omega$", Phys. Lett. **198B** (1987) 577-582
- H. Albrecht *et al.* (ARGUS collaboration), "Determination of α_S from a measurement of the direct photon spectrum in $\Upsilon(1S)$ decays", Phys. Lett. **199B** (1987) 291-296
- H. Albrecht *et al.* (ARGUS collaboration), "An upper limit on D^0-$\overline{D}^0$ mixing", Phys. Lett. **199B** (1987) 447-450
- H. Albrecht *et al.* (ARGUS collaboration), "B meson decays into charmonium states", Phys. Lett. **199B** (1987) 451-456
- H. Albrecht *et al.* (ARGUS collaboration), "Measurement of $\eta' \to \pi^+\pi^-\gamma$ in $\gamma\gamma$ collisions", Phys. Lett. **199B** (1987) 457-461
- H. Albrecht *et al.* (ARGUS collaboration), "A measurement of the tau lifetime", Phys. Lett. **199B** (1987) 580-584
- H. Albrecht *et al.* (ARGUS collaboration), "An improved upper limit on the ν_τ-mass from the decay $\tau^- \to \pi^-\pi^-\pi^-\pi^+\pi^+\nu_\tau$", Phys. Lett. **202B** (1988) 149-153
- H. Albrecht *et al.* (ARGUS collaboration), "Observation of the charmed baryon Λ_C in e^+e^- annihilation", Phys. Lett. **207B** (1988) 109-114
- H. Albrecht *et al.* (ARGUS collaboration), "Hyperon production is e^+e^- annihilation at 10 GeV center of mass energy", Z. Phys. **C39** (1988) 177-786
- H. Albrecht *et al.* (ARGUS collaboration), "Measurement of D_S^*-D_S mass difference", Phys. Lett. **207B** (1988) 349-354
- H. Albrecht *et al.* (ARGUS collaboration), "Observation of charmless B meson decays", Phys. Lett. **209B** (1988) 119-126
- H. Albrecht *et al.* (ARGUS collaboration), "Search for D^0 decays into lepton pairs", Phys. Lett. **209B** (1988) 380-384
- H. Albrecht *et al.* (ARGUS collaboration), "Search for the decay $B \to K^*\gamma$", Phys. Lett. **210B** (1988) 258-262
- H. Albrecht *et al.* (ARGUS collaboration), "Observation of inclusive B meson decays into Λ_C^+ baryons", Phys. Lett. **210B** (1988) 263-266
- H. Albrecht *et al.* (ARGUS collaboration), "Lifetimes of charmed mesons", Phys. Lett. **210B** (1988) 267-272
- H. Albrecht *et al.* (ARGUS collaboration), "A search for $\omega\phi$ and $\phi\phi$ production in the reactions $\gamma\gamma \to K^+K^-\pi^+\pi^-\pi^0$ and $\gamma\gamma \to 2K^+2K^-$", Phys. Lett. **210B** (1988) 273-277

- H. Albrecht *et al.* (ARGUS collaboration), "Observation of the charmed baryon Σ_C in e^+e^- annihilation", Phys. Lett. **211B** (1988) 489-492
- H. Albrecht *et al.* (ARGUS collaboration), "First observation of $\gamma\gamma \to K^{*+}K^{*-}$", Phys. Lett. **212B** (1988) 528-532
- H. Albrecht *et al.* (ARGUS collaboration), "Measurement of the decays $\tau^- \to K^{*-}\nu_\tau$ and $\tau^- \to \rho^-\nu_\tau$", Z. Phys. **C41** (1988) 1-5
- H. Albrecht *et al.* (ARGUS collaboration), "Upper Limits for the Decay of τ-leptons into η-mesons", Z. Phys. **C41** (1988) 405-411
- H. Albrecht *et al.* (ARGUS collaboration), "B Meson decays to $D\pi$ and $D\rho$", Phys. Lett. **215B** (1988) 424-428
- H. Albrecht *et al.* (ARGUS collaboration), "Observation of the orbitally excited $\Lambda(1520)$ Baryon in e^+e^- annihilation", Phys. Lett. **215B** (1988) 429-434
- H. Albrecht *et al.* (ARGUS collaboration), "ARGUS: A universal detector at DORIS II", NIM **A275** (1989) 1-48
- H. Albrecht *et al.* (ARGUS collaboration), "Measurement of the reaction $\gamma\gamma \to \rho^+\rho^-$", Phys. Lett. **217B** (1989) 205
- H. Albrecht *et al.* (ARGUS collaboration), "Inclusive ϕ-production in e^+e^- interactions in the energy region of the Υ-resonances", Z. Phys. **C41** (1989)557-566
- H. Albrecht *et al.* (ARGUS collaboration), "Measurement of D^{*+} Polarization in the Decay $\overline{B}^0 \to D^{*+}l^-\overline{\nu}$", Phys. Lett. **219B** (1989) 121
- H. Albrecht *et al.* (ARGUS collaboration), "Observation of $D^{*0}(2459)$ in e^+e^- Annihilation", Phys. Lett. **221B** (1989) 422
- H. Albrecht *et al.* (ARGUS collaboration), "Search for exclusive radiative decays of $\Upsilon(1S)$ and $\Upsilon(2S)$ mesons", Z. Phys. **C42** (1989)349-354
- H. Albrecht *et al.* (ARGUS collaboration), "Measurement of inclusive B meson decays into baryons", Z. Phys. **C42** (1989)519-525
- H. Albrecht *et al.* (ARGUS collaboration), "Two Photon Production of Final States with a $p\overline{p}$ Pair", Z. Phys. **C42** (1989)543-548
- H. Albrecht *et al.* (ARGUS collaboration), "Results on Baryon Antibaryon Correlations in e^+e^- Annihilation", Z. Phys. **C43** (1989)45-53
- H. Albrecht *et al.* (ARGUS collaboration), "Measurement of D^0 decays into $\overline{K}^0\omega$, $\overline{K}^0\eta$, $\overline{K}^{*0}\eta$", Z. Phys. **C43** (1989)181-184
- H. Albrecht *et al.* (ARGUS collaboration), "Measurement of the Decay $B^0 \to D^{-}l^+\nu$", Phys. Lett. **229**(1989)175
- H. Albrecht *et al.* (ARGUS collaboration), "Observation of $\Delta(1232)^{++}$ Production in e^+e^- Annihilations around 10 GeV", Phys. Lett. **230B**(1989)169

- H. Albrecht *et al.* (ARGUS collaboration), "Observation of the Charged Isospin Partner of the $D^{*0}(2459)$", Phys. Lett. **231B**(1989)208
- H. Albrecht *et al.* (ARGUS collaboration), "Inclusive production of charged pions, charged and neutral kaons and antiprotons in e^+e^- annihilation at 10 GeV and in direct Upsilon decays", Z. Phys. **C44**(1989)547-555
- H. Albrecht *et al.* (ARGUS collaboration), "Search for $b \to s\gamma$ in Exclusive Decays of B Mesons", Phys. Lett. **229B**(1989)304-308
- H. Albrecht *et al.* (ARGUS collaboration), "Resonance Decomposition of the $D^*(2420)^0$ Through a Decay Angular Analysis", Phys. Lett. **232B**(1989)398-404
- H. Albrecht *et al.* (ARGUS collaboration), "Measurement of the Lifetime Ratio $\tau(B^+)/\tau(B^0)$", Phys. Lett. **232B**(1989)554-560
- H. Albrecht *et al.* (ARGUS collaboration), "A study of Cabibbo-suppressed D^0 decays", Z. Phys. **C46**(1990)9-14
- H. Albrecht *et al.* (ARGUS collaboration), "Inclusive π^0 and η meson production in electron positron interactions at $\sqrt{s} = 10$ GeV", Z. Phys. **C46**(1990)15-23

Accepted or submitted for publication in refereed journals

- H. Albrecht *et al.* (ARGUS collaboration), "Search for $b \to s$ *gluon* in B Meson Decays", DESY 89-096
- H. Albrecht *et al.* (ARGUS collaboration), "Observation of a New Charmed-Strange Meson", DESY 89-119
- H. Albrecht *et al.* (ARGUS collaboration), "Study of Antideuteron Production in e^+e^- Annihilation at 10 GeV Centre-of-Mass Energy", DESY 89-144
- H. Albrecht *et al.* (ARGUS collaboration), "Observation of Semileptonic Charmless B Meson Decays, DESY 89-152
- H. Albrecht *et al.* (ARGUS collaboration), "Search for Rare Semileptonic B-Meson Decays", DESY 89-163
- H. Albrecht *et al.* (ARGUS collaboration), "Evidence for a Higher Twist Effect in Electron Positron Annihilation into Hadrons at 10 GeV Centre of Mass Energy", DESY 89-164
- H. Albrecht *et al.* (ARGUS collaboration), "Search for $b \to sX^+X^-$ in Exclusive Decays of B Mesons", DESY 89-166
- H. Albrecht *et al.* (ARGUS collaboration), "Measurement of K^+K^- Production in $\gamma\gamma$ Collisions", DESY 89-179.

In preparation

- H. Albrecht *et al.* (ARGUS collaboration), "Angular Correlations in $\gamma\gamma \to \rho^+\rho^-$"
- H. Albrecht *et al.* (ARGUS collaboration), "Study of pp and $\Lambda\Lambda$ Production in e^+e^- Annihilation at 10 GeV Center of Mass Energy"
- H. Albrecht *et al.* (ARGUS collaboration), "Observation of the Decay $D_s \to \eta'\pi$"
- H. Albrecht *et al.* (ARGUS collaboration), "Search for $b \to s$ *gluon* in B Meson Decays Into Baryonic Final States"
- H. Albrecht *et al.* (ARGUS collaboration), "Search for Hadronic $b \to u$ Decays"
- H. Albrecht *et al.* (ARGUS collaboration), "Spin-parity analysis of the reaction $\gamma\gamma \to \rho^0\rho^0$"
- H. Albrecht *et al.* (ARGUS collaboration), "Search for Semileptonic B Decays into Baryons"
- H. Albrecht *et al.* (ARGUS collaboration), "Exclusive hadronic decays of B mesons"
- H. Albrecht *et al.* (ARGUS collaboration), "Measurement of the Charmed-Strange Baryon Σ_c Production in e^+e^- Annihilation at 10 GeV Center of Mass Energy"

Presented in International Conferences

- K. W. Mclean, (ARGUS collaboration), "QCD Results From ARGUS", talk presented at the Third Lake Louise Winter Institute, "Quantum Chromodynamics: Theory and Experiment", ed. B. A. Campbell, A. N. Kamal, F. C. Khanna, M. K. Sundaresan, World Scientific.

Appendix C

Expressions For The Two-Photon Luminosity

This appendix derives the principal formulae describing the kinematics of $\gamma\gamma$ collisions using procedures outlined by Bonneau[192] and Budnev[45]. Two-photon collisions at e^+e^- storage rings can also be described as inelastic Bhabha scattering events – it is only the weak-coupling of electromagnetic interactions that allows these processes to be interpreted as collisions between photons. The general kinematics of the final state are determined by QED – the process being separable into two distinct steps: the production and decay of the $\gamma\gamma$ system. The former is exactly calculable while the latter is largely unknown except in the case of pure QED processes and resonance production. The full matrix element for the process $e^+e^- \to e^+e^-\gamma^*\gamma^* \to e^+e^-X$ (figure C.1) is then

$$T^X = \frac{e^2}{q_1^2 q_2^2}[\bar{u}(p_1', \sigma_1')\gamma^\mu u(p_1, \sigma_1)][\bar{v}(p_2', \sigma_2')\gamma^\nu v(p_2, \sigma_2)]A^X_{\mu\nu}. \tag{C.1}$$

The conventions used are those of Bjorken and Drell[193] except that $\hat{p} = \gamma^\mu p_\mu$. The notation used is given below:

- $p_i \to$ momenta of colliding e^+e^-,
- $p_i' \to$ momenta of scattered e^+e^-,
- $q_i = p_i - p_i' \to$ momenta of virtual photons,
- $\epsilon_i \to$ polarization vectors for virtual photons,
- $s = W^2_{\gamma\gamma} = (q_1 + q_2)^2 \to$ invariant mass squared of the $\gamma\gamma$ system,
- $E_i' = p_i'^0 \to$ energy of the scattered e^+e^-,
- $\omega_i = q_i^0 \to$ energy of the virtual photons,
- $\theta_i \to$ scattering angle of beam particle i,
- $k_j \to$ momenta of the j^{th} particle in the final state $\gamma\gamma \to X$.

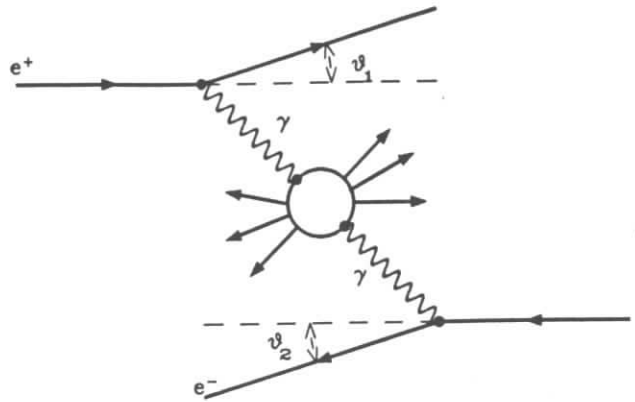

Figure C.1: $e^+e^- \to e^+e^-\gamma^*\gamma^* \to e^+e^-X$

The matrix element for $\gamma\gamma \to X$ depends only on s, q_1^2, q_2^2 and the helicity states of the colliding photons. Since the photons are virtual, scalar helicity states are allowed but the contributions of these to the cross section are suppressed. Squaring the matrix element, averaging over the spins of colliding particles and summing over the final-state spins yields

$$\begin{aligned} |M|^2 &= \frac{1}{4}\frac{(4\pi\alpha)^2}{(q_1^2 q_2^2)^2} Tr[\frac{(\hat{p}_1' + m_e)\gamma^\mu(\hat{p}_1 + m_e)\gamma^{\mu'}}{4m_e^2}] \cdot \\ &\quad Tr[\frac{(\hat{p}_2' - m_e)\gamma^\nu(\hat{p}_2 - m_e)\gamma^{\nu'}}{4m_e^2}] \cdot A^{X*}_{\mu'\nu'} \cdot A^X_{\mu\nu}, \\ I_i^{\mu\mu'} &= Tr[(\hat{p}_i' \pm m_e)\gamma^\mu(\hat{p}_i \pm m_e)\gamma^{\mu'}] \\ &= 4m_e^2 g^{\mu\mu'} + 4[p_i'^\mu p_i^{\mu'} + p_i'^{\mu} p_i^{\mu'} - g^{\mu\mu'}(p_i \cdot p_i')]. \end{aligned}$$

The trace was evaluated using the following formulae:

$$\begin{aligned} Tr(\hat{a}\hat{b}\hat{c}\hat{d}) &= 4[(a\cdot b)(c\cdot d) + (a\cdot d)(b\cdot c) - (a\cdot c)(b\cdot d)], \\ 2m_e^2 &= q_i^2 + 2p_i \cdot p_i'. \end{aligned}$$

Including factors for normalization of the incident and scattered $e^\pm$ wavefunctions, final-state phase space, and the relativistic flux factor, the cross section for $e^+e^- \to e^+e^-\gamma^*\gamma^* \to e^+e^-X$ is found to be

$$\begin{aligned} d\sigma &= \frac{(\pi\alpha)^2}{q_1^2 q_2^2}\rho_1^{\mu\mu'}\rho_2^{\nu\nu'}A^{X*}_{\mu'\nu'}A^X_{\mu\nu}\frac{\delta(q_1 + q_2 - \sum_{j\in X} k_j)(2\pi)^4}{\sqrt{(p_1\cdot p_2)^2 - m_e^4}}\frac{d^3p_1' d^3p_2' d\Gamma}{(2\pi)^6 E_1' E_2'} \\ &= \frac{(\pi\alpha)^2}{q_1^2 q_2^2}\rho_1^{\mu\mu'}\rho_2^{\nu\nu'}\frac{W_{\mu'\nu',\mu\nu}}{\sqrt{(p_1\cdot p_2)^2 - m_e^4}}\frac{d^3p_1' d^3p_2'}{(2\pi)^6 E_1' E_2'}, \end{aligned} \tag{C.2}$$

where

$$\begin{aligned} I_i^{\mu\nu} &= -2q_i^2\rho_i^{\mu\nu}, \\ d\Gamma &= \sum_{Spins}\Pi_{j\in X}\left[\frac{N_j d^3k_j}{E_j(2\pi)^3}\right], \\ W_{\mu'\nu',\mu\nu} &= \int A_{*\mu'\nu'}A_{\mu\nu}\delta(q_1+q_2-\sum_{j\in X}k_j)(2\pi)^4 d\Gamma, \end{aligned}$$

Note that the definition of $W^{\mu'\nu',\mu\nu}$ given above differs from that of Budnev [45] by a factor of 1/2. N_j accounts for the difference in wavefunction normalizations for fermions($N_j = m_f$) and bosons ($N_j = \frac{1}{2}$). The hadronic tensor, $W^{\mu\nu,\mu'\nu'}$, can be related to the imaginary part of the forward scattering amplitude in $\gamma^*\gamma^* \to \gamma^*\gamma^*$ via the optical theorem. Naively, this tensor has $256 = 4^4$ independent components. Gauge invariance reduces this number to 81, since

$$q_{1,\mu}W^{\mu'\nu',\mu\nu} = q_{1,\nu}W^{\mu'\nu',\mu\nu} = q_{2,\mu'}W^{\mu'\nu',\mu\nu} = q_{2,\nu'}W^{\mu'\nu',\mu\nu} = 0.$$

If the process is invariant under parity, rotation, and time-reversal transformations the number of independent amplitudes reduces to 8. This is most easily observed when all tensors are represented in the helicity basis, as the parity transformation simply changes the sign of the helicity. In the $\gamma\gamma$ system this corresponds to interchanging the colliding photons. Rotation invariance forces (in terms of the helicity basis defined below) $a - a' = b - b'$. Invariance under the exchange of the primed and unprimed superscripts corresponds to time-reversal Invariance. The helicity basis, $e(\pm1)$, $e(0)$ is defined as

$$\begin{aligned} q_i^\mu e_{i,\mu} = 0, \qquad & e^*(a)e(b) = (-1)^a\delta_{ab}, \\ e_2(\pm1) = e_1(\mp1), \qquad & e_i^*(\pm1) = -e_i(\mp1), \\ e_1(0) = iQ_1, \qquad & e_2(0) = -iQ_2, \end{aligned}$$

with

$$\begin{aligned} Q_1 &= \sqrt{\frac{-q_1^2}{(q_1\cdot q_2)^2 - q_1^2q_2^2}}\left[q_2 - q_1\frac{(q_1\cdot q_2)}{q_1^2}\right], \\ W_{a'b',ab} &= e_1^{*\mu'}(a')e_2^{*\nu'}(b')W^{\mu'\nu',\mu\nu}e_1^\mu(a)e_2^\nu(b), \\ W_{a'b',ab} &= W_{-a'-b',-a-b} = W_{ab,a'b'}. \end{aligned}$$

The Q_i four vector is orthogonal to the i^{th} photon momentum vector and its transverse helicity vectors – it is therefore parallel to the scalar helicity vector. Similarly, one can define a tensor, $R_{\mu\nu}$, that projects any vector into the two-dimensional subspace orthogonal to both the photon and the helicity-0 vectors, i.e. that subspace generated by the helicity ±1 vectors

$$\begin{aligned} R^{\mu\nu} &= R^{\nu\mu} = -g^{\mu\nu} + X^{-1}[(q_1q_2)(q_1^\mu q_2^\nu + q_1^\nu q_2^\mu) - q_1^2q_2^\mu q_2^\nu - q_2^2q_1^\mu q_1^\nu], \\ X &= (q_1q_2)^2 - q_1^2q_2^2. \end{aligned} \tag{C.3}$$

Using $R^{\mu\nu}$ and the Q_i^μ one can construct projection operators to select each symmetry class of the hadronic tensor. These operators project the appropriate helicity state from the density matrices: $\rho_i^{\mu\nu}$. The $\gamma\gamma$ cross sections for various combinations of photon polarizations are given below. σ_{SS} and σ_{TT} represent the cross sections for scattering of scalar, and transversely polarized virtual photons, respectively. As they represent the collisions of off-shell photons these are not, strictly speaking, "physical" cross sections. On the other hand, they represent the hadronic matrix element in the process without the QED contribution muddying the waters. It is also easier conceptually to view the process as two-photon collisions with the QED factors absorbed in the "luminosity" for the initial state; these are

$$\begin{aligned} W_{SS} &= 4\sqrt{X}\sigma_{SS} = W_{00,00}, \\ W_{TS} &= 4\sqrt{X}\sigma_{TS} = W_{+0,+0} = W_{-0,-0}, \\ W_{TS}^\tau &= 4\sqrt{X}\tau_{TS} = \frac{1}{2}(W_{++,00} + W_{0+,-0}), \\ W_{TS}^a &= 4\sqrt{X}\tau_{TS}^a = \frac{1}{2}(W_{++,00} - W_{0+,-0}), \\ W_{TT} &= 4\sqrt{X}\sigma_{TT} = \frac{1}{2}(W_{++,++} + W_{+-,+-}) = \frac{1}{2}(W_{--,--} + W_{-+,-+}), \\ W_{TT}^\tau &= 4\sqrt{X}\tau_{TT} = W_{++,--} = W_{--,++}, \\ W_{TT}^a &= 4\sqrt{X}\ \tau_{TT}^a = \frac{1}{2}(W_{++,++} - W_{+-,+-}). \end{aligned} \tag{C.4}$$

$\sqrt{X}$ is the flux factor for the $\gamma\gamma$ collision given in equation C.3 and the factor of 4 arises from the normalization of boson wavefunctions (i.e. $1/2E$ for "external" boson lines or m/E for external fermion lines; the $E_{\gamma_1}E_{\gamma_2}$ factor from the wavefunction normalization is absorbed into the invariant flux factor – Bjorken and Drell[193], p.113). Some of the corresponding projection operators are

$$\begin{aligned} R_{SS}^{\mu'\nu',\mu\nu} &= Q_1^\mu Q_1^{\mu'} Q_2^\nu Q_2^{\nu'} = e_1^\mu(0)e_1^{\mu'}(0)e_2^\nu(0)e_2^{\nu'}(0), \\ R_{TS}^{\mu'\nu',\mu\nu} &= R_1^{\mu\mu'}Q_2^\nu Q_2^{\nu'} = (e_1^\mu(1)e_1^{\mu'}(1) + e_1^\mu(-1)e_1^{\mu'}(-1))e_2^\nu(0)e_2^{\nu'}(0), \\ R_{TT}^{\mu'\nu',\mu\nu} &= R_1^{\mu\mu'}R_2^{\nu\nu'} = (e_1^\mu(1)e_1^{\mu'}(1) + e_1^\mu(-1)e_1^{\mu'}(-1))(e_2^\nu(1)e_2^{\nu'}(1) + e_2^\nu(-1)e_2^{\nu'}(-1)). \end{aligned} \tag{C.5}$$

The τ amplitudes correspond to spin flips for both photons and do not contribute if the scattering planes of the beam particles are unmeasured. The τ^a amplitudes only contribute if the beam particles are polarized[194]; i.e., if the $R_{\tau^a}^{\mu'\nu',\mu\nu}$ were calculated explicitly using equations C.2 and C.5, the result would cancel to zero – one must include the correct spin projection operators in the trace calculation to avoid this. Only the TT terms survive for real photons as the scalar degree of freedom disappears in this limit. The final expression for the cross section – the form that most commonly appears in the literature – is then

$$\begin{aligned} d\sigma = \frac{\alpha^2}{16\pi^4 q_1^2q_2^2}\sqrt{\frac{(q_1\cdot q_2)^2 - q_1^2q_2^2}{(p_1\cdot p_2)^2 - m_e^4}}[&4\rho_1^{++}\rho_2^{++}\sigma_{TT} + 2\rho_1^{00}\rho_2^{00}\sigma_{SS} + \\ &2|\rho_1^{+-}\rho_2^{+-}|\tau_{TT}\cos 2\phi + 2\rho_1^{++}\rho_2^{00}\sigma_{TS} + 2\rho_1^{00}\rho_2^{++}\sigma_{ST} \end{aligned}$$

$$-8|\rho_1^{+0}\rho_2^{+0}|\tau_{TS}\cos\phi]\frac{d^3p_1'd^3p_2'}{E_1'E_2'}, \qquad \text{(C.6)}$$

where

$$\begin{aligned}
q_i^2 &= -4E_iE_i'\sin^2(\theta_i/2) - q_{i\min}^2 < 0, \qquad q_{i\min}^2 = m_e^2\omega_i^2/(E\cdot E_i'),\\
2\rho_1^{++} &= \rho_1^{\mu\nu}R^{\mu\nu} = X^{-1}(4E\omega_2 - q_2^2 - q_1q_2)^2 + 1 + 4m_e^2/q_1^2,\\
\rho_1^{00} &= \rho_0^{\mu\nu}Q_1^\mu Q_1^\nu = X^{-1}(4E\omega_2 - q_2^2 - q_1q_2)^2 - 1,\\
|\rho_1^{+0}| &= \sqrt{(\rho_1^{00}+1)|\rho_1^{+-}|},\\
|\rho_1^{+-}| &= \rho_1^{++} - 1.
\end{aligned}$$

This expression is not integrable analytically. The various approximations made in integrating this expression are generically called DEPA's or double equivalent-photon approximations. The first approximation usually made in integrating the $\gamma\gamma$ luminosity amplitudes is to neglect terms of higher order in q^2. As a natural result of this, only transverse photons are considered, and any q^2 variation of $\sigma_{\gamma\gamma}$ is usually ignored – it is assumed that q^2 is negligible compared to any other mass scale in the final integration range. This approximation is sufficient for small-angle tagging and can be applied, with caution, to 0° tagging. With the assumption that q^2, m_e^2 are negligible except in relation to each other, the following simplifications are possible:

$$\begin{aligned}
2\rho_1^{++} &= X^{-1}(4E\omega_2 - q_2^2 - q_1q_2) + 1 + 4m_e^2/q_1^2\\
&= (\frac{2E}{\omega_1} - 1)^2 + 1 + 4m_e^2/q_1^2,\\
X &= (q_1q_2)^2 - q_1^2q_2^2 = \frac{1}{4}W^4 - 2W^2(q_1^2+q_2^2) + (q_1^2-q_2^2)^2,\\
&\simeq (q_1q_2)^2 \simeq 4\omega_1^2\omega_2^2\\
s &= (q_1+q_2)^2 = 4\omega_1\omega_2 + 4m_e^2 - E_1'E_2'(1-\cos\theta_1\cos\theta_2 - \sin\theta_1\sin\theta_2\cos(\phi_1-\phi_2))\\
&\simeq 4\omega_1\omega_2.
\end{aligned}$$

The terms neglected in the approximation for s are higher order in θ or m_e. As small q^2 implies small θ ($q_i^2 \simeq -E_iE_i'\theta_i^2 - Q_{i,\min}^2$), these terms are negligible.

Appendix D

Monte Carlo Techniques

A "Monte Carlo" is nothing more than an extravagant numerical integration program. The basic purpose of this type of computer program, as it is commonly applied in particle physics, is the generation of a set of n-dimensional vectors distributed according to a given mathematical function. For instance, a set of four-vectors representing particles whose production is described by a known differential cross section. One advantage of this representation, even for a simple distribution that is analytically integrable, is that cuts can be applied that are difficult to express analytically in terms of the integration variables, and the cuts themselves can be "fuzzy" (though this last type of cut can be treated in an analytic, if somewhat painful, way simply by introducing an additional dimension of integration). The Monte Carlo programs described here attempt to calculate the visible cross sections for various processes with the acceptance losses introduced by detector geometry and trigger arrangements included. It is impossible to integrate the $\gamma\gamma$ differential cross sections analytically, even for simple final-state topologies!

All Monte Carlo programs must use some sort of random number generator. The most commonly used program of this type is called a "pseudorandom" generator, and is a standard part of most computer system libraries. A pseudorandom number generator[195] produces a well defined and reproducible sequence of numbers evenly distributed in the interval $(0,1)$. The most common algorithm used produces an integer sequence – each number being produced by multiplying the previous number (starting with a seed number provided by the user) by a very large number. The operation of multiplication then produces an integer overflow (i.e. it results in a number greater than the largest integer allowed by the CPU word size, 2^{n-1} where $n = 16, 32$, or 60) which is automatically truncated leaving the least significant digits behind. The truncated number is divided by the largest integer allowed to produce a number in the range $(0,1)$. This procedure results in a nearly uncorrelated sequence, but since only a finite number of integers are available from the computer, the sequence must repeat itself eventually. For an optimized algorithm the maximum period of the generator approaches 2^{n-1} numbers – the maximum number of different positive integers given a computer word length n. Correlations in inefficient generators often show up as a linear structure in scatter plots of (X_n, X_{n-m}) where X_n is the n^{th} number of the sequence.

The simplest Monte Carlo algorithm is known as the "Hit or Miss" method. For a one dimensional function this can be visualized quite easily. Given a function, $x \rightarrow f(x)$, representing an unnormalized differential probability distribution, the extreme values of x and $f(x)$ define a rectangular area in the $(x, f(x))$ plane. Many (x, y) are then generated evenly throughout the rectangle using a pseudorandom number generator. For each x value generated, $f(x)$ is calculated, and if the second random number satisfies $y \leq f(x)$, the "event" is accepted; i.e., the accepted numbers, (x, y), will have the required distribution. In other words, the program generates points evenly distributed in the rectangle defined by the extreme values of dependent and independent variables and the fraction of these points that falls in the area under the function is used to calculate the area of the function. The normalized value of the function, $w(x) = f(x)/f(x)_{max}$, is often called a "weight". It is apparent that

$$I = \int_{x_{min}}^{x_{max}} f(x')dx' = \frac{V \cdot N_{accepted}}{N} = \frac{V}{N}\sum_{N} w = V \cdot \bar{w}, \tag{D.1}$$

where N is the total number of points in the rectangle, $N_{accepted}$ is the number of these that fall inside the function's area, and V is the area of the rectangle. There are two ways of calculating the result of the integration: one uses the number of accepted events, $N_{accepted}$, and the other uses the sum of weights. The latter method reduces to a simple numerical integration method with the independent variable points chosen randomly. It is more CPU-time efficient, as extra random numbers, used to decide if an event is accepted or not, are not needed. It is also more accurate, as the error of a Monte Carlo integration behaves as $V \cdot \sigma(w(x))/\sqrt{N}$, where $\sigma(w(x))$ is the variance of the function weights:

$$M(w(x)) = \frac{\int\ldots\int w(x)d^n x}{\int\ldots\int d^n x} = \frac{1}{V \cdot f_{max}} \int \ldots \int f(x)d^n x \tag{D.2}$$

$$\sigma(w(x)) = \sqrt{\frac{\int\ldots\int (w(x) - M(w(x)))^2 d^n x}{\int\ldots\int d^n x}} \tag{D.3}$$

$$\sigma(w(x)) = \sqrt{(\sum w^2 - (\sum w)^2/N)/N}. \tag{D.4}$$

If one only uses the number of accepted "events", the error is $I/\sqrt{N_{accepted}}$ – only a small portion of the available information is used so the error is increased. For an N-dimensional integration the "Hit or Miss Method" generalizes very easily:

1. Given N-independent variables $\{(x^i_{min}, x^i_{max}),\ 1 \leq i \leq N\}$ and the dependent variable $0 \leq f(\vec{x}) \leq y_{max}$, generate a random number within the specified limits for each of the $N+1$ variables $\{\vec{x}; y\}$. Count these trial events by incrementing n_g.

2. If $y \leq f(\vec{x})$ count the "event" as accepted, i.e. increment n_a. These accepted events have weight one.

3. Calculate cuts on the function (i.e. $m \leq n$ dimensional hypersurfaces) if the events survives then count this as a "detected" event, i.e. increment n_d.

4. Repeat steps 1-3 as many times as possible, given computer time cost, availability, the patience of one's colleagues etc.

5. The value of the integral with just the cartesian limits is

$$I = \int \ldots \int f(x)d^n x = \frac{n_a}{n_g} y_{max} \Pi_{i=1,N}(x^i_{max} - x^i_{min}), \tag{D.5}$$

while the value with cuts is obtained by substituting $n_d \rightarrow n_a$. If $f(\vec{x})$ represents a cross section for a physical process, the events passing the cut in the second step can be treated as real events for detector design, background, or acceptance calculations.

One can calculate partially integrated distributions by filling histograms with the appropriate coordinate x^i or with a function of several coordinates.

For one-dimensional distributions many better integration methods exist. The trapezoidal rule divides the integration region into sections and takes the value of the function at the center of each section, approximating the function by a set of trapezoids. The error of this method[196] is $\sim 1/n^2$. The trapezoidal rule integrates exactly polynomials of degree 1 (straight lines). Higher-order quadrature techniques exist (integrating exactly polynomials of correspondingly high degree) but convergence for these methods slows as dimension of integration increases, while a Monte Carlo's convergence rate is independent of dimension. Monte Carlo techniques also have the conceptual advantage that they can be used to produce "events of weight one". The relative errors of various integration algorithms[196] are shown in Table D.

Integration Method & Uncertainty for d-dimensions, N events
Monte Carlo — $\sim 1/\sqrt{N}$
Trapezoidal Rule — $\sim N^{-2/d}$
Simpson's Rule — $\sim N^{-4/d}$
Gauss' Rule (of order m) — $\sim N^{-(2m-1)/d}$

Table D.1: Uncertainty of various integration algorithms.

More efficient methods of Monte Carlo event generation exist. If a one-dimensional distribution is analytically integrable and the integrand invertible, the distribution can be generated exactly using a flat random number distribution as input to the algorithm. Consider:

$$F(x) = \int_{x_{min}}^{x} f(x')dx' \tag{D.6}$$

$$u = \frac{F(x)}{f(x)_{max}} \tag{D.7}$$

$$\frac{dn}{dx} = \frac{f(x)}{f(x)_{max}} \tag{D.8}$$

$$\frac{dn}{du} = \frac{dn}{dx} \cdot \frac{dx}{du} = 1. \tag{D.9}$$

The variable, u, therefore has a constant distribution. From this one calculates $x = F^{-1}(F(x_{max}) \cdot u)$. If the u's are generated by a pseudorandom number generator the numbers, x, will have the desired frequency distribution, $f(x)$. For a multidimensional distribution, e.g. $f(x,y) = g(x)h(x,y)$, this becomes slightly more complicated. One must first generate x using $F_y(x) = \int_{y_{min}}^{y_{max}} f(x,y)dy$ as the input distribution (i.e. generate x for any y) and having generated x generate y from the full distribution with x fixed – $f(x,y)$ is proportional to the conditional probability of x given y. If the function can be written as $f(x,y) = g(x)h(y)$ both distributions can be generated independently. When a complicated distribution can be separated into several additive positive definite expressions and exact algorithms can be built for each of these separately, the Monte Carlo can be split into "sub-generators". In this case the final distribution is generated by giving each additive term a probability defined by its contribution to the total integral and branching to one of the "sub-generators" accordingly (each decision being made by generating a new pseudorandom number).

One can combine the "Hit or Miss" and the "Exact" methods to produce an algorithm known as "Importance Sampling". In this technique the complicated cross section that is being integrated, $f(\vec{x})$, is first approximated by a simpler function, $g(\vec{x})$, which is amenable to the "Exact" method, and the N dependent variables are generated according to this distribution. The generation of these random vectors replaces the generation of vectors over the larger volume used in the "Hit or Miss" method – if the approximation is good, only a small fraction of the "wasted volume" of the simple algorithm remains. For a given $\vec{x}$ the probability of an event lying inside the $(N+1)$-volume defined by $f(\vec{x})$ is $w(\vec{x}) = f(\vec{x})/g(\vec{x})$ i.e. $g(\vec{x})$ replaces $f(\vec{x})_{max}$ in the weight calculation resulting in a higher average weight. It is assumed that $g(x)$ is normalized so that the weight has a maximum value ≤ 1. The main advantages of this method are dependent on the quality of the approximation. If this is good, the efficiency for producing events of weight one, $\frac{\#accepted}{\#generated}$ is improved, and the variance is much smaller, leading to faster convergence. It occasionally becomes necessary to use several different approximations to the function in different regions of phase space. This is more complicated but can improve the convergence of the program. Each region is then given a weight, proportional to the maximum weight of the approximation used (ideally they should all be equal to 1) and the integral of the approximate function.

In summary, the general problem treated by Monte Carlo techniques is the evaluation of

$$R = \int \dots \int_V r(\vec{\rho}) d^n \rho, \tag{D.10}$$

which can be discretized (via the "Hit or Miss" Method) as:

$$R = \frac{V}{N} \sum r(\vec{\rho}_i) = V < r >_V, \tag{D.11}$$

where $\vec{\rho}_i$ are N points randomly distributed in the n-dimensional volume of integration.

One can change the variables of integration ("Importance Sampling") $\vec{\rho} \rightarrow \vec{\alpha}$:

$$R = \int \dots \int_W r(\vec{\rho}) J(\vec{\rho}) d^n \alpha = W < rJ >_W = \frac{W}{N} \sum_i r(\vec{\rho}_i) \cdot J(\vec{\rho}_i). \tag{D.12}$$

If the Jacobian of the transformation, $J(\vec{\rho}_i)$, is chosen so as to smooth the dynamic range of the integration, the efficiency of the Monte Carlo improves. Clearly the optimum is $J(\vec{\rho}) = r(\vec{\rho})^{-1}$, which in effect requires an analytic solution to the integral – it also, reasonably enough, causes the variance of the result to go to zero:

$$\Delta R = \frac{W}{\sqrt{N}} \sigma(rJ)_W = \frac{1}{N} \sqrt{\sum (w - \bar{w})^2} = \frac{1}{N} \sqrt{\sum w^2 - (\sum w)^2 / N}. \tag{D.13}$$

The integrands in the preceding equations are generally referred to as statistical weights. These determine the relative importance of the event. The last step in the "Importance Sampling" algorithm turns these into "events of weight one", i.e., events of equal importance or probability. If one calculates an observable using every weighted event, the statistical fluctuation is less. When using $w = 1$ events only the standard "experimental" $1/\sqrt{N}$ fluctuation remains.

Appendix E

Statistical Methods

The general problem addressed by the statistical techniques used in elementary particle physics is that of describing a set of measurements via parameters inspired by some physical model. The maximum-likelihood method is widely advertised [197] as the most efficient way of doing this. Given Q parameters ($\vec{\lambda} = (\lambda_1, ...\lambda_Q)$) describing a set of N_{data} experimental events, each consisting of M measurements $\vec{X}^i = (X_1^i, ...X_M^i)$, and a probability density function, $f(\vec{X}|\vec{\lambda})$, for observing $\vec{X}$ given the parameters $\vec{\lambda}$, the likelihood function is defined as:

$$L = \prod_{j=1}^{N_{data}} f(\vec{X}^j|\vec{\lambda})$$

This is simply the probability for observing the existing data set; it is a function of $\vec{\lambda}$. The principle of maximum likelihood states that the best estimate of the parameters maximizes this function. Frequently, the logarithm of this function is used instead, as this has various advantages in computation. To determine the errors on the set of parameters, one expands the logarithmic likelihood function about its maximum (at λ_0) in a Taylor's series. For a single parameter the logarithmic likelihood reduces to

$$\log L(\lambda) = \log L(\lambda_0) + \frac{1}{2}(\frac{d^2 \log L}{d\lambda^2})_{\lambda_0}(\lambda - \lambda_0)^2,$$

as the first derivative of L is zero at the maximum. On taking the exponential of this, the analogy to a Gaussian distribution with $\sigma = (-1/(\frac{d^2L}{d\lambda^2})_{\lambda_0})^{1/2}$ is obvious; this can then be identified as the error on λ. In the case of several parameters one can extract a covariance matrix, in analogy with a multivariate Gaussian distribution ([2], p.75):

$$[V^{-1}]_{ij} = -(\frac{\partial^2 L}{\partial\lambda_i \partial\lambda_j})_{\vec{\lambda}_0}.$$

To the extent that the likelihood distribution is not Gaussian at its maximum, this method of error estimation is an approximation. One often defines asymmetric errors such that:

$$\log L(\lambda_0) - \log L(\lambda_0 + \Delta\lambda^+) = \tag{E.1}$$

$$\log L(\lambda_0) - \log L(\lambda_0 - \Delta\lambda^-) = \frac{1}{2}, \tag{E.2}$$

which corresponds to a 67% confidence interval. For Gaussian distributions the two definitions coincide.

A simple application of the maximum-likelihood method is to determine the parameters describing an angular distribution in the case of constant acceptance:

$$\frac{d\sigma}{d\cos\theta} = \sigma \cdot f(\cos\theta, \zeta)$$

$$f(\cos\theta, \zeta) = \frac{1 + \zeta\cos^2\theta}{2(1 + \zeta/3)}. \tag{E.3}$$

One can simply take the normalized angular distribution, $f(\cos\theta, \zeta)$, as the probability density function. Notice that the total number of events is *not* a parameter in this application; this is constrained to be N_{data} by the normalization of $f(\cos\theta, \zeta)$. One can, more generally, use Poisson statistics to similar ends:

$$Po(n|\bar{n}) = \frac{\bar{n}^n \cdot e^{-\bar{n}}}{n!},$$

$$\bar{n} = S \cdot \sigma,$$

where S is the sensitivity (defined as the number of events expected to be observed per unit cross section, including luminosity and acceptance). Adding the logarithm of this to the logarithmic likelihood (e.g. multiplying independent probabilities) one obtains:

$$\log L = \sum \log f(\cos\theta, \zeta) + n_{data} \log\bar{n} - \bar{n} - \log n_{data}!$$

This has the expected trivial solution $\bar{n} = n_{data}$ due to the simplicity of the situation. This relaxation of the normalization in E.3 is often referred to as the "extended maximum-likelihood method". This is really a misnomer as it simply replaces one p.d.f. by another – the Poisson distribution is automatically normalized.

The general case is more complex. One can consider the N_{data} events observed as partitioning the phase space, $\vec{X}$, into bins Δ_i, $i = 1, N_{data}$. The average number of events predicted in the j^{th} bin is then

$$\bar{n}_j(\vec{\lambda}) = \int_{\Delta_j} S(\vec{X}) \cdot \sigma(\vec{X}, \vec{\lambda}) \prod_{i=1\to M} dX_i$$

$$= \langle\sigma(\vec{X}, \vec{\lambda})\rangle_{\Delta_j} \Delta S_j,$$

and the Poisson likelihood for each bin is then simply $Po(1, \bar{n}) = \bar{n}e^{-\bar{n}}$. The only "extension" to the maximum-likelihood method now required is to apply the likelihood equation not to N_{data} events from a single probability distribution function but to single events taken from N_{data} density functions:

$$\log L = \sum_{data} Po(1, \bar{n})$$

$$= \sum_{data} \log\bar{n}_i(\vec{\lambda}) - \int S(\vec{X}) \cdot \sigma(\vec{X}, \vec{\lambda}) \prod_{i=1\to M} dX_i.$$

If one then makes the assumption that the measured $\vec{X}^i$ values are equivalent to the average $\vec{X}$ values in the i^{th} bin one arrives at

$$\log L = \sum_{data} \log \sigma(\vec{\lambda}, \vec{X}_i) - \int S(\vec{X}) \cdot \sigma(\vec{X}, \vec{\lambda}) \prod_{k=1 \to m} dX_k + \sum_{data} \log \Delta S_j, \qquad \text{(E.4)}$$

where the ΔS_j are parameter independent and can therefore be ignored when maximizing the function. This likelihood function is rather useful in that the terms dependent on the data and acceptance are separately calculable. At first sight the most dangerous aspect of this expression is its dependence on an artificial binning Δ_i. This is actually illusory. On partitioning any bin Δ_i into a filled bin Δ_{i_1} and an empty bin Δ_{i_2} no change in the *parameter dependent* part of the expression appears (this process can be iterated to arrange any binning). The empty bin contributes a term $-\bar{n}_{i_2}$ to the likelihood, while the filled bin contributes $\log(\bar{n}_{i_1}) - \bar{n}_{i_1}$. Since $\bar{n}_i = \bar{n}_{i_1} + \bar{n}_{i_2}$, the value of the integral in E.4 does not alter. The contribution to the argument of the logarithm, $\bar{n}_{i_1}$, will get smaller, but this last change affects only the ΔS_i. A similar argument leads to the realization that there is no actual approximation involved in using $\sigma(\vec{X}^i, \vec{\lambda})$ as evaluated at the data points. One can arrange the bins as small as necessary about each X^i.

The parameters λ_i (such as resonance masses and widths) can be constrained to the results of previous measurements $(\lambda_i^* \pm \Delta\lambda_i^*)$ by the addition of a term: $-\chi^2(\lambda_i)/2$, where $\chi^2 = (\lambda_i - \lambda_i^*)^2/(\Delta\lambda_i^{*2} + \Delta\lambda_{i,sys}^{*2})$ and $\Delta\lambda_{i,sys}^*$ is the systematic error estimated for the parameter in the current measurement.

The sensitivity function, $S(\vec{X})$, used above is generally calculated numerically by Monte Carlo techniques. In the maximum-likelihood analyses described in this thesis, Monte Carlo events are generated with a constant final state cross section $\sigma_{\gamma\gamma}$ - the events are then distributed in phase space according to the $\gamma\gamma$ luminosity. The combined e^+e^- luminosity, $\gamma\gamma$ luminosity correction, acceptance, and trigger probability is then introduced for each Monte Carlo event as a weight

$$W = P_R \cdot P_T \cdot P_A \cdot \frac{L_{data} \cdot \sigma_{MC}}{N_{MC}},$$

where

1. $P_R(= 0, 1)$ is the probability of the event being reconstructed, passing the standard selection cuts (EXPDST, EXTWOP etc.), and having two charged tracks within a region of the detector containing the trigger fiducial region (typically $P_\perp >$ 0.1 GeV/c and $|\cot\theta| < 1.3$),
2. P_T is the trigger probability of the event as calculated by the TRIGGR simulation,
3. $P_A(= 0, 1)$ is the probability of the event passing the analysis cuts,
4. L_{data} is the experimental luminosity used,
5. N_{MC} is the total number of Monte Carlo events generated,

6. σ_{MC} is the integral of the $\gamma\gamma$ luminosity with a constant $\gamma\gamma$ cross section over the final state phase space.

The integral in E.4 is then calculated as

$$\int S(\vec{X}) \cdot \sigma(\vec{X}, \vec{\lambda}) \prod_{k=1 \to m} dX_k = \sum_j W_j \cdot \sigma(\vec{X}^j, \vec{\lambda}). \qquad \text{(E.5)}$$

The expression derived for the likelihood is then maximized using a computer program such as MINUIT [198]. For a large number of data and Monte Carlo events this can be very time consuming. The repeated calculation of the integral in equation E.5 is particularly computer intensive, as the number of Monte Carlo events should be much larger than the number of experimental events. Luckily, one can often simplify the calculation. In the K^+K^- analysis described in the text the cross section can be factored as:

$$\frac{d\sigma(W_{\gamma\gamma}, \cos\theta, \vec{\lambda})}{d\Omega} = \sum_{JM} \sigma_{JM}(W_{\gamma\gamma}, \vec{\lambda}) Y_{JM}(\theta, \phi)$$

One can then take moments of the sensitivity for the different partial waves contributing to the cross section. These one-dimensional distributions, functions of $W_{\gamma\gamma}$, can then be histogrammed using bin sizes of the same order as the detector resolution (5 MeV/c^2), with negligible loss of accuracy and a considerable increase in the efficiency of the computer analysis. At this point the stability of computer algorithm for finding the maximum can be improved, if the distributions of the sensitivity moments is smoothed. This is done using an algorithm based on cubic spline smoothing provided by the HBOOK package of CERNLIB.

The maximum-likelihood method represents the most efficient use of the available data. The least-squares method is a slightly less efficient way of extracting parameters from a data sample, adequate for analyses that are not limited by the statistics available (e.g. the η' analysis in this thesis). In this method the distribution to be fit is formatted as a histogram with sufficiently large bins that Gaussian statistics apply. A χ^2 is then defined as:

$$\chi^2 = \sum_{bins} \frac{(X_{theory} - X_{data})^2}{\Delta X_{theory}^2 + \Delta X_{data}^2}$$

this corresponds to a likelihood function of $-\chi^2/2$. The change required for a 1σ error corresponds to a change in the χ^2 of 1. This method has the advantage of producing an absolute probability of fit defined by the χ^2 and number of degrees of freedom [2]. The likelihood method, at least in the limit discussed above, can be used only to provide relative qualities of fits. This limitation is due to the ambiguity in the parameter independent part of the likelihood function. As one might expect, the least-squares method develops difficulties in situations with low statistics which may lead to bias in the result, e.g. in fitting a strong signal on a small background the latter may be distorted, as the Gaussian error calculation is not applicable. This would result in an overestimate of the signal. One can easily define a binned maximum-likelihood method

that does not have this difficulty by defining the error definition used in the χ^2 to correspond to 67% Poisson likelihoods for bins with limited statistics.

Statistical errors (Δ_i) on each parameter are calculated as the change required to decrease the maximum likelihood by 0.5 with all other parameters fixed. In contrast, the change (Δ_i') required to decrease the likelihood by 0.5 with all parameters free is used to calculate the error due to correlations between the parameters: $\Delta_i^{\rm corr} = \sqrt{\Delta_i'^2 - \Delta_i^2}$. The difference between the two quantities can be visualized easily in the case of a two-dimensional fit. For a Gaussian distribution, the contour of constant likelihood $l_{max} - 0.5$ is a skew ellipse in the parameter plane centered on the point of maximum likelihood. If one uses this point as the coordinate origin, the statistical error on a parameter is the intercept of the error ellipse with the parameter axis, while Δ_i' is half the range of the parameter over the error ellipse. It is more common to use the larger error (Δ_i') as the statistical error. One must stress that, in the analyses presented here, this additional error is not ignored but treated as a contribution to the systematic error – the combined statistical and systematic error is independent of this discussion.

This convention is chosen as the error due to parameter correlations is more appropriately treated as a systematic error. Admittedly, this error is sensitive to statistical fluctuations in backgrounds (η' analysis) or additional continuum or resonant contributions (K^+K^- analysis). However, it is also sensitive to the ansatz made for the functional form of these contributions – a systematic effect. Introducing parameter constraints in the likelihood function combines the unconstrained statistical error of the parameter with the error used in the constraint. This error is a combination of the statistical and systematic errors on the previous measurements, that determine the constraint, and the systematic error of the current measurement. Because of these ambiguities, it is simpler to use the unambiguous segregation of the errors described.

The error calculated from the shape of the likelihood function does not take into account statistical error in the Monte Carlo integral. This is difficult to introduce into the likelihood method from the beginning of the derivation. One would have to introduce a statistical error on each bin of the distribution E.4, which would correspond to introducing as many parameters (for the distribution of Monte Carlo normalizations) as there were Monte Carlo events. One rather tedious way to estimate this quantity is to divide the Monte Carlo data into n sub-samples and plot the variance of the fit results against n to extrapolate to $n = 1$. However, given that the final likelihood function is only sensitive to the Monte Carlo through the integral, the uncertainty in the integral (0.7% in the K^+K^- analysis) should translate directly into an uncertainty in the maximum value of the likelihood. This is still another advantage of the maximum-likelihood method – if one were to try to unfold the experimental cross sections by dividing histograms filled with experimental data by histograms of the Monte Carlo sensitivity, the fluctuations of the Monte Carlo in each bin would couple to the result. In the likelihood method these fluctuations are consigned to the parameter independent part of the integral. As the standard error in each parameter is defined as that required to decrease the likelihood by 0.5, the contribution of Monte Carlo statistics increases

the standard error by 1.014 for the K^+K^- analysis. This is smaller than any error on the error, which is perhaps a sufficiently awkward phrase to warrant the termination of this discussion.

Appendix F

TRIGGR: A Trigger Simulation For ARGUS

The first section of this manual describes the general properties of the TRIGGR program. The second section is meant as a brief introduction to the use of the program. It is followed by several examples and some sections on special applications (in particular use of the program with the Kinematical Analysis Language – KAL). The remaining sections provide detailed information on the individual subroutines.

F.1 Introduction

To simulate the ARGUS trigger, H. D. Schultz (DESY) developed a program to analyze output from the ARGUS simulation program, SIMARG. For each SIMARG event this program summed the appropriate shower counter pulse heights for each trigger element, determined the LTF masks set using the drift chamber TDC information, and then proceeded to analyze the trigger logic and determine whether the event was triggered. This program had several limitations:

- The trigger thresholds were described by step functions.
- The thresholds had been determined only for experiment 2 (1983) and it is not clear if they were determined with the calibration and energy scale appropriate for Monte Carlo data.
- The LTF efficiency was not derived directly from data and was included only via the introduction of a constant probability for deleting TDC hits during the unpacking of the drift chamber information.
- There was no provision for the variation of drift chamber efficiency with particle type, path-length, or momentum.
- It was up to the user to wander through a maze of trigger periods (now numbering 38). Only the first 5 periods were installed in the program. Though most of these periods were repetitions of old trigger logics, the thresholds of the trigger elements and efficiencies of the LTF changed over time.

- The program was not optimized for "black box" use as a post-processor for SIMARG.

An extended version of the program that remedies these faults has been developed along with a collection of programs for extracting the evolving trigger thresholds and efficiencies from experimental data. The current version of the program has constants installed for all data up to the end of experiment 6 (1988).

The new version of the trigger program has several differences:

- The probability of a given pulse height setting a trigger element has been determined from redundantly triggered multihadron (EXMUHA) data and fitted to a function that reproduces the experimental threshold shape to better than 1% RMS.
- The energy scale for the Monte Carlo has been checked and the trigger pulse heights calculated in such a way that they represent values of the analog sum of scintillator pulse heights and not total energy in the shower counter. (i.e., they are not corrected for the energy deposited in lead, as this is not done in the hardware).
- One can override the GHEISHA/SIMARG simulation of hadronic showers and use shower energy distributions determined directly from experimental data for pions and kaons.
- The shape of the LTF efficiency distribution has been determined for each trigger period from Bhabha events.
- The dependence of the LTF efficiency on the specific energy loss in each drift cell (as determined by particle mass, momentum, and path-length) has been derived from the variation of the Bhabha LTF efficiency with polar angle.
- The VAX online filter has been introduced in the simulation for the appropriate subset of the trigger history. Relevant statistics are also printed out on termination.
- The program accesses a user supplied logical function (UCUTTR) that allows the choice of trigger periods in a simple manner.
- A second logical function (UCUTRN) allows the user to introduce quality, experiment, run, and center of mass energy restrictions. These cuts should be the same as employed in the analysis of the data. This information is extracted from the ARGUS run file.
- The program calculates, for each event, either a trigger probability or an event weight. These are luminosity weighted averages over all experimental periods chosen by the user (via UCUTTR, UCUTRN).
- Luminosity weighted distributions of center of mass energy ($\sqrt{s}$), as selected by UCUTRN, are accumulated for each trigger period in the program initialization. These are accessed by a third user supplied function, UENG, which is used to scale the event weight for $\sqrt{s}$ variations in cross section if desired.

- When given the "Monte Carlo luminosity" (in a fourth user defined subroutine, UASIGN) the program will return an event weight – the number of data events the Monte Carlo event represents. It will normalize the Monte Carlo data for the experimental luminosity automatically. This also allows the introduction of the $\gamma\gamma$ luminosity in a simple manner in two-photon analyses.
- Provisions are made (via UASIGN) to mix several sets of Monte Carlo data with different normalizations (i.e. different background sources or SIMARG runs for various detector configurations) and to assign them to different subsets of the experimental luminosity (e.g. SIMARG data generated with the VDC present can be assigned to the appropriate trigger periods etc.).
- On termination the program prints out detailed statistics.
- The systematic error involved has been studied in detail.

F.2 A Brief Users Guide for TRIGGR

This is included for the convenience of those collaboration members who may wish to use this program. The usual applications envisioned are to run the program as:

1. part of the ARGUS reconstruction job for SIMARG data,
2. a separate job with the calculated weight stored on a separate disk data set for future use in histogramming jobs,
3. part of the users standard analysis job.

The trigger simulator must use full format events from SIMARG as input – it needs access to the drift chamber TDC information, the raw shower counter pulse height information, and the raw ToF counter hit information. For this reason it is difficult to run TRIGGR externally to the ARGUS reconstruction environment because the program needs calibration and geometry constants for its calls to DTUNPK, SHUNPK, and TFUNPK. The first two of these calls must be made from the TRIGGR package even if the unpacks have already been done by the reconstruction because different parameters are used. In previous versions of the package, this repetition introduced some conflicts which have, hopefully, been resolved. The SIMARG Monte Carlo input must also have been processed by the ARGUS reconstruction program (the current version expects ARG11). It is recommended that one calls the TRIGGR routine from PHMAIN (the standard entry provided for physics analysis) while running the normal ARGUS program with the reconstruction turned off (RC OFF), i.e., in a separate job following the actual reconstruction.

The trigger program is written in FORTRAN66 in order to maintain compatibility with the ARGUS reconstruction software. There are two sets of source/object libraries necessary to link the trigger program. The versions on the DESY IBM are 'F15MCL.TRIG11.V04S/L' (which contains most of the routines), and '...V03S/L' which contains the LTF simulation. The corresponding V01 and V02 libraries contain the

software used to extract the pre-trigger and LTF efficiency constants respectively. VAX versions of these libraries are also available.

Though it is possible to run the full LTF simulation in a normal call to the TRIGGR program, this is not advised. The LTF simulation takes up almost as much computer time as the ARGUS reconstruction itself. One generally wants to repeat the trigger simulation several times with different parameters. As these do not affect the LTF simulation it is best to run it as a separate job and save the output. This is set up in the file LTFDUMP which calls the LTF simulation routines from a PHMAIN and should be run with the normal ARGUS reconstruction program with "RC OFF". The output is written on unit 13 in a format convenient for the trigger program and needs the data file 'F15HDS.MASKAR.DAT'. This file provides constants describing the LTF mask set. Sample command files are given in #LTFDUMP in the V04 library. At this stage, the drift chamber hit acceptance probability (defined by the "CU DT MCE 1.0" control card) is supposed to be 100%.

At this point, it is probably best to read the sections on the routines UCUTRN, UCUTTR, UASIGN, UENG, and TRIGGR, and then return to the examples listed below. One should note that most of the routines are heavily commented, hence useful information can also be found there. An example of the JCL needed to run the trigger program can be found in the #TRIGGER member in the V04 library.

F.3 Example 1: Trigger calculation for $\gamma\gamma \to \eta'$

In this example the variable WEIGHT represents the number of real events each Monte Carlo event represents. The full LTF simulation has been previously stored on disk and is read from unit 13. The drift chamber efficiency distributions used are those calculated from good quality runs and the entire ARGUS trigger history is simulated. Finally, the trigger calculation is done 8 times and averaged in order to sample the LTF efficiency and better reflect the shape of the trigger thresholds. The weight is then stored on unit 77 in a format designed to be easily transferable between the VAX and the IBM. The call to TRGEND calculates various statistics.

```
      SUBROUTINE PHMAIN
      COMMON/VWT/N,W
%MACRO CZDATA
      DIMENSION WEIGHT(5)
      CALL TRIGGR(1,2,WEIGHT,0,8)
      WRITE(77)4,WEIGHT,NHDEXP,NHDRUN,NHDEVT
C ACCUMULATE STATISTICS
      N=N+1
      W=WEIGHT+W
      RETURN
      END
      SUBROUTINE USERTE
```

```
      COMMON/VWT/N,W
      CALL TRGEND
      PRINT 101,N,W
101   FORMAT('   NUMBER OF EVENTS DUMPED:',I6,' TOTAL WEIGHT:',F15.7)
      RETURN
      END
```

The luminosity per trigger period is calculated using only experiments 2, 4, 5, and 6 and good quality runs:

```
      LOGICAL FUNCTION UCUTRN(NRNFLG,XRNECM,NRNMFL,NRNSFL,NRUN,NEXP)
C
C   NRNFLG - RUNFLAG
C   XRNECM - CMS ENERGY
C   NRNMFL - M-FLAG
C   NRNSFL - S-FLAG
C   NRUN   - RUN#
C   NEXP   - EXP#
C
C    EXAMPLES:
C NO CUTS (DEFAULT)
      UCUTRN= NRNFLG.GE.0 .AND. NEXP.NE.3 .AND. NEXP.LT.7
      RETURN
      END
```

Only those trigger periods with a minimum LTF threshold (excluding HESH) of two are simulated (member CTRGDAT includes comments describing the different variables accessible):

```
      LOGICAL FUNCTION UCUTTR(ITRIG)
%MACRO CTRGDAT
      I=MIN0(IBOTH(ITRIG),ICPPT(ITRIG),IMATRX(ITRIG))
      UCUTTR=I.EQ.2
      RETURN
      END
```

There are two types of Monte Carlo events on the input data set. 39022 events generated with SIMARG experiment -1 in order to simulate experiment 2, and 39022 events run with SIMARG experiment -4 (with VDC simulation enabled) in order to simulate all later experiments. The cross section divided by the two-photon width of the η' was calculated by the generator as .052713 nb/keV. Note that if these separate Monte Carlo data samples were supposed to cover the same segment of experimental luminosity then one would use YMCLUM(1)=YMCLUM(2)=1480.5456 and IMCEXP(1)=IMCEXP(2)=8.

```
      SUBROUTINE UASIGN
%MACRO CMCLUM
      NUNMC=2
```



```
C 78044 EVENTS  INVERSE PICOBARNS MC LUMI (SIGMA=.052713 NBARN/KEV)
      YMCLUM(1)=1480.5456/2.
C 1 CORRESPONDS TO ALL EXPERIMENTS
C 2,3,4,5,6 CORRESPOND TO EXPERIMENTS 2-6
C 7 CORRESPONDS TO EXPERIMENT 4,5,6
C 8 CORRESPONDS TO ALL EXPERIMENTS BUT EXPERIMENT 3 BAD AREAS
      IMCEXP(1)=2
C FORMAT ABS(EXP#)*10000+FIRST RUN#
      IMCMIN(1)=10001
C FORMAT ABS(EXP#)*10000+LAST RUN#
      IMCMAX(1)=19999
C
      YMCLUM(2)=1480.5456/2.
      IMCEXP(2)=7
      IMCMIN(2)=20001
      IMCMAX(2)=29999
      RETURN
      END
```

The correction for the energy dependent two-photon luminosity is made as the ratio of the expression for resonance production in the double equivalent-photon approximation (DEPA). Which is good enough for this calculation as it is already a small effect (1-2%) and the inaccuracies largely cancel in the ratio.

```
      FUNCTION UENG(ITRIG,EGEN)
C ITRIG - CURRENT TRIGGER PERIOD
C EGEN  - ENERGY FROM MONTE CARLO EVENT RECORD
%MACRO CTSTAT
C SCALING FACTOR AS A FUNCTION OF THE TWO-PHOTON FINAL STATE
C MASS AND THE CENTER OF MASS ENERGY.
      FF(X,S)=LOG(S/4./.0005110034**2)**2*(-(2.+X)**2*LOG(X)-
     @  2.*(1.-X)*(3.+X))
C EXTRACT AN ENERGY RANDOMLY FROM THE LUMINOSITY WEIGHTED HISTOGRAM
C FOR THIS TRIGGER PERIOD
      S2=HRNDM1(11000+ITRIG,DUMM)**2
      S1=EGEN**2
      X2=.95757**2/S2
      X1=.95757**2/S1
      UENG=FF(X2,S2)/FF(X1,S1)
C ACCUMULATE STATISTICS
      ENG=ENG+UENG
      NENG=NENG+1
      RETURN
      END
```

F.4 Example 2: Events of Weight 1

In this example the trigger probability is returned. The events are then turned into events of weight 1 by a standard Monte Carlo algorithm and written to unit 2. The variable NLOOPS is set to one because there is little point in sampling the probability accurately if one is going to discard most of the events. The fast LTF simulation is used with the efficiency parameters calculated from runs of all qualities.

```
      SUBROUTINE PHMAIN
      COMMON/VWT/N,W
%MACRO CZDATA
      DIMENSION WEIGHT(5)
      CALL TRIGGR(1,-1,WEIGHT,0,1)
      N=N+1
      W=WEIGHT+W
      IF(W.GT.RNDM(0))RETURN
      CALL OUTEV(2)
      RETURN
      END
```

The luminosity per trigger period is calculated using only experiments 2 and 4. Only runs with extremely bad run flags are omitted.

```
      LOGICAL FUNCTION UCUTRN(NRNFLG,XRNECM,NRNMFL,NRNSFL,NRUN,NEXP)
C
C   NRNFLG - RUNFLAG
C   XRNECM - CMS ENERGY
C   NRNMFL - M-FLAG
C   NRNSFL - S-FLAG
C   NRUN   - RUN#
C   NEXP   - EXP#
C
C    EXAMPLES:
C NO CUTS (DEFAULT)
      UCUTRN= NRNFLG.GE.-40 .AND. NEXP.NE.3 .AND. NEXP.LT.5
      RETURN
      END
```

There is one type of Monte Carlo event on the input data set and ILEV=0. Hence, there is no need for a complicated UASIGN. The default is used.

```
      SUBROUTINE UASIGN
      NUNMC=1
      RETURN
      END
```

There is no correction for center of mass energy:


```
      FUNCTION UENG(ITRIG,EGEN)
      UENG=1.
      RETURN
      END
```

F.5 Using KAL with TRIGGR

The easiest way to use TRIGGR for KAL is to set TRIGGR to generate the event trigger probability and then eliminate events as in example 2. One then needs to have nothing further to do with the trigger simulation.

This technique is often quite inefficient (the efficiency is simply the average trigger probability) and eliminates the possibility of using event weights. It is better to proceed as in example 1 and store the event weight or probability information on a separate data set. This data set can then be accessed through the CALLFORT statement in KAL during subsequent analysis.

F.6 Source Documentation

Routines written or modified by the user

There are normally five routines that the user either has to modify (USERTE, PHMAIN) or supply for the program (UCUTTR, UCUTRN, UASIGN). If the user desires to adjust the weight of each event to simulate a cross section dependent on beam energy an additional routine, UENG, must be supplied. These are all supplied with sensible defaults and examples in the V04 library.

Documentation Members

There are five documentation members:

HISTORY: A modified version of the ARGUS trigger list and the official trigger list of this program - some of the normal ARGUS trigger periods have been subdivided due to sudden changes in drift chamber efficiency etc.

BUGFIXS: A record of all modifications.

FASTMAN: An early version of this users manual.

NEWS: News about recent improvements.

NEWVERS: The changes recommended when installing a new version.

TRIGGER: The LATEX source for this manual.

VAXIBM: Modifications recommended in moving the source from the VAX to the IBM and back.

Block Data Routines

These are all in member BLOCDATA. These routines contain full specifications of the ARGUS trigger history, the fraction of online filter rejects accepted, the pre-trigger threshold shapes, and the LTF efficiency distribution in each trigger period.

Common Blocks

There are four common block or macro members:

1. CMCLUM: Information used for event normalization and data set mixing.
2. CTRGDAT: Trigger geometry and logic history.
3. CTRSTO: The trigger element pulse heights for the current event generated by the call to TRBLD.
4. CTSTAT: Scalars that are used to estimate the trigger element and average LTF efficiency together with various other statistics on termination.

Various other common blocks link the block data information to the routine THRESH which parametrizes the threshold and efficiency shapes. These commons appear only in these two routines.

DTUN00

This is included for use with program LTFDUMP or with the full LTF simulation (LTFMC) when run from TRIGGR. It is a modified version of the ARGUS reconstruction routine DTUNPK. There is an additional common block that passes the layer 17 hit information to LTFDUMP. This is an artifact of the study of the LTF efficiency when a very abbreviated version of DTUNPK was used that only unpacked layer 17 and ran independently of ARGUS. This slight modification allows LTFDUMP output to be compatible with the programs originally used to calculate the LTF efficiency. The current version should run without interfering with the reconstruction.

In addition, the routine is modified so that it will not randomly discard hits to simulate drift chamber inefficiency – for the trigger simulation this is done elsewhere (TRIGGR, ELTF3). For the normal DTUNPK, a card, "CU DT MCE 0.95" would discard 5% of the drift chamber hits. Old versions of the TRIGGR and LTFDUMP programs, using DTUNPK directly, would either require a modification of the card or override it in the source code – which would produce an incorrect drift chamber efficiency for the pattern recognition and track fitting if the TRIGGR program was run with the reconstruction turned on. Finally, no "AND" is required between the TDC hits and ADC hits (as in the LTF hardware). Enforcing this option with the old DTUNPK by setting the control variable LDTUNP=1 also interfered with the reconstruction standards.

ELTF1,ELTF2

These routines generate the LTF efficiency according to a luminosity weighted distribution of individual run efficiencies for each trigger period. The distributions were parametrized by the sum of two Gaussians. ELTF1 returned the efficiency as determined by high quality runs (run flags greater than -10) while ELTF2 returned the efficiency with relaxed quality cuts (run flags greater than -40). In May 1989 these routines were replaced by ELTF3.

ELTF3

The LTF efficiency for individual tracks is parametrized as:

$$\eta_{LTF} = \eta_{ToF} \cdot \alpha \cdot (1 - exp(-\beta(\frac{\delta E}{\gamma})^2))$$

where η_{ToF} is the the fraction of live ToF counters for each trigger period; δE is the theoretical energy loss in each drift cell as a function of particle type, momentum, and path-length; and γ is the energy loss in a drift cell for a 5 GeV electron at $\theta = 90°$ (the $\delta E/\gamma$ ratios are generated in the call to routine LTF). α and β are constants fitted to the distribution of Bhabha LTF efficiency a function of $\cot\theta$:

$$\eta_{LTF}(Bhabha) = \eta_{ToF} \cdot \alpha \cdot (1 - exp(-\beta(1 + \cot^2\theta))).$$

These are determined separately for each trigger period. This parametrization replaces that of ELTF1 and ELTF2. The approximation of a constant LTF efficiency during each trigger period produces negligible effect.

LTF

This routines simply branches to LTFFA, LTFRD, or LTFMC depending on the absolute value of LTFFLG (1,2,3 respectively). It returns a simulated LTF bank and is called from TRIGGR.

LTFDUMP

This is a version of PHMAIN that writes the LTF information calculated by Dr. Schultz's LTF simulation to disk so that it can be retrieved by TRIGGR (via LTFRD) at a later date. The full LTF simulation requires a significant amount of time and it is best that it is done once and saved. This lets the trigger program run roughly twenty times faster. The program produces an output data set on unit 13 which is usually small enough to fit on disk (the size will be approximately 44 bytes per charged track) and needs 'F15HDS.MASKAR.DAT' on unit 12. There is some extra information in this dump as it uses the same format as that used to compress EXPDST's for the LTF efficiency determination. If one wishes to simplify the dump one should also make changes in LTFRD.

LTFFA

This is the fast LTF simulation, and is called from LTF. It is not as complete as the full simulation (LTFMC). The maximum number of charged tracks it produces is limited by the number of tracks found by the pattern recognition. The real LTF often produces several masks for one drift chamber track – compensating to an extent for drift chamber inefficiency. LTFFA uses the reconstructed charged track bank as a starting point - it takes the track's layer 17 hit and Tof Counter hit (TFUNPK is assumed to have been called by TRBLD) and calculates the LTF mask number. The ratio of energy loss per drift cell to that expected for a 5 Gev electron at $\theta = 90°$ is also calculated and stored for later use in scaling the LTF efficiency.

LTFLOS

This is a slight modification version of Dr. Schultz's LTFLOS from the V03 library.

LTFMA

This routine is called from LTFMC and LTFRD and does the reverse of LTFFA. It matches masks from the full Schultz LTF simulation to fitted drift chamber tracks. It then uses the Monte Carlo track matched to the fitted track to identify the particle and calculate the drift cell energy loss ratio as in LTFFA. If no match is found between the fitted track and a Monte Carlo generated track the most likely hypothesis based on ToF and dE/dX information is used and if neither of these is available the particle is assumed to be a pion.

LTFMC

This is the interface to Dr. Schultz's original LTF simulation routines LTFRES, and LTFLOS (initialization). This routine is called from LTF. The full LTF generator is normally run with 100% drift chamber efficiency in the unpack of the TDC hits (there is no inefficiency of this type in the SIMARG simulation). Individual LTF masks are eliminated later in the program (TRIGGR, ELTF3) to simulate the experimental efficiency. The principal reason for this is that to repeat the full LTF simulation 38 times (for each trigger period) for each event with different drift chamber efficiencies would consume an incredible amount of computer time. It is also difficult to see how one could install particle type dependences on this level. Additionally, the LTF efficiency is easily determined directly from Bhabha events, but not the drift chamber efficiency.

LTFRD

This is called from LTF and reads the full LTF simulation output from unit 13 (a file written by LTFDUMP). The order of events on unit 13 does not have to match those from the input Monte Carlo data set (the program will search unit 13 until it finds a match to input event or loops completely). This allows the user to save time by only

calling the TRIGGR program for events that pass his analysis cuts - LTFRD will then skip over the events on unit 13 that were rejected until unit 13 catches up.

MCTYPE

This subroutine determines which of the user-specified Monte Carlo data types corresponds to the current event (as defined in UASIGN). If there is only one data type specified (this is the default) the routine is not called.

PLOTXX,SYSSYM

These are dummy routines to prevent the ARGUS detector display graphics from being included in the executable module.

SHUN00

This is a special version of SHUNPK. It is called from TRBLD in order to unpack the pulse heights needed to build the analog sums over trigger elements. This version is needed as special values of XSHEND, XSHBAR are used in the trigger simulation. The newer versions of SHUNPK in the reconstruction override these. These variables are used in the normal reconstruction to convert the energy in the scintillator to the total energy (energy in scintillator and lead). These numbers are different for the barrel and endcap counters because of the different sampling rates. They also differ for data and SIMARG Monte Carlo. The difference represents a scale factor needed to convert the Monte Carlo pulse height to the same scale as the data pulse height (XSH(data)/XSH(Monte Carlo)) which is used to determine the trigger thresholds. This scaling has been checked for minimum ionizing particles which are the most sensitive to threshold effects. In older versions of the package the call in TRBLD was made to the normal SHUNPK which interfered with the reconstruction if run simultaneously.

SHUNRD

This routine is an alternate version of SHUN00 which recreates the shower counter pulse height bank from Monte Carlo traced track bank information. The energy deposited is derived from experimental data and replaces that from the GHEISHA/EGS simulation in SIMARG. This is, at present, only available for pions and kaons. The approximation is made that the total energy of each shower is concentrated in the counter which had the highest energy in the original GHEISHA/EGS simulation.

SHUNMT

This routine an alternate version of SHUN00 and is used to check the approximation made in SHUNRD. The entire energy from each GHEISHA/EGS shower is concentrated in the central counter of each shower.

TETOT,THESH,TCPPT

This set of routines provides the threshold shape parametrization, they have as arguments the pulse height in the trigger element and return an efficiency. The threshold functions are reproduced well by "S" curves:

$$P_{element} = ((\frac{\alpha}{X})^{\beta} + 1)^{-1}$$

where $P_{element}$ is the probability of setting the discriminator for a pulse height X. The parameter α is the nominal threshold ($P = 0.5$) while β controls the steepness of the rise. For the ETOT parametrization β is a constant, while for the CPPT and HESH a linear interpolation between two limiting values is used. In principle, these functions should actually be a convolution of a step function and a pulse height dependent Gaussian representing the resolution (dominated, at this level, by the variation of calibration constants over a trigger element). However, this functional form reproduces the threshold shapes to better than 1% RMS.

THFILT

This is a version of Dr. Schultz's VAX event filter modified for offline use with the trigger program.

THRESH

This routine is called from TRIGGR. It provides access to the various threshold parametrization functions (TETOT, THESH, and TCPPT) and the old LTF simulation routines (ELTF1, ELTF2). THRESH serves as a buffer between these routines and the trigger program. These routines are all included in the same source library member along with the new LTF simulation function, ELTF3, a set of random number generators (RN, RANKIN, RANKOU, GAUZ), and a program to print out the threshold and efficiency parameters (PARDMP).

TRBLD

This routine is a collection of several routines from Dr. Schultz. The pulse heights from individual shower counters are summed to build the trigger element pulse height. This routine calls TFUNPK and SHUN00.

TRCPPT,TRETOT,TRHESH,TRMATX

These routines simulate the corresponding pre-triggers. The corresponding threshold parametrizations (TETOT etc.) are called to decide which trigger elements are set.

TREVIN

This is the initialization of the trigger program, instigated by the first call to TRIGGR. The program loops over the entire run file calling UCUTTR and UCUTRN to determine

the luminosity of each trigger period required by the user. The luminosity weighted energy distribution for each trigger period is also stored in HBOOK histograms for use in correcting event weights for the beam energy distribution. UASIGN and PARDMP are also called.

TRGEND

This is the termination routine for the trigger program. It prints out the trigger acceptance for each trigger period requested and the luminosity averaged trigger acceptance. It also prints out the average LTF efficiency (the probability that the LTF will produce one or more masks if a track hits a ToF counter) and the probability of the CPPT, HESH, and ETOT being set if there is more than 3 MeV scintillator energy in a trigger element (this value is slightly misleading as it is suppressed by tails of showers running into adjoining trigger elements). The histograms containing the CMS energy distributions for each trigger period are deleted here.

TRIGGR

This is the main program of the trigger simulation. The standard call to TRIGGR is:

```
CALL TRIGGR(ILEV,LTFFLG,WEIGHT,ITTYPE,NLOOP)
```

If ILEV=0 the variable WEIGHT returns the luminosity averaged trigger probability:

$$P_{trigger} = \frac{\sum_i L_i \cdot P_i}{\sum_i L_i},$$

where the summations are over trigger periods, P_i is the trigger probability for the i^{th} period, and L_i the luminosity (as selected by UCUTRN, UCUTTR). For all ILEV nonzero the event weight is returned:

$$W = \frac{\sum_i L_i \cdot P_i}{L_{MC}},$$

where L_{MC} is the Monte Carlo luminosity for the event being processed (defined by UASIGN). LTFFLG controls the LTF simulation, if this is positive, efficiency values calculated from good quality runs are used (run flag 0), if negative all reasonable runs are used (run flag greater than -40). If |LTFFLG|=1 a fast LTF simulation (LTFFA) using only the information from ToF, drift chamber layer 17, and the reconstructed track bank is performed. |LTFFLG|=2 reads the full LTF bank information from unit 13, while |LTFFLG|=3 enables the full LTF simulation (very slow). If ITTYPE is greater than 0 only trigger period ITTYPE is simulated, otherwise all trigger periods are simulated. NLOOP controls the number of times the individual trigger probability, P_i, is calculated for each trigger period – the average value is returned. In any single loop $P_i = 0, 1$. It is much simpler to reproduce the trigger logic by deciding whether each trigger element is hit according to the calculated efficiency rather than use these efficiencies for each element to derive an efficiency for the whole trigger analytically. Averaging repeated calculations of the trigger efficiency compensates for this simplification.

TRIGGR is the main body of the trigger simulation. On the first entry the routine TREVIN is called. At this point MCTYPE is called to determine the Monte Carlo type of the current event and TRBLD is called to create the pulse height sums for the different trigger elements. A call to LTF provides an mask bank generated with 100% drift chamber efficiency and a list of scaling parameters for each LTF mask (see ELTF3). At this point the program starts looping over the trigger periods. For each trigger period the LTF efficiency is generated for each mask by ELTF3 and then the LTF bank is "filtered" randomly to reflect this. A new reduced LTF bank is created for later use in the simulation of the online filter. The subroutines TRETOT, TRCPPT, TRHESH, and TRMATX then set up the words found normally in the trigger bit box bank of the PDP record in real data (the event record is not changed, this information is accessible only through the TRIGGR code). At this point the VAX filter simulation is done if it was turned on for the current trigger period. Finally, the pre-trigger is checked against the LTF to see if a true trigger was formed and the event weight or trigger probability is calculated.

UASIGN

This function is provided to allow the user to correctly normalize and mix several Monte Carlo data sets. If the user has only one Monte Carlo data set this routine can almost be ignored (see example 2). The user must provide the trigger program (through the common blocks in UASIGN) with the Monte Carlo luminosity, the first and last run numbers for each Monte Carlo data type (a data type being segregated because of either a different event generator or a different SIMARG experiment number), and a code for the Monte Carlo data type that tells what part of the ARGUS history it is supposed to simulate. Details of this are given in the comments of the sample version of the subroutine. For each user defined data type the acceptance for each trigger period together with the average acceptance is printed out by TRGEND.

UCUTRN

The logical function UCUTRN allows the user to make, what should be, the same run quality and data type cuts as are made in the analysis of real data. This is necessary so that TRIGGR (q.v.) can calculate the average of the trigger efficiency over the trigger history. The user should write UCUTRN so that it is true for all values of the run flags, experiment and run numbers which are used in the analysis of the real data which the Monte Carlo is designed to simulate. The arguments passed to UCUTRN include the run flag, the run energy, the S & M flags, and the experiment and the run numbers they refer to.

UCUTTR

The logical function UCUTTR has only one argument, the trigger period reference number. The purpose of UCUTTR is to allow the user to make cuts on the trigger logic – to restrict the trigger periods to simulate. The default is to simulate all trigger

periods (unless the cuts of UCUTRN leave them with zero luminosity). In the macro file CTRGDAT there are several arrays in which the trigger threshold and logic parameters are stored, there are also comment cards describing the purpose of each array. These should be used to make a decision in UCUTTR. In this way one can make a consistent trigger quality decision without troubling oneself with too many of the details of the ARGUS trigger history.

UENG

This routine is supplied to allow the user to alter the weight of each event in order to compensate for the energy distribution of the ARGUS history. Clearly, for simulation of most channels, particular the Υ resonances, this is irrelevant. But for tau physics or continuum charm production it may be useful. Two gamma physics is the ideal case as the change in beam energy results only in a change to the $\gamma\gamma$ luminosity for a particular final state and not in a change in the final-state kinematics itself. The value returned by UENG should be the ratio of the cross section at a CMS energy generated according to the luminosity weighted energy distribution saved by TREVIN to the cross section at the CMS energy used for the Monte Carlo generation.

USERTE

This user supplied routine should always call TRGEND.

Appendix G

The GAGA Monte Carlo for Two-Photon Event Generation

The GAGA Monte Carlo is intended as a simple, easily extendable, event generator for two-photon physics. In the current version (GAGA105) provisions have been made for detector and trigger simulation. An interface (SIMGG07) between this program and the full ARGUS detector simulation (SIMARG) has been written. This interface program also provides access to the $\gamma\gamma$ QED event generators of Daverveldt, Behrends and Kleiss [29]. The present package includes generators optimized for production of both continuum final states and narrow resonances. Additionally, provision has been made for the implementation of complicated final-state topologies and their matrix elements.

This appendix describes the control of the generator from the user's main program and some details of the algorithms employed in the luminosity and final-state generation. Note that the GAGA105 library member, DOCUM, describes programming details such as variable definitions, bank structure and common block usage together with a short comment on the purpose of each member of the library. The member BUGS includes any new information on modifications, extensions, or corrections to this software.

The two-photon event generator operates in four distinct steps:

1. Generation of the four vectors of the scattered $e^{\pm}$ and the $\gamma\gamma$ final state, distributed according to the product of the $\gamma\gamma$ cross section (specified by the user through variable ITYP) and the luminosity for transverse photon collisions [45].
2. Phase-space generation of a particular final-state topology (specified through variable IRTYP).
3. Conversion of the phase-space distribution to that of the requested decay matrix element (controlled by variable IMTYP).
4. Simulation of the event trigger, detector acceptance, and experimental resolution.

The first three steps are accessed via a call to INGG:


```
      INCLUDE 'GG105:CGAGA.FOR'
C RANDOM GENERATOR INITIALIZATION
      CALL RNSET(1124651)
C MATRIX ELEMENT FLAG (=0, FLAT)
                  IMTYP  =  0
C FINAL STATE TOPOLOGY FLAG (=0, THEN NO FINAL STATE GENERATION)
                  IRTYP  =  0
C CROSS SECTION FLAG (=1, FLAT)
                  ITYP   =  1
C  MINIMUM,MAXIMUM ANGLES FOR ELECTRON,POSITRON PRODUCTION (RADIANS)
                  THMIN  =  .000
                  THMAX  =  PI
C  MINIMUM,MAXIMUM MASS OF FINAL STATE (GEV/C**2)
                  WMIN   =  1.
                  WMAX   =  2.5
C  LUMFLG=0,1,2 CONTINUUM; NARROW RANGE; NARROW RESONANCE
       LUMFLG=0
C  IRHO= 0->CONSTANT PROPAGATOR, 1->VDM, 2->GVDM
       IRHO=2
1      IF(MTIME(0).LT.50000)GO TO 900
C GENERATE TWO-PHOTON FINAL STATE
       CALL INGG(&900)
C
C FILL HISTOGRAMS, WRITE TO DISK ETC. (ONLY CMS
C                          VARIABLES AVAILABLE WITH IRTYP=0)
C
       GO TO 1
900    CALL OUTPUT
       STOP
       END
```

The call to INGG generates the events. The four vectors of the final state can then be found in the common block VCSB, the format of which is described in DOCUM. In this example the final-state generation is turned off (IRTYP=0 and IMTYP irrelevant), so the program will only calculate the convolution of the two-photon luminosity and the cross section requested, integrated over the kinematic range specified by WMIN< $W_{\gamma\gamma}$ <WMAX and THMIN< $\theta_{e^{\pm}}$ <THMAX. The value of the integral is printed out by the call to OUTPUT, along with statistics on the approximate cross section and accept/reject rate of the nested importance sampling algorithms. In a normal run (where a final state would be generated and events saved), the convolution of the $\gamma\gamma$ luminosity and cross section would be used to normalize the sensitivity for the final state (see appendix E). In this case (ITYP=1), the cross section is constant so only the total $\gamma\gamma$ luminosity is calculated. To determine what cross sections and propagators are currently available see member SIGMA. In this subroutine, ITYP controls a branch to the different cross-section subroutines and IRHO controls a branch to the propagator subroutines. To introduce new cross sections or propagators simply extend these branches.

There are three different algorithms available for $\gamma\gamma$ luminosity generation. LUMFLG=0 accesses subroutine LUMGN0, a continuum generator that is optimized to generate a wide $W_{\gamma\gamma}$ range, while LUMFLG=1,2 access generators (LUMGN1,LUMGN2) optimized for narrow mass ranges. These generators all use the exact α^2 luminosity for transverse photons discussed in appendix C (equation C.7) and differ only in the approximate cross sections used to generate the initial state before the exact distribution is generated by importance sampling (appendix D). With LUMFLG=0, the photon energies $(E_{\gamma 1}, E_{\gamma 2})$ and $e^{\pm}$ scattering angles $(\theta_1, \theta_2, \phi_1, \phi_2)$ are used as the independent variables for the Monte Carlo generation with the approximate luminosity:

$$\frac{d^6L^*}{dE_{\gamma 1}dE_{\gamma 2}d\Omega_1 d\Omega_2 d\phi_1 d\phi_2} = \frac{\alpha^2}{32\pi^4}\frac{(E-E_{\gamma 1})}{Q_1^2}\frac{(E-E_{\gamma 2})}{Q_2^2}\frac{E^2}{E_{\gamma 1}E_{\gamma 2}}$$

This expression has the advantage that the variables for each beam particle are independent. These variables are then generated, separately for each beam particle, in three steps:

1. The $E_{\gamma i}$ are generated according to E_γ^{-1} spectra defined by the kinematic limits of $W_{\gamma\gamma}$.
2. These are converted into the θ-integrated forms of the above distributions by appropriate importance sampling (weighting with $\ln(Q^2_{max}(E_{\gamma i})/Q^2_{min}(E_{\gamma i}))$).
3. The $\cos\theta_i$ are then generated exactly according to distributions $(E-E_{\gamma_i})/(E_{\gamma i}Q_i^2)$.
4. The ϕ_i are generated uniformly on the interval $(0, 2\pi)$.

With LUMFLG=1 or 2, a change of variables (with the appropriate Jacobian) is made from $E_{\gamma 1}$ and $E_{\gamma 2}$ to $\eta^* = \ln(E_{\gamma 1}/E_{\gamma 2})$ (pseudo-rapidity) and $W^{*2} = 4E_{\gamma 1}E_{\gamma 2}$ (pseudo-mass). These new variables are good approximations to the rapidity and final-state mass (chapter 1). These approximations are used only to steer the event generation into a useful kinematical region – the final-state mass and luminosity are still distributed according to the exact expressions of appendix C.

The weight used in the importance sampling algorithm is calculated by subroutines ZLUM, ZLUM1, or ZLUM2 for LUMFLG=0,1,2 respectively. This routine returns the value:

$$W = \frac{d^6L_{TT}}{dE_{\gamma 1}dE_{\gamma 2}d\Omega_1 d\Omega_2 d\phi_1 d\phi_2} \Big/ \frac{d^6L^*}{dE_{\gamma 1}dE_{\gamma 2}d\Omega_1 d\Omega_2 d\phi_1 d\phi_2}$$

note that the Jacobian of any change of variables will cancel. It is straightforward to alter this routine to generate events with a different $\gamma\gamma$ luminosity. For instance, to generate vector particles in the final state, one would simply substitute the expression for L_{ST} for L_{TT}. With LUMFLG> 0 there is some distortion near (within 1 MeV/c^2) the boundaries of the mass distributions as the pseudo-mass is only generated within the true mass range specified by WMIN and WMAX. This problem is easily avoided by extending these variables a small amount.

LUMFLG=2 generates events with an initial Breit-Wigner pseudo-mass distribution and needs the additional parameters (from common /CGAGA/) RES (resonance mass) and WIDLUM (resonance width). As the pseudo-mass is slightly different from the true final-state mass, the interval WMIN→WMAX should be quite wide compared to the resonance width. LUMFLG=2 is used to increase the efficiency of resonance generation. On using this option one should still install a proper resonance shape in SIGMA as the Breit-Wigner distribution of LUMFLG=2 is cancelled by the importance sampling, the use of this distribution in the initial generation only increases the algorithm's efficiency for resonances – it does not affect the final mass distribution. For optimum efficiency WIDLUM should be slightly greater than the true resonance width used in SIGMA.

LUMFLG=0,1,2 should give the same results (within the statistical error of the Monte Carlo integrations) for the same ITYP. For resonance generation the efficiency increases with LUMFLG. However, due to the use of the pseudo-mass in the generation algorithm with LUMFLG=2, this becomes less efficient than the LUMFLG=1 case when generating very narrow resonances ($\Gamma < 1$ MeV/c^2). This effect can be compensated for by making WIDLUM rather larger than the actual width of the resonance as introduced in SIGMA.

The variable IRTYP defines the topology of the final state. This is controlled by the matrix IMULT and the entries in this matrix correspond to the numbers of various types of stable particles in the final state. The value of IMULT(IRTYP,I) for I=1,5 corresponds to the number of $\pi^{\pm}$, $K^{\pm}$, K^0_s's, π^0's, and γ's respectively. If the generator is run independently of SIMARG the K^0_s and π^0 are decayed instantly while the charged particles are allowed to decay in flight (after which they are not traced). If the generator runs with SIMARG only the π^0's decays are generated and the rest of the tracking is left to the SIMARG program. The generator randomly assigns charges to the $K^{\pm}$ and $\pi^{\pm}$ but (so long as the user asks for an even number of charged particles!) produces a charge balanced final state. The matrix IMULT is initialized in member BLKDTA, so one can determine the correspondence between topology and IRTYP by listing that subroutine. For instance IRTYP=1 generates a $\pi^+\pi^-$ pair, IRTYP=2 generates a K^+K^- pair and IRTYP=3 generates a $\pi^+\pi^-\gamma$ final state.

The subroutine DECAY generates the final state once the $\gamma\gamma$ kinematics have been generated by INGG. DECAY calls the following major subroutines:

- GENERA generates phase-space decays given the invariant mass produced by the $\gamma\gamma$ luminosity generation and a particle mass list produced by DECAY.
- MATRIX weights the phase-space final state with a user-specified matrix element.
- DSPEC decays any special particles requested.

After the call to MATRIX, events of weight one are generated by the "hit or miss" method and the particles are boosted to the laboratory frame.

In addition to the topology selected by IRTYP, one can add special particles (ρ, ω etc.) to the final state. A list of the codes identifying each special particle/decay mode combination can be found in members DSPEC, BLKDTA and DOCUM. In the following example two ω particles are generated (the user is responsible for making sure the final

state has the right charge and quantum numbers, one can request a $\gamma\gamma \to K^{*+}\omega$ decay if one must):

```
      INCLUDE 'GG105:CDETECT.FOR'
      INCLUDE 'GG105:COUT.FOR'
      INCLUDE 'GG105:CGAGA.FOR'
      INCLUDE 'GG105:CTRIG.FOR'
      INCLUDE 'GG105:CSPEC.FOR'
      LOGICAL TAG
      COMMON/VCSB/P(16,100)
      EXTERNAL VECSUB
C RANDOM GENERATOR SEED
      CALL RNSET(1124651)
C FINAL STATE FLAG
                  IMTYP  =  2
                  IRTYP  =  17
                  ITYP   =  1
C SPECIAL PARTICLES OMEGA/3    K*/4   K*BAR/5
                  NSPEC  =  2
                  ISPEC(1) = 3
                  ISPEC(2) = 3
C  MINIMUM,MAXIMUM ANGLES FOR ELECTRON,POSITRON PRODUCTION (0-PI)
                  THMIN  =  .000
                  THMAX  =  PI
C  MINIMUM,MAXIMUM FINAL STATE MASSES
                  WMIN   = 1.6
                  WMAX   = 2.0
C  LUMFLG =0,1,2 CONTINUUM; NARROW RANGE; NARROW RESONANCE
C  RES    =   MASS OF RESONANCE (LUMFLG=2)
C  WIDLUM>=   WIDTH OF RESONANCE (LUMFLG=2)
      LUMFLG=0
      IRHO=2
C  TIME LEFT TERMINATION (2 MINUTES (VAX))
1     IF(MTIME(0).LE.1200000) GOTO 2
C  GENERATOR ENTRY OR DISK READ
      CALL INGG(&2)
C TRIGGER
      CALL TRIGGR(&1,&1,2.07,.04,TAG)
      IF(TAG)GO TO 1
C
C FILL HISTOGRAMS, WRITE TO DISK ETC.
C
      GO TO 1
2     CALL OUTPUT
      STOP
      END
```


In this example there are no stable particles (IRTYP=17) in addition to the $\omega\omega$ (setting IRTYP=0 would prevent the generation of any final state decay). Care should be taken with decays like $\omega \to 3\pi$ and $\eta \to 3\pi$; the routine DEC3PI in the current version will give the same Dalitz plot structure (appropriate for the ω). Both matrix elements should be installed, with an appropriate branch, in future versions of the program. In DECAY, the masses of the special particles are generated according to a simple relativistic Breit Wigner. If this produces a minimum final-state mass greater than the $W_{\gamma\gamma}$ generated by the luminosity algorithm the generation of masses for all special particles requested is repeated until the final state is kinematically allowed. This method can introduce some threshold distortions into the line shapes! There is also a call to the routine TRIGGR shown in the example, this will be discussed below.

The line shape used in the generation of special particles is a simple relativistic Breit-Wigner with a constant width, an integrable form which is optimal for Monte Carlo generation. In addition to the threshold problem discussed above, many analyses call for more complicated resonance descriptions. In these situations one should generate the final-state topology in terms of stable particles – one then fills IMULT(IRTYP,1-5) with the number of each of these desired for the final state (if the topologies already installed in the program are not sufficient). The decay is generated according to phase space and structure is imposed on it (resonances, Bose-Einstein correlations etc.) by including the appropriate matrix element. The phase-space decay fills a common block:

```
COMMON/GENOUT/PCM(5,18),WT
```

where PCM(1-4,I) is the four vector of the I^{th} particle in the final state and PCM(5,I) is its mass. One should then write a program that calculates a matrix element from these four vectors, normalizes the matrix element so that it has a maximum value of one, and multiplies the variable WT by this quantity. A call to this new routine should be installed in the routine MATRIX. This routine branches according to the value of ICHAN(IMTYP,IRTYP) so one should also modify this in the main program or BLKDTA routine so that the correct branch to the new subroutine is made. If ICHAN(IMTYP,IRTYP) has a negative value the program stops, if it is zero the decay is generated according to phase space. At present only two particle decay generators for $|JM) = |22), |21), |20), |00)$ and a three particle decay generator for the $\rho\gamma$ final state have been installed.

After a call to INGG, the array P(16,100) in common /VCSB/ will contain the four vectors of the generated particles and some additional information on parent particles (see member DOCUM). These vectors can be processed through a fast detector and trigger simulation package accessed by a call to TRIGGR (see the last example). The first two parameters of this subroutine are error return labels. The first return is used if the final state is not triggered while the second exit is taken if the final state is not triggered and reconstructed (which implies that all generated particles are within the fiducial region with tags allowed). The third and fourth variables are the maximum value of $|\cot\theta|$ and the minimum value of $P_\perp$ required for a particle to be considered reconstructed (if these are extended outside the fiducial region of the detector they

are ignored by TRIGGR). The fifth argument of the TRIGGR subroutine is a logical variable that is true if one of the beam particles is tagged (within the region specified). TRIGGR smears the four vectors of the charged tracks and photons, and the new values are copied to the array P(16,100) in /VCSB/ so that both the original and smeared values are accessible. As yet, the routine TRIGGR includes only the geometry of the pre-triggers, LTF, and detector. Efficiencies and the effects of multiple scattering, energy loss, and calorimeter showers are not included. Charged particles are allowed to decay in flight though the daughter particles are not traced. The charged particles are not traced further than the ToF counters in any case. A call from TRIGGR to the routine PID produces ToF and dE/dX particle identification information in common block /XI2/CHI2(2,5,10) (the format is described in member DOCUM).

Bibliography

[1] J. Schwinger (ed.), *"Selected Papers on Quantum Electrodynamics"*, Dover, 1958.

[2] Particle Data Group, *"Review of Particle Properties"*, Phys. Lett. 204B(1988).

[3] H. Albrecht *et al.* (ARGUS), Phys. Lett. 202B(1988)149.

[4] F. E. Close, *"An Introduction to Quarks and Partons"*, Academic Press, New York, 1979.

[5] M. Gell-Mann, Phys. Lett. 8(1964)214.

[6] G. Zweig, CERN TH-401,402 (1964), and in *"Symmetries in Elementary Particle Physics"*, A. Zichichi (ed.), New York, Academic Press, 1965.

[7] J. I. Friedman and H. W. Kendall, Ann. Rev. Nucl. Sci. 22(1972)293.

[8] M. Gell-Mann, *"The Eightfold Way"*, W. A. Benjamin, New York, 1964;
S. Okubo, Prog. Theor. Phys. 27(1962)949.

[9] S. L. Wu, Phys. Rep. 107(1984)54.

[10] C. Llewellyn-Smith, Phys. Rep. 3(264)1974.

[11] K. W. McLean (ARGUS), in *"Proceedings of the Third Lake Louise Winter Institute"*, B. A. Campbell *et al.* (eds.), World Scientific, 1988.

[12] M. Kobayashi and T. Maskawa, Prog. Theor. Phys. 49(1973)652.

[13] S. Glashow, Nucl. Phys. B22(1961)579;
S. Weinberg, Phys. Rev. Lett. 19(1967)1264;
A. Salam and J. C. Ward, Phys. Lett. 13(1964)13;
C. H. Lai (ed.), *"Gauge Theory of Weak and Electromagnetic Interactions"*, World Scientific, 1981.

[14] G. Arnison *et al.*, Phys. Lett. B122(1983)103;
G. Arnison *et al.*, Phys. Lett. B126(1983)398;
M. Banner *et al.*, Phys. Lett. B122(1983)476;
P. Bagnia *et al.*, Phys. Lett. B129(1983)130.

[15] H. Albrecht *et al.* (ARGUS), Phys. Lett. 192B(1987)245.

[16] W. J. Marciano, in *"Eighth Workshop on Grand Unification"*, K. C. Wali (ed.), Syracuse, New York, World Scientific, 1987, p. 185.

[17] M. S. Turner, *"Intersection between Elementary Particle Physics and Cosmology"*, T. Piran and S. Weinberg (eds.), Jerusalem, World Scientific, 1984, p.125.

[18] M. Jacob, CERN preprint TH/84-3807, 1984.

[19] E. Radermacher, CERN Preprint EP/84-041, 1984;
K. H. Mess, B. H. Wiik, DESY Preprint 82-011, and talks given at the "Les Houches Summer School", 1981.

[20] M. Delbruck, Z. Phys 84(1933)144.

[21] R. R. Wilson, Phys. Rev. 90(1953)720.

[22] E. Iacopini, paper presented at the "International School of Physics of Exotic Atoms: Fourth Course on Fundamental Interactions in Low-Energy Systems", Erice, Italy, 1984.

[23] H. Euler and B. Kockel, Nass. Wiss. 23(1935)246;
H. Euler, Ann. Physik 26(1936)398;
A. I. Akhiezer, Phys. Zeit. Sow. 11(1937)263;
R. Karplus and M. Neuman, Phys. Rev. 83(1951)776;
B. deTollis, Nuovo Cimento 32(1964)757, 35(1965)1182;
H. Cheng, E. C. Tsai, and X. Zhu, Phys. Rev. D26(1982)922.

[24] F. Low, Phys. Rev. 120(1960)582.

[25] E. Fermi, Z. Phys 29(1924)315;
C. Weizsäcker, Z. Phys. 88(1934)612;
E. J. Williams, Proc. Roy. Soc. London (Series A) 139(1933)163; Phys. Rev. 45(1934)729.

[26] D. A. Williams *et al.* (Crystal Ball at DORIS), Phys. Rev. D38(1988)1365;
D. A. Williams, *" Formation of the Pseudoscalars, π^0, η, and η' in the Reaction $\gamma\gamma \to \gamma\gamma$"* (Ph.D. thesis), Harvard, 1987.

[27] F. Calogero and C. Zemach, Phys. Rev. 120(1960)1860.

[28] L. D. Landau and E. M. Lifshitz, Sov. Phys. 6(1934)244.

[29] F. A. Berends, P. H. Daverveldt, and R. Kleiss, Nucl. Phys. B253(985)441, and Comp. Phys. Comm. 40(1986)185.

[30] S. J. Brodsky *et al.* (eds.), *"Proceedings of The International Colloquium on Photon-Photon Collisions in Electron-Positron Storage Rings"*, Paris, Journal de Physique, 35, Coll. C-2, Suppl.3

[31] J. F. Gunion (ed.), *"Proceedings of the International Conference on Two-Photon Interactions"*, Lake Tahoe, 1979.

[32] G. Cochard and P. Kessler (eds.), *"$\gamma\gamma$ Collisions, Proceedings of the International Workshop"*, Amiens, Springer-Verlag, 1980.

[33] G. W. London (ed.), *"Proceedings of the IVth International Workshop on $\gamma\gamma$ Interactions"*, Paris, 1981.

[34] Ch. Berger (ed.), *"Photon-Photon Collisions, Vth International Workshop"*, Aachen, Springer-Verlag, 1983.

[35] R. L. Lander (ed.), *"Photon-Photon Collisions, VIth International Workshop"*, Granlibakken, USA, 1984.

[36] A. Courau and P. Kessler (eds.), *"Photon-Photon Collisions, VIIth International Workshop"*, Paris, World Scientific, 1986.

[37] *"Proceedings of the VIIIth International Workshop on Photon-Photon Collisions"*, Jerusalem, 1988.

[38] W. Wagner, PITHA 83/03, lectures given at the "7th Nordic Meeting on Elementary Particle Physics", Spatind, 1982.

[39] H. Kolanoski, *"Two-Photon Physics at e^+e^- Storage Rings"*, Springer-Verlag, 1984.

[40] J. H. Field, LPNHE 84-04, *"Photon-Photon Collisions"*, submitted to Reports on Progress in Physics.

[41] Ch. Berger and W. Wagner, *"Photon-Photon Reactions"*, Phys. Rep. 146(1987)1.

[42] S. Cooper, *"Meson Production in Two-Photon Collisions"*, Annual Review of Nuclear and Particle Physics (1988).

[43] H. Kolanoski and P. Zerwas, DESY 87-175, and *"High Energy-Electron Positron Physics"*, World Scientific, A. Ali and P. Soding eds., 1988.

[44] S. J. Brodsky, T. Kinoshita, and H. Terazawa, Phys. Rev. Lett. 972(1970)25; Phys. Rev. D4(1971)1532;
H. Terazawa, Rev. Mod. Phys. 45(1973)615.

[45] V. M. Budnev, I. F. Ginzburg, G. V. Meledin, and V. G. Serbo, Phys. Rep. 15C(1975)181.

[46] F. M. Renard, Z. Phys. C14(1982)209.

[47] M. Poppe, *"Exclusive Hadron Production in Two-Photon Interactions"*, International Journal of Modern Physics, A1(1986)545.

[48] B. C. Shen, talk given at [31], 1982.

[49] M. S. Chanowitz, talks given at [35], 1983 and [37], 1988.

[50] A. M. Eisner, talk given at the "IInd Symposium on High Energy e^+e^- Reactions", Nashville, 1984.

[51] H. J. Behrend, DESY 84-062, talk given at the "Symposium on High Energy e^+e^- Interactions", Vanderbilt University, 1984.

[52] J. H. Field, *"The Two-Photon Radiative Widths of Light Mesons As A Test of Gauge Theories With Integrally Charged Quarks"*, DESY 85-110.

[53] K. Wacker (Crystal Ball), talk given at the "1985 EPS Conference on High Energy Physics", Bari, Italy, 1985.

[54] H. Marsiske *et al.* (Crystal Ball), DESY 86-1037, talk given at the "XXIII International Conference on High Energy Physics", Berkeley, California, 1986;

[55] J. Haissinski, in [36] and LAL 86/16, 1986.

[56] S. L. Cartwright, talk given at "Physics in Collision VI", Chicago, RAL-86-100, 1986.

[57] J. Olsson, DESY 87-136, talk given at the "1987 International Symposium on Lepton and Photon Interactions at High Energies", Hamburg, West Germany, 1987.

[58] A. Levy, DESY 88-115, talk given at the "Rochester Conference", Munich, 1988.

[59] H. Kolanoski, DESY 88-167, talk given at the "IXth European Symposium on Antiproton-Proton Interactions and Fundamental Symmetries", Mainz, 1988.

[60] G. Gidal, LBL-26172, talk given at the "BNL Workshop on Glueballs, Hybrids, and Exotic Hadrons", Upton, N.Y., 1988.

[61] S. J. Brodsky, summary talk in [37].

[62] L. D. Landau, Sov. Phys. Dok. 60(1948)207;
C. N. Yang, Phys. Rev. 77(1950)242.

[63] H. Aihara *et al.* (TPC/$\gamma\gamma$), Phys. Rev. Lett. 57(1986)2500; Phys. Rev. D38(1988)1; Phys. Lett. B209(1988)107.

[64] G. Gidal *et al.* (Mark II/PEP), in *"Proceedings of the XXIInd International Conference on High Energy Physics"*, Berkeley, World Scientific, 1986;
G. Gidal *et al.* (Mark II/PEP), Phys. Rev. Lett. 59(1987)2016.

[65] Presented by CELLO in [37].

[66] P. Hill *et al.* (JADE), Z. Phys. C42(355)1989.

[67] G. Gidal *et al.* (Mark II/PEP), Phys. Rev. Lett. 59(1987)2012.

[68] P. M. Patel, talk given at the "BNL Workshop on Glueballs, Hybrids, and Exotic Hadrons", Upton, N.Y., 1988.

[69] S. L. Adler, Phys. Rev. 177(1969)2426;
J. S. Bell and L. Jackiw, Nuovo Cimento 60A(1969)47.

[70] H. W. Atherton *et al.*, Phys. Lett. 158B(1985)81.

[71] C. Bemporad *et al.*, Phys. Lett. 26B(1967)380.

[72] A. Browman *et al.*, Phys. Rev. Lett. 32(1974)1067.

[73] A. Weinstein *et al.* (Crystal Ball at SPEAR), Phys. Rev. D28(1983)2896.

[74] W. Bartel *et al.* (JADE), Phys. Lett. 160B(1985)421.

[75] H. Aihara *et al.* (TPC/$\gamma\gamma$), Phys. Rev. D33(1986)844.

[76] N. A. Roe *et al.* (ASP), Phys. Rev. D41(1990)17;
N. A. Roe, SLAC-0338, *"Resonance Production in Two-Photon Interactions"* (Ph.D. thesis), 1988.

[77] J. K. Bienlein (Crystal Ball at DORIS), DESY 88-165.

[78] G. S. Abrams *et al.* (Mark II at SPEAR), Phys. Rev. Lett. 43(1979)477;
P. Jenni *et al.* (Mark II), Phys. Rev. D27(1983)1031.

[79] W. Bartel *et al.* (JADE), Phys. Lett. 113B(1982)190.

[80] H. J. Behrend *et al.* (CELLO), Phys. Lett. 114B(1982)378; erratum 125B(1983)518.

[81] Ch. Berger *et al.* (PLUTO), Phys. Lett. 142B(1984)125.
M. Feindt, *"Study of Two-Photon Production of η' Mesons with the Detector PLUTO"*, (diploma thesis, in german), DESY 84-03, 1984.

[82] M. Althoff *et al.* (TASSO), Phys. Lett. 147B(1984)487 and [199].

[83] G.Gidal (Mark II), talk given at the "XVIth Symposium on Multiparticle dynamics", Kiryat-Anavim, Israel, LBL-19992, 1985.

[84] H. Albrecht *et al.* (ARGUS), Phys. Lett. 199B(1987)457.

[85] H. Aihara *et al.* (TPC/$\gamma\gamma$), Phys. Rev. 35D(1987)2650;
B. K. van Uitert, *"Formation of η' Mesons in Photon-Photon Collisions"* (Ph.D. thesis), State University of Utrecht, Netherlands, 1986;
K. A. Schwitkis, *"A Study of Resonance Production in Two-Photon Interactions"* (Ph.D. thesis), University of California at Santa Barbara, 1987.

[86] A. Blinov *et al.* (MD1), Novosibirsk Preprint 87-92, 1987.

[87] G. Gidal *et al.* (Mark II), Phys. Rev. Lett. 59(1987)2012.

[88] D. Antreasyn *et al.* (Crystal Ball at DORIS), Phys. Rev. D33(1987)2633.

[89] J. Olsson (JADE), in [37].

[90] H. Aihara *et al.* (TPC/$\gamma\gamma$), Phys. Rev. D38(1988)1;
H. Aihara *et al.* (TPC/$\gamma\gamma$), Phys. Rev. Lett. 64(172)1990.

[91] W. Bartel *et al.* (JADE), Phys. Lett. 160B(1985)421.

[92] Ch. Berger *et al.* (PLUTO), Phys. Lett. 94B(1980)254.

[93] A. Roussarie *et al.* (Mark II at SPEAR), Phys. Lett. 105B(1981)304.

[94] R. Brandelik *et al.* (TASSO), Z.Phys. C10(1981)117.

[95] W. R. Frazer, in [34];
J. Dainton, talk given at the "EPS International Conference on High Energy Physics", J. Guy and C. Costain (eds.), Brighton, 1983.

[96] J. R. Smith *et al.* (Mark II at PEP), Phys. Rev. D30(1984)851;
J. R. Smith, *"Two-Photon Production of the f_0 Meson"* (Ph.D. thesis), University of California at Davis, RX-1171, 1982.

[97] A. Courau *et al.* (DELCO), Phys. Lett. 147B(1984)227.

[98] Ch. Berger *et al.* (PLUTO), Z. Phys. C26(1984)199.

[99] H. J. Behrend *et al.* (CELLO), Z.Phys. C23(1984)223.

[100] H. Aihara *et al.* (TPC/$\gamma\gamma$), Phys. Rev. Lett. 57(1986)404.

[101] R. P. Johnson, *"Measurements of Charged Two Particle Exclusive States in Photon-Photon Interactions"* (Ph.D. thesis), SLAC-294, 1986.

[102] Mark II collaboration in [37], 1988.

[103] I. Adachi *et al.* (TOPAZ), KEK-Preprint-89-156, 1989, submitted to Physics Letters B.

[104] C. Edwards *et al.* (Crystal Ball at SPEAR), Phys. Lett. 110B(1982)82.

[105] D. Antreasyn *et al.* (Crystal Ball at DORIS), Phys. Rev. D33(1986)1847;
H. Marsiske, *"$\pi^0\pi^0$ Production in Photon-Photon Reactions"*, (Ph.D. thesis, in german), DESY-F31-88-02, 1988.

[106] H. Albrecht *et al.* (ARGUS), DESY 89-179.

[107] G. Menessier, Z. Phys C16(1983)241.

[108] Ch. Berger *et al.* (PLUTO), Phys. Lett. 149B(1984)427.

[109] M. Althoff *et al.* (TASSO), Z. Phys. C31(1986)537 and [199].

[110] H. Aihara *et al.* (TPC/$\gamma\gamma$), contributed paper #297 to the Proceedings of The 1987 International Symposium on Lepton and Photon Interactions at High Energies, Hamburg, West Germany, 1987;
A. Eisner *et al.* (TPC/$\gamma\gamma$), contributed paper to the Proceedings of the International Europhysics Conference on High Energy Physics, Uppsalla, 1987.

[111] H. J. Behrend *et al.* (CELLO), DESY 89-177, 1989.

[112] M. Althoff *et al.* (TASSO), Phys. Lett. 121B(1983)216.

[113] H. Aihara *et al.* (TPC/$\gamma\gamma$), Phys. Rev. Lett. 57(1986)404.

[114] G. Gidal (Mark II), in [36].

[115] Ch. Berger *et al.* (PLUTO), Z. Phys. C37(1988) 329.

[116] H. J. Behrend *et al.* (CELLO), Z. Phys. C43(1989)91.

[117] ARGUS Collaboration, DESY proposal PRC 83/06.

[118] K. W. McLean, *"Two-Photon Physics With The ARGUS Detector"* (M.Sc. thesis), McGill University, Montreal, 1985.

[119] S. E. Baru *et al.* (MD1), INP Novosibirsk preprint, 1984.

[120] T. Jensen *et al.* (CLEO), DOE/ER/01545-429, 1989, presented at the 1989 International Symposium on Heavy Quark Physics, Ithaca, N.Y., 1989;
W. Y. Chen *et al.* (CLEO), CLNS-89/963, 1989.

[121] D. A. Bauer, UCSB-HEP-89-05, presented at the B Factory Workshop, Syracuse, N.Y., 1989;
E. Maina, DFTT-4/88, presented at the Workshop on Heavy Quark Factories, Cormayeur, Italy, 1987.

[122] J. H. Field, in [34], 1983.

[123] J. C. Sens, CERN-EP/88-99, and in [37], 1988;
P. M. Zerwas, PITHA-88/18, and in [37], 1988.

[124] H. Hasemann *et al.*, DESY Internal Report F15-Pro 148, October 1978.

[125] W. R. Innes *et al.*, Phys. Rev. Lett. 39(1977)1240;
S. W. Herb *et al.*, Phys. Rev. Lett. 39(1977)252.

[126] K. Berkelman, Phys. Rep. 98(1983)145;
D. Besson *et al.* (CLEO), Phys. Rev. Lett. 54(1985)381;
D. M. J. Lovelock *et al.* (CUSB), Phys. Rev. Lett. 54(1985)377.

[127] G. Eigen *et al.* (CUSB), Phys. Rev. Lett. 49(1982)1612;
K. Han *et al.* (CUSB), Phys. Rev. Lett. 49(1982)1616;
C. Klopfenstein *et al.* (CUSB), Phys. Rev. Lett. 51(1983)160;
F. Pauss *et al.* (CUSB), Phys. Lett. 130B(1983)439.

[128] W. Funk, *"Inclusive $\pi^{\pm}$, $K^{\pm}$, $\bar{p}$ Production in Electron-Positron Annihilation and $\Upsilon(1S)$ Resonance Decays"* (diploma thesis, in german), Universität Heidelberg, 1988.

[129] H. Albrecht *et al.* (ARGUS), Nucl. Instr. and Meth. 275(1989)1.

[130] H. Nesemann, *"Proceedings of the International Symposium on Production and Decay of Heavy Hadrons"*, Heidelberg, 1986;
H. Nesemann and K. Wille, DESY Internal Report M-83-09, 1983 and I.E.E.E. Trans. Nucl. Sci. 30(1983)1998;
K. Wille, DESY Report 81-047, 1981;
H. Neseman, J. Susta, F. Wedstein and K. Wille, *"Proceedings of the 11th International Conference on High Energy Accelerators"*, Geneva, 1980.

[131] R. K. Bock *al.* (editors), *"Formulae and Methods in Experimental Data Evaluation I: General Glossary"*, CERN, 1984.

[132] H. Albrecht et al. (ARGUS), Phys. Lett. 210B(1988)267;
D. J. Gilkinson, *"Measurements of Charmed Meson Lifetimes"* (Ph.D. thesis), University of Toronto, 1987.

[133] R. L. Childers and Y. Oku, Technical Report DESY-F15-83-01, DESY, 1983.

[134] M. Danilov *et al.*, Nucl. Instr. and Meth. 217(1983)153.

[135] G. H. Trilling and A. D. Johnson, LBL Internal Memo TG-301, 1978;
H. Kapitza, Technical Report, DESY 1986.

[136] J. A. McKenna, *"Production and Decay of the D_S and D_S^* Mesons in e^+e^- Annihilation"* (Ph.D. thesis), University of Toronto, 1987.

[137] F. Sauli, in *"Experimental Techniques in High Energy Physics"*, T. Ferbel (ed.), Addison-Wesley, 1987.

[138] L. Malter, Phys. Rev. 50(1936)48.

[139] M. Danilov *et al.*, Nucl. Instr. and Meth. A274(1989)189.

[140] A. Nilsson, ARGUS Software Note #36, 1986.

[141] B. Rossi, "*High Energy Particles*", section 53, Prentice-Hall, 1952.

[142] J. Hasemann, "*Proceedings of the International Conference on Instrumentation for Colliding Beam Physics*", Stanford 1982, SLAC-250, 80;
Y. Oku, "*A Study of Particles Produced in e^+e^- Annihilation at a Center-of-Mass Energy of Around 10 GeV, using Ionization Loss Measurements*" (Ph.D. thesis), Lund University, 1985.

[143] J. C. Yun, "*A Vertex Chamber for ARGUS*" (M.Sc. thesis), Carleton University, Ottawa, 1984;
K. W. Edwards *et al.*, Nucl. Instr. and Meth. A252(1986)384.

[144] R. Heller *et al.*, Nucl. Instr. and Meth. A235(1985)26.

[145] R. Heller, Preprint IHEP-HD/ARGUS/81-1, University of Heidelberg, 1981;
R. Heller, "*Study of Hadronic Transitions Between Υ' and Υ with the ARGUS Detector*" (Ph.D. thesis, in german), Universität Heidelberg, 1984.

[146] W. Hoffmann *et al.*, Nucl. Instr. and Meth. 163(1979)77, 195(1982)475;
A. Drescher *et al.*, Nucl. Instr. and Meth. A205(1983)125, A216(1983)35, A237(1985)464, A249(1983)277.

[147] K. Kleinknecht, "*Particle Detectors*", Phys. Rep. 84(1984)2.

[148] J. Spengler, private communication.

[149] A. Drescher, "*Measurement of Inclusive Spectra of π^0 and η Mesons in the Energy Region of the Υ-Resonances with the ARGUS Detector*", (Ph.D. thesis, in german), Universität Dortmund, 1987.

[150] R. L. Ford and W. R. Nelson, SLAC-210/UC-32, 1978.

[151] A. Arefiev *et al.*, DESY 83-025 and Instr. Exp. Tech. 29(1986)333.

[152] B. Fominykh and V. Matveev, ARGUS Software Note #14.

[153] S. Weseler, "*A Study of The Semi-leptonic Decays of B(5270) Mesons with the ARGUS Detector*" (Ph.D. thesis, in german), Universität Heidelberg, 1986.

[154] C. W. Darden, ARGUS Software Note #4, 1983.

[155] H. D. Schultz and H. J. Stuckenberg, "*Proceedings of the Topical Conference on the Application of Microprocessors in High Energy Physics Experiments*", Geneva 1983, CERN 81-07, 94;
H. D. Schultz, private communications.

[156] R. Wurth and H. D. Schulz, "*Proceedings of the Third International Conference on Instrumentation for Colliding Beam Physics*", Novosibirsk (1984) 179.

[157] K. Strahl, private communications.

[158] H. Albrecht, ARGUS Internal Note.
U. Mathiesen, ARGUS Software Note #29.

[159] C. Hast, (diploma thesis, in german), Universität Dortmund, 1988.

[160] G. Braunshausen, "*Luminosity Measurement For ARGUS With Bhabha Scattering As Gauge Reaction*" (diploma thesis, in german), Universität Heidelberg, IHEP-HD 84-005, 1984.

[161] H. Gennow, DESY Technical Report, F15-85-02, 1985.

[162] D. Kamp, ARGUS Software Note #42, 1986;
H. Fesefeldt, DESY Technical Report, 1984.

[163] R. Brun *et al.*, CERN Technical Report DD/78/2, 1978.

[164] H. Albrecht *et al.* (ARGUS), Phys. Lett. 179B(1986)403.

[165] Ch. Berger *et al.* (PLUTO), Nucl. Phys. B202(1982)189;
H. Kolanoski, in [34], 1983.

[166] L. Shabhazian (Ph.D. thesis), McGill University, Montreal, (1982).

[167] G. Tsipolitis and A. Nilsson, private communications.

[168] G. Köpp, T. Walsh, and P. Zerwas, Nucl. Phys. B70(1974)461.

[169] J. D. Jackson, Nuovo Cimento 34(1964)1644.

[170] K. M. Blatt and V. F. Weisskopf, "*Theoretical Nuclear Physics*", (John Wiley and Sons, New York) (1952) pp.359-365 and pp.386-389.

[171] A. Rittenberg, "*Properties of the η' Meson*" (Ph.D. thesis), Berkeley, UCRL 18863, 1969.

[172] J. Olsson, DESY, private communication.

[173] D. Coffmann *et al.* (Mark II at SPEAR), SLAC-PUB-4424, 1988, to be published in Physical Review D.

[174] S. J. Brodsky and G. P. Lepage, Phys. Rev. D24(1981)1808.

[175] D. Faiman, H. J. Lipkin, and H. R. Rubinstein, Phys. Lett. 59B(1975)269.

[176] D. G. Hitlin, talk given at the "BNL Workshop on Glueballs, Hybrids, and Exotic Hadrons", Upton, N.Y., 1988.

[177] E. H. Kada, P. Kessler, and J. Parisi, Phys. Rev. D39(1989)2657.

[178] D. M. Binnie *et al.*, Phys. Lett. 83B(1979)141.

[179] J. Jousset *et al.* (DM2), LAL 88-25, 1988, submitted to Physical Review D.

[180] D. Coffmann *et al.* (Mark III), Phys. Rev. D38(1988)2695.

[181] J. F. Donoghue, B. R. Holstein, and Y. C. R. Lin, Phys. Rev. Lett. 55(1985)2766;
J. Gasser and H. Leutwyler, Nucl. Phys. B250(1985)465;
G. Grunberg, Phys. Lett. 168B(1986)141.

[182] J. L. Rosner, Phys. Rev. D27(1983)1101, and refs. 4-15 quoted therein.

[183] R. M. Baltrusaitis et al. (Mark III), Phys. Rev. D32(1985)2883.

[184] H. Suura, T. Walsh, and B. Young, Lett. Nuovo Cimento 4(1972)505.

[185] J. Babcock and J. L. Rosner, Phys. Rev. D14(1976)1286.

[186] V. M. Budnev and A. E. Kaloshin, Phys. Lett. 86B(1979)351.

[187] P. Singer, Phys. Lett. 124B(1983)531.

[188] S. Godfrey and N. Isgur, Phys. Rev. D32(1985)189;
T. Barnes, in [36], 1986.

[189] S. B. Berger and B. T. Feld, Phys. Rev. D8(1973)3875.

[190] L. Bergstroem *et al.*, Z. Phys. C16(1983)263.

[191] L. Köpke and N. Wermes, *"J/ψ Decays"*, Phys. Rep. 174(1989)67.

[192] G. Bonneau, M. Gourdin, and F. Martin, Nucl. Phys. B34(1973)573.

[193] J. D. Bjorken and S. D. Drell, *"Relativistic Quantum Mechanics"*, McGraw-Hill, 1964.

[194] D. A. Dicus, Phys. Rev. D14(1977)2524.

[195] K. Binder and D. Stauffer, *"Applications of the MC Method"*, Topics in Current Physics 36, Springer-Verlag, 1983.

[196] F. James, *"Formulae and Methods in Experimental Data Evaluation III: Numerical Integration"*, Section N, CERN, 1984.

[197] S. Brandt, *"Formulae and Methods in Experimental Data Evaluation III: Elements of Probability and Statistics"*, Section J, CERN, 1984.

[198] F. James and M. Roos, Comp. Phys. Comm. 10(1975)343;
F. James and M. Roos, CERN Computer Center Program Library long write-up D506, CERN, 1987.

[199] R. Mir, *"Formation of Resonances with Final State Photons In Two-Photon Interactions and Development of Calorimetric Techniques"* (Ph.D. thesis), Weizmann Institute, 1986.

The Author's Personal Contributions to the ARGUS Experiment

The body of this thesis describes my personal contributions to the physics analysis of the ARGUS experiment. These include the analysis of η' production in $\gamma\gamma$ collisions published in 1986 [84] and the analysis of K^+K^- production to be published in 1990 [106]. I was also closely involved with the publication of the papers on $\gamma\gamma$ physics produced by the ARGUS collaboration.

During my three year residency at DESY I worked shifts on the detector in the course of collecting data. This work involved continuous monitoring of the data quality and the functioning of the various components while the storage ring was operational.

My principal contributions to the analysis software of the experiment are:

i) The creation of a versatile two-photon luminosity generator, together with a final state decay generator, and a fast simulation program for the ARGUS detector. These programs are described in appendix G and have also been used by the OPAL experiment.

ii) An interface between my two-photon collision generator, other event generators, and the SIMARG detector simulation program.

iii) Optimization of a trigger simulation program written by H. D. Schulz. This included the introduction of the effect of the VAX Online filter, experimentally determined pre-trigger threshold shapes, drift chamber efficiency distributions (including particle mass and geometric effects), and provisions to properly sample the time variation of both the efficiencies and the trigger logic.

iv) Ongoing experimental measurement of the efficiencies of the experiment for this trigger program and data quality monitoring.

v) Production of EXTWOP two-prong tapes for general use in the collaboration.

vi) Verification of the effects of the VAX Online filter before its introduction.

vii) Introduction of a Vertex Detection Chamber extension to the LTF (developed on the IBM by H. D. Schulz and a Lund University student) in the VAX Online filter.

viii) Translation and maintenance of existing IBM and VAX software for the VAX 11/785 at McGill, and distribution of this software to collaborating institutions.